ABSTRACT

Title of Document: FUNDAMENTAL UNDERSTANDING OF SOFC CATHODE DURABILITY; A KINETICS AND CATALYSIS STUDY

Yi-Lin Huang, Doctor of Philosophy, 2015

Directed By: Professor Eric D. Wachsman,
Department of Materials Science & Engineering

Solid oxide fuel cells (SOFC) have been demonstrated as great prospects for electrochemical conversion of fuels, providing both high efficiency and high power density. Understanding the fundamentals of the oxygen reduction reaction (ORR) mechanisms is necessary to further improve cathode performance. Two different testing systems, gas phase isotopic oxygen exchange and electrical conductivity relaxation, were built to study the kinetics of cathode powders and bulk samples, respectively. A robust strategy was established to extract kinetic parameters from transient response curves for a variety of materials and conditions using numerical solutions. *In-situ* gas phase isotopic oxygen exchange, which provides real-time information about cathode surface kinetics, was used to determine the ORR mechanisms and the interactions of other gaseous species with the solid surface for two cathode materials: $La_{0.6}Sr_{0.4}Co_{0.2}Fe_{0.8}O_{3-x}$ (LSCF) and $(La_{0.8}Sr_{0.2})_{0.95}MnO_{3\pm x}$ (LSM). LSCF has a faster dissociation reaction than LSM, and the limiting step is the

surface exchange. Additionally, LSM likely contains different vacancy concentrations in the near surface region and in the bulk. A mathematic model is further established to unify surface exchange rates from different experiments and link solid-state diffusion to surface heterogeneous catalysis. In addition, the long-term durability of these materials is a major challenge. A novel technique called isotope saturated temperature programmed exchange (ISTPX) has been developed to determine the temperature and PO_2 range that is preferable for the exchange of water and CO_2 on LSM and LSCF. The presence of CO_2 and water indicates blocking effects on the LSCF surface from 300°C to 600°C, possibly resulting in two separate degradation mechanisms. On the other hand, CO_2 and water exchange with LSM through homoexchange mechanism with a relatively minor impact. Based on isotope exchange results, surface modified LSCF cathodes were fabricated. The surface modification of LSCF through Mn ion implantation enhances the chemical surface exchange coefficient (k_{chem}) from 4.4×10^{-4} cm/s to 1.9×10^{-3} cm/s at 800°C. The aims of this study are to increase knowledge and information about the ORR. The results allow us to further investigate the ORR mechanisms as well as to engineer new cathode materials/structures that can improve cathode performance and durability.

FUNDAMENTAL UNDERSTANDINGS OF SOFC CATHODES DURABILITY; A KINETICS AND CATALYSIS STUDY

By

Yi-Lin Huang

Dissertation submitted to the Faculty of the Graduate School of the
University of Maryland, College Park, in partial fulfillment
of the requirements for the degree of
Doctor of Philosophy
2015

Advisory Committee:
Professor Eric D. Wachsman, Chair
Professor Bryan Eichhorn
Assistant Professor Dongxia Liu
Assistant Professor Liangbing Hu
Professor Lourdes G. Salamanca-Riba

Acknowledgements

First, I thank my advisor Dr. Wachsman for his guidance and providing this opportunity for me to freely explore the knowledge of science. I thank Dr. Karen Gaskell of the Surface Analysis Center at the University of Maryland for her assistance and expertise in XPS. I thank Dr. Dongxia Liu for the fruitful discussion in the heterogeneous catalysis.

In addition, I thank my project collaborator Christopher Pellegrinelli. I will never forget the time we spent together. I thank the SECA project colleagues, Joshua Taillon and Dr. Salamanca-Riba. It is my honor to have this opportunity to work with you. I thank fellow group members, Colin Gore, Ashley Lydie Ruth, Ke-Ji Pan, Gregory Hitz, Thomas Hays, Adam Jolley, and Mann Sakbodin. You are always really helpful. I thank Dr. Hee Sung Yoon. Dr. Mohammed Hussain Abdul Jabbar, and Dr. Kang Taek Lee for teaching me a lot, especially Dr. Yoon. Thank all of my "American' friends who assisted me settled in U.S. and thank my "non-American" friends to accompany me. I will remember all your kindness.

For all, I thank my family for their supports. I thank my parents for their selfless love and having faith in me. I thank my brother and my sister for taking cares of me for years. I thank Hsiang-Yuan for always staying by my side to walk through everything and tolerating me.

I am the luckiest person in the world because of you all.

Table of Contents

List of Tables

List of Figures

Abbreviation

1:1 IIE: 1:1 Isothermal Isotope Exchange

A: Thermodynamic Factor

D^*: Self-Diffusion Coefficient

D_{chem}: Chemical Diffusion Coefficient

ECR: Electrical Conductivity Relaxation

IEDP: Isotope Exchange Depth Profiling

IIE: Isothermal Isotope Exchange

ISTPX: Isotope Saturated Temperature Programmed Exchange

J_O: Oxygen Flux

k^*: Self-Surface Exchange Coefficient

k_{chem}: Chemical Surface Exchange Coefficient

L_C: Characteristic Length

LSCF: $La_{0.6}Sr_{0.4}Co_{0.2}Fe_{0.8}O_{3-\delta}$

LSM: $La_{0.8}Sr_{0.2}MnO_{3\pm\delta}$

MIEC: Mixed Ionic Electronic Conducting

OCV: Open Circuit Voltage

ORR: Oxygen Reduction Reaction

PO_2: Oxygen Partial Pressure

PCO_2: Carbon Dioxide Partial Pressure

PD_2O: Heavy Water Partial Pressure

R_0: Homoexchange

R_1: Single Heteroexchange

R_2: Double Heteroexchange

R_{ex}: Rate of Heteroexchange

RMSE: Root Mean Square Error

SOFC: Solid Oxide Fuel Cells

T_θ: Isokinetic Temperature

TPX: Temperature Programmed Exchange

TPD: Temperature Programmed Desorption

V_O: Oxygen Vacancy

XPS: X-Ray Photoelectron Spectroscopy

SIMS: Secondary Ion Mass Spectrometry

SSITKA: Steady State Isotopic Kinetic Transient Analysis

YSZ: Yttria Stabilized Zirconia

Ψ: Steady State Exchange Fraction

Chapter 1: Introduction

1.1 Introduction to Solid Oxide Fuel Cells (SOFC)

Recently, significant effort has been made to achieve a sustainable energy economy. Fuel cells are one of the most promising devices that can provide clean energy by directly converting fuels to electricity through electrochemical oxidation[1-4]. The energy converting process is not governed by the same thermodynamic cycle as combustion engines, meaning the process is not limited by Carnot efficiency. It can reach over 60% electrical efficiency and exceed 90% overall efficiency in combined heat and power applications[5,6]. Solid oxide fuel cells (SOFCs) offer potential advantages over other fuel cell technologies. The high operating temperature enables SOFCs to use a variety of hydrocarbon-based fuels and is therefore compatible with common fuels such as natural gas[7]. Another important aspect of SOFCs is that they are based on solid-state energy conversion, meaning there are no moving parts, thus reducing both noise and the chance of mechanical failure. SOFCs present an alternative to combustion-based electricity generation, and are both cleaner and more efficient.

Figure 1-1 shows a schematic of the working principle of SOFCs. A SOFC consists of three main parts: a porous cathode, a porous anode, and a dense electrolyte sandwiched between. The oxygen reduction reaction (ORR) occurs on the cathode (air side) where oxygen molecules are reduced to become oxygen ions (O^{2-}). These O^{2-} ions are then available to transport through an ion-conducting electrolyte to the

anode (fuel side) where they can oxidize a fuel, such as H_2 or methane (CH_4). If we assume H and CH_4 are the fuels, the chemical reactions can be written as follows:

Cathode reaction: $\frac{1}{2}O_2 + 2e^- \rightarrow O^{2-}$ [1-1]

Anode reaction: $H_2 + O^{2-} \rightarrow H_2O + 2e^-$ [1-2]

or $CH_4 + 6O^{2-} \rightarrow CO_2 + 2H_2O + 12e^-$ [1-3]

Overall reaction: $H_2 + \frac{1}{2}O_2 \rightarrow H_2O$ [1-4]

or $CH_4 + 3O_2 \rightarrow CO_2 + 2H_2O$ [1-5]

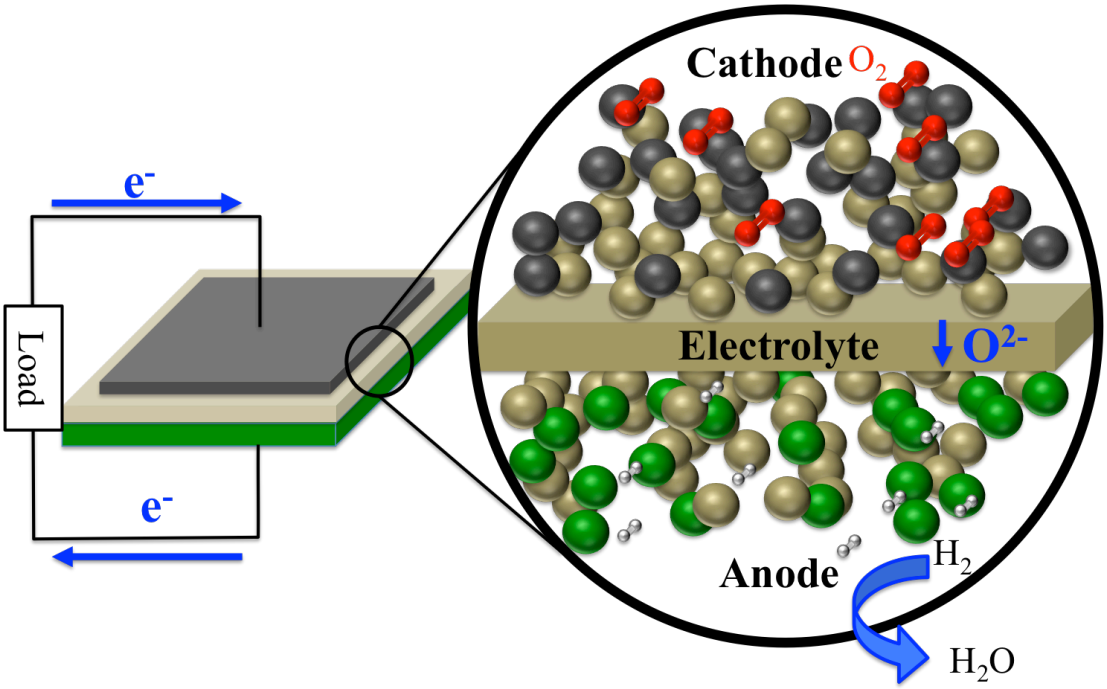

Figure 1-1. Schematic of the working principle of SOFCs. Electrons go through the leads while oxygen ions transport through the electrolyte. Oxygen molecules (red) are reduced on the cathode (grey) to become oxygen ions (O^{2-}). O^{2-} can transport through the ion-conducting electrolyte (tan) to the anode (green) to oxidize a fuel.

The open circuit voltage (OCV) of the SOFC is related to the oxygen partial pressure at each electrode, and can be calculated using the Nernst equation:

$$\text{OCV} = \frac{RT}{4F}\ln\left(\frac{PO_2^{anode}}{PO_2^{cathode}}\right) \qquad [1\text{-}6]$$

where T is the operating temperature, R is the gas constant, F is the Faraday constant, and PO_2 is the oxygen partial pressure.

1.2 Polarization Loss

Ideally, all OCV can contribute to the load. However, polarization losses from the various components decrease the output voltage. Figure 1-2 (a) shows the current-voltage profile of SOFCs and the different polarization losses[8]. The ohmic losses, η_{ohmic}, are caused by the Ohmic resistance of the electrolyte and electrode materials. The concentration loss, $\eta_{concentration}$, arises from the mass transfer process due to the gas diffusion in the porous electrodes at high current densities. The activation loss, η_{act}, the dominant polarization, is due to the oxygen reduction reaction (ORR). Specifically, the kinetic losses of the adsorption/dissociation chemical reaction and charge transfer of active oxygen species at the triple phase boundary (TPB) are the contributing factors.

Since all polarization losses in SOFCs are related to either the catalytic reactions on anode and cathode, or the ionic transport in solid, all reactions are thermally activated and the contribution of each polarization loss is a function of temperature. Figure 1-2 (b) shows the polarization loss of each component as a function of operating temperature in a SOFC[9]. These two graphs clearly show that when operating near the intermediate temperature range (IT, <700°C), losses due to the polarization resistance increase dramatically and limit the fuel cell's performance.

The majority of this cell polarization results from the inefficiencies of the ORR, which occurs at the cathode/electrolyte interface. Thus, this thermally activated ORR is a fundamental issue when trying to reduce the operating temperatures in SOFCs to intermediate temperatures.

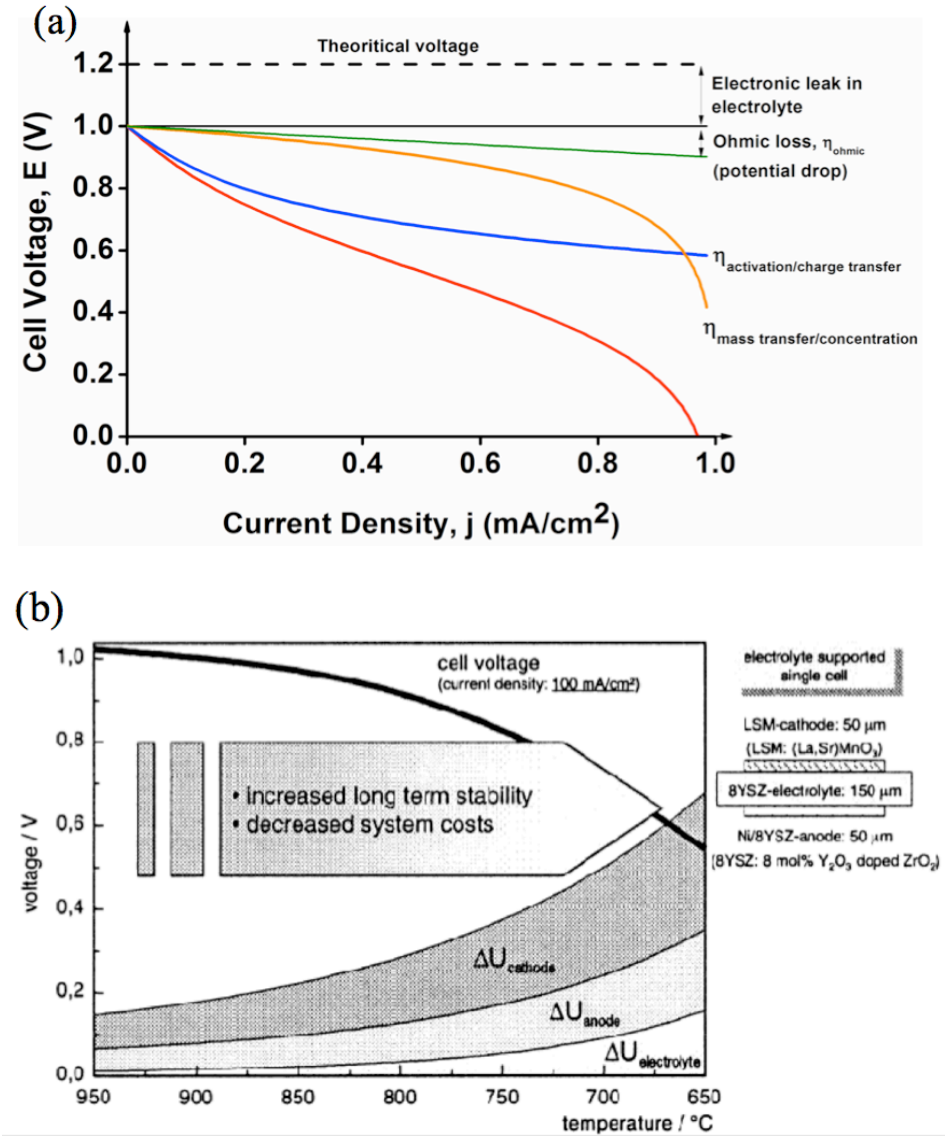

Figure 1-2 (a) Polarization losses as a function of current density in a SOFC. The red line represents the sum of all losses[8]. (b) Cell voltage and polarization losses (Δ U) at constant current density of 100mA/cm^2 as a function of operating temperature [9].

The ORR consists of a series of reaction steps, including gas diffusion, adsorption, charge transfer, dissociation, surface diffusion, incorporation, and bulk

diffusion. For different cathode materials, there are different reaction pathways with different limiting steps. It's essential to determine the limiting step for the reactions because it contributes the most to the polarization loss. Intermediate oxygen species on the cathode surface are also very important because they are the active intermediate products that are participating in the reactions. Another important factor is the activity of available sites.

Previous investigations have led to the use a simplified two-step reaction model to describe the ORR. The first step is the dissociation. The cathode surface can adsorb O_2 on the active surface sites, and then catalyze the dissociation to break the O-O bond in O_2. The second step is the incorporation, where the dissociated oxygen atom can incorporate into the lattice structure. Understanding of the ORR is crucial for the development of new cathode materials.

1.3 Perovskite Cathode Materials

Because of the high polarization loss due to the ORR, the selection of suitable cathode materials is critical for the SOFCs. Materials with the perovskite structure, such as $La_{0.6}Sr_{0.4}Co_{0.2}Fe_{0.8}O_{3-x}$ (LSCF) and $(La_{0.8}Sr_{0.2})_{0.95}MnO_{3-x}$ (LSM), have been widely used because of their catalytic activity attributed to surface oxygen vacancies and partially filled *d*-orbital of the B site transition metal[10-13]. It's generally accepted that stoichiometric $La_{0.8}Sr_{0.2}MnO_{3\pm\delta}$ and $La_{0.6}Sr_{0.4}Co_{0.2}Fe_{0.8}O_{3-\delta}$ are the optimized compositions due to their thermal expansion matching electrolyte materials such as YSZ and GDC respectively. This thermal expansion match is very important to maintain the mechanical strength and high electronic and/or ionic conductivity of the device.

In the ABO_3 perovskite structure, rare earth metals, such as La and Sr, occupy the A sites and the B sites are filled with transition metals, such as Fe and Co, or Mn. This structure often offers good electronic conduction at high temperature because of the octahedral symmetry around the transition metal[14,15]. The hole conduction is based on the small polaron conduction mechanism where charge can hop between the overlapping of 3d orbitals of transition metals. Based on the theoretical calculation, the transition metals in the perovskite structure account for the adsorption of O_2 due to the overlapping of d-orbitals, and are believed to be directly related to the reduction of O_2.

To maintain charge neutrality, the substitution of Sr(2+) to La(3+) in the A site need to be compensated by either the oxidation of the transition metals in the B site or create oxygen vacancies to maintain the charge balance. The defect equation using Kröger-Vink Notation can be expressed as:

$$[Sr_{La}'] = [B_B^{\bullet}] + [V_O^{\bullet\bullet}] \qquad [1\text{-}7]$$

The change of valence state of the transition metals will introduce various defects and lead to a change in oxygen stoichiometry. Changing oxygen partial pressure and temperature will vary the concentrations of defects, such as oxygen vacancies, in the structure and alter the catalytic properties of the materials. Therefore, all the rate constants, energy barriers, concentrations of vacancies, and number of available surface sites are variables that depend on temperature and oxygen partial pressure.

1.3.1 $La_{0.8}Sr_{0.2}MnO_{3\pm\delta}$ (LSM)

Though LSM and LSCF have a similar perovskite structure, the material properties of LSM and LSCF are quite different. The substitution of Sr in La site enhances the p-type electronic conductivity to 150 S/cm at 1000°C, and the charge imbalance is compensated by the oxidation of Mn. Therefore, LSM generally has excess oxygen in the lattice and has a stable oxygen stoichiometry even at low oxygen partial pressure (PO_2=10^{-10} atm), resulting in poor ionic conductivity[12 14-18]. The lack of oxygen vacancies limits the ionic conductivity to 10^{-7} - 10^{-6} S/cm from 900°C to 1000°C. At low temperature, LSM generally has an oxygen excess sublattice with cation vacancies. By altering temperature, PO_2, or the applied polarization, LSM can be engineered to be either super- or sub-stoichiometry. The conductivity of LSM can reach a maximum about 150 S/cm. The long-term stability and thermal expansion of LSM makes it's a good candidate for SOFC cathode. However, the high cathodic polarization of LSM at intermediate temperature limits its application. Therefore, it's important to understand the oxygen reduction reaction of LSM to further develop the cathode materials.

1.3.2 $La_{0.6}Sr_{0.4}Co_{0.2}Fe_{0.8}O_{3-\delta}$ (LSCF)

Because the ORR requires both good ionic and electronic conduction for the reduction of oxygen to take place, LSCF with double doping of Co and Fe in B site can contribute to more oxygen vacancies and high nonstoichiometry, leading to a good mixed ionic electronic conducting (MIEC) material[14,15,17,18]. At low temperature, the compensation of the charge balance due to the substitution of Sr to La is based on the oxidation of transition metals. At higher temperature, unlike LSM,

LSCF prefers to compensate the change balance by forming oxygen vacancies. The concentration of $B_B^{\bullet}$ is reduced to compensate for the formation of oxygen vacancies at higher temperature[19]:

$$2B_B^{\cdot} + O_O^{x} \leftrightarrow 2B_B^{x} + \frac{1}{2}O_2 + V_O^{\cdot\cdot} \qquad [1\text{-}8]$$

Cobalt in the B site provides a good catalytic activity, but suffers from the disadvantages such as high thermal expansion (about $20*10^{-6}$ K^{-1}) and the easy formation of secondary phases. Although the additional substitution of Fe to the B site decreases conductivity, it also restricts thermal expansion and prevents the formation of secondary phases. The high nonstoichiometric LSCF can provide a high concentration of vacancy, leading to an increase of ionic conductivity. The composition of $La_{0.6}Sr_{0.4}Co_{0.2}Fe_{0.8}O_{3-\delta}$[19] has an ionic conductivity of 0.23 S/cm and an electronic conductivity of 252 S/cm at 900°C with a transference number of $9x10^{-4}$. A transference number, also known as ionic transport number, is the fraction of ionic current divided by the total current passing through the conductor.

1.4 Cathode Durability

One of the biggest challenges in current development of SOFCs for the commercial market is the durability of cathode materials under working conditions [20-22]. The long-term performance of the SOFC is found to have degradation issues when the cathode is exposed to gases such as CO_2, H_2O, and Cr vapor[23-30]. The degradation of cathode performance can be classified into two categories, reversible and irreversible degradation [28]. Reversible degradation, such as blocking effects, can be recovered after removing the contaminants or through thermal re-activation.

Irreversible degradation, including microstructure coarsening, electrode decomposition, interdiffusion, and secondary phase formation, can lead to the permanent deterioration in the cathode/electrolyte and limit the kinetics of oxygen transport. Different cathode materials are found to have different dominant degradation mechanisms. For example, Sr segregation on the surface is one of the main causes of degradation for LSCF[21,31-33]. LSM, on the other hand, has been found to have manganese interdiffusion problems and the formation of an insulating layer, La_2ZrO_7, at the cathode-electrolyte interface[20,34-36].

There are a number of different gases, some being components of air and others developing due to sealing and interconnects, that may interact with the cathode. The influence of these interactions depends on concentrations of each species, activation energies for the reactions, as well as temperature and PO_2. The surface configuration of the cathode is very important for it's ability to catalyze the ORR. The components of air that may have a significant effect on cathode durability are CO_2 and H_2O. The presence of CO_2 and H_2O in SOFC cathode has been reported to cause some effects[23,37-46]. Nelson et al.[27,28] report that the performance of LSM/YSZ cell degrades with the presence of H_2O. Benson et al. [23] uses IEDP with SIMS to probe the degradation of LSCF with the presence of H_2O and CO_2. Zhao et al. [26] show that CO_2 causes different effects on different cathode materials with different activation energy. Little is known about how each of the contaminant gases may interact with the surface. There is a need to explore the fundamental interactions with CO_2 and how CO_2 containing atmospheres effect the performance of these metal oxides.

Chapter 2: Theory and Techniques

2.1 Surface Exchange and Diffusion

Quantitatively describing the multi-reaction steps of the surface exchange on cathodes is critical for the understanding of the ORR. The surface exchange coefficient (k) is a parameter that quantifies the rate of surface reactions on the cathode surfaces. k, (cm/s), represents the proportionality coefficient between the oxygen flux and the thermodynamic driving force for the transfer of oxygen molecules into oxygen ions:

$$k = \frac{J_O}{(C_g - C_S)} \qquad [2\text{-}1]$$

where J_O is the oxygen flux, C_g and C_s are the oxygen concentration in gas and solid phase, respectively.

There have been a variety of techniques aimed at gaining an understanding of the mechanisms and kinetics governing the ORR, which is crucial for understanding cathode polarization. Generally, there are three types of experiments to probe the ORR based on the different potential force to drive oxygen ions [47,48]:

2.1.1 Electrical potential

The first type of experiment is based on an electrical measurement. A small electrical potential gradient is applied to the system, which leads to the movement of ionic current in the counter direction due to charge balance. The response signal in the impedance can be measured and the impedance spectra can be attributed to the sum of each reaction step with a corresponding time constant[49,50].

2.1.2 Chemical potential

The second type of experiment is to apply a chemical potential, such as a change in oxygen partial pressure, to induce a change in material properties, such as the response in conductivity or a variation in the mass of the solid. Relaxation plots, which illustrate the return of a perturbed system back into equilibrium, contain kinetic information of the material to establish a new equilibrium. For example, Itoh et al.[51,52] studied the relaxation curves of valance state of Co and Fe in LSCF after a rapid change in PO_2. Zeng et al.[53] used thermogravimetric analysis (TGA) to determine the kinetics of materials by studying the transient mass change during the change of PO_2. Preis et al.[54] measured the change in the oxygen flux of MIEC materials, during the change PO_2 to determine k and D values. Consequently, the kinetic parameters can be extracted from each relaxation curve. Among all of the applied chemical potential experiments, electrical conductivity relaxation is the most popular technique to determine the kinetic parameters because the experimental set up is relatively inexpensive and facile. Also the method provides reliable, and fast results.

2.1.3 Tracer

The third approach is to use an isotope of oxygen as a tracer to probe the self-surface exchange and self-diffusion process without any external applied field. In contrast to external applied field disturbances, tracer experiments provide no electrochemical potential to drive oxygen ions. In tracer experiments, ^{16}O and ^{18}O are assumed to exhibit identical transport behaviors. Because of the tracer concentration gradient, the self-surface exchange coefficient (k^*) and self-diffusion coefficient (D*) can be determined by considering the exchange flux of ^{18}O, or the counterbalanced

flux of ^{16}O. The driving force is the isotopic distribution. The chemical potential of this reaction can be written as[55]:

$$\mu^* = \mu^{0}* + RT\ln c^* \qquad [2.2]$$

where μ* is the tracer's chemical potential and μ^0* is the tracer's chemical potential at a given standard state. c* is the tracer concentration. R is the universal gas contant (8.314 J/mol•K) and T is the temperature in Kelvin. The oxygen self-diffusion is related to the chemical diffusion coefficient via the thermodynamic factor, A:

$$A = \frac{1}{RT}\frac{\partial \mu_{\mathrm{O}}}{\partial \ln c_{\mathrm{O}}} = \frac{D_{chem}}{D^*} \qquad [2\text{-}3]$$

In equation [2-3], c_o is the oxygen concentration in solid. μ_o is the chemical potential of atomic oxygen and can be expressed as a function of temperature and oxygen partial pressure:

$$\mu_{\mathrm{O}} = \mu_{\mathrm{O}}^{\ 0} + RT\ln c_{\mathrm{O}} \qquad [2\text{-}4]$$

The thermodynamic factor can be expressed in the term:

$$A = \frac{1}{2}\frac{\partial \ln(P\mathrm{O}_2)}{\partial \ln c_{\mathrm{O}}} \qquad [2\text{-}5]$$

The chemical surface exchange coefficient (k), which is driven by the applied electrochemical potential, can also be linked to the self-surface exchange coefficient (k^*)[55,56]. Lane et al.[57] explain the relationship between k^* and k_{chem}. In the surface exchange process, small increments of change in $P\mathrm{O}_2$ have a linear relationship with oxygen concentration. Also, the change in μ_o is equivalent to the oxygen partial pressure. Therefore, k_{chem} can be expressed as k^* multiples the thermodynamic factor (A):

$$k_{chem} = \frac{k * c_O}{RT} \frac{\Delta \mu_O}{\Delta c_O} \cong k * A \qquad [2\text{-}6]$$

In this work, two different techniques are used to study both the bulk and the surface of materials: electrical conductivity relaxation to determine the kinetic parameters of bulk materials, and tracer experiments to determine the kinetics rates of the ORR from powder samples. These different approaches allow us to have greater insight into the ORR.

2.2 Electrical Conductivity Relaxation

Electrical conductivity relaxation (ECR) is a common technique to investigate oxygen transport properties[58-60] In this technique, a dense sample with well-defined dimensions is subjected to a rapid change in PO_2 to force oxygen in and out of the sample, resulting in a change in the concentration of defects. This change in defect concentration will lead to a change in the electrical conductivity, which can be acquired by four-probe DC measurements during the re-equilibration process. The results can be fit with Crank's solution for diffusion[61]:

$$\frac{\sigma(t) - \sigma(0)}{\sigma(\infty) - \sigma(0)} = M(t) = 1 - \left[\sum_{n=1}^{\infty} \frac{2L^2 \exp\left(- \frac{\beta_n^2 D_{chem}(t - t_0)}{(T/2)^2} \right)}{\beta_n^2 \left(\beta_n^2 + L^2 + L \right)} \right] \qquad [2\text{-}7]$$

$$\beta_n \tan \beta_n = L \qquad [2\text{-}8]$$

$$L = \frac{T}{2} \frac{k_{chem}}{D_{chem}} \qquad [2\text{-}9]$$

In the above equations, $\sigma(t)$ is the conductivity of the sample at time (t), and M(t) is the accumulated total amount of oxygen leaving or entering the sample at time (t). T is the sample thickness, k_{chem} is the chemical surface exchange coefficient, D_{chem} is the chemical diffusion coefficient, and β_n are the infinite roots of the Equation [2-8]. The characteristic length (L), is a function of the dimension of sample size, k_{chem}, and D_{chem}, is an important kinetic parameter to determine the dominant reactions. Large L values mean that the surface exchange is fast enough to assume that the diffusion is the rate limiting step. On the contrary, when L values are close to zero, the diffusion process is so fast that the surface exchange process is the rate-limiting step. Equation [2-7], describing the accumulation curve of incorporated oxygen as a function of time, consists of infinite terms resulting from the roots of characteristic length (L). To extract the kinetic parameters accurately, it is necessary to develop an analytic solution to fit the experimental data with the diffusion Equation [2-7]. The details of the fitting analysis will be discussed in Chapter 7 based on numerical calculations.

2.3 Isotope Exchange Experiments

ECR provides a k_{chem} for an overall ORR when in fact the reaction is a multistep process. Other techniques for analyzing the kinetics of the ORR are based on labeled oxygen. By introducing isotopically labeled oxygen into the system, the interactions between oxygen and the cathode surface can be traced. In the isotope exchange experiments, it is assumed that (1) different isotopes are identical and equivalent, (2) the isotopic effects are negligible, and (3) all lattice oxygen of the solid oxide are considered to be equivalent with the same transport phenomena. Isotope exchange is a powerful tool to observe the kinetics of heterogeneous catalytic

reactions[62-67]. However, most isotope tracer experiments are limited in their scope. Typically, these experiments take one of two approaches: either solid phase *ex-situ* isotope exchange depth profiling (IEDP) with secondary ion mass spectrometry (SIMS) or gas phase isotopic oxygen exchange.

2.3.1 Isotope exchange depth profiling (IEDP) with secondary ion mass spectrometry (SIMS)

In IEDP, the sample is exposed to an isotopic environment at a given temperature and a given time to acquire the isotopic distribution profile as a function of the distance in the solid sample[68-70]. The isotopic distribution curve can then be fitted with the diffusion equation to extract the kinetic parameters[61]:

$$\frac{C(x,t)-C(0)}{C(g)-C(0)} = erfc\left(\frac{x}{2\sqrt{Dt}}\right) - \exp(Lx + L^2 Dt)\,erfc\left(\frac{x}{2\sqrt{D*t}} + L\sqrt{D*t}\right) \quad [2\text{-}10]$$

$$L = a\frac{k*}{D*} \quad [2\text{-}11]$$

where C(x,t) is the error function distribution of ^{18}O concentration as a function of x, which denotes to the distance from the surface, at time *t*. C(0) is the ^{18}O concentration at the surface before the isotope exchange, C(g) is ^{18}O concentration in the gas phase, and *a* represents the sample thickness. *k** and D* denote to self-surface exchange coefficient and self-diffusion coefficient, respectively. IEDP provides a straightforward approach to visualize the surface exchange and diffusion processes. Also, it is relatively easy to extract *k** and D* without excessive data processing. Because of the *ex-situ* process, IEDP lacks the ability to distinguish the surface reaction steps involved. In addition, if various reactants are presented on the solid surface, their interactions cannot be detected.

2.3.2 Gas phase isotopic oxygen exchange

On the other hand, gas phase oxygen isotope exchange can observe the interactions between each reactant and the solid surface. Steady-state isotopic-kinetic transient analysis (SSIKTA)[65,67,71,72] is a well-established technique for studying the kinetics of heterogeneous catalysis. SSIKTA, where the focus is on the kinetics of oxygen adsorption on the surface, is well suited for explaining reaction mechanisms, and extracting kinetic properties such as identification of intermediate species, concentrations of intermediates, available surface sites, and determination of possible reaction routes. The data needs to be carefully analyzed in order to obtain accurate results. Isotopically labeled reactants are introduced to the system and the isotope responses of intermediate species and products provide the relaxation time constant. Based on the time constants of each reaction, the kinetics of the catalytic activity of the solid surface can be determined. SSITKA allows for the investigation of the reactions at the site level. Previous SSIKTA experiments have focused mostly on the reactions occurring on the surface of the material, not the mass transport exchange into the bulk material. For SOFC cathodes, we are particularly interested in reactions in which gaseous oxygen is being incorporated into the catalyst.

2.4 Isothermal Isotope Exchange (IIE)

Isothermal isotope exchange (IIE) is a technique used to investigate the mass transport at the gas-solid interface[73-79]. IIE is very similar to SSIKTA, but IIE is focused on the kinetics of the gas-solid exchange. In IIE, the system rests in a fixed temperature and oxygen partial pressure. Therefore, the composition and the nonstoichiometry of the materials tested remain the same. The gas mixture passes

continuously through a bed of powder in a plug flow reactor at a constant flow rate, as shown in Figure 2-1.

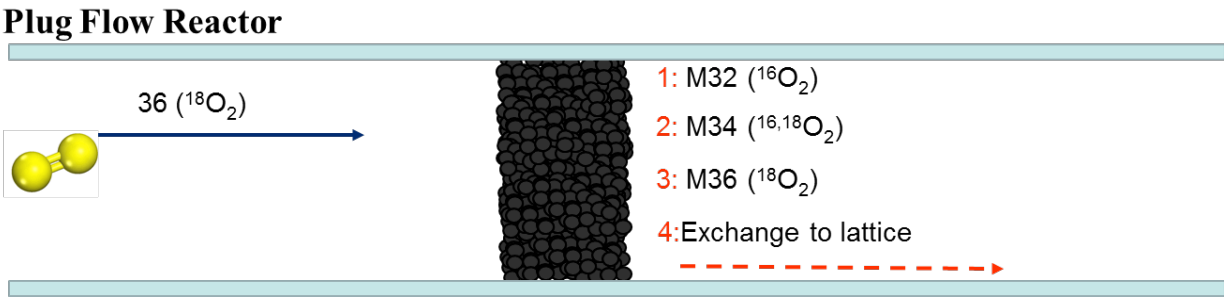

Figure 2-1. A schematic drawing of a plug flow reactor. $^{18}O_2$ continuously flows through the powder in a plug flow reactor. Because $^{18}O_2$ is the only ^{18}O source and the ^{18}O exchanges to lattice is the "product" in this reaction, the gaseous byproducts $^{16}O_2$, $^{16}O^{18}O$, and $^{18}O_2$ signal can be used to monitor the surface reactions in real time.

The composition of the gas mixture and the powder in the reactor remains stationary. Because the product is the ^{18}O exchanged into lattice, the isotope response of $^{16}O_2$, $^{16}O^{18}O$, and $^{16}O_2$, (m/z=32,34, and 36, respectively) are the byproducts of a series of reactions. These oxygen isotopologues carry the information of the surface exchange and diffusion processes in real time. Based on the data analysis of *in-situ* SSIKTA, we can develop a steady-state kinetic model to comprehensively de-convolute the surface reaction steps. The details of the analysis of IIE are presented in Chapter 3. The real-time observation of isotope exchange profiles can help to characterize the dissociation of oxygen molecules at the oxide surface as well as the conduction of oxygen ions within the oxide.

2.5 Heterogeneous Catalysis Approach

The activation energy for the intermolecular reactions is significantly high because the exchange needs to overcome high repulsion forces to break the coupled

electron pair, resulting from a consequence of the Pauli exclusion principle[66,80,81]. The energy barrier to break the bonding between the two oxygen in O_2 is substantially high and the existence of the catalysts to catalyze the reactions is necessary. When considering the heterogeneous catalysis, the exchange of O_2 with the solid surface can be divided into three types[66,72,82,83], as shown in Figure 2-2.

2.5.1 Homoexchange (Homogeneous Exchange)

The first one is homoexchange. With the presence of a catalyst, two oxygen molecules can be dissociatively adsorbed on the solid surface and exchanged with each other:

$$^{18}O_2 + {}^{16}O_2 + 4* \longleftrightarrow 2\,{}^{16}O\,{}^{18}O + 4* \qquad [2\text{-}12]$$

where * denotes the available surface site for the catalytic reaction. The homoexchange process with the catalyst on the solid surface involves the interexchange between two oxygen molecules. This homoexchange process is denoted by the R_0 exchange mechanism because none of lattice oxygen participates in the reaction, as shown in Figure 2-2 (a).

(a) Homoexchange

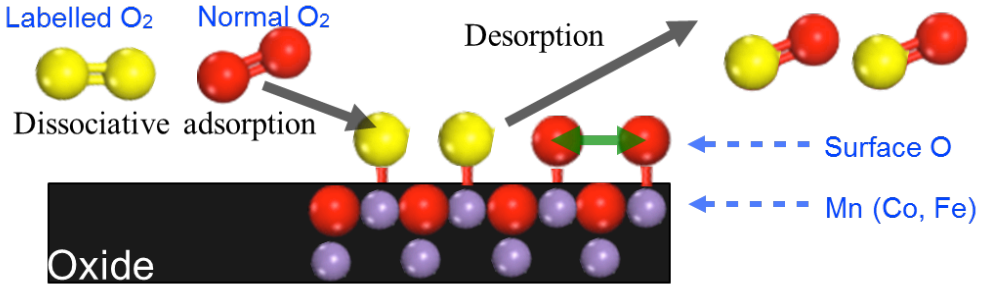

(b) Single Heteroexchange

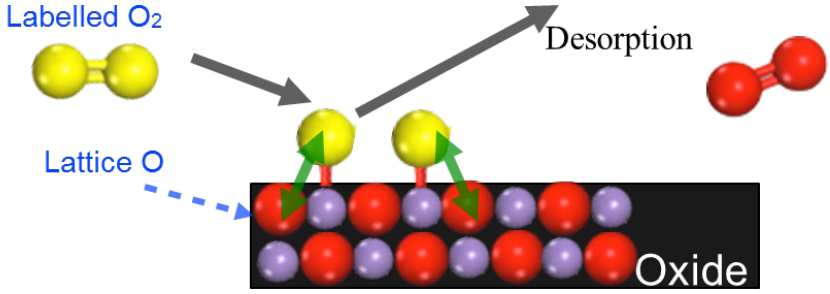

(c) Double Heteroexhange

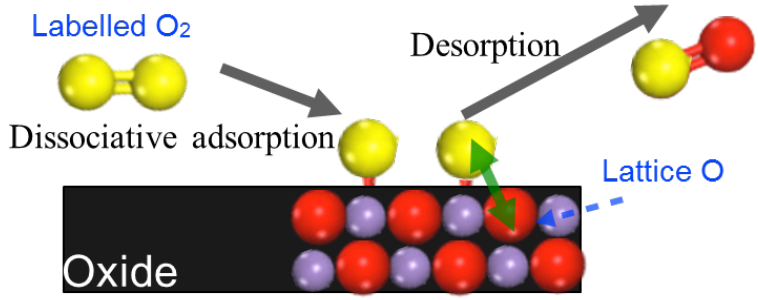

(d) Surface Vacancy Exchange Mechanism

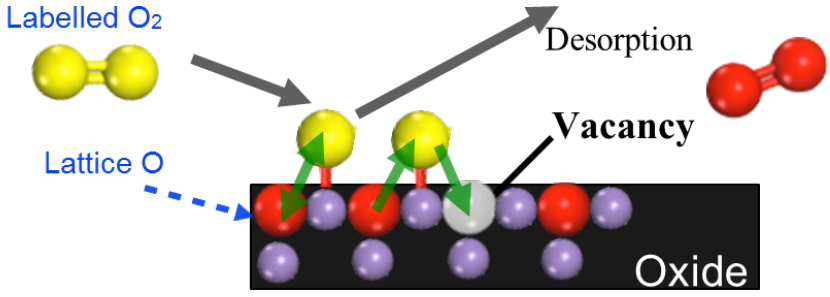

Figure 2-2. Schematic draws for 3 different types of oxygen exchange on the solid surface (a) homoexchange, (b) single heteroexchange, and (c) double heteroexchange. (d) The surface vacancy exchange mechanism for the heteroexchange process is shown.

2.5.2 Heteroexchange (Heterogeneous Exchange)

Another exchange mechanism is heteroexchange. As shown in Figure 2-2 (b) and (c), based on the numbers of lattice oxygen participating in the reaction, the heteroexchange can be divided into single heteroexchange or double heteroexchange, denoted as R_1 and R_2 mechanisms, respectively. The heteroexchange involves the exchange between oxygen in O_2 and lattice oxygen. The mechanisms can be expressed by the following reactions:

$$^{18}O_2 + {}^{16}O_O \longleftrightarrow {}^{16}O{}^{18}O + {}^{18}O_O \qquad [2\text{-}13]$$

$$^{18}O_2 + 2{}^{16}O_O \longleftrightarrow {}^{16}O_2 + 2{}^{18}O_O \qquad [2\text{-}14]$$

The single heteroexchange and double heteroexchange can be directly related to the intermediate oxygen species participating in the ORR. In the R_1 exchange mechanism in Equation [2-13], atomic oxygen is considered to be an active species at the gas-solid interface, while the R_2 exchange mechanism in Equation [2-14] is resulted from the contribution of molecular oxygen. The heteroexchange can be associated with the exchange between oxygen in gas and solid phase through the surface vacancy exchange mechanism, as shown in Figure 2-2 (c). A dissociatively adsorbed oxygen incorporates into a surface vacancy and another lattice oxygen moves out the lattice site to the surface.

Because the temperature and PO_2 are fixed during the exchange process, available surface sites and surface vacancies should remain constant. Equation [2-13] can be rewritten in such form that include the presence of surface vacancy in the surface exchange process:

$$^{18}O_2 + 2^{16}O_O + 2V_O \longleftrightarrow {}^{16}O_2 + 2^{18}O_O + 2V_O \qquad [2\text{-}15]$$

The heteroexchange that converts oxygen from gas to solid is important for the SOFC applications because the solid oxygen can be transported through the electrolyte and then used to oxidize fuels. Most catalytic studies focus only on either the gaseous products or the diffusion process into the porous catalysts. Few of them concentrate on the self exchange process for the mass transfer of reactants to the solid catalyst. Therefore, it is important to create a link between the surface catalytic activity and the solid state diffusion process.

2.6 Solid State Approach: Two-Step Reaction Model

In the solid-state, oxygen molecules that are transferred into oxygen ions and transported to the anode side through an electrolyte are those actually contributed to the overall electrochemical reactions. We have proposed a mechanistic model of the main steps of the ORR. The model is based on a two-step reaction mechanism across the heterogeneous gas-solid interface[66,76,84]. The multi-steps of the ORR can be simplified in two elementary steps: (1) ***dissociative adsorption*** and (2) ***incorporation*.** Figure 2-3 is a schematic of the two-step reaction. The cathode surface can be seen as a catalysis bed, where $^{18}O_2$ are absorbed and dissociated into single isotope oxygen atoms (^{18}O). The single isotope oxygen atoms have the possibility to either incorporate into the solid phase or recombine with another oxygen atom on the surface and desorb back to a gas phase molecule. The concentrations of $^{16}O_2$, $^{16}O^{18}O$, and $^{18}O_2$ provide information about the ORR on the cathode surface. Consider the two-step reaction model:

2.6.1 Dissociative Adsorption

Dissociative adsorption of reactants on the surface of the catalyst is the first step for most heterogeneous catalysis reactions reactions[84,85]. In general, the adsorbed oxygen atoms and the molecules in the gas phase are assumed to be at equilibrium. The reaction equation can be written as:

$$O_2 + 2* \longleftrightarrow 2O_* \qquad [2\text{-}16]$$

where the symbol * denotes available surface sites and O_* represents the oxygen occupied in a surface site. The adsorption of oxygen involves the reaction of an oxygen molecule with an available active site to give an intermediate product. This step describes the equilibrium between gas and the solid surface.

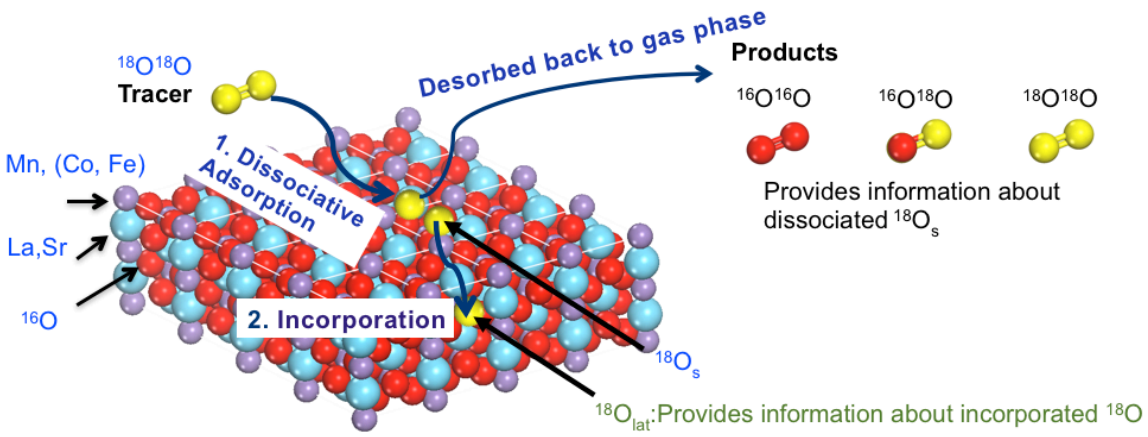

Figure 2-3. Schematic of two-step reaction: 1. Dissociative adsorption and 2. Incorporation. Gas phase products of isotope oxygen are listed in the figure. ^{18}O atom (yellow) was used as a tracer to help identify different oxygen reaction paths, and distinguish from the background ^{16}O (red).

2.6.2 Incorporation

The second step of the ORR is incorporation. During incorporation, oxygen needs to overcome the energy barrier to bond into the crystal structure.

$$O_* + V_O \longleftrightarrow O_O + * \qquad [2\text{-}17]$$

where O_o denotes the oxygen occupied in the oxygen site. This equation describes the surface-solid reactions and the equilibrium between the surface and the solid. Based on the two-step reaction model, we can link the surface catalysis on the solid surface with the solid state diffusion process in the solid phase. We can also determine the effects of other gaseous reactants on the ORR. Therefore, this research builds the bridge between the heteroexchange in heterogenous catalysis and the diffusion in solid state ionics. The results are essential for the development of the new cathode materials.

Chapter 3: Oxygen Isotope Exchange Experiments on SOFC Cathode Materials

3.1 Introduction to Isotope Exchange

Solid oxide fuel cells (SOFC) can provide clean energy by directly converting fuels to electricity through electrochemical oxidation. To broaden the real applications, it is important to decrease operating temperature of SOFCs to intermediate temperatures (500°C-800°C)[3,7]. At intermediate temperature, losses due to polarization resistance limit the fuel cells performance. The majority of this cell polarization is due to the inefficiencies of the ORR, which occurs at the cathode. Understanding the fundamentals of the ORR mechanism and accurately obtaining kinetic rates is necessary to further improve cathode performance. There have been a variety of techniques aimed at gaining an understanding of the mechanisms and kinetics governing the ORR, a crucial part for understanding cathode polarization[86]. Electrical conductivity relaxation (ECR) is a common measurement to investigate oxygen transport properties [56,87,88]. In this technique, a dense sample is used and the oxygen partial pressure of the environment is rapidly changed to force oxygen in or out of the sample, resulting in a change of electrical conductivity. The conductivity profile is acquired and fit with Crank's solutions for diffusion[61]. We can then obtain the chemical diffusion coefficient (D_{chem}) and the surface exchange coefficient (k_{chem}) for the material. However, ECR's accuracy is limited by the sample size and is

dependent on the electrical conductivity of the sample. Also, ECR provides a k_{chem} for the overall ORR, when in fact the reaction contains multiple steps.

Other techniques for analyzing the kinetics of the ORR are based on isotopically labeled oxygen [62-67]. By introducing isotopically labeled oxygen, most commonly $^{18}O_2$, into the system we can understand how oxygen interacts with the cathode surface and/or bulk by tracking the isotope tracer either *in-situ*, or *ex-situ*. Isotope exchange is a powerful tool to observe the kinetics of heterogeneous catalytic reactions, however, most isotope tracer experiments are limited in their scope. Typically these experiments take one of two approaches; either ex-situ isotope exchange depth profiling (IEDP) with secondary ion mass spectrometry (SIMS)[89,90] or steady-state isotopic-kinetic transient analysis (SSIKTA)[63,65,67,91] where the focus is on the catalysis of gaseous reactants to gaseous products on the surface. In IEDP the samples are annealed in isotope gas for a period of time at a set temperature. Then, the samples are quenched, and a depth profile of the isotopically labeled oxygen is mapped using SIMS. The isotope distribution profiles are then fit using Crank's solutions to the diffusion equations to extract the tracer surface exchange coefficient (k_{ex}^*) and tracer diffusion coefficient (D^*). However, IEDP is limited by the ex-situ processing and lacks the ability to distinguish the surface reaction steps involved. On the other hand, SSIKTA is a well-established technique for studying the kinetics of heterogeneous catalysis. SSIKTA is well suited for explaining reaction mechanisms and extracting kinetic properties such as identification of intermediate species, concentrations of intermediates, available surface sites, and determination of possible reaction mechanisms. The data needs to be delicately analyzed in order to obtain

accurate results. Previous SSIKTA experiments have focused mostly on the reactions occurring at the surface of the material, but not the mass transport exchange into the catalyst. For SOFC cathodes we are particularly interested in reactions in which gaseous oxygen is being incorporated into the catalyst.

Isothermal isotope exchange (IIE)[73,76,78] is a technique we use to investigate the mass transport across the gas-solid interface. IIE is very similar to SSIKTA, but IIE is focused on the kinetics of gas-solid exchange, and is performed at a set temperature. Based on the data analysis of *in-situ* SSIKTA, we developed a steady-state kinetics model to comprehensively de-convolute surface reaction steps. The sample is held at a constant temperature and oxygen partial pressure, allowing us to extract kinetic rates from the transient response of the ^{18}O tracer. The real-time observation of isotope exchange profiles can help to characterize the dissociation of oxygen molecules at the oxide surface as well as measure the conduction of oxygen ions within the oxide.

In this study, we attempt to determine the ORR mechanism and kinetic rates for two perovskite cathode materials: $La_{0.6}Sr_{0.4}Co_{0.2}Fe_{0.8}O_{3-x}$ (LSCF) and $(La_{0.8}Sr_{0.2})_{0.95}MnO_{3\pm x}$ (LSM). These two materials were chosen because they are the most commonly used by industry. LSM is a pure electronic conductor with negligible ionic conductivity, and LSCF is a mixed ionic electronic conductor (MIEC). In this ABO_3 structure, La and Sr occupy the A sites and the B sites are filled with the transition metals Fe and Co, or Mn. Changing oxygen partial pressure and temperature will vary the concentrations of defects (oxygen vacancies) in the structure and therefore the catalytic properties of the materials. As the concentration

of oxygen vacancies increases, the number of available surface sites for dissociation and incorporation also increases. Therefore, all the rate constants, energy barriers, concentrations of vacancies, and number of available surface sites are variables that depend on temperature and oxygen partial pressure. IIE has the potential to separate this multi-step reaction and quantify the effects of each variable. Therefore, to understand the overall ORR for these cathodes and further separate the contributions from each variable, IIE is performed at different oxygen partial pressures and temperatures. A simplified equation is derived to determine the surface exchange rate of cathode material based on a two-step reaction model, and relationships are drawn between the different rate constants for the ORR.

3.2 Experimental

Details of the experimental set up can be found in our previous works ([73,76,78]). To best represent the materials used in industry, commercially available LSCF (Praxair), and LSM (Fuel Cell Materials) powders were purchased. BET measurements show that the surface areas of the LSM and LSCF powders are 5.6 m^2/g and 6.5 m^2/g, respectively. Therefore, LSCF and LSM are weighted out so the surface areas are normalized to 0.1 m^2 to allow for direct comparison. The particle size from BET and light scattering of LSCF and LSM are 300nm and 700nm, respectively. Then, the powder was placed in the center of a quartz tube plug-flow reactor. The flow rate is fixed at 20 SCCM using mass flow controllers and a 2 mm inner diameter quartz tube is placed beneath the powder to reduce gas residence time. The reactor effluent is fed through a capillary to a quadrupole mass spectrometer where the composition is analyzed and recorded. ^{16}O and ^{18}O are assumed to be

identical and the isotopic effects are ignored. Particles are assumed to be uniform in size and spherical in shape. Calibrations for the isotope exchange experimental set up are listed in Appendix A. Calibrations for the Isotope Exchange Experimental Set Up.

Before each IIE experiment, the sample powder is first pretreated at 800°C in an $^{16}O_2$ environment (the most common oxygen isotope) for 30 minutes to ensure that the powder surface is clean and converted completely to normal isotope oxygen (^{16}O). After the pretreatment, the sample is brought to the temperature of interest and equilibrated in $^{16}O_2$ (AIRGAS, 99.999%). In a separate line, an equal PO_2 of isotope $^{18}O_2$ (Sigma-Aldrich; 95% pure) and a small amount of argon (Airgas; 0.1%), used as an inert tracer, is flowed. Then, the gas entering the system is quickly switched from $^{16}O_2$ to $^{18}O_2$ using a pneumatic valve actuator. The evolution of gas phase oxygen isotopologues is monitored using mass spectrometry.

3.3 Isotope Exchange Theoretical Background

To identify different oxygen reaction paths, gaseous $^{18}O_2$ is used as a tracer. The cathode surface can be seen as a catalyst bed, where $^{18}O_2$ are adsorbed and dissociated on the surface into single oxygen atoms (^{18}O). The ^{18}O atoms have the possibility to either incorporate into the lattice (solid phase) or recombine with another oxygen atom on the surface and desorb back to a gas phase molecule. Gas phase products can be monitored by mass spectrometry. The concentrations of $^{16}O_2$, $^{16}O^{18}O$, and $^{18}O_2$, corresponding to m/z signals 32, 34, and 36 respectively, provide information about the dissociation of $^{18}O_2$ on the cathode surface. Throughout an IIE experiment, the system maintains a fixed temperature and a fixed oxygen partial pressure. Therefore, the system is at a quasi-steady state, meaning that the total

available surface sites, total concentration of oxygen vacancies, and reaction rates are all constants [65,66,91].

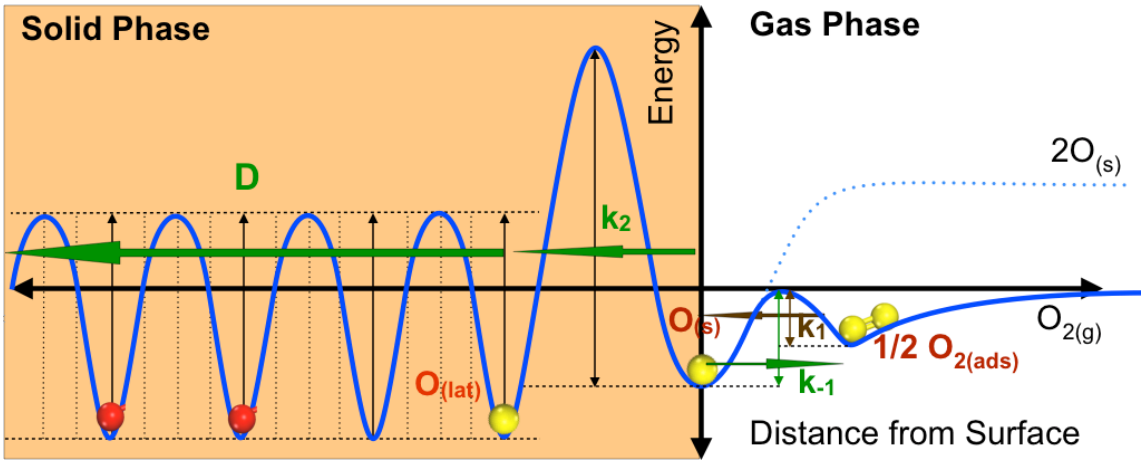

Figure 3-1. One-dimensional potential energy diagram for $^{18}O_2$ interacting with a clean cathode surface. Oxygen molecules are dissociatively adsorbed on the surface. The $^{18}O_S$ has two different pathways for reaction: (1) desorption, back to the gas phase (2) incorporation into the solid phase. The incorporation rate is dependent on $^{18}O_s$ overcoming the energy barrier between the surface and the bulk. The diffusion of $^{18}O_{lat}$ through the lattice can be modeled as a periodic potential well, and quantified by the self-diffusion coefficient (D).

To understand the ORR mechanism on cathode materials, a model based on a two-step reaction mechanism across the heterogeneous gas-solid interface was built to simulate the IIE results[21]. The coupled reactions can be shown in two elementary steps: (1) *dissociative adsorption* (2) *incorporation.* A 1-dimensional potential energy diagram for $^{18}O_2$ molecules interacting with a clean oxide surface is shown in Figure 3-1. k_1 describes spontaneous adsorption and the ability to dissociate oxygen molecules into atoms. At high temperature the energy level of an adsorbed oxygen atom becomes lower than the energy level of an oxygen molecule[84,85]. Therefore, when oxygen molecules are close enough to adsorb onto the cathode surface, spontaneous dissociation will occur. To incorporate into the cathode lattice, the ^{18}O

atom on the surface needs to overcome the energy barrier between two-dimensional surface bonding and three-dimensional lattice bonding. k_2 describes the ability of the ^{18}O tracer atom to incorporate into lattice structure. After the ^{18}O atom is incorporated, a periodic potential well, between oxygen lattice sites, describes the conduction of ^{18}O through the lattice. The tracer diffusion coefficient (D) is used to quantify the rate of this self-diffusion. Consider the two-step reaction model with self- surface exchange and diffusion:

3.3.1 Isotope Exchange: Dissociative Adsorption

Adsorption of reactants on the surface of the catalyst is the first step in the ORR as for most heterogeneous catalysis reactions[84,85]. The total number of available sites (S) is a function of temperature and oxygen partial pressure. Each active site is assumed to be equivalent and can only be occupied by a single reactant. The adsorption of oxygen involves the reaction of an oxygen molecule with an available active site to give an intermediate product ($O*$). In general we may assume the adsorbed oxygen atoms and the oxygen molecules in the gas phase are at equilibrium. In this case, we may write the reaction equation as:

$$O_2 + 2* \underset{k_{-1}}{\overset{k_1}{\leftrightarrow}} 2O_* \qquad [3\text{-}1]$$

where $*$ denotes an available active site and $O*$ is an oxygen atom occupying an active site, with forward and reverse rate constants k_1 and k_{-1}. The corresponding rate expression is

$$r_1 = \frac{d[O_{2(g)}]}{dt} = \overrightarrow{k_1} P_{O_2} \Theta_*^2 - \overleftarrow{k_{-1}} \Theta_O^2 \qquad [3\text{-}2]$$

where Θ^* is the fraction of available active surface sites and Θ_O denotes the fraction of active sites occupied by an oxygen atom. The first term corresponds to adsorption while the second term describes desorption. At equilibrium, the forward reaction rate and the reverse reaction rate are equal, yielding:

$$r_1 = \vec{k_1} P_{O_2} \Theta_*^2 - \overleftarrow{k_{-1}} \Theta_O^2 = 0 \qquad [3\text{-}3]$$

The oxygen partial pressure at equilibrium can be expressed as

$$P_{O_2} = \frac{\Theta_O^2}{K_1 \Theta_*^2} \qquad [3\text{-}4]$$

This is also known as Langmuir equilibrium. Now consider that ^{18}O gas is introduced to the system. The total oxygen partial pressure is now the sum of the three possible oxygen isotopologues:

$$P_{O_2} = {}^{32}P_{O_2} + {}^{34}P_{O_2} + {}^{36}P_{O_2} \qquad [3\text{-}5]$$

The surface coverage, Θ_O, is the mixture of ^{16}O ($^{16}\Theta_O$) and ^{18}O ($^{18}\Theta_O$):

$$\Theta_O = {}^{16}\Theta_O + {}^{18}\Theta_O \qquad [3\text{-}6]$$

Substituting Equation [3-5] and Equation [3-6] into Equation [3-4] we get:

$${}^{32}P_{O_2} + {}^{34}P_{O_2} + {}^{36}P_{O_2} = \frac{\left({}^{16}\Theta_O^2 + 2\,{}^{16}\Theta_O\,{}^{18}\Theta_O + {}^{18}\Theta_O^2\right)}{K_1 \Theta_*^2} \qquad [3\text{-}7]$$

The concentrations of oxygen isotopologues are the products after multi-surface reactions on cathode surface and can be expressed as a function of surface coverage of $^{16}\Theta_O$ and $^{18}\Theta_O$. In a plug-flow reactor reactants are continuously flowing through the sample, allowing for constant interaction with the sample. Considering that inlet gas can either react with or flow past the cathode surface, we can separate the outlet gas into two parts: one is without surface reactions and the other is after a

series of surface reactions. The ratio of reacted and non-reacted outlet gas is a function of temperature and determined by the catalytic activity of the solid surface. The overall reaction can be expressed as:

$$^{36}N_{O_2}{}^{inlet} \xrightarrow{catalysis=} {}^{36}N_{O_2}{}^{Non-react} + (^{32}N_{O_2} + {}^{34}N_{O_2} + {}^{36}N_{O_2})^{react} \quad [3\text{-}8]$$

Therefore, oxygen partial pressures of $^{16}O_2$, $^{16}O^{18}O$, and $^{18}O_2$ at each time can then be converted into numbers of $^{16}O_2$, $^{16}O^{18}O$, and $^{18}O_2$ molecules that can be detected by mass spectrometry:

$$^{32}N_{O_2}{}^{outlet} = SA\frac{^{16}\Theta_O^2}{K_1\Theta_*^2} \quad [3\text{-}9]$$

$$^{34}N_{O_2}{}^{outlet} = SA\frac{2^{16}\Theta_O{}^{18}\Theta_O}{K_1\Theta_*^2} \quad [3\text{-}10]$$

$$^{36}N_{O_2}^{outlet} = {}^{36}N_{O_2}^{non-exchange} + SA\frac{^{18}\Theta_O^2}{K_1\Theta_*^2} \quad [3\text{-}11]$$

where A is the surface area of the sample, and $^{32}N_{O2}{}^{oulet}$, $^{34}N_{O2}{}^{oulet}$, and $^{36}N_{O2}{}^{oulet}$ are the total numbers of molecules for each oxygen isotopologue after isotope exchange. The above equations describe how the measured values of the oxygen isotopologues are related to the surface concentrations of ^{16}O and ^{18}O. It describes the relationship between gaseous oxygen and the isotopic configuration of the cathode surface.

3.3.2 Isotope Exchange: Incorporation

The second step of the ORR is the exchange of surface oxygen atoms with lattice oxygen. It is important to note that this step involves the transition from surface bonding to lattice bonding, resulting in an increase in the coordination number (number of bonds) of the O-site. The reaction equation can be written as:

$$O_* + V_O \underset{k_{-2}}{\overset{k_2}{\leftrightarrow}} O_O + * \qquad [3\text{-}12]$$

where k_2 and k_{-2} are the rate constants for the forward and reverse reactions, respectively. At equilibrium, the net reaction rate is equal to zero.

$$r_2 = \overrightarrow{k_2}\Theta_O[V_O] - \overleftarrow{k_{-2}}[O_O]\Theta_* = 0 \qquad [3\text{-}13]$$

The surface coverage of oxygen atoms Θ_O can be expressed as a function of the oxygen concentration in the lattice $[O_O]$ and oxygen vacancy concentration $[V_O]$ in the near surface region:

$$\Theta_O = \frac{[O_O]\Theta_*}{K_2[V_O]} \qquad [3\text{-}14]$$

where K_2 is the equilibrium constant. At a given temperature and oxygen partial pressure, K_2, $[V_O]$, Θ_*, and $[O_O]$ are all constant, but ^{18}O and ^{16}O concentrations vary with time. Inserting $[O_O]= [^{16}O_O]+[^{18}O_O]$ into the equation. The surface coverage can be expressed as,

$$^{16}\Theta_O + {}^{18}\Theta_O = \frac{\left([^{16}O_O]+[^{18}O_O]\right)\Theta_*}{K_2[V_O]} \qquad [3\text{-}15]$$

The surface coverage of ^{16}O and ^{18}O are directly related to the exchange rate of surface ^{18}O with lattice ^{16}O. The flux is proportional to the concentration gradient between $^{18}\Theta_O$ and $[^{18}O]$:

$$J_{18O} = SA\frac{d^{18}\Theta_{O,lat}}{dt} = SA\left[R_{ex}(^{18}\Theta_O - {}^{18}\Theta_{O,lat})\right] \qquad [3\text{-}16]$$

where J_{18O} is the ^{18}O flux into lattice. S denotes the total number of surface sites and A is the total powder surface area. $^{18}\Theta_{O,lat}$ is the ^{18}O fraction of lattice oxygen. The above equation describes the 2-dimensional oxygen exchange flux from the surface to the near surface region of lattice. The rate of heteroexchange (R_{ex})[92,93] designates the rate of heteroexchange and it describes the 2-dimensional oxygen incorporation from surface to near-surface sites per unit time per unit surface area. R_{ex} is proportional to the oxygen flux and can be related to the mechanistic equilibrium constants K_1 and K_2 through the reaction rate equation, which should depend only on the material properties. $^{18}\Theta_{O,lat}$ is the fraction of ^{18}O in the near-surface region. $SA^{18}\Theta_O$ is the total available 2-dimensional oxygen surface sites for ^{18}O to exchange with lattice ^{16}O. If gas-surface exchange is significantly faster than lattice-surface exchange, $S^{18}\Theta_O$, from the perspective of the latter exchange, can be equated to total oxygen surface sites. The time dependent concentrations of $[^{18}O_O]$ can be obtained by solving the equation. When $^{18}\Theta_{O,lat}=^{18}\Theta_O$ the system is at equilibrium. The integration limits are from $^{18}\Theta_{O,lat}=0$ at t=0 to $^{18}\Theta_{O,lat}=^{18}\Theta_O$ at t=∞. The ^{18}O exchanged in the lattice can be expressed as:

$$[^{18}O_O] = SA^{18}\Theta_O(1 - e^{-R_{ex}t}); \qquad [3\text{-}17]$$

$$[^{16}O_O] = SA^{16}\Theta_{O,lat} = SA\Theta_O e^{-R_{ex}t} \qquad [3\text{-}18]$$

$[^{18}O_O]$ and $[^{16}O_O]$ are the 2-Dimensional concentrations of ^{18}O and ^{16}O in the near surface region. The time dependent concentration profile of ^{18}O and ^{16}O in the lattice can be obtained. We can link the rate of heteroexchange (R_{ex}) with the fundamental reaction incorporation rate constant k_2, according to the amount of ^{18}O

that exchanges with lattice oxygen. Considering the net reaction of ^{18}O tracer exchange with lattice ^{16}O in Equation [3-13] and equation [3-16]:

$$SAr_2^* = SA\overrightarrow{k_2}[V_O]^{18}\Theta_O - SA\overleftarrow{k_{-2}}\Theta_*[^{18}O_O] = \frac{d(SA^{18}\Theta_{O,lat})}{dt} = SA\left[R_{ex}(^{18}\Theta_O - ^{18}\Theta_{O,lat})\right] \quad [3\text{-}19]$$

The surface coverage $^{18}\Theta_O$ is only a function of K_1 and the oxygen partial pressure. At t=0 when the system is switched from normal $^{16}O_2$ to isotope $^{18}O_2$, the ^{18}O concentration inside the powder $[^{18}O_O]=0$:

$$r_2 = Sk_2[V_O]^{18}\Theta_O = \frac{d([^{18}O_O])}{dt} = R_{ex}(^{18}\Theta_O) \quad [3\text{-}20]$$

$$R_{ex} = Sk_2[V_O] \quad [3\text{-}21]$$

The rate of heteroexchange (R_{ex}) with units (1/s) can be directly linked to the fundamental kinetic rate k_2, the forward reaction rate from surface to lattice oxygen, through the concentration of oxygen vacancies, $[V_O]$.

The equilibrium constant K_1 and K_2 represent the steady state concentration of each species in the near surface region. K_1 describes the equilibrium between gas and surface, and K_2 describes the equilibrium between surface and solid. The stoichiometry of the material can be linked directly to the equilibrium constants, K_1 and K_2 by substituting from Equation [3-4] into Equation [3-14]:

$$K_2K_1^{1/2}P_{O_2}^{1/2} = \frac{[O_O]}{[V_O]} \quad [3\text{-}22]$$

From a solid-state point of view, the difference in volumetric concentration between the gas and solid phases is the driving force for oxygen to enter of leave the

solid[61]. After incorporation, the movement of oxygen in the lattice can be described by the diffusion process. The boundary condition of the diffusion process can be shown as:

$$J_{18O} = k_{ex}\left([^{18}O_s] - [^{18}O_{lat}]\right) = -D\frac{\partial[^{18}O_{lat}]}{\partial r} \quad [3\text{-}23]$$

where $[^{18}O_s]$ and $[^{18}O_{lat}]$ are 3-Dimensional concentrations (unit: #/cm^3). The isotopic gradient between surface and bulk is a linear driving force, and can be described by the surface exchange coefficient (k_{ex}). k_{ex}, multiplied by the volumetric concentration gradient is equal to the flux (#/cm^2/s). D is the diffusion coefficient (cm^2/s) and a is the radius of the sphere powder. Consider Crank's solution for diffusion into a sphere with surface reaction[61]:

$$\frac{C(t)-C_\infty}{C_0-C_\infty} = \frac{2La}{r}\left[\sum_{n=1}^{\infty}\frac{\exp\left(-\frac{\beta_n^2 D(t)}{a^2}\right)}{\left(\beta_n^2 + L(L-1)\right)}\frac{\sin(\beta_n r/a)}{\sin(\beta_n)}\right] \quad [3\text{-}24]$$

The β_n's are the roots of

$$\beta_n \cot\beta_n + L - 1 = 0 \quad [3\text{-}25]$$

$$L = a\frac{k_{ex}}{D} \quad [3\text{-}26]$$

Here r is the distance from the powder center. C(t), C(∞), and C(0) are the concentrations of ^{18}O at time t, at equilibrium, and at the beginning of the exchange. Also, to directly compare with literature results, we can convert the kinetic data to get the ^{18}O diffusion profiles. Surface exchange coefficient (k_{ex}) and diffusion coefficient (D) can be obtained by fitting the ^{18}O accumulation curve with the diffusion

equations, which is similar to the data processing in ECR[56,87,88] and IEDP[89,90]. The accumulated ^{18}O exchange curve for diffusion into sphere with surface exchange is:

$$\frac{M(t)}{M_\infty} = 1 - \left[\sum_{n=1}^{\infty} \frac{6L^2 \exp\left(-\frac{\beta_n^2 D(t-t_0)}{a^2} \right)}{\beta_n^2 \left(\beta_n^2 + L^2 - L \right)} \right] \qquad [3\text{-}27]$$

M(t) is the accumulated ^{18}O in the powder at time t and M(∞) is the total amount ^{18}O accumulated when diffusion occurs over an infinite amount of time.

To extract kinetic parameters more efficiently from experiments, we can simplify Crank's solution based on the experimental conditions. In the surface exchange controlled region the diffusion process in the solid is considered to be quick and to not limit the reaction. At this particular condition, as a result of L<<1, the first root of solutions for Equation [3-27], β_1, is much larger than the subsequent roots. Therefore, the contributions from the other roots are and can be ignored. Then, we can use a series expansion to approximate Equation [3-27]:

$$\beta_1^{\,2} \cong 3L \qquad [3\text{-}28]$$

The concentration of ^{18}O, C(t), on the surface, when r=a, can then be described by:

$$\left. \frac{C(t) - C_\infty}{C_0 - C_\infty} \right|_{r=a} \cong \exp\left(-\frac{3kt}{a} \right) \qquad [3\text{-}29]$$

The time dependent exchange flux J(t) diffusing into the lattice from the surface can also be simplified to:

$$\frac{J(t)}{J(0)} = \frac{4\pi a^2 D \left(\frac{\partial C_1}{\partial r} \right)\Big|_{r=a}}{4\pi a^2 D \left(\frac{\partial C_1}{\partial r} \right)\Big|_{r=a,t=0}} \cong \exp\left(-\frac{3k_{ex}t}{a} \right) \qquad [3\text{-}30]$$

The accumulated ^{18}O curve M(t) now can be expressed as such:

$$\frac{M(t)}{M_\infty} = 1 - \exp\left(-\frac{3k_{ex}t}{a}\right) \qquad [3\text{-}31]$$

Therefore, in the surface exchange controlled region, all the diffusion equations can be simplified to a first order chemical reaction, and the incorporation process can be expressed by one simple k_{ex} term because the diffusion process no longer limits the reaction. The relationship between R_{ex} and k_{ex} is the relationship between catalysis in 2-dimensions and 3-dimensions, as shown in the difference in the boundary conditions in Equation [3-16] and Equation [3-23]:

$$R_{ex} \cong \frac{3k_{ex}}{a} \qquad [3\text{-}32]$$

R_{ex} values, corresponding to the catalytic ability for oxygen incorporation on the 2-dimensional cathode surface, are calculated from the flux of ^{18}O. Multiplying R_{ex} by a factor representative of the powders volume to surface ratio, the 2-dimensional rate of heteroexchange (R_{ex}) can be converted to a 3-dimensional surface exchange coefficient (k_{ex}), which is more widely used in literature[56,75,94,95]. We can then compare the theoretical model to experimental results.

Due to the small particle diameter (~300 nm) of the powder used in IIE, the corresponding L values in Equation [3-26] are equal to $\sim 10^{-5} k_{ex}/D$. This order of sample thickness allows this technique to be really sensitive to surface reactions. The testing sample will normally fall into surface exchange control regime unless D is much smaller than k, such as the case in LSM.

3.4 Results and Discussion

3.4.1 Trend in LSCF

IIE of LSCF at 400°C is shown in Figure 3-2 (a). The gas phase O_2 molecules, surface intermediate oxygen species, and lattice oxygen are all at kinetic equilibrium. At 400°C, IIE of LSCF starts to show the dissociation of $^{18}O_2$ at the beginning of the isotope switch (at t=0). The inlet $^{18}O_2$ concentration $^{18}N_{O2}$ is $3.3x10^{-7}$ moles. The initial concentration of $^{18}O_2$ is about $1.1x10^{-7}$ ($^{18}N_{O2}{}^{\text{non-exchange}}$), meaning that almost 2/3 of inlet $^{18}O_2$ ($^{18}N_{O2}{}^{\text{exchange}}$) are dissociated on the LSCF surface and 1/3 of inlet $^{18}O_2$ are just flowing through LSCF powder without participating in the reaction (or a non-observable homoexchange), as shown in equation [3-8]. Dissociation is the limiting reaction step at this temperature.

By monitoring the $^{16}O_2$, $^{16}O^{18}O$, $^{18}O_2$ signals we can trace the movement of ^{18}O through a series of reactions. At the same time, we can also calculate the flux, or exchange of the ^{18}O tracer with the oxygen in the solid phase. In IIE, knowing the amount of $^{18}O_2$ that is flowing into the reactor and the amount leaving the system, from the levels of the $^{16}O^{18}O$ and $^{18}O_2$ signals, we can calculate what we assume to be the ^{18}O flux into the lattice:

$$J(t)\big|_{r=a} = 2^{32}N_2(t) + {}^{34}N_2(t) \qquad [3\text{-}33]$$

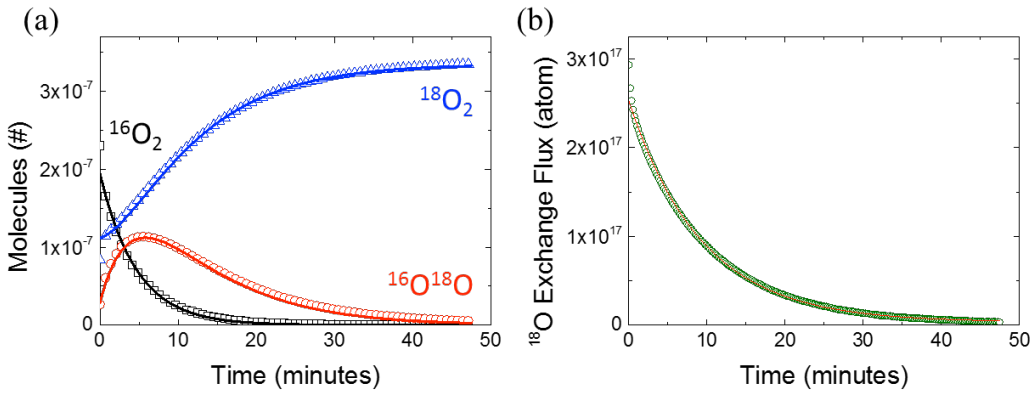

Figure 3-2. Fitting of experimental IIE data of LSCF at 400°C with simulated models in (a) Gas phase oxygen fractions, and (b) the flux of ^{18}O into the solid phase. (Symbols are experimental data points and lines are fitting results).

$J(t)|_{r=a}$ is the ^{18}O flux at the surface. Based on Equation [3-9]-[3-11], the surface coverage of ^{18}O and ^{16}O can be calculated. Figure 3-3 shows $^{16}\Theta_O$ and $^{18}\Theta_O$ on LSCF at 800°C under PO_2=0.025. The surface oxygen isotopic coverage curve indicates that the reaction is first order. The theoretical model fits the experimental data of gas phase profiles of $^{16}O_2$, $^{16}O^{18}O$, and $^{18}O_2$ for LSCF at 800°C in PO_2=0.025, as shown in Figure 3-2 (a). Figure 3-2 (b) shows the flux of ^{18}O into the solid phase as a function of time and the rate of heteroexchange R_{ex} is derived to be about $1.79*10^{-3}$ (1/s) from Equation [3-16]. Plotting the flux of ^{18}O into lattice versus time provides a convenient way to verify that the reaction follows first-order kinetics, suggesting that the boundary conditions in Equation [3-16] hold.

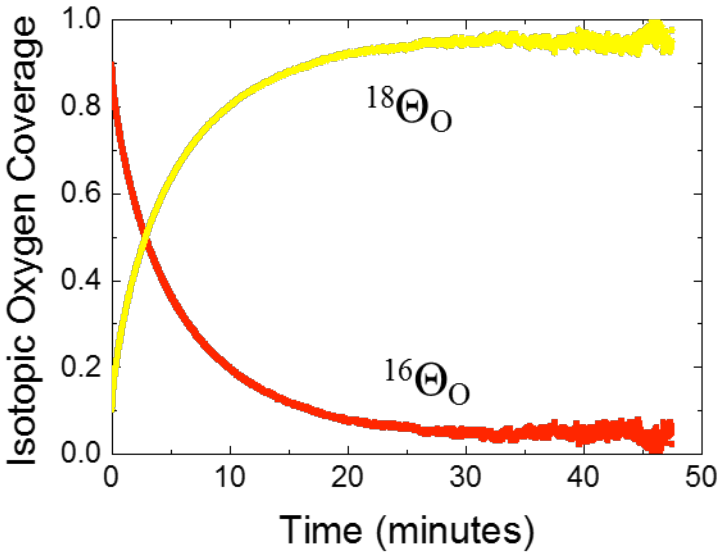

Figure 3-3. Coverage of ^{16}O (red) and ^{18}O (yellow) on surface of LSCF derived from IIE of LSCF at 800°C. The exchange of isotope oxygen indicates the surface exchange shows a first order reaction.

To compare R_{ex} to the surface exchange coefficient, k_{ex}, we can fit the total exchange curve as a function of time to Crank's solutions to extract k_{ex}. The amount of ^{18}O accumulated into lattice can be calculated from the mass balance of the system. We can integrate the real-time information from IIE to get the accumulated ^{18}O.

$$M(t) = \int_0^t \mathrm{J}(t)\Big|_{r=a} = \int_0^t 2^{32}\mathrm{N}_2(t) + {}^{34}\mathrm{N}_2(t) \qquad [3\text{-}34]$$

Figure 3-4 shows the ^{18}O conversion curve as a function of time ($M(t)/M(\infty)$) for IIE of LSCF at 800°C. Fit with the diffusion equation in Equation [3-27], the surface exchange coefficient (k_{ex}) of LSCF is $8.3*10^{-9}$ (cm/s) and is consistent with $R_{ex}=1.79*10^{-3}$ (1/s) (converted to $k_{ex}=8.4*10^{-9}$cm/s) acquired from Equation [3-16] using the relationship in Equation [3-31]. The value of k_{ex} can be directly linked to R_{ex} based on Equation [3-32]. Using literature values extracted from IEDP-SIMS, we can

estimate the value of D* for LSCF at 400°C to be about $1.3x10^{-10}$ cm^2/s, one order magnitude smaller than the observed k_{ex} value from this study. Therefore, the L value for LSCF at 400°C is on the order of 10^{-4}, indicating a surface exchange limited region. The values of k_{ex} we calculated are consistent with current literature values [56,75,94,95].

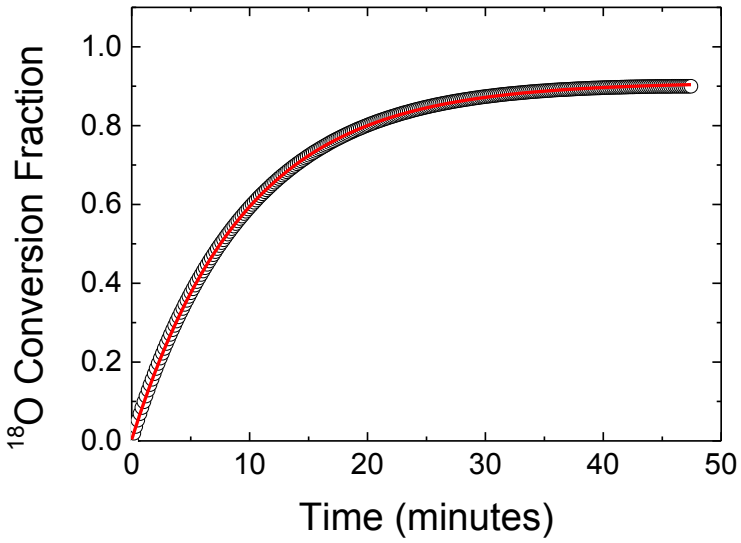

Figure 3-4. ^{18}O conversion fraction curve from IIE of LSCF in PO_2=0.025 at 800°C

The temperature dependence of k for LSCF is investigated to extract the resulting activation energies for each of the reaction steps. Figure 3-5 (a) to (d) shows IIE of LSCF from 350°C to 450°C in PO_2=0.025. The corresponding ^{18}O exchange flux for (a), (b), (c), and (d) are displayed in Figure 3-5 (e), (f), (g), and (h), respectively. Symbols are experimental data and lines are fitting results. At 300°C, no observable exchange occurs and all inlet $^{18}O_2$ molecules pass through LSCF powder without any surface reactions, suggesting that at this temperature LSCF is limited by dissociation. At 375°C, IIE of LSCF shows dissociation of a sizable portion of inlet

$^{18}O_2$, suggesting that LSCF has a good catalytic activity towards the dissociation of oxygen above this temperature. The low temperature ^{18}O exchange flux is shown in Figure 3-5 (d)-(f). By removing the contribution of the non-exchange fraction in Equation [3-11], the ^{18}O flux can be expressed as a single first order exchange. All curves of ^{18}O exchange flux at different temperatures follow first order reactions, suggesting that oxygen diffusion in LSCF does not limit the reaction above 375°C, but the gas-solid incorporation process does.

Higher temperature IIE of LSCF at PO_2=0.025 from 500°C to 800°C are shown in Figure 3-6 (a), (b), (c), and (d). All ^{18}O exchange flux for these temperatures show first order reactions as shown in Figure 3-6 (e), (f), (g), and (h). However, it is a concern that the curves have almost identical shapes, as shown in in Figure 3-6 (a), (b), (c), and (d). Insensitivity to changes in temperature for IIE above 500°C suggests that the limiting factor at these temperatures is the amount of oxygen flowing into the system, as this would have a first order dependence[78]. It is common for kinetics experiments on catalysts to be performed in reactant excess regions, where the amount of reactant will not be able to limit the level of conversion.

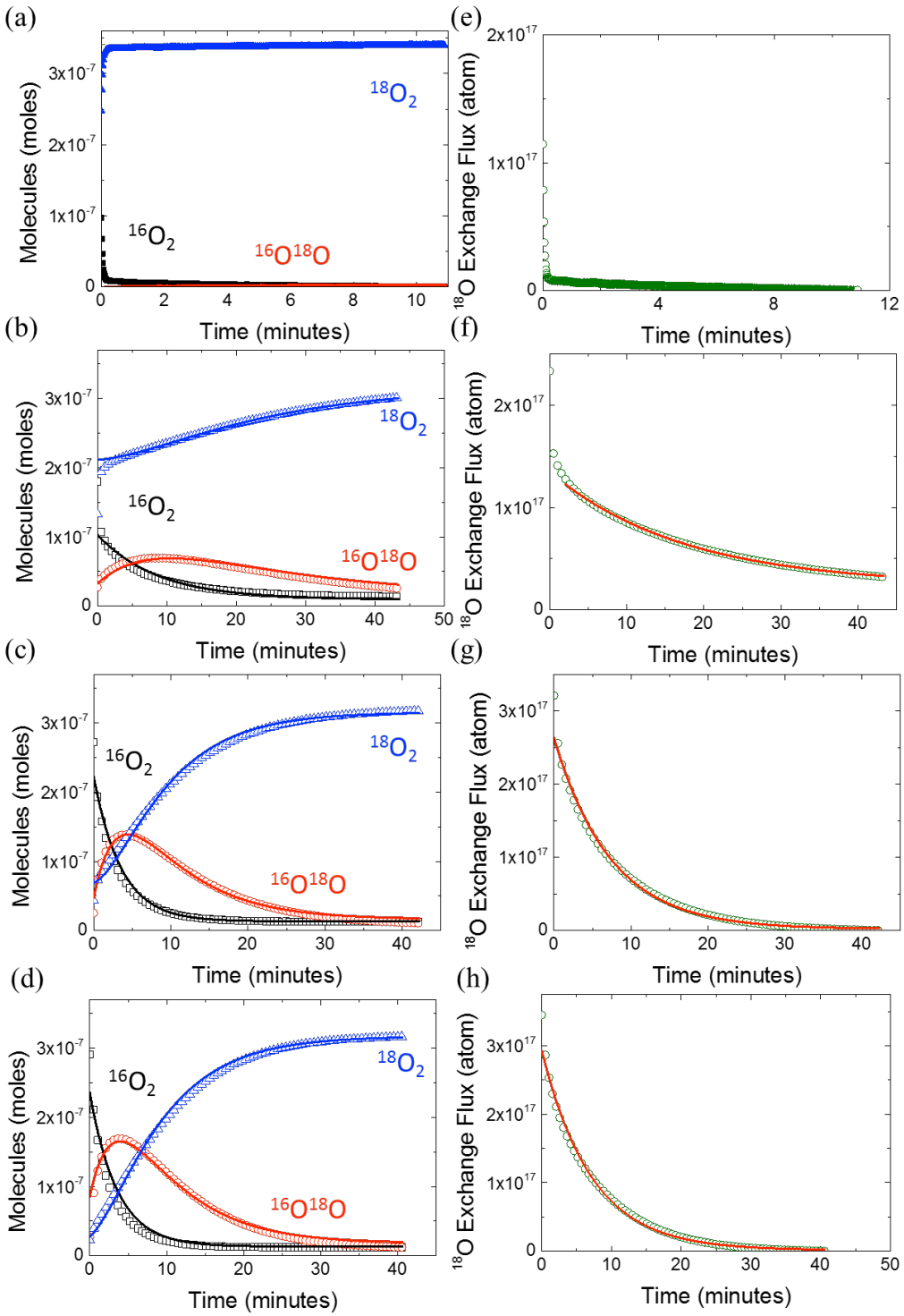

Figure 3-5. IIE of LSCF in PO_2=0.025 at intermediate temperatures without limited by the gas diffusion: gas phase oxygen fraction at (a) 350°C, (b) 375°C, (c) 425°C, and (d) 450°C; the flux of ^{18}O into the solid phase at (e) 350°C, (f) 375°C, (g) 425°C, and (h) 450°C. The initial concentration of $^{18}O_2$ indicates whether the dissociation limits the reactions. (Symbols are experimental data points and lines are fitting results).

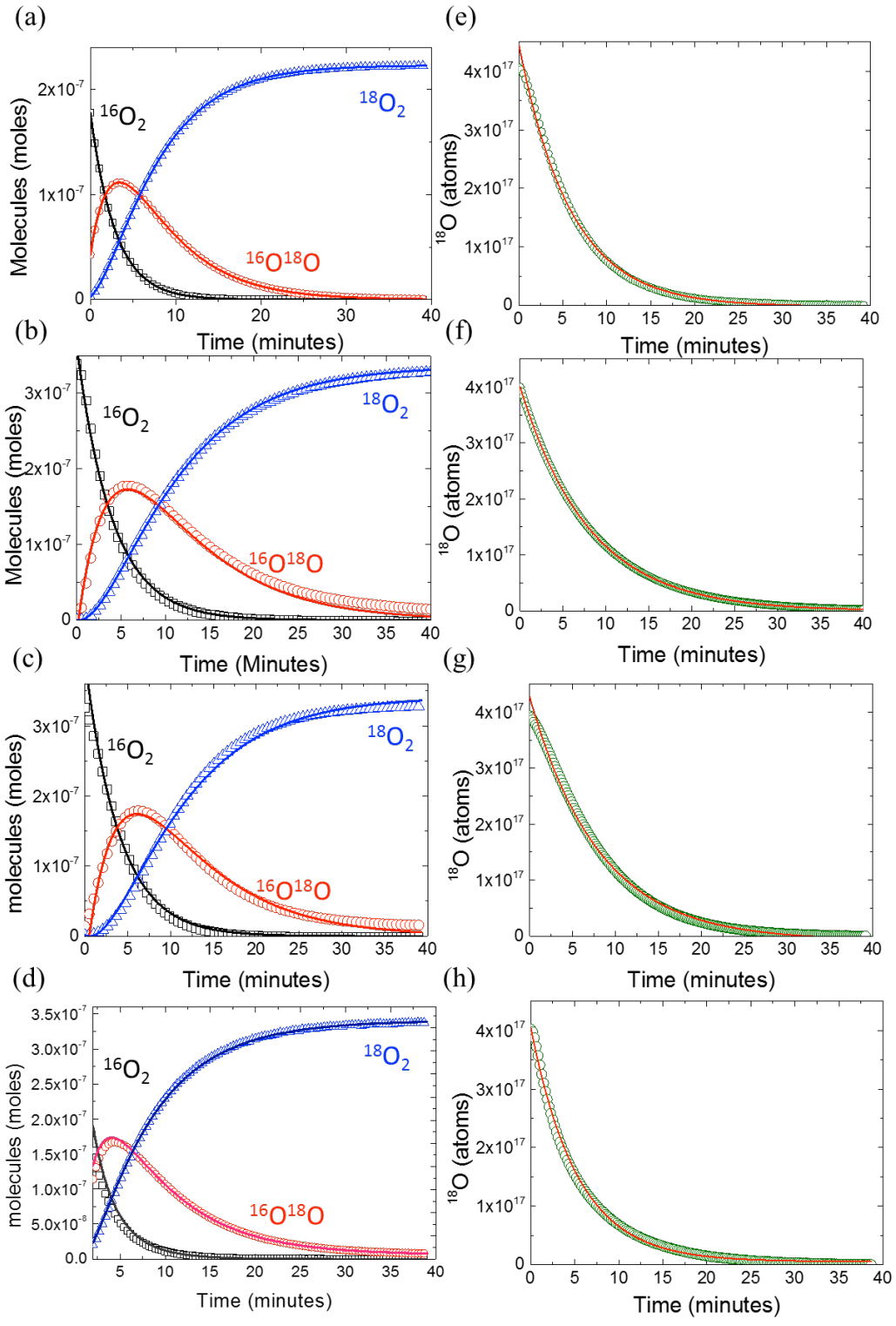

Figure 3-6. IIE of LSCF at different temperatures: gas phase oxygen fraction at (a) 500°C, (b) 600°C, (c) 700°C, and (d) 800°C; the flux of ^{18}O into the solid phase at (e) 500°C, (f) 600°C, (g) 700°C, and (h) 800°C. (Symbols are experimental data points and lines are fitting results).

All of the elementary reaction steps, including dissociation, incorporation, and diffusion, are thermally activated processes, and each of them has a different temperature dependence. Therefore, we can study isotope exchange experiments based on different temperature regions to separate the reaction steps with different apparent activation energies. Figure 3-7 shows the Arrhenius plot of k_{ex} with respect to reciprocal temperature. In the higher temperature region (500°C - 800°C), the surface exchange coefficient (k_{ex}) shows only a slight increase as the temperature increases with an apparent activation energy of ~8 kJ/mol. The observed low activation energy at high temperature demonstrates that the amount of oxygen flowing through the LSCF powder per unit time limits the number of reactions that can be detected. At low temperature, the apparent activation energy is about 42.3 kJ/mol, which the surface exchange is the main contribution. The literature values of k_{ex} from IEDP-SIMS[23] show an activation energy of about 180 kJ/mol. The apparent activation energy from gas phase oxygen isotopic exchange is about one quarter of the value from IEDP-SIMS. Due to the small particle size of IIE experiments, the activation energy from IIE might be closer to the real value for the surface exchange process.

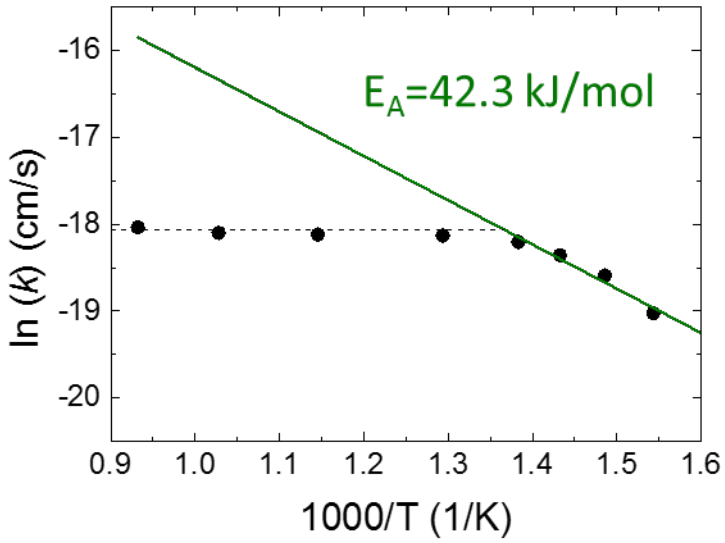

Figure 3-7. Arrhenius plot of surface exchange coefficient (k_{ex}) to the temperature with an apparent activation energy (E_A)=42.3 kJ/mol from 375°C to 450°C.

To further understand properties, such as active site to surface area ratio and oxygen partial pressure dependence, IIE of LSCF was conducted at different oxygen partial pressures (PO_2=0.015 and PO_2=0.02) in the temperature range from 375°C to 450°C, as shown in Figure 3-8. By changing the PO_2 of the gas flowing into the reactor, we observed that the exchange rate increases as the oxygen partial pressure increases. The number of available active sites for oxygen to adsorb/dissociate onto the cathode powder surface is also directly related to the oxygen partial pressure through the Langmuir adsorption isotherm[84].

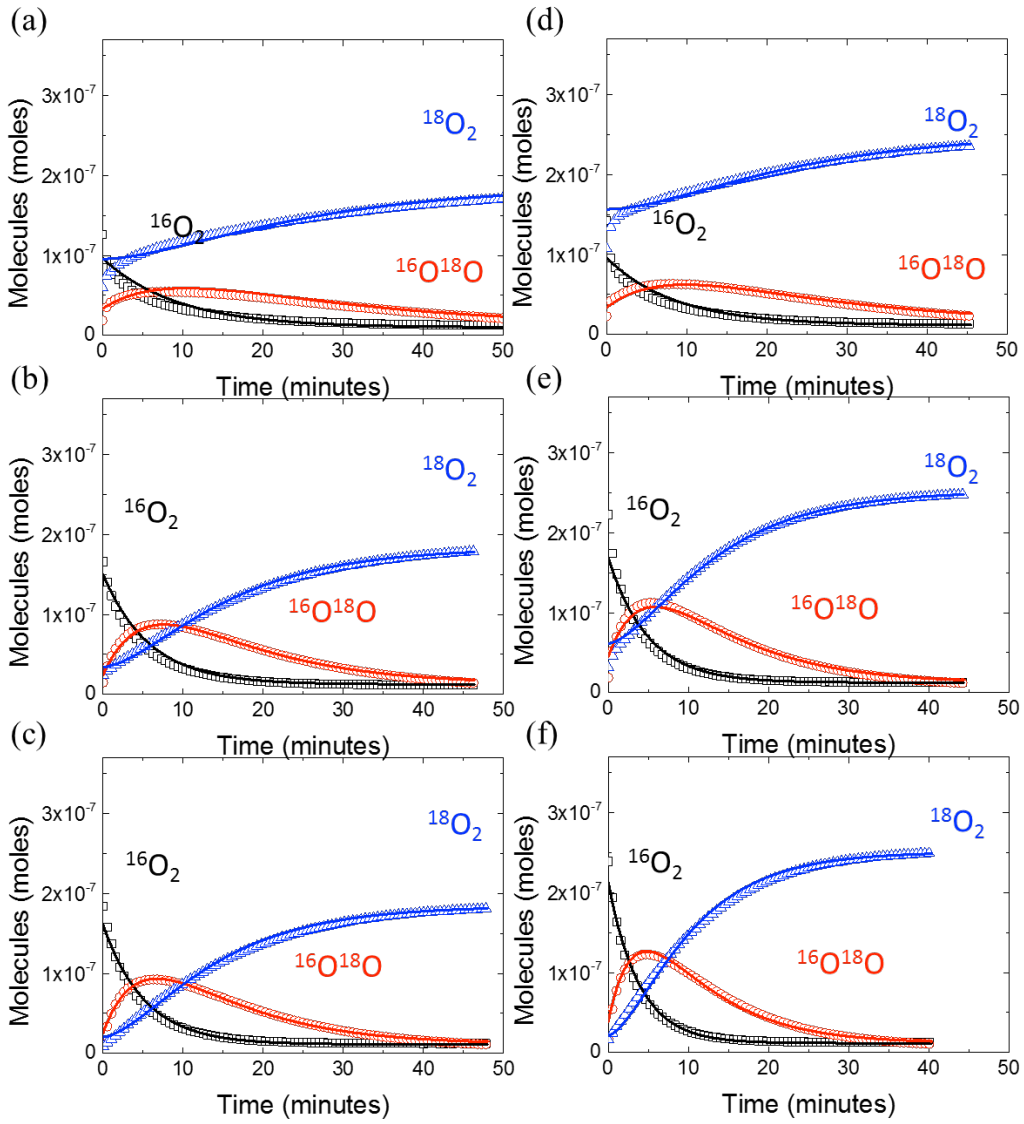

Figure 3-8. IIE of LSCF in different PO_2 at intermediate temperatures: gas phase oxygen fraction in PO_2=0.015 at (a) 375°C, (b) 425°C, and (c) 450°C, and in PO_2=0.02 at (d) 375°C, (e) 425°C, and (f) 450°C; Symbols are experimental data points and lines are fitting results).

The best-fit k_{ex} values at different temperatures are summarized in the double-log plot in Figure 3-9. The plot of log(PO_2) vs. log(k_{ex}) shows a linear relationship at all different temperatures with slopes between 0.87 and 1. This linear relationship between PO_2 and k could provide the information about the intermediate oxygen species that participate in the reaction. If the surface exchange is pure double heteroexchange, the slope is one because both oxygen atoms in O_2 molecule

contribute to the exchange process. If surface exchange is completely dominated by single heteroexchange, only one out of two oxygen in O_2 participates in the reaction, and the slope should be 0.5. A slope between 0.87 and 1 indicates double heteroexchange mechanisms dominates the surface exchange on LSCF from 375°C to 450°C and one of the possible intermediate oxygen species that is participating in the surface exchange on LSCF is peroxide (O_2^{2-}).

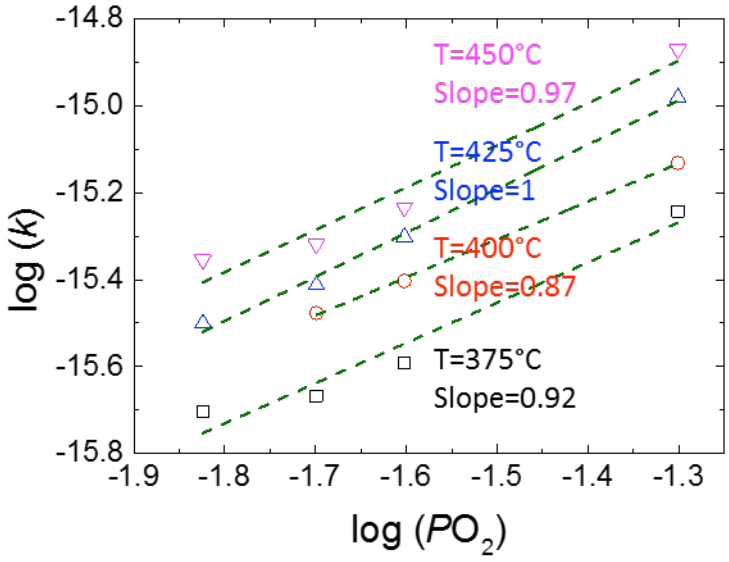

Figure 3-9. log k_{ex} versus log PO_2 for LSCF at the temperature range from 375°C to 450°C. The temperatures and linear fitting results in slopes as listed in the figure.

3.4.2 Trend in LSM

Surface exchange processes for LSM are different than those for LSCF because of its lack of oxygen vacancies. The super-stoichiometric LSM offers a limited number of oxygen vacancies even at high temperature. Figure 3-10 (a) shows IIE of LSM at 800°C in PO2=0.025, and the 18O exchange flux into LSM lattice is shown in Figure 3-10 (b). Green dots are the experimental data and cannot be fitted

well with a simple first order reaction, as shown in blue line. The exchange process in LSM is co-limited by several factors and could not be explained by a single exchange model.

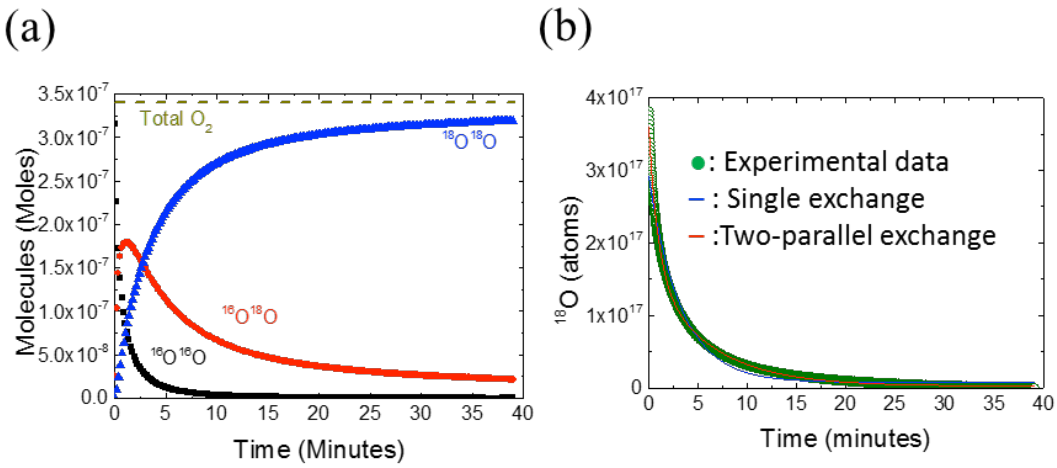

Figure 3-10. (a) IIE of LSM in PO_2=0.025 at 800°C and (b) the corresponding ^{18}O flux with single exchange and two-parallel exchange model fit.

One possible explanation is the presence of two-parallel exchange mechanisms on the LSM surface. Here, we consider that LSM provides two parallel pathways for oxygen to incorporate into the lattice. One pathway is relative slow, and the diffusion process is likely via vacancy exchange mechanism, the other pathway is fast and is possibly through grain boundaries. Ivanov, et al.[96], and De Souza et al.[97], report that the diffusion along grain boundaries may dominate the diffusion process for LSM in the intermediate temperature range. Therefore, it is reasonable to assume that oxygen atoms on the surface can be transported to the bulk by either of these exchange mechanism. The boundary condition can be written as:

$$J_{18O} = \frac{d^{18}\Theta_{O,lat}}{dt} = \left[S_{ex,fast} AR_{ex,fast} (^{18}\Theta_O - ^{18}\Theta_{O,lat}) + S_{ex,fast} AR_{ex,slow} (^{18}\Theta_O - ^{18}\Theta_{O,lat})\right] \quad [3\text{-}35]$$

where $R_{ex,fast}$ and $R_{ex,slow}$ represent the fast and slow exchange rates on LSM, $S_{ex,fast}$A and $S_{ex,slow}$A represent the available surface sites for the fast and slow exchange, respectively. The ^{18}O exchange flux derived from a two-parallel exchange model shows a good fit for the experimental data in Figure 3-10 (b).

Figure 3-11 shows IIE of LSM in different PO_2 at 800°C. The two-parallel exchange model (red curve) fits the experimental data better than the single exchange model (blue curve). The results are summarized in table II. k_{fast} has a positive relationship with increases in PO_2. On the contrary, k_{slow} appears to be insensitive to changes in PO_2. Because the oxygen stoichiometry of LSM is relatively insensitive to PO_2, the slow exchange pathway could be attributed to bulk diffusion via vacancies and the fast exchange process could be related to grain boundary diffusion.

Figure 3-12 shows IIE of LSM at different temperatures in PO_2=0.025. The two-parallel exchange mechanisms model (red curve) shows a good fit with experimental data (green dot). Best-fit $R_{ex,fast}$ and $R_{ex,slow}$ values are listed in table II. Both $R_{ex,fast}$ and $R_{ex,slow}$ show a negative temperature dependence. Though two-parallel exchange model fits the experimental data of isotope exchange well, it still fails to explain the inverse temperature dependence.

One possible reason might be related to the difference in oxygen vacancy concentration between the near surface region and the bulk of LSM. At lower temperatures, the majority of vacancies appear in the near surface region, and the thickness of this region is small. As the temperature increases, the depth of the near surface region increases, providing higher concentrations vacancies that could contribute to the exchange process. On the other hand, the bulk of LSM still

maintains a relatively low concentration of vacancies even at elevated temperature, limiting diffusion to the near surface. The non-uniformity in vacancy concentration in the near-surface versus the bulk may cause the appearance of two separate diffusion rates, and prevent a simple model being sufficient. As shown in Figure 3-10, all of $^{18}O_2$ flowing to LSM powder are dissociated at the beginning of the switch, suggesting that LSM has a good catalytic activity towards the dissociation of oxygen molecules at 800°C. The formation of $^{16}O^{18}O$ is determined by the surface coverage ratio of ^{18}O to ^{16}O and the peak position of $^{16}O^{18}O$ indicates the exchange time for ^{18}O to cover half of the surface. IIE of LSM shows a precedent shift than in LSCF. It could be explained by the low ionic conductivity of LSM limiting the diffusion of ^{16}O from the inner position of LSM powder to surface. The surface of LSM is quickly exchanged from ^{16}O to ^{18}O in the first 5 minutes of exchange, and the long-tail of $^{16}O^{18}O$ signal points out that the exchange process is still ongoing with a slow diffusion process of ^{16}O to the surface. The results suggest that the diffusion of oxygen between near surface region and bulk is a limiting step for the ORR on LSM. From IIE of LSM, it suggests that LSM has a higher concentration of surface vacancy in the near surface region but a lower concentration of vacancy in the bulk, resulting in a non-constant diffusion coefficient (D) as a function of distance from the powder center. Due to the non-uniform concentration of vacancies in LSM, both surface exchange coefficient (k_{ex}) and diffusion coefficient (D) are difficult to extract from IIE using the diffusion equations. De Souza et al.[68] reported D* and k* values from SIMS of $5*10^{-15}$ (cm^2/s) and $6*10^{-9}$ (cm/s). From these values the calculated characteristic length [12] of LSM is about $8*10^{-7}$ cm at 800°C. In our experiments, the

sample thickness is equal to the radius of the powder and is on the order of 10^{-5} cm. For LSM at 800°C the value of L(=a/L_c) is around 10-100, suggesting that diffusion process limits the overall reaction. Though IIE of LSM is a really surface-sensitive technique with a small sample thickness, the extremely low D value still limits the exchange process.

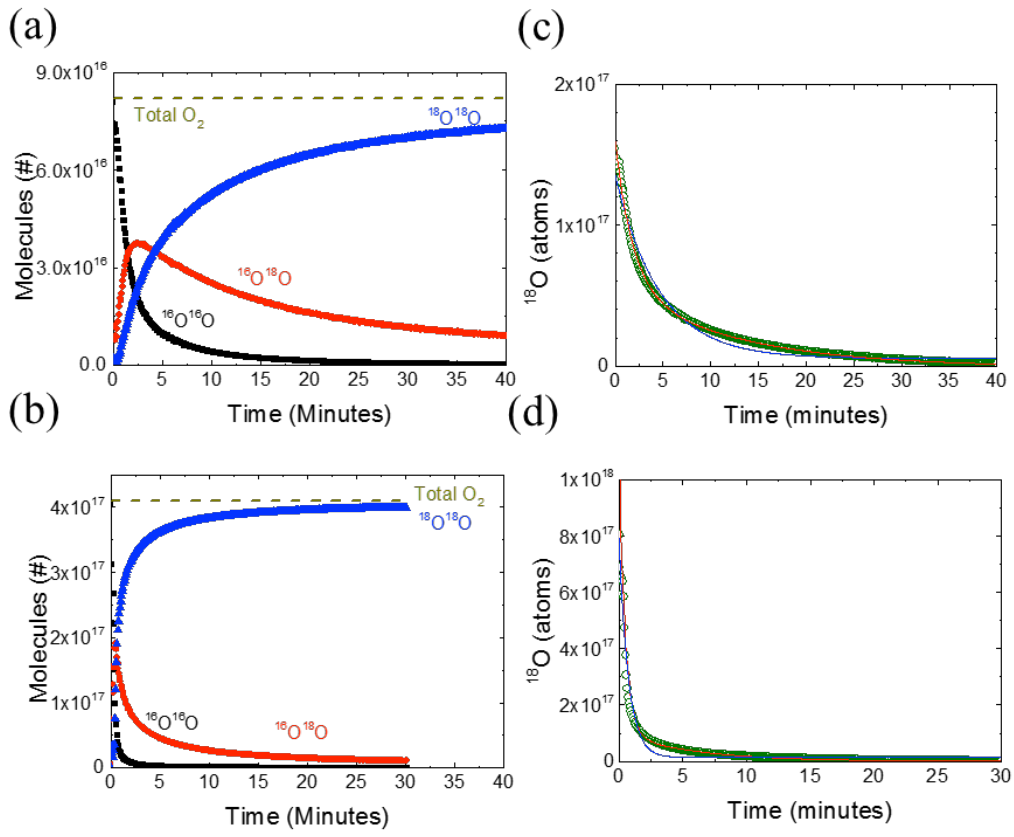

Figure 3-11 . IIE of LSM in different PO_2 at 800°C: gas phase oxygen fraction in PO_2= (a) 0.01, and (b) 0.05; the flux of ^{18}O into the solid phase in PO_2= (c) 0.01, and (d) 0.05. Symbols are experimental data points and lines are fitting results with a single (blue), or two-parallel (red) exchange model.

Table 3-I. Fitting parameters for LSM in PO_2=0.025 at different temperatures

T(°C)	PO_2	$R_{ex,slow}$ (1/s)	$R_{ex,fast}$ (1/s)
750	0.025	$2.9*10^{-3}$	$3.37*10^{-2}$
800	0.01	$1.36*10^{-3}$	$9.26*10^{-3}$
800	0.025	$2.8*10^{-3}$	$1.8*10^{-2}$
800	0.05	$2.66*10^{-3}$	$3*10^{-2}$
850	0.025	$2.5*10^{-3}$	$1.25*10^{-2}$

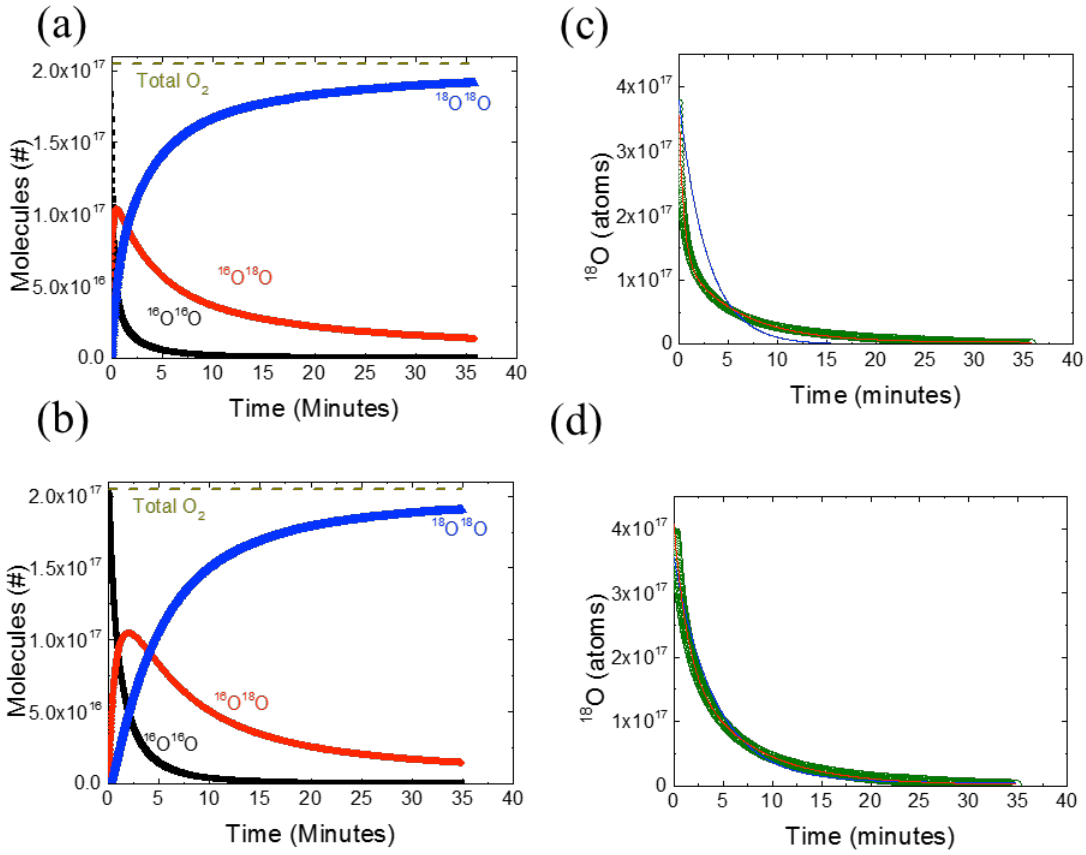

Figure 3-12. IIE of LSM in PO_2=0.025 at different temperature: gas phase oxygen fraction at (a) 750°C and (b) 850°C; the flux of ^{18}O into the solid phase at (c) 750°C and (d) 850°C. (Symbols are experimental data points and lines are fitting results).

A comparison of LSM and LSCF isotope conversion profiles and ^{18}O flux as a function of time is shown in Figure 3-13. LSCF is a good ionic conductor, and almost all lattice ^{16}O are exchanged with ^{18}O. Over the same time length LSM exchanges

only half of the total number of lattice oxygen to ^{18}O. This is most likely caused by the lack of vacancies in the bulk of the material. Based on [21], the high R_{ex} of LSM could be a result of the high concentration of surface vacancies rather than a high rate constant for incorporation. In summary, the oxygen exchange process for LSM appears to be more complicated than exchange for LSCF. This complexity may arise due to the oxygen stoichiometry of LSM at higher temperature and the effect of oxygen vacancies on the various exchange and conduction mechanisms.

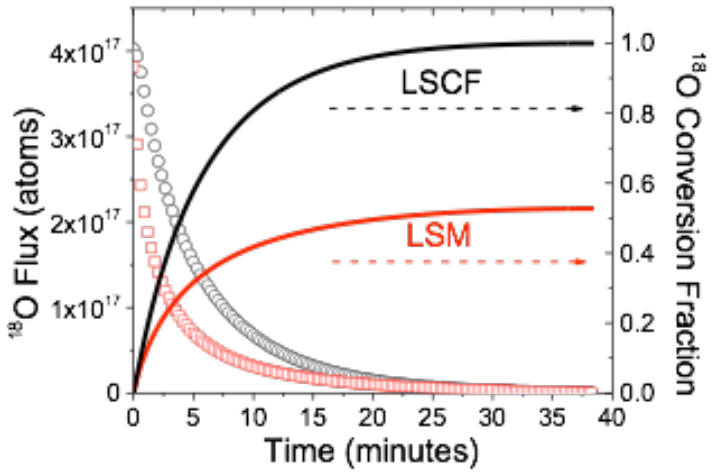

Figure 3-13. A comparison of LSCF and LSM in the conversion fraction and ^{18}O exchange flux as a function of time.

3.5 Conclusions

Isotope exchange is a powerful technique to probe the kinetics of heterogeneous catalysis on SOFC cathodes. The overall ORR can be visualized and quantified by tracing the movement of labeled oxygen. We have demonstrated IIE of LSCF and LSM at different temperatures and oxygen partial pressures, allowing the kinetics rates to be obtained. A mathematic model has been developed to unify extracted surface exchange rates that are consistent with values found in literature for

other experiments, such as conductivity relaxation and SIMS. The relationship between equilibrium constant K_1 K_2 and the nonstoichiometry is also established. The difference between R_{ex} and k_{ex} is the contribution of surface vacancies. The bridge between solid state diffusion and surface heterogeneous catalysis has been linked by the heteroexchange rate coefficient (R_{ex}) and surface exchange coefficient (k_{ex}). A two-step reaction model has been proposed to describe the ORR mechanism and the difference between LSCF and LSM has been discussed. LSCF has a faster dissociation reaction than LSM, and the limiting step of the ORR for LSCF at high temperature is the surface exchange process.

The isotope exchange profile of LSCF at intermediate and high temperatures can be explained by a simple first order reaction with different rate limiting mechanisms. At intermediate temperatures, the surface exchange is the rate-limiting step. At high temperatures, due to the limitation of the isotope exchange experimental set-up, there is a 100% conversion rate of the ^{18}O flowing through the system. Therefore, this may limit the observation of actual kinetic rates. The experimental design of plug-flow isotope exchange experiments is really important because the observed results may be inaccurate due to improper design.

LSM exhibits a pure electrical conductor at temperature lower than 750°C with minimum surface vacancies. LSM shows a relative lower incorporation and dissociation rate than LSCF. LSM has an exchange flux with possible a two-parallel exchange pathway or a different vacancy concentration in the near surface region and in the bulk. Studies of isotope exchange can greatly contribute to the elucidation of the interactions between molecular oxygen and the cathode surface. Isotope exchange

can help characterize the dissociation of oxygen molecules at the oxide surface as well as the conduction of oxygen ions within the oxide. The kinetic data based on IIE results can provide insight about what is actually happening during the ORR. The results allow us to further investigate the degradation mechanisms present in the ORR as well as to design and engineer new cathode materials/structures that can prevent such degradation from occurring.

Chapter 4: Fundamental Impact of Humidity on SOFC Cathode Degradation

4.1 Introduction

Solid oxide fuel cells (SOFC) electrochemically oxidize fuels for the generation of electricity. Two key advantages of SOFCs are their high efficiency and ability to utilize more fuels than just high purity H_2. This fuel flexibility stems from the dissociation and transport of oxygen from the cathode to the anode, where the fuels are oxidized[1-4]. Unfortunately, cathode degradation under real working conditions is a factor that limits SOFC performance[22,38,43,46,98,99].

The long term durability of these materials is a major challenge, due to the high temperature required for the thermally activated oxygen reduction reaction (ORR) as well as the variety of gases present during operation[10,100]. The impurities present in air on the cathode side of the cell could induce undesirable reactions. Some of these impurities, such as Cr or silica[29,41,101-104], arise due to the interconnect materials while some are inherent in ambient air, such as humidity and CO_2 [39].

Humidity has been found to degrade the performance of $(La_{0.8}Sr_{0.2})_{0.95}MnO_{3-x}$ (LSM) and $La_{0.6}Sr_{0.4}Co_{0.2}Fe_{0.8}O_{3-x}$ (LSCF) based cells[23,29,37,42,44,45,105-107]. This degradation can be either reversible or irreversible[44]. However, there is no conclusive evidence showing, fundamentally, how water participates in the degradation process, and it is hard to quantify the effect of water in different operating conditions and aging times. In order to improve the stability of cathodes at elevated temperature in

the presence of water, a contaminant that is challenging to avoid, we need to understand the fundamental role that humidity plays in the ORR occurring on the cathode surface.

The application of heterogeneous catalysis techniques to the kinetics of cathode powders can provide fundamental insight in understanding degradation due to gas contaminants. Isotope exchange is a useful technique for determining the mechanistic steps comprising the ORR. Isotope exchange depth profiling (IEDP) with secondary ion mass spectrometry (SIMS) has shown the effects of contaminants on the cathode after exposure to both a contaminant and isotopically labeled oxygen for a set period of time at a constant temperature[23,29]. By fitting the isotope distribution profiles with diffusion equations, the tracer-surface exchange coefficient (k^*) and tracer-diffusion coefficient (D^*) can be obtained to quantitatively describe the degradation effects on the ORR. However, the *ex-situ* nature of IEDP-SIMS limits the techniques ability to probe the interaction between contaminants and the cathode, and can only be performed under pre-defined temperatures and partial pressures.

Oxygen isotope exchange with gas-phase analysis can provide greater experimental parameter flexibility, as well as *in-situ* determination of intermediate species. In this study, we use temperature programmed isotope exchange (TPX)[76,77,108-113] to probe the exchange behavior between water and the cathode surface as a function of temperature, PO_2, and water vapor concentration. To focus on the exchange between the contaminant and the cathode surface, an experiment called isotope saturated temperature programmed exchange (ISTPX) has been designed[114,115]. Contaminant gasses are introduced into a reactor that contains a

powder sample that was previously exchanged with ^{18}O. The contaminant gasses can then exchange with the isotopically labeled oxygen in the powder lattice, creating isotopically labeled contaminant gasses. This type of experiment can show exchange between the contaminant and the powder, without gas phase isotopically labeled oxygen exchanging first. In addition, such an experiment, in combination with TPX can help to differentiate between the various types of exchange that can occur on the cathode surface. ISTPX was performed under a variety of PO_2 and PH_2O conditions to determine how they alter the exchange kinetics. Another benefit of ISTPX is the ability to probe the surface under significantly higher PO_2 conditions (near ambient) without the limitations caused by the price of $^{18}O_2$ and saturation of the signals being recorded using mass spectrometry. When studying the exchange between water, oxygen and the cathode surface, it is important to note that main mass charge ratio peak of H_2O (18 m/z) overlaps with the main $^{18}O_2$ cracking mass. However, the overlap of these peaks can be avoided by using deuterium oxide (D_2O), allowing us to trace the movement of ^{18}O by monitoring the signal of normal $D_2{}^{16}O$ (m/z=20) and isotopically labeled $D_2{}^{18}O$ (m/z=22) without the effects of the fraction of ^{18}O.

In TPX, the cathode surface can be seen as a catalyst bed, where $^{18}O_2$ molecules are adsorbed on the surface and then dissociated into single ^{18}O atoms. The single atoms then have the possibility to either incorporate into the cathode lattice or recombine with other oxygen atoms on the surface and desorb back into the gas phase as molecules. Using *in-situ* isotope exchange, gas phase products can be monitored by mass spectrometry. The intensity of m/z signals 32, 34, and 36, corresponding to the concentration of $^{16}O^{16}O$, $^{16}O^{18}O$, and $^{18}O^{18}O$, respectively. These concentrations can

provide information about the dissociation of $^{18}O_2$ on the cathode surface. In the presence of D_2O, the dissociated ^{18}O on the surface can exchange with the oxygen in the contaminant molecules and form isotope contaminants, $D_2{}^{18}O$. This by-product can provide information about the surface interaction between oxygen molecules and water. In the case of ISTPX, the lattice oxygen is isotopically labeled and can exchange with gaseous $^{16}O_2$ and/or $D_2{}^{16}O$, allowing us to directly investigate the surface exchange process at the gas-solid interface as a function of temperature. Consequently, the temperature and PO_2 regions where contaminant reactions dominate have been demonstrated for the first time. The water participates in the oxygen exchange process, and both PO_2 and temperature changes the impact of water on the cathodes.

4.2 Experimental

Commercially available powders of $La_{0.6}Sr_{0.4}Co_{0.2}Fe_{0.8}O_{3-x}$ (LSCF), from Praxair, and $(La_{0.8}Sr_{0.2})_{0.95}MnO_{3-x}$ (LSM), from Fuel Cell Materials, were used. The amount of powder was normalized by surface area to 0.1 m^2 for each sample. BET measurements show that the surface areas of the LSM and LSCF powders are 5.6 m^2/g and 6.5 m^2/g, respectively. Therefore, 0.015g of LSCF and 0.018g of LSM were used to maintain constant surface area. The benefit of testing powders is that the thickness of the material is the particle size (~80-500 nm for this study), which is much smaller than their characteristic thickness[12,73,74], allowing for kinetic measurements to be made in a surface exchange controlled regime.

The details of the experimental set up can be seen in our previous work[10,73,74,100]. For isotope exchange experiments the system consists of four sections:

gasses/contamination sources; oxygen isotope gas stream; a temperature controlled quartz reactor; and an Extrel QMS quadrupole mass spectrometer, as shown in Figure 4-1. In the first part of the system, tanks of pure helium and pure oxygen, as well as a variety of concentrations of oxygen (all balanced in He) are connected to mass flow controllers (MKS) to accurately control PO_2. The gas stream can either flow to the reactor directly or through a water bubbler to humidify the gas. The oxygen isotope portion consists of $^{18}O_2$ isotope gas (Sigma-Aldrich; 95% pure) and helium with a small amount of argon (0.1%) used as an inert tracer. A K-type thermocouple, which is connected to the temperature controller and controls the furnace directly, is placed at the top of the powder sample in order to obtain a more accurate temperature.

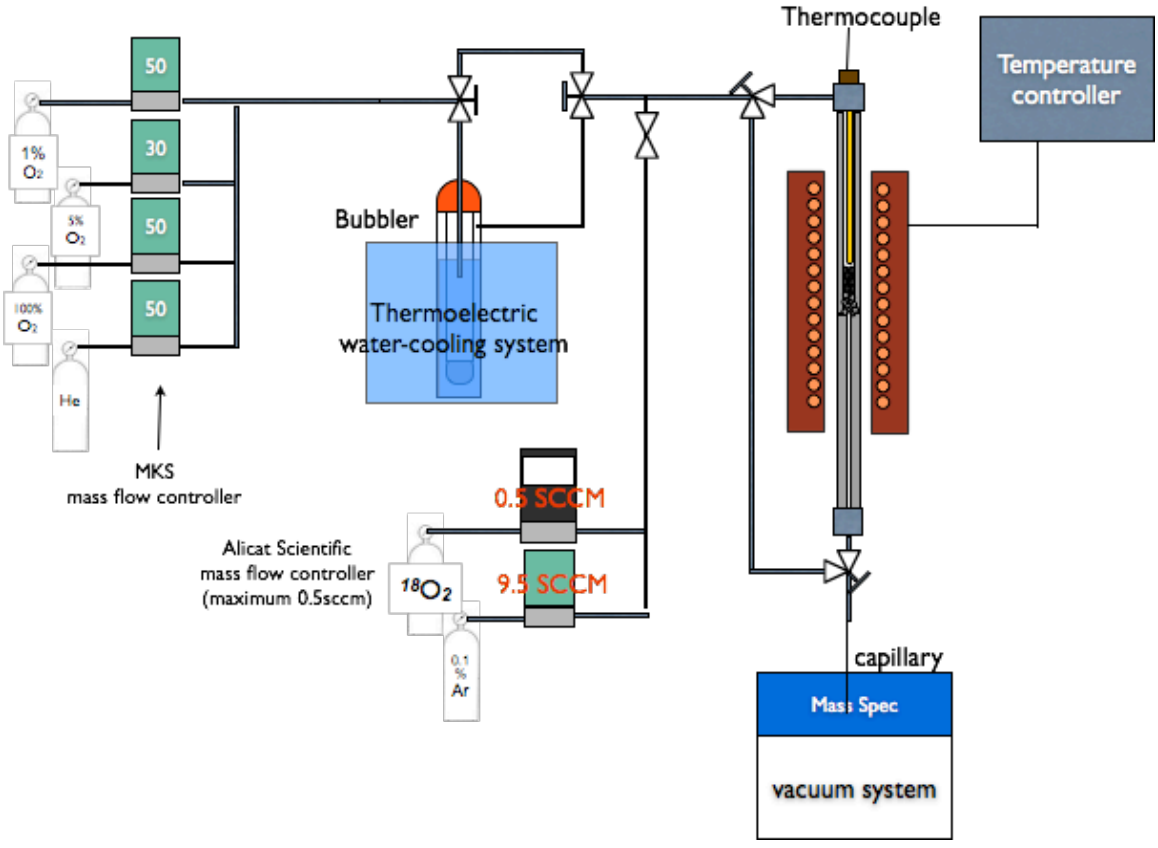

Figure 4-1. Experimental set up of the Isotope exchange

The flow rate is fixed at 20 SCCM, so the time for the gas to traverse the entire sample (~2mm in height) is approximately ~0.1-0.15 seconds. The reactor effluent then flows through a capillary to the quadrupole mass spectrometer where the composition is analyzed and recorded. A cooling system was installed in order to provide a controlled low concentration of water vapor to study the interaction of water and to avoid condensation issues in the high vacuum mass spectrometer system. The concentration of D_2O was calibrated by flowing different amounts of gas through the impinger at different bath temperatures, and then balanced with bypass gas to establish a total fixed flow rate 20 SCCM. The temperature of water bath has a deviation of +/- 0.2°C during each experiment, ensuring a relatively constant concentration of water vapor. D_2O vapor pressure is determined using temperature readings and a temperature/vapor pressure database provided by NIST.

TPX is a characterization technique to observe the interaction between isotopically labeled gas phase oxygen, and solid phase 'normal' oxygen as a function of temperature. First, the powder is pretreated at 800°C under an $^{16}O_2$ environment for 30 minutes to ensure that the powder surface is clean and has reached thermodynamic equilibrium. After the pretreatment, the powder is cooled down to room temperature to ensure the powder is rich with 'normal' ^{16}O. After reaching room temperature, pure He is flowed to stabilize all of the gas signals. Then the sample is heated under different concentration of isotopically labeled $^{18}O_2$ balanced with He at a fixed ramp rate of 30°C /min. The different m/z signals of oxygen species and contaminant species are recorded using the quadrupole mass spectrometer. The influence of water on the oxygen catalyst can be observed from changes in the

various isotopes generated from oxygen and water as a function of time and temperature.

To further probe the interaction between contaminants and lattice oxygen at different temperatures, a technique called ISTPX was developed. The powder was first exchanged with $^{18}O_2$ at 800°C for about 30-40 minutes. Because LSCF is a good mixed ionic electronic conductor (MIEC) and LSM is a poor ionic conductor, it is expected that LSCF will fully exchange all of it's O lattice sites to ^{18}O, whereas LSM will not. Based on the mass balance between inlet and outlet oxygen molecules, LSCF powder is almost fully saturated with ^{18}O and for LSM roughly 50% of the powder is exchanged with ^{18}O, indicating that the inner lattice sites have probably not exchanged fully. After equilibrating the powder with^{18}O, each sample was placed in the center of a continuous flow quartz reactor and heated from 50°C to 800°C at a constant ramp rate of 30°C/min. A flow rate of 20 SCCM was established over the sample with various concentrations of O_2 and D_2O balanced with He. The rise and fall of different mass/charge (m/z) signals of the oxygen and contaminant species, 20 ($D_2{}^{16}O$), 22 ($D_2{}^{18}O$), 32 ($^{16}O_2$), 34 ($^{16}O^{18}O$), 36 ($^{18}O_2$), is monitored using the quadrupole mass spectrometer. From these profiles, the rate of $D_2{}^{16}O$ exchange with the lattice ^{18}O as a function of temperature was determined. We can trace the movement of ^{18}O to directly probe the interaction of contaminants in the ORR at different temperatures. Therefore, the influence of water on the oxygen catalyst can be observed from the presence of ^{18}O in the effluent gas molecules. ISTPX experiments can further expand upon the PO_2-Water-Temperautre relationship. Most

importantly, these experiments are not limited by $P^{18}O_2$ because the tracer is in the solid phase, allowing for an expanded set of available conditions and parameters.

4.3 Theory

Consider that an SOFC cathode material operates with a two-step oxygen reduction mechanism[66,76,84]:

1. Dissociative Adsorption:

$$O_{2(g)} + 2* \underset{k_{-1}}{\overset{k_1}{\leftrightarrow}} 2O_* \qquad [4\text{-}1]$$

2. Incorporation:

$$O_* + V_O \underset{k_{-2}}{\overset{k_2}{\leftrightarrow}} O_O + * \qquad [4\text{-}2]$$

Where * denotes an available surface site, and O_* is a surface adsorbed oxygen, O_o is a lattice oxygen in the surface layer and V_O represents a surface oxygen vacancy. k_1 and k_{-1} are the rate constants for oxygen adsorption and desorption. k_2 and k_{-2} represent the rate constants for the forward and reverse incorporation processes.

There are three possible oxygen exchange mechanisms, proposed by Klier et al. [82], and Boreskov et al.[83]. The first one is homogeneous exchange and it is the exchange between two oxygen molecules in the same phase, specifically the gas phase for our case. For homogeneous exchange no lattice oxygen participates in the exchange reaction, although the surface of the cathode does catalyze the reaction. Homogeneous exchange, or homoexchange for short, can be described by Equation [4-3], [4-4], where two gas molecules adsorb and dissociate on the surface, and then

recombine with other oxygen atoms and desorb back into the gas phase. We will also refer to homoexchange as the R_0 mechanism, and from Equation [4-3], [4-4] we can see that both pure and scrambled products can be formed[116].

$$^{16}O_{2(g)} + {}^{18}O_{2(g)} + 4* \overset{K_{R0}}{\leftrightarrow} 2\,{}^{16,18}O_{2(g)} + 4* \qquad [4\text{-}3]$$

or

$$^{16}O_{2(g)} + {}^{18}O_{2(g)} + 4* \overset{K_{R0}}{\leftrightarrow} 2\,{}^{18}O_{2(g)} + {}^{16}O_{2(g)} + 4* \qquad [4\text{-}4]$$

where K_{R0} is the equilibrium constant for homoexchange.

The second type of exchange is heterogeneous exchange, in which gas phase oxygen exchanges with solid phase oxygen. There are two types of heteroexchange that can occur, single exchange, which will be denoted as the R_1 mechanism, and double exchange denoted as the R_2 mechanism. The R_1 and R_2 are described below in Equation [4-5] and [4-6]

$$^{18}O_{2(g)} + {}^{16}O_{O} \overset{K_{R1}}{\leftrightarrow} {}^{16,18}O_{2(g)} + {}^{18}O_{O} \qquad [4\text{-}5]$$

$$^{18}O_{2(g)} + 2\,{}^{16}O_{O} \overset{K_{R2}}{\leftrightarrow} {}^{16}O_{2(g)} + 2\,{}^{18}O_{O} \qquad [4\text{-}6]$$

where K_{R1} and K_{R2} are the equilibrium constants for single and double heteroexhange, respectively.

For SOFCs, heteroexchange is very important because it includes both dissociation and incorporation into the material, which is necessary for transporting oxygen to the anode. In a typical TPX experiment, dissociative adsorption and incorporation occur in series. Since both of these reactions are thermally activated, they occur more readily at higher temperatures, increasing exchange levels

throughout the heating process. Also, it is important to note that there is no external driving force for these reactions, and that exchange of ^{18}O and ^{16}O occurs randomly through tracer based surface exchange and bulk diffusion. Therefore it is important to relate the levels of exchange to the concentration profiles in the gas and solid phases.

When $^{18}O_2$ molecules are initially introduced into the system at low temperature, there is not enough thermal energy to overcome the energy barrier to break the O=O bond, ~500kJ/mol. As temperature increases however, the cathode material, LSM or LSCF, acts as a catalyst and helps to lower the energy barrier required to dissociate oxygen. An example of this reaction is shown in Equation [4-7].

$$^{18}O_{2(g)} + 2* \underset{k_{-1}}{\overset{k_1}{\leftrightarrow}} 2^{18}O_* \qquad [4\text{-}7]$$

$^{18}O_*$ is the intermediate oxygen species, dissociatively adsorbed on the surface. In this temperature range, homoexchange dominates on the surface, and incorporation does not occur. As the powder reaches higher temperature, $^{18}O_*$ on the surface can incorporate into oxygen surface vacancies and then diffuse into the material bulk. This diffusion can be seen as the mixing of ^{18}O and ^{16}O in the bulk of the material, and can be described by self (or tracer) diffusion. Equation [4-8], [4-9] describes the multiple steps involved in heteroexchange, which can be simplified as shown in Equation [4-10].

$$^{18}O_* + V_O \underset{k_{-2}}{\overset{k_2}{\leftrightarrow}} {}^{18}O_O + * \qquad [4\text{-}8]$$

and

$$^{16}O_O + * \underset{k_2}{\overset{k_{-2}}{\leftrightarrow}} {}^{16}O_* + V_O \qquad [4\text{-}9]$$

$$^{16}O_O + {}^{18}O_* \overset{K_{inc}}{\leftrightarrow} {}^{16}O_* + {}^{18}O_O \quad [4\text{-}10]$$

where K_{inc} is the equilibrium constant for incorporation.

Due to the high catalytic activity of perovskites, contaminants such as water can interact with the cathode surface. When water is present on the surface, it can also be dissociatively adsorbed, blocking the dissociation of oxygen molecules. One proposed mechanism for the dissociative adsorption of D_2O is shown in Equation [4-11]

$$D_2{}^{16}O_{(g)} + 3* \underset{k_{-3}}{\overset{k_3}{\leftrightarrow}} {}^{16}O_* + 2D_* \quad [4\text{-}11]$$

Then $^{18}O_*$ can either exchange with lattice $^{16}O_O$, or exchange with the normal ^{16}O in D_2O. The overall reaction can be seen in Equation [4-12]. k_3 and k_{-3} are the rate constants for D_2O adsorption and desorption. In another case, water can exchange with lattice oxygen then desorb back into the gas phase, shown in Equation [4-13]. For both of these cases, the result is D_2O exchange an ^{16}O with an ^{18}O, resulting in a scrambled $^{16,18}O_2$ product.

$$D_2{}^{16}O_{(g)} + {}^{18}O_{2(g)} \leftrightarrow D_2{}^{18}O_{(g)} + {}^{16,18}O_{2(g)} \quad [4\text{-}12]$$

$$D_2{}^{16}O_{(g)} + {}^{18}O_O \leftrightarrow D_2{}^{18}O_{(g)} + {}^{16}O_O \quad [4\text{-}13]$$

For ISTPX, ^{18}O is saturated on the surface of the solid phase and O_2 and D_2O gases are flowed through the powder. In such an experiment a variety of different products can be formed, these are summarized in Equation [4-14][4-15][4-16]

$$D_2{}^{16}O_{(g)} + {}^{16}O_{2(g)} + {}^{18}O_O \leftrightarrow D_2{}^{18}O_{(g)} + {}^{16}O_{2(g)} + {}^{16}O_O \quad [4\text{-}14]$$

Or $$D_2{}^{16}O_{(g)} + {}^{16}O_{2(g)} + {}^{18}O_O \leftrightarrow D_2{}^{16}O_{(g)} + {}^{16,18}O_{2(g)} + {}^{16}O_O \quad [4\text{-}15]$$

Or $$D_2{}^{16}O_{(g)} + {}^{16}O_{2(g)} + 2{}^{18}O_O \leftrightarrow D_2{}^{16}O_{(g)} + {}^{18}O_{2(g)} + 2{}^{16}O_O \quad [4\text{-}16]$$

Therefore, the benefits of the ISTPX is that we can detect the different gas-solid reactions among different gas species and directly observe the heteroexchange process, which involves lattice oxygen. The fraction of the exchange in Equation [14], [15], and [16] is a function of temperature, mainly depending on the energy barrier. Through ISTPX, we are able to probe the dominant exchange reactions on LSM and LSCF as a function of temperature and PO_2.

4.4 Results and Discussion

Figure 4-2 (a) and (b) show TPX of LSM with and without the presence of 0.3% D_2O in 25000ppm $^{18}O_2$. Without the presence of water, the oxygen exchange curve shows two exchange peaks, an α peak starting at 300°C and a high temperature β peak with an onset temperature around 600°C. These exchange peaks are consistent with previous temperature programmed desorption (TPD) data[117,118], and are a result of the change in valance state of Mn. The formation of $^{16}O^{18}O$ begins at 300°C, revealing that oxygen molecules begin to dissociate on the LSM surface at this temperature. When water molecules are present, the available ^{18}O atoms on the

surface begin to exchange with D_2O at 400°C. The D_2O signal of TPX of LSM in 3000ppm D_2O is shown in Figure 4-2 (c). The D_2O signal shows an extra $D_2{}^{18}O$ exchange peak between the α and β peaks. This peak does not represent the change in valence state of Mn, rather it is a result of Mn being catalytically active toward homoexchange of gas phase O_2 and water. A comparison with TPX of just O_2 on LSM, shows significantly less exchange occurring without the presence of water, supporting the previous statement. The consumption of $^{18}O_2$ and formation of $^{16}O^{18}O$ between 400 and 700°C indicates the dominance of homoexchange between gaseous O_2 and water. At higher temperature the heteroexchange of $^{18}O_2$ gas, with LSM surface oxygen, dominates.

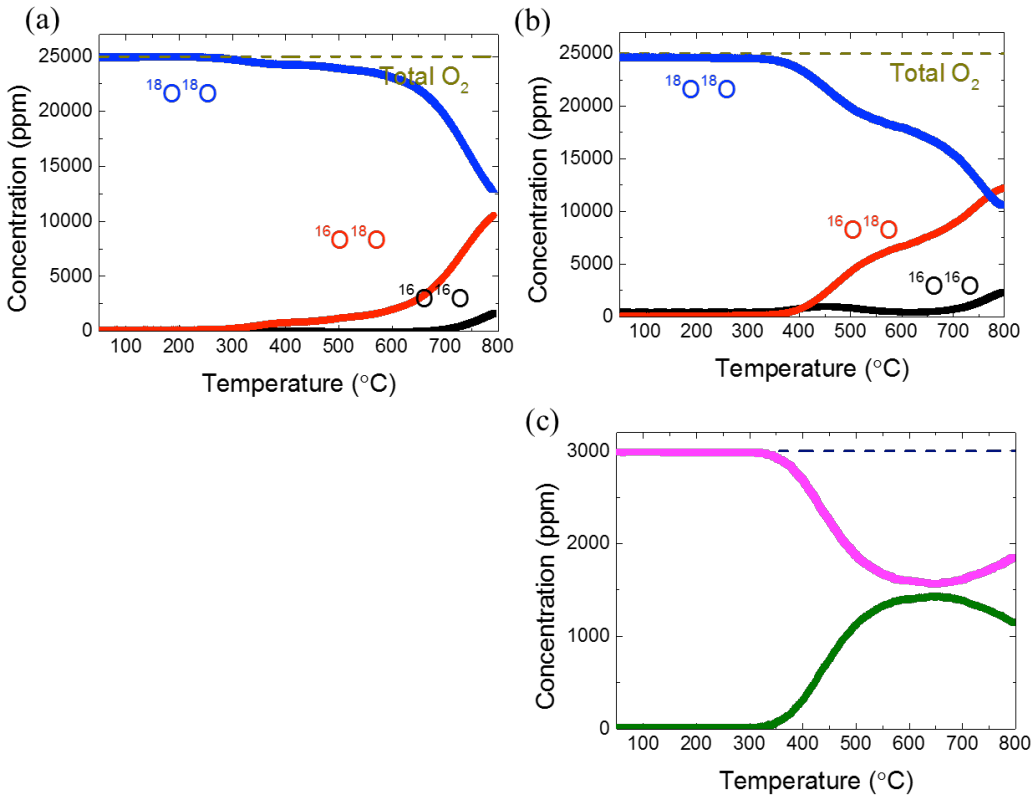

Figure 4-2. TPX of LSM (a) without H_2O, (b) O_2 with 3000ppm D_2O, and (c) D_2O signal

To investigate the heteroexchange between water vapor and the cathode surface, ISTPX has been conducted with D_2O only, balanced in He. Figure 4-3 shows ISTPX of LSM in different concentrations of D_2O: (a) 3000ppm, (b) 6000ppm, and (c) 12000ppm. In 3000ppm D_2O, LSM begins to exchange with $D_2{}^{16}O$ around 300°C and a small portion of isotopically labeled $D_2{}^{18}O$ is observed from 300-800°C.

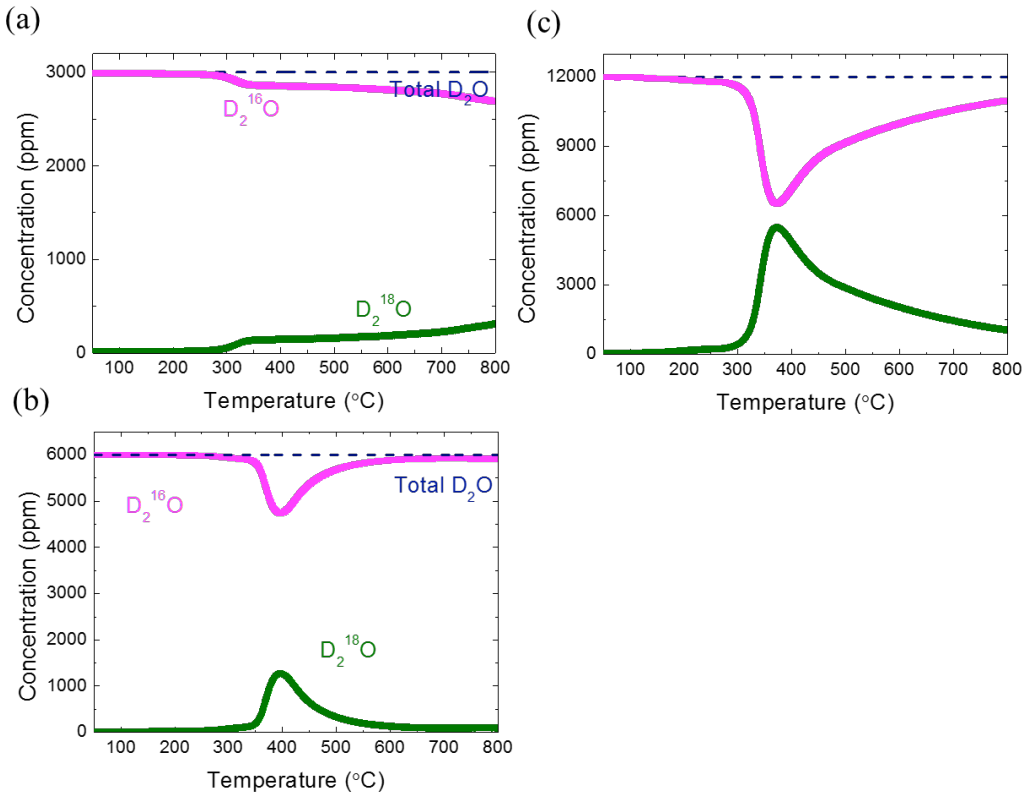

Figure 4-3. ISTPX of LSM in (a) 3000, (b) 6000, and (c) 12000 ppm D_2O

Compared with TPX, which can only probe heteroexchange of contaminants after the surface exchanges with $^{18}O_2$, ISTPX allows us to probe the interaction at lower temperatures, before O_2 heteroexchange will occur. In the higher concentrations of D_2O, LSM exhibits an exchange peak with water around 300-400°C, as shown in Figure 4-2 (b) and (c). Since there is no other ^{18}O source other than the ^{18}O saturated LSM surface, the exchange peak here should be due to

heteroexchange only. The results also suggest that LSM has the ability to split water above 300°C, and in a recent paper Yang et al.[119] further confirm that LSM could split water by thermochemical cycling between 800 and 1400°C.

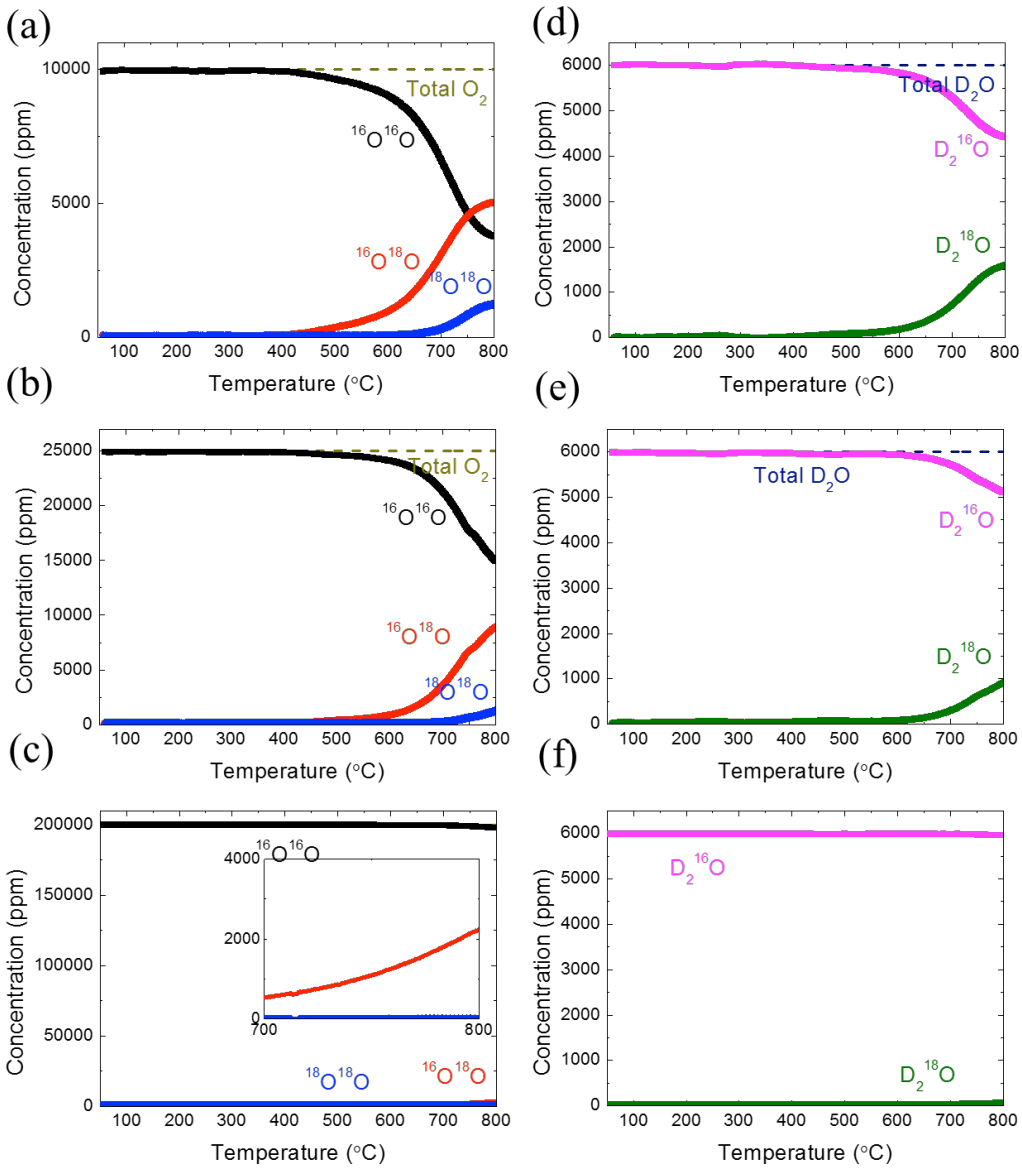

Figure 4-4. The O_2 signal of ISTPX of LSM in the presence of 6000ppm D_2O under PO_2= (a) 1%, (b) 2.5%, and (c) 20% atm, and D_2O signal in PO_2= (d) 1%, (e) 2.5%, (f) 20% atm.

We are also interested in the catalytic effects when there are multiple reactants flowing to the cathode powder. Figure 4-4 shows the O_2 signals for ISTPX of LSM in

the presence of 6000ppm D_2O under PO_2= (a) 0.01, (b) 0.025, and (c) 0.20, and D_2O signals in PO_2= (d) 0.01, (e) 0.025, and (f) 0.20. The exchange peak of water with LSM around 350-400°C disappears when both O_2 and D_2O are flowed, suggesting that the presence of O_2 hinders the exchange between water and LSM. In this case, both O_2 and water exchange with LSM are shifted to higher temperatures. The oxygen starts to exchange with LSM lattice ^{18}O at 500°C and D_2O begins at 600°C Because the stoichiometry of LSM is stable for a relatively large PO_2 range, the decrease of the fraction of O_2 exchange with the increase of PO_2 may not be affected by the surface vacancies concentration but may be due to the higher concentration of gaseous O_2 to exchange with lattice ^{18}O at the same time. At higher PO_2, the LSM lattice has fewer surface vacancies that can participate in the reaction. We can compare TPX in Figure 4-2 to ISTPX in Figure 4-4 (b) and (e), which have the same PO_2. The only difference is the ^{18}O source: gas phase $^{18}O_2$ for TPX and solid phase ^{18}O. The extra peak in TPX at around 400-600°C is due to the homoexchange between O_2 and water on the LSM surface. This peak suggests that LSM is good at dissociation of O_2 and water without the participation of lattice oxygen.

The exchange between the LSM surface and water decreases when the oxygen partial pressure increases, indicating that the exchange between O_2 and LSM and water and LSM are competing with each other. When the oxygen partial pressure increases to 0.20 atm, the oxygen exchange between water and LSM are not observable. Figure 4-5 shows ISTPX of LSM in different concentrations of D_2O: oxygen signal in D_2O= (a) 4500ppm (b) 6000ppm, and D_2O signal in D_2O= (c)

4500ppm (d) 6000ppm. The increase in water concentration does not significantly change the exchange curves for both water and O_2.

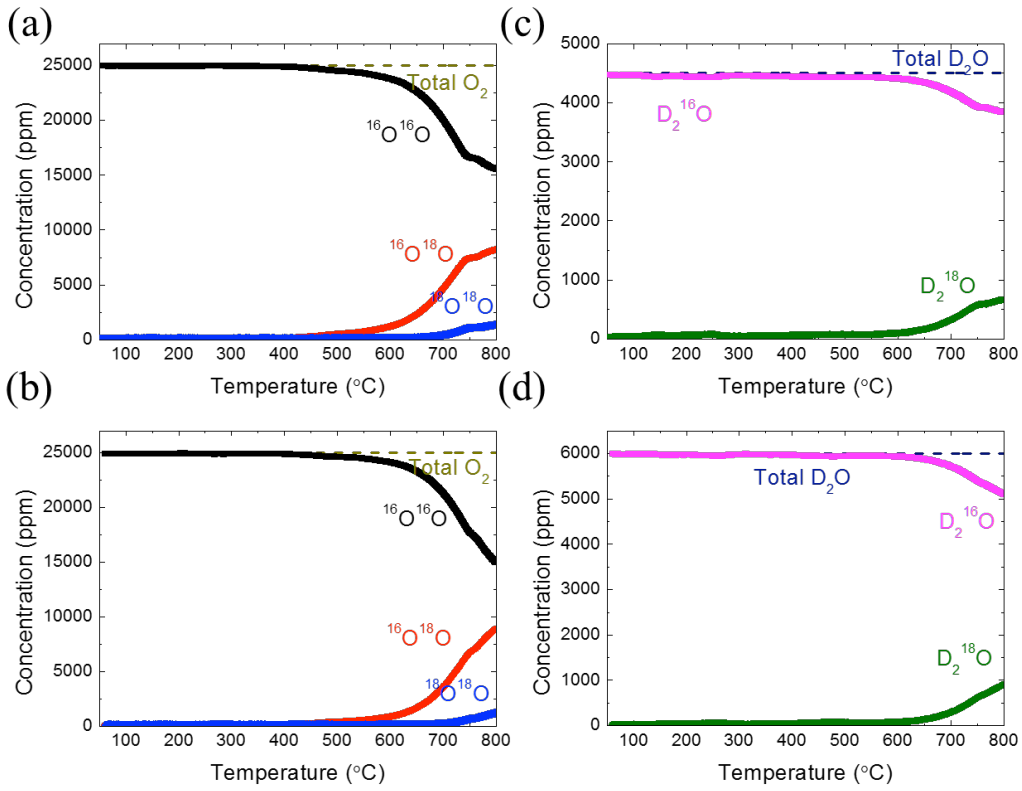

Figure 4-5. ISTPX of LSM in 25000ppm O_2 with different concentration of D_2O : O_2 signal in D_2O= (a)4500ppm, (b) 6000ppm, and D_2O signal in D_2O= (c) 4500ppm, (d) 6000ppm.

Water exchange with LSCF is significantly different than with LSM. For one, LSCF shows a higher activity toward the dissociation of water, at lower temperature. Figure 4-6 shows ISTPX of LSCF in 6000ppm D_2O without the presence of O_2. The exchange of oxygen between water and the LSCF surface is observable at 200°C and has an exchange peak at 350°C. Although we expect water exchange with LSCF to be thermally activated, we can clearly see a decrease in the exchange rate as the temperature increases above 350°C. The amount of ^{18}O that has exchanged with water at these lower temperatures does not equate to the total amount of ^{18}O in the

saturated LSCF powder, leading to two possible mechanisms. First, the sluggish transport of oxygen ions in the lattice at lower temperatures limits the diffusion of ^{18}O to the surface, as is the case with LSM. However, LSCF, a good MIEC, should not be limited by the diffusion process, allowing for the possibility that full exchange between water and LSCF is limited to the lower temperature region, due to alternate dominant reactions at higher temperatures.

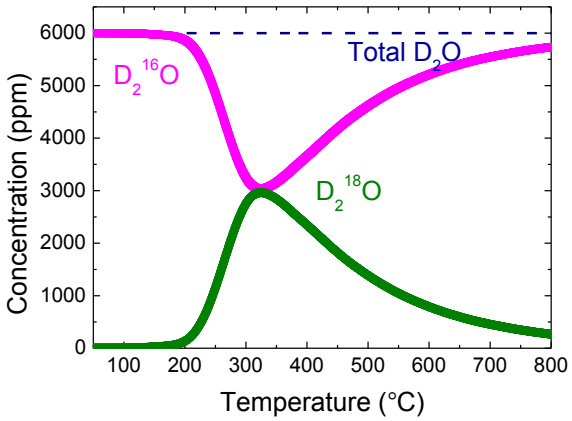

Figure 4-6. ISTPX of LSCF in 6000ppm D_2O

It is well known that LSCF is much more sensitive to changes in PO_2, affecting the vacancy concentration and the catalytic properties of the material[120,121]. Figure 4-7 shows ISTPX of LSCF in 6000ppm D_2O with different oxygen partial pressures: O_2 signals in PO_2= (a) 0.0025, (b) 0.025, and (c) 0.20 atm., D_2O signals in PO_2= (d) 0.0025, (e) 0.025, and (f) 0.20 atm. As the oxygen partial pressure increases, the exchange between LSCF and water switches from one exchange peak to two exchange peaks, one is around 300°C and the other is around 420°C. When the temperature is higher than 420°C, the $D_2{}^{18}O$ signal decreases. This is likely due to the limited amount of solid phase ^{18}O in the sample. The exchange rate at 300°C in water

decreases as the oxygen partial pressure increase; in contrast, the exchange peak around 420°C remains at a similar intensity and appears to be independent of the oxygen partial pressure. The independence of water exchange peak to the oxygen partial pressure around 420°C suggests that LSCF surface prefers to adsorb water rather than O_2, and this activity toward adsorption of water may block the exchange between O_2 and LSCF. On the other hand, the dependence of water when the oxygen partial pressure increases, the exchange between O_2 and LSCF converges at certain temperatures: 450°C for $^{16}O^{18}O$ and 500°C for $^{18}O_2$. The first water exchange peak, around 300°C, does not overlap with the oxygen exchange peaks. The second exchange peak at 420°C is overlaps with the oxygen exchange peaks.

The water vapor pressure effects on LSCF were studied by fixing PO_2 at 0.025 and flowing different concentrations of D_2O. Figure 4-8 shows ISTPX of LSCF in different concentrations of D_2O: the O_2 signals are shown in (a) 6000ppm, (b) 9000ppm, (c) 12000ppm, (d) 15000ppm D_2O, and D_2O signals in (e) 6000ppm, (f) 9000ppm, and (g) 12000ppm, and (h) 15000ppm D_2O. Compared with the absence of oxygen in the reactant in Figure 4-6, LSCF shows two separate exchange peaks with water when both oxygen and water are flowed. One exchange peak is at 300°C and the other exchange peak is at 420°C. The D_2O evolution curves present similar shapes, regardless of the concentration of D_2O flowing to the system. LSCF has an exchange peak with $^{16}O_2$ around 500°C. The $^{16}O^{18}O$ and $^{18}O_2$ signals decrease when the concentration of water increases, meaning that more lattice ^{18}O exchanges with water.

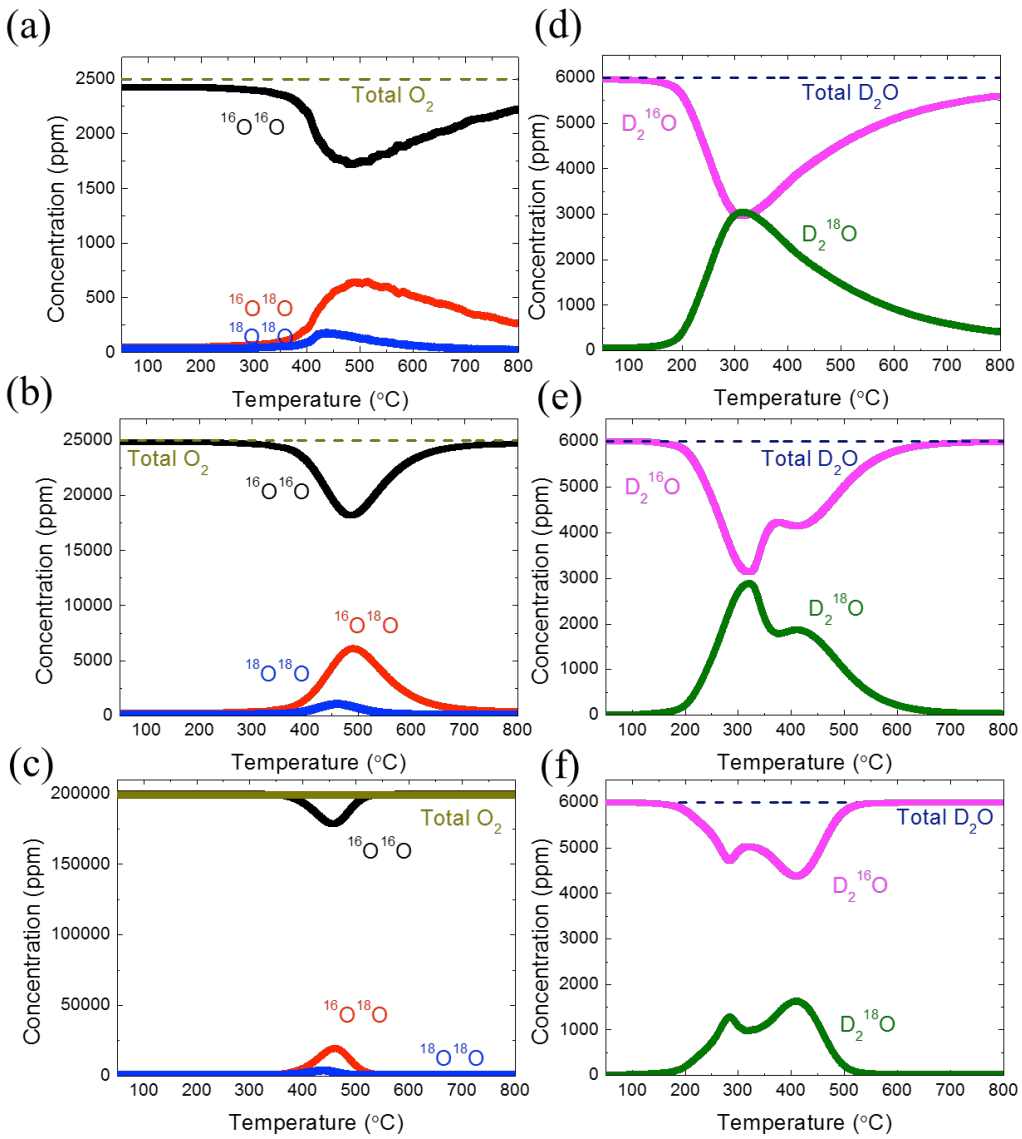

Figure 4-7. ISTPX of LSCF in 6000ppm D_2O with different oxygen partial pressure: O_2 signal in PO_2= (a) 0.25% (b) 2.5% and (c) 20%. D_2O signal in PO_2= (d) 0.25% (e) 2.5% and (f) 20%.

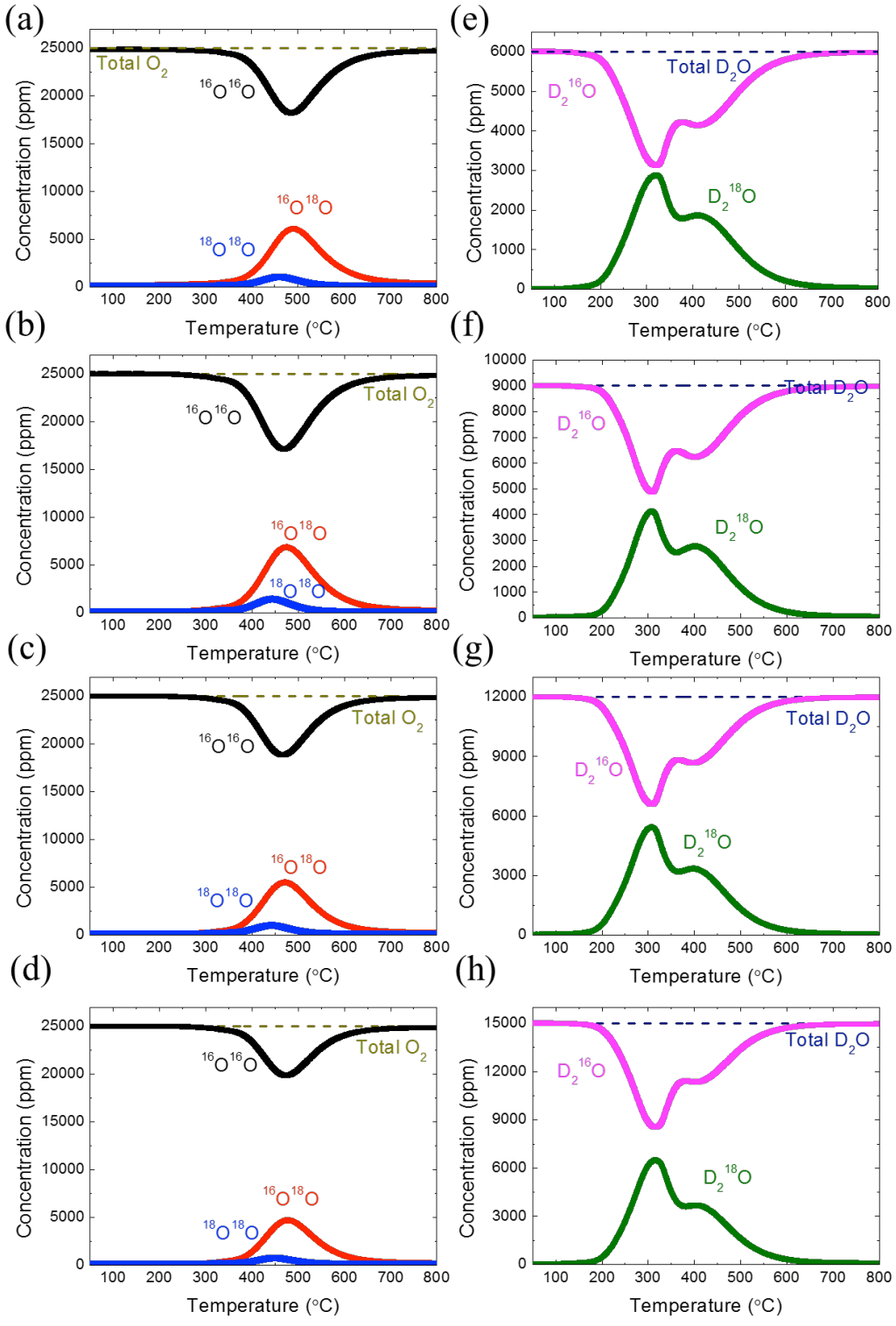

Figure 4-8. ISPTX of LSCF in different concentration of D_2O: O_2 signal in (a) 6000ppm, (b) 9000ppm, (c) 12000ppm, and (d) 15000ppm, and D_2O signal in (e) 6000ppm, (f) 9000ppm, (g) 12000ppm, and (h) 15000ppm

Figure 4-9 and summarizes the results of TPX and ISTPX for LSM and LSCF respectively, providing information as to when the temperature and PO_2 ranges where ^{18}O-isotope-exchange reaction rates of water with LSM and LSCF powders are the highest and the lowest. Figure 4-9 (a) shows a 3D plot of the Temperature-PO_2 diagram in which water dominates surface exchange on LSM. The projection of the 3D plot, shown as a contour plot is shown in Figure 4-9 (b). At low PO_2 (pure helium gas flow), water exchanges with LSM around 300°C. When both O_2 and water are flowed through the powder, the water exchange with LSM around 300°C is limited and shows a high temperature exchange peak above 650-700°C. We might expect that under the lowest tested PO_2 condition, pure He bubbled through water impinger, that the water exchange peak at 300°C occurs due to a change in valence state of Mn. With pure helium gas (AIRGAS, 99.999%), which has a PO_2 order of 10^{-9} atm, LSM is expected to have a higher concentration of surface vacancies, which may cause a higher exchange rate of LSM in the lower temperature region. However, at a higher PO_2 (10^{-2} atm) we no longer see an exchange peak between LSM and water, which may be a result of LSM's stoichiometric stability[121,122]. Another possibility is that the presence of O_2 limits the water exchange on LSM around 300°C, suggesting that water and O_2 have competitive adsorption on the LSM surface and LSM prefers to bond to O_2, not water. The two temperature ranges for the water exchange with LSM are consistent with the change of stability of valance states of manganese [57,122-126], and at these temperature ranges, Mn in the B site of ABO_3 shows the ability to actively change valence states.

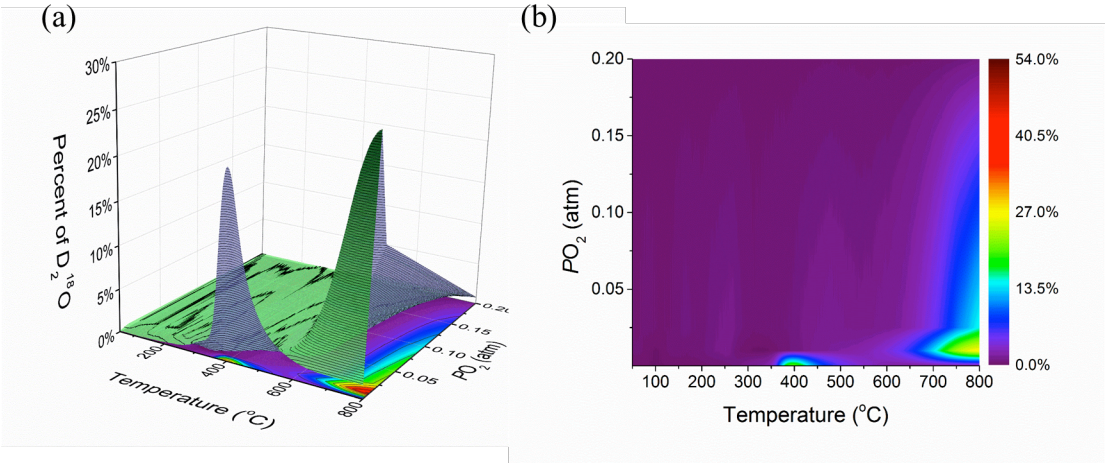

Figure 4-9. A 3D surface plot (a) and a contour plot (b) of water exchange with LSM as a function of PO_2 and temperature, for data gathered from temperature programmed exchange experiments.

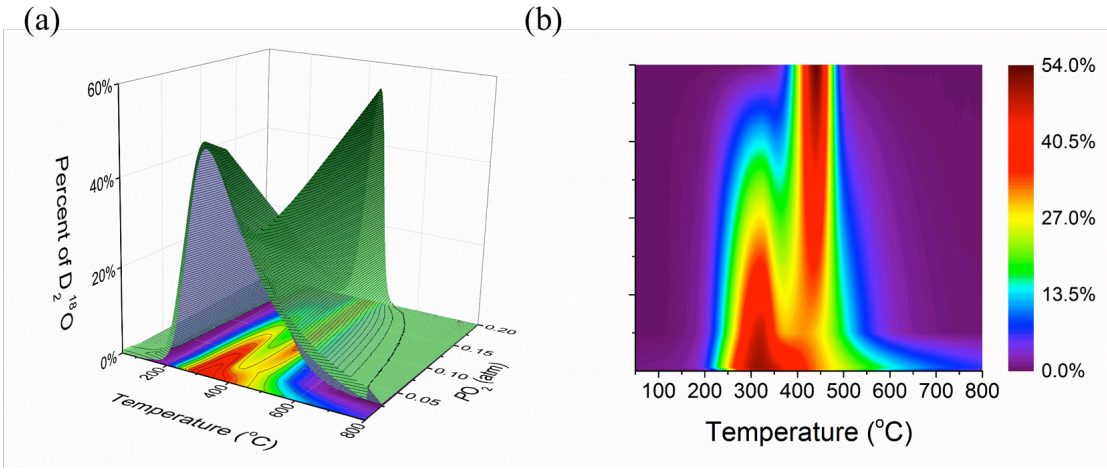

Figure 4-10. A 3D surface plot (a) and a contour plot (b) of water exchange with LSCF as a function of PO_2 and temperature, for data gathered from temperature programmed exchange experiments.

The 3D and contour plots of water exchange with LSCF as a function of PO_2 and temperature are shown in Figure 4-10. Compared to LSM, LSCF shows an intense exchange reaction with water. This may be due to the high concentration of vacancies in the near surface region. Without the presence of O_2, the main water exchange peak with LSCF is at 300°C. When PO_2 increases, this water exchange peak starts to decrease and another water exchange peak at 420 °C appears. The results indicate that the water exchange with LSCF has two different exchange

mechanisms, resulting in two distinct exchange peaks at different temperatures. At PO_2=0.20 atm., the first water exchange peak vanishes and the second exchange peak is the only exchange peak. The first peak is sensitive to PO_2, suggesting that O_2 and water are competitively adsorbed on the LSCF surface near 300°C.

Figure 4-11 shows the fraction of the accumulated ^{18}O that is exchanged to different gases from (a) LSM and (b) LSCF at the fixed PO_2=0.025 atm. It summarizes the impact of water partial pressure on the oxygen exchange rate. The blue curve represents the total fraction of ^{18}O that is exchanged to gas phase O_2 and the red curve shows the fraction of ^{18}O that is exchanged to O_2 in the form of $^{16}O^{18}O$. The green curve is the fraction of ^{18}O that exchanged to water. For LSM, the oxygen exchange rate increases above 700°C which is due to the increased heteroexchange between the gas and the cathode material. The exchange fraction to the water increases when water partial pressure increases, indicating the higher concentration of water would dynamically participate in the ORR. For LSCF, water exchange dominates between 200 and 500°C. As a function of PH_2O, O_2 and water exchange with LSCF in parallel at higher temperature.

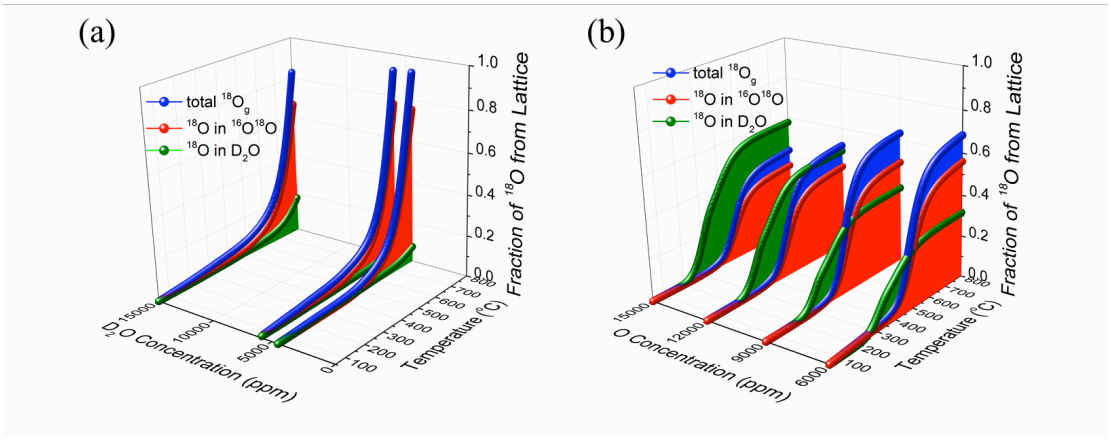

Figure 4-11. Accumulated ^{18}O exchange fraction of T-PD_2O diagram of (a) LSM and (b) LSCF.

This is the first time the effects of water on oxygen exchange for SOFC cathode materials have been studied using isotope exchange. These effects have been visualized for LSCF and LSM as a function of temperature and operating conditions. Our results indicate that the interaction of water with LSCF is much greater than for LSM, and therefore potentially detrimental to the overall cathode stability and performance. The high concentration of surface vacancies and MIEC of LSCF, leads to high activity for the entire material surface and promotes the heteroexchange of water. The exchange process for water may provide an alternate, more favorable route for the formation of secondary phases, cation clustering, or the transition between ordered and disordered states, making these imperfections more kinetically and thermodynamically favorable. Therefore, the continuous exchange of oxygen atoms between water and the surface may eventually lead to permanent degradation.

4.5 Conclusions

Isotope oxygen exchange is a powerful tool to observe the heterogeneous catalysis behavior of SOFC cathodes and to understand the impact of water on the ORR mechanisms. TPX can provide information about the effect of water on the dissociation and incorporation of oxygen gas. Alternatively, ISTPX can provide information about any interaction contaminants have with the materials at lower temperatures, due to the location of the tracer in the solid phase. LSM exchange with O_2 shows heteroexchange peaks with onset temperatures around 300°C and above 600°C, and homoexchange with water in between. ISTPX has been successfully conducted at various oxygen partial pressures and water vapor concentrations to study the effects of water on oxygen surface exchange kinetics as a function of temperature.

We have demonstrated the temperature and PO_2 range that is preferable for the heteroexchange of water on LSM and LSCF. The competitive adsorption/desorption process between O_2 and water on cathode surfaces is observed, as well as the dominant regions of each gas at different temperatures and concentrations. LSM has a higher stability with the presence of humidity than LSCF and the sub-stoichiometry in the near surface region plays an important role in water exchange for both materials. The kinetic results provided here help to elucidate the degradation mechanisms for these important cathode materials. The relationship between the cathodes catalytic properties in the presence of water and O_2 provide information necessary for realistic SOFC operating conditions. The results suggest that the degradation of SOFC cathodes may occur more readily at lower temperature ranges or during temperature cycling. The existence of water in the air may block the pathway of the ORR.

Chapter 5: Fundamental Impact of CO_2 on SOFC Cathode Degradation

5.1 Introduction

Perovskites, with the general formula ABO_3, are known for their unique, tunable material properties, such as thermal expansion, catalytic activity, electronic conductivity, and ionic conductivity. One major application of perovskites is as the cathode for solid oxide fuel cells (SOFCs) to catalyze the oxygen reduction reaction. SOFCs are a promising technology for direct electrochemical conversion of fuels to electricity, providing high efficiency as well as fuel flexibility. Unfortunately, degradation of cathode materials under real working conditions is a factor that currently limits SOFC applications [3,22,38,46,106,124]. When the oxide catalyst is exposed to atmospheric air, the highly active surface is not limited to reactions with oxygen gas, there are a number of other gaseous components present in the air that may also react with the cathode. This constant adsorption/dissociation and recombination/desorption causes the rearrangement of surface atoms, including the generation and annihilation of surface vacancies. Ultimately, constant cycling of the material can lead to lattice imperfections such as cation clustering, the displacement of cations, and the formation of secondary phases [127]. Therefore the long-term durability of current SOFC cathodes is one of the major challenges for large-scale commercialization[37,39,40,44,101,128-130]. In order to improve the stability of cathodes at elevated temperatures in the presence of CO_2, unavoidable in atmospheric air, we

need to have a fundamental understanding of the various gas-solid interactions that can occur.

$(La_{0.8}Sr_{0.2})_{0.95}MnO_{3\pm\delta}$ (LSM) and $La_{0.6}Sr_{0.4}Co_{0.2}Fe_{0.8}O_{3-\delta}$ (LSCF) are two of the most commonly used cathode materials for SOFCs. Although both LSM and LSCF have the same ABO_3 structure, with La and Sr occupying the A sites and transition metals occupying the B sites, they have quite different intrinsic material properties. LSM is an electronic conductor at elevated temperature, and maintains oxygen super-stoichiometry across a wide range of PO_2's and temperatures [131-133]. LSM has been shown to have a good electro-catalytic activity [134,135] for oxygen dissociation, credited mostly to the B-site Mn. Recently LSM has been shown as a redox material for solar thermochemical splitting of H_2O and CO_2 by employing the ability of dissociation molecules and the thermochemical cycling of a non-stoichiometric LSM [127,136,137]. In contrast, LSCF is a well-known mixed ionic electronic conductor (MIEC). For LSCF, it is thermodynamically favorable to form anion vacancies to compensate for the charge balance caused by the oxidation of Co and Fe during changes in chemical potential [57,58,88]. Therefore, the catalytic activity and oxygen ion conduction of this material can vary based on working conditions. LSCF has also been used for other applications, such as oxygen-permeation membranes[57,138].

One of the issues for deployment of LSM and LSCF as SOFC cathodes is the stability of the material under long-term use in working environments. There are a number of different gases, some being components of air and others developing due to sealing and interconnects, that may interact with the cathode. These interactions

depend on concentrations of each species, activation energies for the reactions, as well as temperature and PO_2. In addition to unwanted reactions, the surface configuration of the cathode is very important for it's ability to catalyze the ORR. Little is known as to how each of the contaminant gases may interact with the surface, possibly forming secondary phases or hindering the ability for O_2 to adsorb and dissociate [37,106,139]. One of the components of air that may have a significant effect on cathode durability is CO_2, as reported in literature [39,40,105,106,128,138,140]. There is a need to explore the fundamental interactions of CO_2 and how CO_2 containing atmospheres effect the performance of these metal oxides.

Isotope exchange is a heterogeneous catalysis technique that can determine the kinetics of multiple gas-solid reactions that occur on the catalyst surface [72]. Using isotopically labeled $^{18}O_2$ gas we can trace the interaction of oxygen with the catalyst surface. The transport properties of ^{18}O are assumed to be identical to those of ^{16}O. Generally, heterogeneous catalysis isotope exchange techniques can be divided into two categories; *ex-situ* analysis of diffusion in the solid, and *in-situ* analysis of exchanged gas compositions. The first, *ex-situ* technique, is isotope exchange depth profiling (IEDP) with secondary ion mass spectrometry (SIMS) [69,70,141,142]. In this technique a sample is thermally treated with isotopically labeled oxygen at a given temperature and exposure time. Subsequently, an isotope depth profile is obtained. The kinetic parameters, tracer diffusion coefficient (D^*) and surface diffusion coefficient (k^*), can be obtained by fitting the isotope distribution profiles in the solid using the diffusion equations. The effects of contaminants on oxygen transport have been quantitatively studied using this technique by comparing changes in k^* due to

the presence of contaminants. Benson et al. [128] has shown the degradation of LSCF in CO_2 atmospheres after annealing samples in various temperature and atmosphere conditions. Because of the *ex-situ* processing of IEDP-SIMS, it lacks the ability to distinguish the temperature, PO_2, and contaminant concentration effects specifically related to the surface reaction mechanisms. To probe the surface specific reactions, we rely on *in-situ* isotope exchange techniques [73-78]. In these techniques, isotopically labeled oxygen is exchanged with the oxide powder and the resulting oxygen isotopologues are analyzed in real-time using a downstream mass spectrometer. This technique provides us the ability to explore the gas-solid heterogeneous reactions, *in-situ*, under a wide range of conditions.

We have utilized two different techniques to probe the surface under different temperature and gas environment conditions. Samples were exposed to a variety of gases while heating up at a fixed ramp rate, while different exchange products are monitored by mass spectrometry. The first is temperature programmed exchange (TPX), where gaseous $^{18}O_2$ is used as the labelled oxygen source [77]. This provides us information on heteroexchange between O_2 gas and solid oxygen in the material, along with homoexchange between O_2 and CO_2. The other technique is isotope saturated temperature programmed exchange (ISTPX), where sample powders are pretreated with ^{18}O to utilize the powder as the isotope source [115,143]. The interactions of various gas components with sample powders at different temperatures can be visualized. ISTPX can provide a more flexible approach to study the interactions of $C^{16}O_2$. The combination of these two types of temperature programmed isotope

exchange experiments can provide overall information about multiple gas-gas and gas-solid reactions.

For the exchange of gaseous oxygen with a metal oxide surface, it is generally accepted that there are three basic mechanisms, proposed by Klier et al. [144] and Boreskov et al. [145]. The first of these mechanisms is homogeneous exchange, which will be referred to as homoechange, and involves two O_2 gas molecules adsorbing on the surface and exchanging a single oxygen atom between them. This is often denoted the R^0 mechanism and can be expressed as:

$$^{16}O_{2(g)} + {}^{18}O_{2(g)} + 4* \leftrightarrow 2^{16,18}O_{2(g)} + 4* \qquad [5\text{-}1]$$

In Equation [5-1], * represents an available surface site for the dissociative adsorption of O_2. If we consider the presence of CO_2 molecules on the oxide surface, the homoexchange reaction between gas phases can be written as:

$$C^{16}O_{2(g)} + {}^{18}O_{2(g)} + 4* \leftrightarrow C^{18}O_{2(g)} + {}^{16}O_{2(g)} + 4* \qquad [5\text{-}2]$$

Or
$$C^{16}O_{2(g)} + {}^{18}O_{2(g)} + 4* \leftrightarrow C^{16,18}O_{2(g)} + {}^{16,18}O_{2(g)} + 4* \qquad [5\text{-}3]$$

In Equation [5-1]-[5-3] no lattice oxygen participates in the R_0 reaction mechanism, with or without the involvement of CO_2. R_0 is merely the exchange of oxygen between gas phase molecules. Although the active surface sites are necessary for the R^0 mechanism, there is no participation of solid oxygen.

Other exchange mechanisms involve gas phase oxygen and either one or two oxygen atoms from the solid oxide participating in the reaction. Equations [5-4] and

[5-5] present the two gas-solid exchange processes known as single and double heteroexchange, denoted R_1 and R_2, respectively.

$$^{18}O_{2(g)} + {}^{16}O_O \leftrightarrow {}^{16,18}O_{2(g)} + {}^{18}O_O \quad [5\text{-}4]$$

$$^{18}O_{2(g)} + 2{}^{16}O_O \leftrightarrow {}^{16}O_{2(g)} + 2{}^{18}O_O \quad [5\text{-}5]$$

In the above equations O_O represents an oxygen atom occupying an oxygen lattice site. CO_2 can also contribute to the heteroexchange. Consider the ISTPX of CO_2 with labelled lattice $^{18}O_O$, the reactions can be either single heteroexchange, Equation [5-6], or double heteroexchange, Equation [5-7]:

$$C^{16}O_{2(g)} + {}^{18}O_O \leftrightarrow C^{16,18}O_{2(g)} + {}^{16}O_O \quad [5\text{-}6]$$

$$C^{16}O_{2(g)} + 2{}^{18}O_O \leftrightarrow C^{18}O_{2(g)} + 2{}^{16}O_O \quad [5\text{-}7]$$

All three exchange mechanisms are thermally-activated processes and the possibility of each exchange process is governed by the thermodynamics of the reaction, as well as temperature and PO_2. Each exchange mechanism has a different reaction enthalpy. For homoexchange reactions, as stated previously, there is no participation from solid phase lattice oxygen. As such, the occurrence of homoexchange can generate isotopically labeled contaminants without causing degradation of the catalyst. On the other hand, heteroexchange, concerning the exchange of lattice oxygen atoms with gaseous oxygen molecules, involves the participation of a surface oxygen vacancy to transport the oxygen, and is more closely related to degradation. It is important to note the inherent differences in the homo and

heteroexchange, especially the sites involved in the reactions, and the energy required for each to occur.

In the case of SOFC cathodes, heteroexchange is better representative of real working principles. Under operating conditions oxygen atoms are electrochemically driven from the cathode, through the electrolyte, to the anode where they oxidize a fuel. We can see that the involvement of lattice sites and the incorporation of oxygen is necessary, and that heteroexchange is more closely related to this process than homoexchange. Previous investigations have led us to believe that SOFC cathode materials operate with a two-step oxygen reduction mechanism [73,78]. The first step is the dissociation of oxygen molecules on the cathode surface. The solid oxide should actively catalyze the breaking of oxygen bonds, creating active surface species. The second step is the incorporation of oxygen into surface vacancies. These active oxygen ions on the surface can then incorporate into an available surface vacancy on the cathode prior to transport.

Due to the high catalytic activity of perovskites, gaseous molecules such as CO_2 and H_2O that are present in the system are able to interact with the cathode surface. In this study, the effects of CO_2 on LSM and LSCF as a function of CO_2 concentration, temperature and PO_2 are investigated using temperature programmed isotope exchange techniques. The concentrations of CO_2 in this study are limited to 5,000ppm in order to remain close to the real working conditions. The presence of different gaseous components on the surface may involve in the sequentially steps for the oxygen reduction reaction. Temperature programmed exchange can elucidate the

various thermally activated reactions and the temperature regions each one dominates in, as well as to help identify different adsorption species.

5.2 Experimental

Here we focus on the study of two common perovskites, LSM and LSCF, with different intrinsic material properties that will be discussed further. Commercial $(La_{0.8}Sr_{0.2})_{0.95}MnO_{3\pm\delta}$ (Fuel Cell Materials) and $La_{0.6}Sr_{0.4}Co_{0.2}Fe_{0.8}O_{3-\delta}$ (Praxair) powders were used. Powder samples were normalized by surface area to 0.1 m^2 for direct comparison of the surface catalytic activity. The weight of LSM and LSCF powder are 0.018g and 0.015g, respectively. Details and schematics of the experimental setup have been provided previously [76] with some modifications. As can be seen in Figure 5-1, there are two separate gas lines connected together before flowing to the reactor. One line provides $^{18}O_2$ (Sigma-Aldrich, 95%) isotope gas balanced in He with a 1000ppm inert Ar tracer to help identify switching between the lines. The flow rate of $^{18}O_2$ is precisely controlled by using a low-flow mass flow controller (Alicat). Tanks of pure He (AIRGAS, 99.999%), different concentrations of CO_2, as well as a variety of concentrations of O_2, all balanced in He, are connected to mass flow controllers (MKS) to accurately control PO_2 and PCO_2. To investigate the heterogeneous catalysis of surface reactions, a plug flow reactor is used. Different gases are continuously flowing to the reactor and all products after surface exchange are monitored in real time.

In TPX, isotopically labeled oxygen is flowed over cathode powders during a temperature ramping process, where the effluent gas is analyzed using a mass spectrometer. Each sample is placed in the center of a continuous flow quartz reactor

and pretreated in an $^{16}O_2$ environment to clean the surface and ensure the powder is saturated with ^{16}O. After pretreatment, samples were heated from 50°C to 800°C at a constant ramp rate of 30°C/min. A flow rate of 20 SCCM was established over the sample and the sample was heated under different concentrations of CO_2 and $^{18}O_2$ balanced with He. The rise and fall of different mass/charge (m/z) signals of oxygen species and carbon dioxide species are monitored using a quadrupole mass spectrometer: 32 ($^{16}O_2$), 34 ($^{16}O^{18}O$), 36 ($^{18}O_2$), 44 ($C^{16}O_2$), 46 ($C^{16}O^{18}O$), 48 ($C^{18}O_2$). From these profiles, the rate of ^{18}O exchange as a function of temperature was determined. This technique allows us to trace the movement of ^{18}O to directly probe the interaction of contaminants in the ORR at different temperatures.

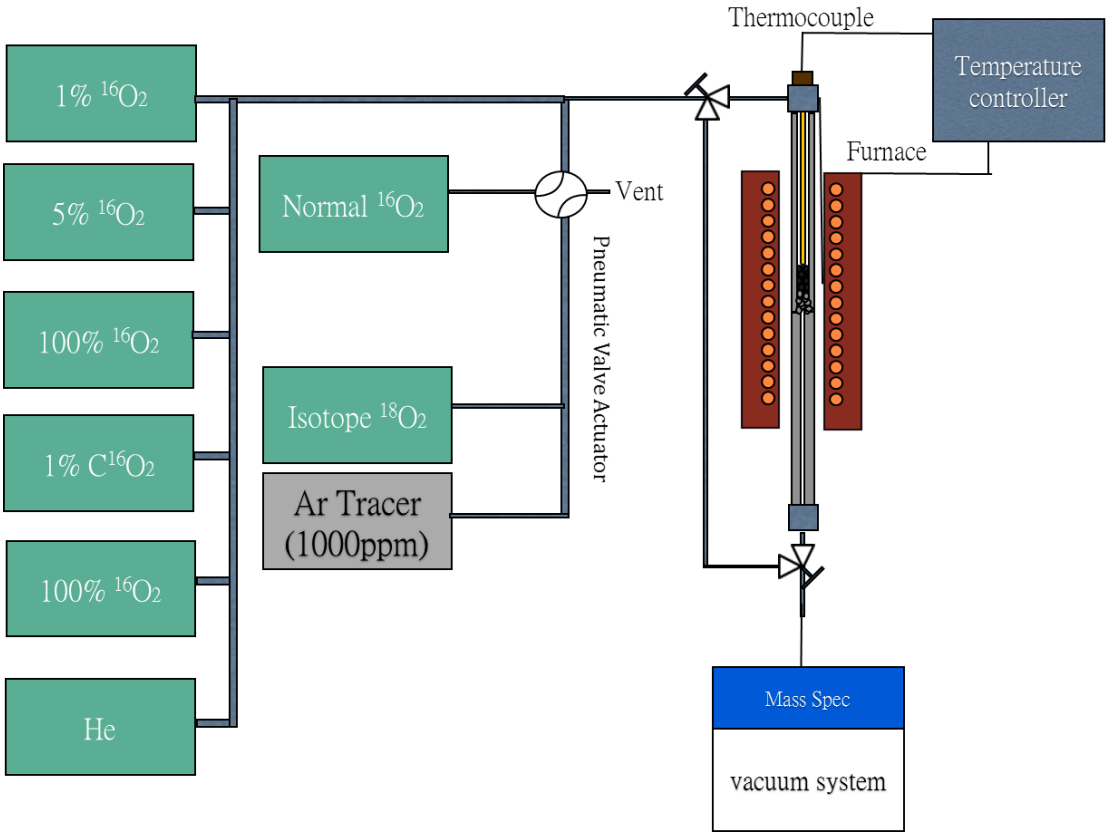

Figure 5-1. Experimental set up of the Isotope exchange

In ISTPX the powder is pretreated under 25000ppm $^{18}O_2$ at 800°C for 30-40 minutes. By pretreating the samples in $^{18}O_2$ at high temperature we are able to saturate the powder with the isotopically labeled ^{18}O. At 800°C, saturation of the two materials correspond to two different levels of exchange. For LSM, after 40 minutes of ^{18}O exposure, approximately half of the total oxygen sites in the material are exchanged. The exchange follows a typical depth profile, with a higher concentration of ^{18}O at the surface, decreasing as you near the center of the powder sphere. In contrast, LSCF saturation corresponds to a fully exchanged lattice. The difference in levels of exchange can be attributed to the ionic conduction properties of the two materials. LSM is known to have little to no bulk oxygen ion conduction, while LSCF is a good MIEC, with relatively high bulk oxygen conductivity. After the powders are saturated with isotopically labeled oxygen and cooled to room temperature, they are exposed to contaminant gases and heated back up to 800°C. Possible exchange products are monitored using a quadrupole mass spectrometer and dominant temperature regions for various reactions are determined.

5.3 Results and Discussion

Figure 5-2 shows TPX of LSCF in 25000ppm $^{18}O_2$ with and without the presence of 2,500ppm CO_2. The open symbol corresponds to TPX of LSCF in 25000ppm $^{18}O_2$. The $^{18}O_2$ in the gas phase begins to exchange with the LSCF surface at 250°C and starts to form gas phase $^{16}O_2$ and $^{16}O^{18}O$. Because the only source of ^{16}O is lattice oxygen in the LSCF, the formation of gaseous $^{16}O_2$ and $^{16}O^{18}O$ is a result of heteroexchange. Almost all of the $^{16}O_2$ is depleted by 460°C and the $^{18}O_2$ signal increases at higher temperature, indicating LSCF powder with 0.1 m^2 surface area has

the ability to dissociate all of the $^{18}O_2$ molecules ($3.4x10^{-7}$ mole/second) flowing through the powder at or above 460°C. We expect that the rate of exchange above this temperature is higher. The re-appearance of the $^{18}O_2$ signal at higher temperature is the product of multiple surface reaction steps after dissociative adsorption and desorption. An $^{16}O_2$ desorption peak is detected at 430°C, and an $^{16}O^{18}O$ desorption peak is detected at higher temperature, around 600°C. The decrease of $^{16}O_2$ and $^{16}O^{18}O$ signals at higher temperature suggests that the concentration of ^{16}O in the powder is decreasing through the combination of oxygen surface exchange and bulk self-diffusion in the LSCF.

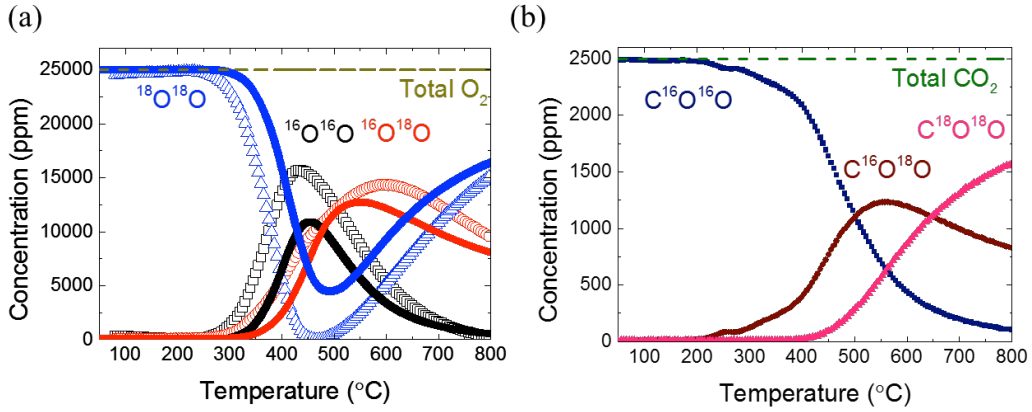

Figure 5-2. TPX of LSCF in 25000ppm $^{18}O_2$ with (closed symbol) or without (open symbol) 2500ppm CO_2 (a) O_2 signal and (b) CO_2 signal

Oxygen exchange signals for TPX of LSCF in 25000ppm $^{18}O_2$ with 2500ppm CO_2 are shown as closed symbols in Figure 5-2 (a). As compared to TPX without the presence of CO_2, the presence of 2500ppm CO_2 delays the exchange of O_2 from 250°C to 300°C. Since the presence of CO_2 shouldn't affect the intrinsic catalytic activity of LSCF, the delay in temperature where exchange begins may be caused by preferential adsorption of CO_2 over O_2, leaving a smaller number of available sites for

oxygen exchange. Also, the consumption of $^{18}O_2$ around 400-500°C reduces. From the formation of $C^{16}O^{18}O$ and $C^{18}O_2$, we can conclude that some of the $^{18}O_2$ molecules exchange with CO_2 instead of lattice oxygen, indicating that CO_2 participates in surface exchange. Figure 5-2 (b) shows the CO_2 exchange signal for TPX of LSCF in 25000ppm O_2 and 2500ppm CO_2. In TPX experiments labelled $^{18}O_2$ is originally only in gas phase, therefore the heteroexchange of CO_2 with labelled ^{18}O can only occur after the temperature region where LSCF has enough catalytic activity to dissociate and incorporate $^{18}O_2$. We can see that the labelled CO_2 signals appear at the same temperature as the O_2 signals. At higher temperature, the O_2 and CO_2 curves share the same shape, suggesting that both CO_2 and O_2 bond to the same surface sites and that the concentrations of the isotopologues are controlled by the ^{16}O:^{18}O ratio on the LSCF surface. From this, along with O_2 only TPX we can determine that the exchange mechanisms are most likely to be heteroexchange, and not homoexchange. The decrease in exchange signals at higher temperature are indicative of a combination of heteroexchange with self-bulk diffusion of ^{18}O into the lattice.

TPX of LSM in 25000ppm $^{18}O_2$ with and without the presence of 2500ppm CO_2 is shown in Figure 5-3. Without the presence of CO_2 (open symbols), the $^{18}O_2$ signal starts to drop significantly above 650-700°C. The temperature range is consistent with the change in valence state of manganese from 3+ to 2+ [122,123,125,132,133,146]. The reduction of Mn in the near surface region could create more available vacancies, leading to an increase in oxygen ion mobility and surface exchange. When 2500ppm CO_2 is present in the system (closed symbol), the $^{18}O_2$ curve appears to be the sum of the two overlapping exchange curves. The formation

of $^{16}O^{18}O$ begins at 300°C, revealing that LSM can catalyze the dissociation of oxygen molecules at this temperature. LSM is a poor ionic conductor and only a limited amount of ^{16}O, located near the surface, can exchange with gases. Therefore, the depletion of $^{18}O_2$ and formation of $^{16}O^{18}O$ between 400-650°C indicates the dominance of homoexchange. CO_2 exchange curves in Figure 5-3 (b) also show a drop in the $C^{18}O_2$ signal, confirming that homoexchange between O_2 and CO_2 occurs between 400-650°C. Above 650°C, the O_2 and CO_2 evolution curves have similar shapes, suggesting that both O_2 and CO_2 share the same reaction sites and heteroexchange dominates in this high temperature region. The difference between TPX of LSM with and without the presence of CO_2 illustrates the roles of CO_2 participating in the ORR. Comparing TPX of LSCF to that of LSM, we can see that LSCF does not show any noticeable CO_2 homoexchange, likely due to difference in stoichiometry between the two materials.

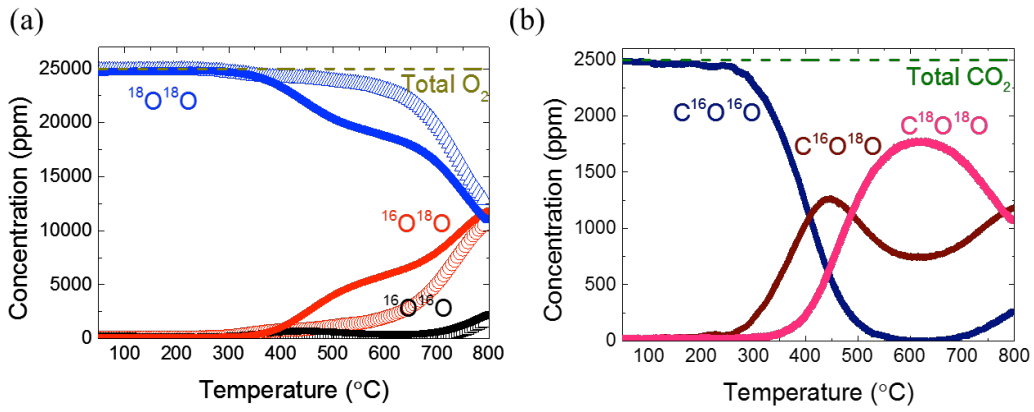

Figure 5-3. TPX of LSM in 25000ppm $^{18}O_2$ with (closed symbol) or without (open symbol) 2500ppm CO_2 (a) O_2 signal a d (b) CO_2 signal

The catalytic activity of LSCF towards CO_2 is investigated by ISTPX. Figure 5-4 shows ISTPX of LSCF while flowing only 2500ppm CO_2 with no oxygen flowing through the reactor. Interestingly, the ^{16}O in CO_2 starts to exchange with lattice ^{18}O

below 100°C. Notice that for TPX experiments, the exchange of CO_2 with the solid surface can only be observed after $^{18}O_2$ gas is dissociated. Due to the labelled ^{18}O in solid phase for ISTPX, the heterexchange of CO_2 with LSCF at lower temperature can be directly observed. When the temperature is lower than 300°C, a single exchange of one oxygen in CO_2 with one lattice oxygen $C^{16}O^{18}O$ dominates and has a peak near 250°C. When the temperature is higher than 300°C, double heteroexchange of oxygen in CO_2 with lattice oxygen $C^{18}O_2$ dominates and forms $C^{18}O_2$. The ratio of $C^{18}O_2$:$C^{16}O^{18}O$ is about 3:1 above 300°C. A linear increase in the $C^{16}O_2$ signal suggests that the LSCF surface is gradually covered with ^{16}O. The temperature range of dominant reaction species remains the same with higher concentrations of CO_2. Based on the results of ISTPX, LSCF shows tremendous catalytic activity towards the dissociation of CO_2.

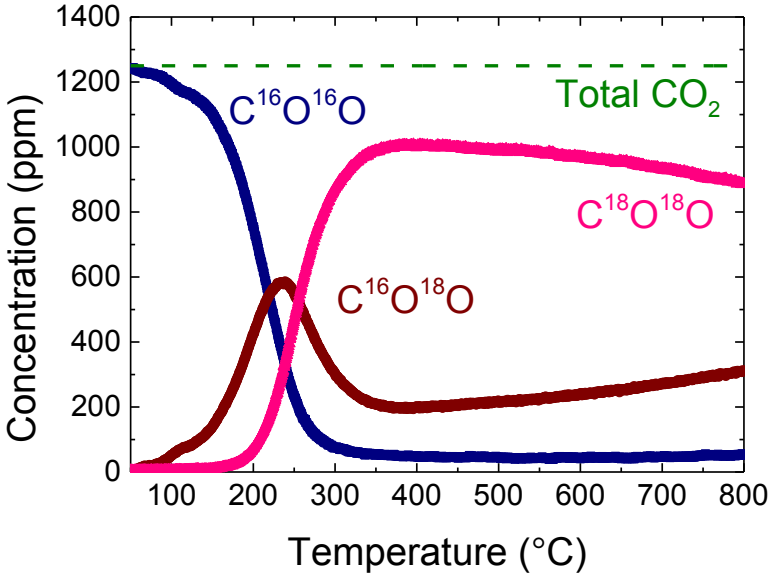

Figure 5-4. ISTPX of LSCF with 1250ppm CO_2

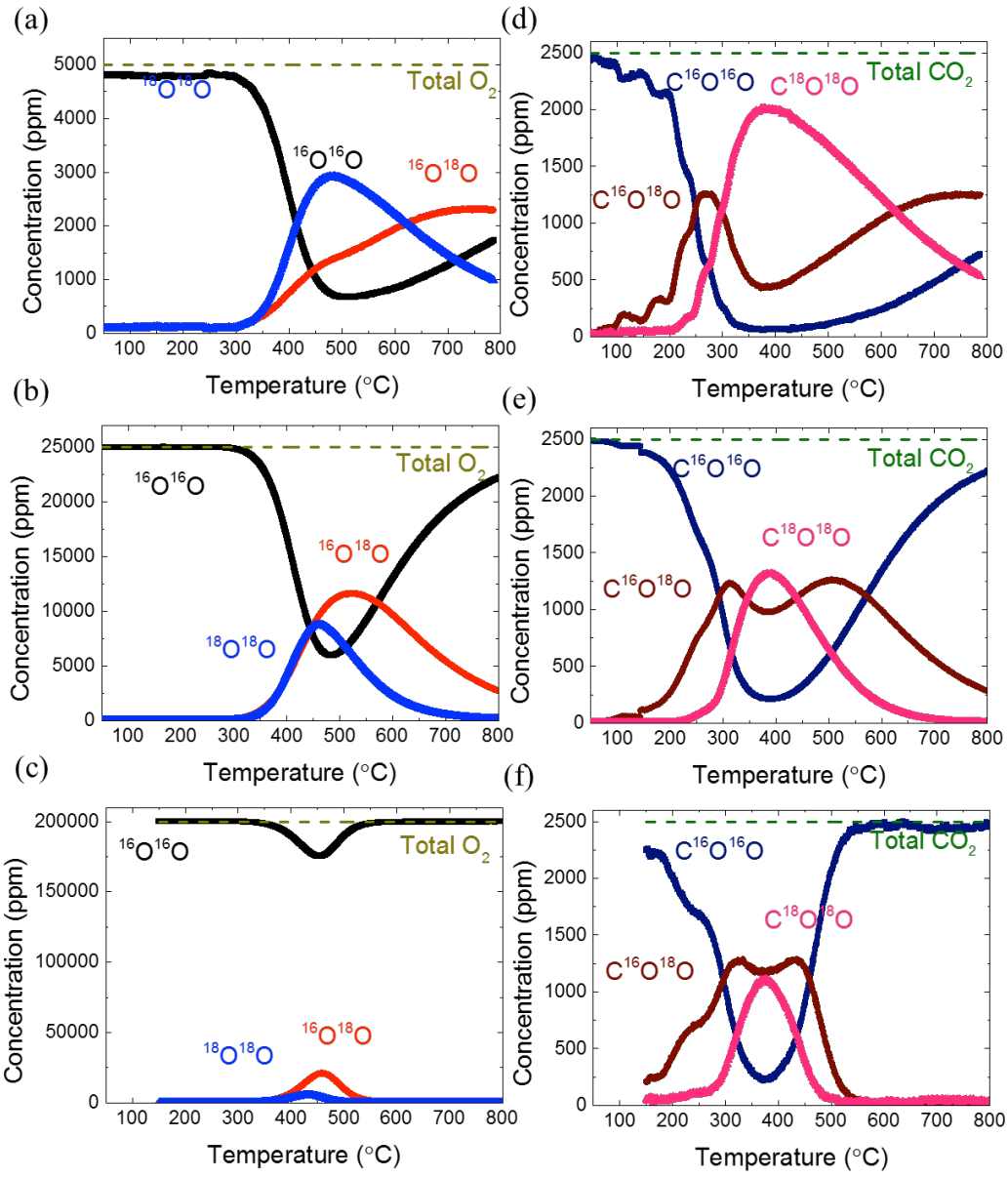

Figure 5-5. ISTPX of LSCF in 2500ppm CO_2 with different oxygen partial pressure: O_2 signal in (a) PO_2=0.5%, (b) 2.5%, and (c) 20%. CO_2 signal in (d) PO_2=0.5%, (e) 2.5%, and (f) 20%.

ISTPX of LSCF with 2500ppm CO_2 and different oxygen partial pressures is displayed in Figure 5-5; O_2 signals for PO_2 = (a) 0.005, (b) 0.025, (c) 0.20, and CO_2 signals for PO_2 = (d) 0.005, (e) 0.025, (f) 0.20 are presented. The oxygen partial pressure is changed from 0.5% up to 20% in order to explore real operating conditions. With the presence of 5000ppm O_2 in the system, O_2 and CO_2 signals

shown in Figure 5-5 (a) and (d), respectively, heteroexchange begins around 350°C. Both oxygen single and double heteroexchange happens at the same temperature, contrary to the single and double heteroexchange for CO_2. The higher temperature for O_2 heteroexchange suggests that the enthalpy for the catalysis of oxygen dissociation is higher than CO_2. The temperature for CO_2 single heteroexchange on LSCF is delayed slightly with the presence of O_2 to around 200°C, suggesting O_2 and CO_2 are competitively adsorbed. The temperature range for CO_2 double heteroexchange remains the same, dominating the surface reaction above 300°C. When PO_2 increases from 0.5% to 2.5%, the fraction of $^{16}O^{18}O$ and $^{18}O_2$ in the gas phase decreases due to the increase of ^{16}O flowing into the system. The $C^{16}O^{18}O$ signal exhibits an exchange curve with two peaks, one at 300°C and the other at 600°C. The first peak may be a result of the change from single heteroexchange of CO_2 to double heteroexchange. The second peak, however, is more likely caused by the decreasing concentration of ^{18}O in the lattice. The $C^{18}O_2$ signal shows an exchange peak at around 400°C. From ISTPX with the presence of both O_2 and CO_2 in the system, we can conclude that LSCF can catalyze both the dissociation of CO_2 and O_2. Also, results indicate that the dissociation of CO_2 has a smaller enthalpy, or a lower energy barrier, requiring a higher temperature for the dissociation of O_2. As PO_2 increases from 0.5% to 20%, the starting temperatures of single and double oxygen heteroexchange remain the same and are not dependent on oxygen partial pressure. As PO_2 increases to 20% there is a larger fraction of $^{16}O_2$ that exchanges with surface ^{18}O, resulting in all ^{18}O being exchanged by 550°C. The exchange of O_2 molecules with surface oxygen of LSCF is really active above 550°C under PO_2=20% but we cannot observe that due to

the depletion of ^{18}O in the system. Figure 5-5 (d)(e)(f) shows the CO_2 profiles at different oxygen partial pressures. All CO_2 exchange profiles under different PO_2 conditions show similar shapes. The only real difference being that under higher PO_2 conditions the concentration of ^{18}O on the surface decreases more quickly due to limited ^{18}O in the material. The peak position of the singly exchanged $C^{16}O^{18}O$ does not shift. The results suggest that CO_2 exchange with LSCF dominates the surface reactions regardless of the concentration of O_2. The exchange of CO_2 molecules with surface oxygen of LSCF is still really active under PO_2=20%. In all of these profiles, both O_2 and CO_2 exchange with lattice oxygen and can the reaction be considered co-dominant, as LSCF has a high activity for the oxygen exchange of both molecules.

LSM, an electronic conductor, has a different interaction with CO_2 than LSCF. Figure 5-6 shows ISTPX of LSM with only 2500ppm CO_2, balanced with He. CO_2 begins to dissociate on LSM above 400°C. Single heteroexchange between CO_2 and LSM dominates the reaction between 400-700°C. Above 700°C, double heteroexchange between CO_2 and LSM dominates. It can also be seen that the level of exchange of CO_2 on LSM increases at a much lower rate than that seen for LSCF. A single heteroexchange peak can be identified around 650-700°C. In comparison with LSCF ISTPX in Figure 5-4, Figure 5-6 shows that LSM has a much lower activity for heteroexchange of CO_2. All of this data indicates that the exchange of CO_2 on LSCF occurs more readily than on LSM.

The catalytic activity of LSM with the presence of both O_2 and CO_2 is studied by ISTPX. ISTPX of LSM with fixed CO_2 concentration (2500ppm) in different oxygen partial pressure are shown in Figure 5-7. With the presence of both CO_2 and

O_2, O_2 starts to exchange with the LSM surface at 400°C. Compared to exchange without the presence of CO_2, there appears to be less double heteroexchange of O_2. As PO_2 increases, we can see the exchange between O_2 and LSM decreases as shown in Figure 5-7 (a-c). We can observe the PO_2 effect on CO_2 exchange by comparing Figure 5-7 (d-f) to Figure 5-6. With the presence of O_2, the heteroexhange between CO_2 and LSM is suppressed, meaning that O_2 might block the CO_2 reaction sites. Another possible explanation is the stoichiometry of LSM under the various PO_2 conditions. When flowing only CO_2 balanced in He (O_2 <1ppb) the low PO_2 in the system may cause a change in LSM's surface stoichiometry from super-stoichiometry to sub-stoichiometry. When increasing PO_2, the surface catalytic activity of LSM also changes, resulting in a decrease of both O_2 and CO_2 heteroexchange activity. An increase of O_2 from 1250ppm to 20% indicated that O_2 and CO_2 demonstrate characteristics of competitive adsorption.

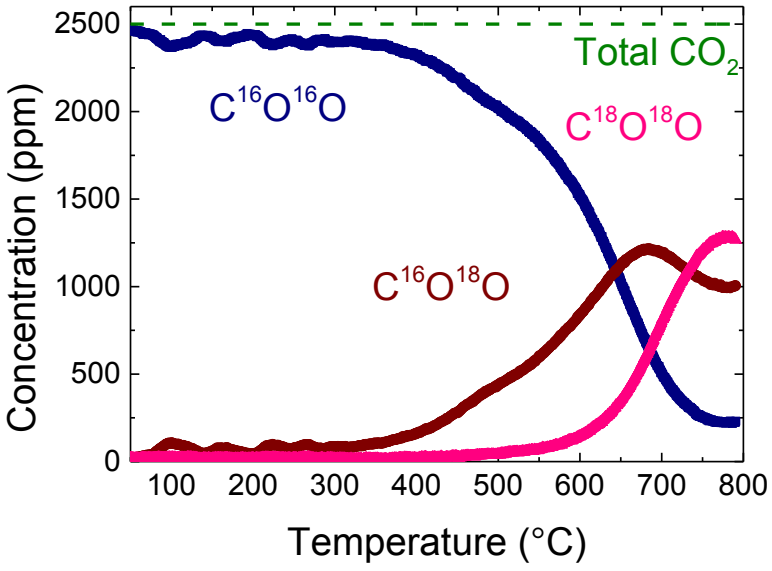

Figure 5-6. ISTPX of LSM in 2500ppm CO_2.

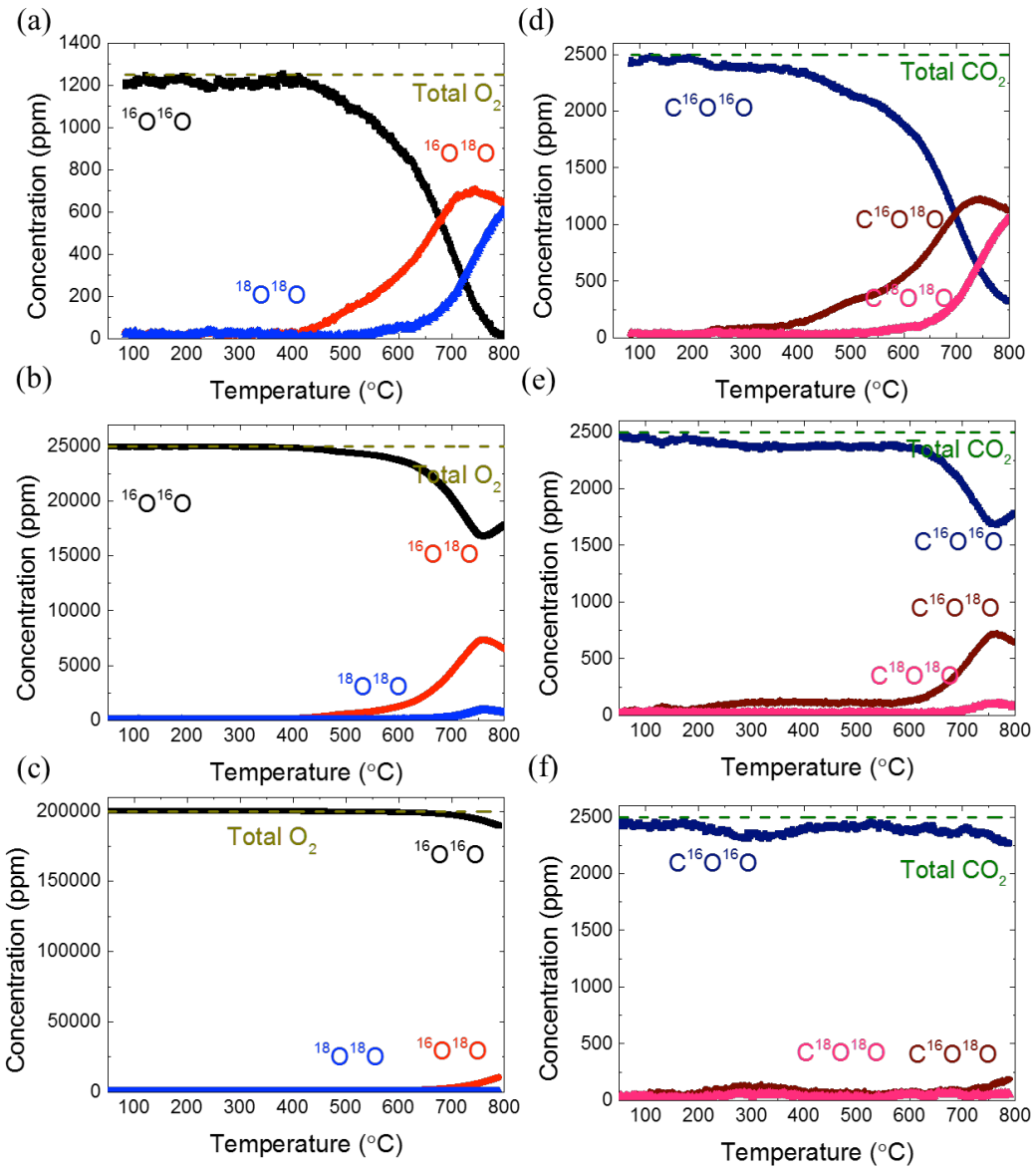

Figure 5-7. ISTPX of LSM in 2500ppm CO_2 with different oxygen partial pressure: O_2 signal in PO_2= (a) 0.125%, (b) 2.5%, and (c) 20%. CO_2 signal in PO_2= (d) 0.125%, (e) 2.5%, and (f) 20%.

CO_2 exchange dominates in low PO_2 for both LSM and LSCF. For LSM, as the concentration of oxygen increases, we can see that CO_2 surface exchange is suppressed, as shown in Figure 5-7(d)(e) and (f). LSCF, shown in Figure 5-5, exhibits a higher overall exchange than LSM. Compared to LSM, CO_2 and O_2 exchange with the LSCF lattice at lower temperatures, due to the difference in bulk oxygen

conduction. The oxygen partial pressure dependence of CO_2 surface exchange on LSCF is displayed in Figure 5-5(d)(e) and (f). For LSCF the surface exchange of CO_2 at higher PO_2 is not suppressed, in contrast to LSM.

Combining TPX and ISTPX provides us an overall understanding of the exchange between O_2, CO_2 and cathode powders. The difference in location of the oxygen tracer for each experiment helps to differentiate between the various homo and heterogeneous exchanges that can take place. The difference between TPX of LSM in Figure 5-3 and ISTPX of LSM in Figure 5-7 (b) and (e) illustrates the contribution of gas-gas homoexchange as a function of temperature. From TPX of LSM, the O_2 signal has a formation of $^{16}O^{18}O$ at 400°C, and a similar response in the CO_2 signal shows a single exchange peak at 450°C and a double exchange peak at 650°C, suggesting that the homoexchange between O_2 and CO_2 on LSM happens in the intermediate temperature range from 300-650°C. This implies that LSM has good catalytic activity for the homoexchange of O_2 and CO_2, but it lacks the ability to incorporate oxygen into lattice. In future investigation it would be interesting to observe how levels of homo and heteroexchange change when LSM is mixed with an oxygen ion conducting material, such as YSZ. Conversely, comparing ISTPX of LSCF with TPX of LSCF, the O_2 and CO_2 evolution curves above 400°C are very similar, suggesting that the homoexchange between O_2 and CO_2 is not substantial in this temperature range.

The CO_2 concentration effect on LSCF and LSM is shown in Figure 5-8 and Figure 5-9. Different CO_2 concentrations, varying from 1250 to 5000ppm, were

flowed into ^{18}O saturated LSCF and LSM powders. All experiments were conducted at PO_2=0.025.

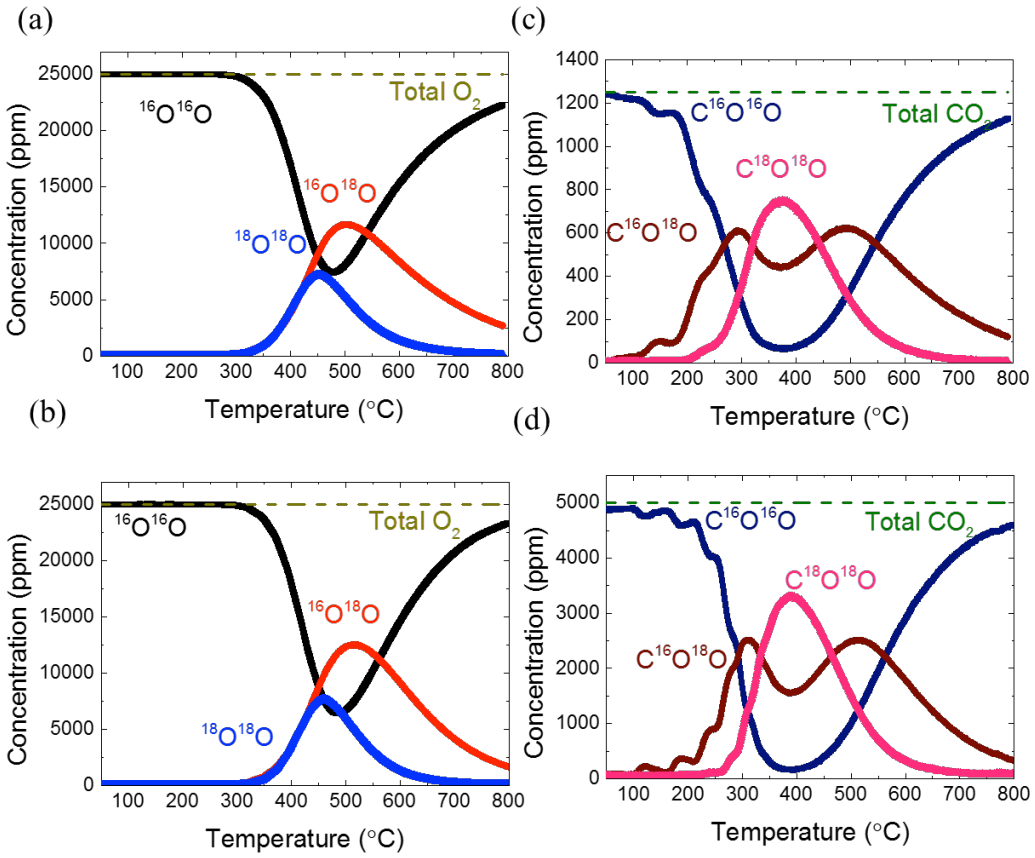

Figure 5-8. ISTPX of LSCF in PO_2 =0.025 with different CO_2 concentration: O_2 signal in CO_2= (a) 1250ppm (b) 2500ppm and CO_2 signal in CO_2= (c) 1250ppm (d) 2500ppm

Figure 5-8 shows ISTPX of LSCF: O_2 signals for CO_2 = (a) 1250ppm and (b) 5000ppm, and CO_2 signals for CO_2 = (c) 1250ppm and (d) 5000ppm. The O_2 curves for the different CO_2 concentrations have very little change. $^{18}O_2$ begins to dissociate at 350°C resulting in the rise of $^{16}O^{18}O$ and $^{18}O_2$ signals, with peaks at 450°C and 550°C, respectively. The formation of $^{16}O^{18}O$ and $^{18}O_2$ happen simultaneously, regardless of PCO_2, and does not share a similar shape with CO_2 exchange curves. When CO_2 concentration increases, more ^{18}O from LSCF exchanges with CO_2, rather

than O_2, but the exchange profiles remain the same shape. $C^{16}O_2$ starts to dissociate on the LSM surface around 200°C, and forms $C^{16}O^{18}O$ and $C^{18}O_2$ subsequently. $C^{16}O^{18}O$ signal shows two exchange peaks at 300°C and 500°C, and $C^{18}O_2$ has an exchange peak at 400°C. ISTPX of LSM with a lower CO_2 concentration, 1250ppm, is shown in Figure 5-9. The exchange curves in Figure 5-9 appear to have almost exactly the same shape as the curves in Figure 5-7 (b) and (e). It seems that the change of CO_2 concentration doesn't significantly change the exchange curves for both LSCF and LSM.

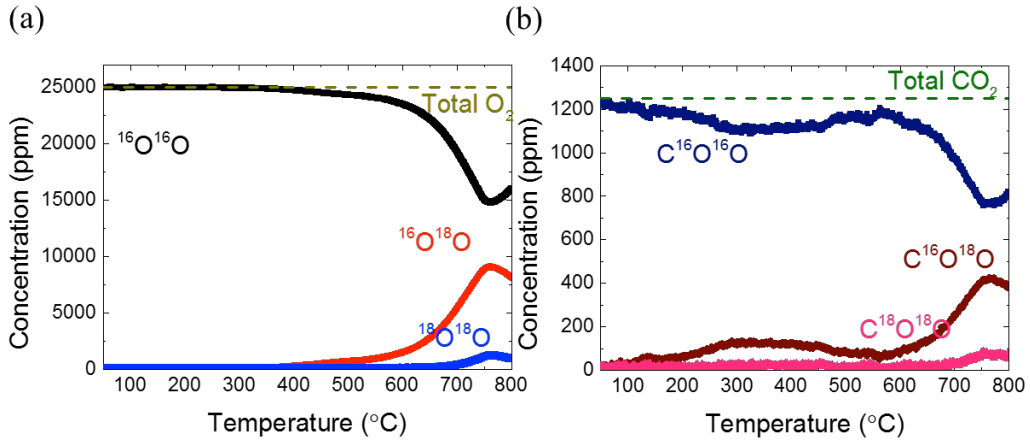

Figure 5-9. . ISTPX of LSM in 25000ppm O2 and 1250ppm CO_2 (a) O_2 signal and (b) CO_2 signal.

The experimental data for isotope exchange experiments of LSCF and LSM has been summarized and the dominant exchange reactions as a function of PO_2 and temperature are presented in Figure 5-10. LSCF, which is a MIEC material, shows better catalytic activity towards the dissociation of CO_2 than LSM, which is known as a good electron conducting material with negligible ion conduction. Figure 5-10 (a) and (b) show the contour plots of both singly-exchanged and doubly-exchanged CO_2 for LSCF as a function of PO_2 and temperature. Results suggest that CO_2 is

heterogeneously exchanged with the LSCF surface and blocking of CO_2 exchange does not occur with the presence of O_2. Singly-exchanged CO_2 begins exchanging at a lower temperature than the doubly- exchanged CO_2, as low as 400°C. The decrease of the singly and doubly exchanged CO_2 above 500°C is caused by the limited amount of ^{18}O in the powder. The interaction of CO_2 with LSCF is substantial in all temperature and PO_2 regions. The singly and doubly exchanged CO_2 for LSCF appear to be two separate exchange mechanisms, and the levels of both exchanges depend on the surface concentrations ^{16}O and ^{18}O.

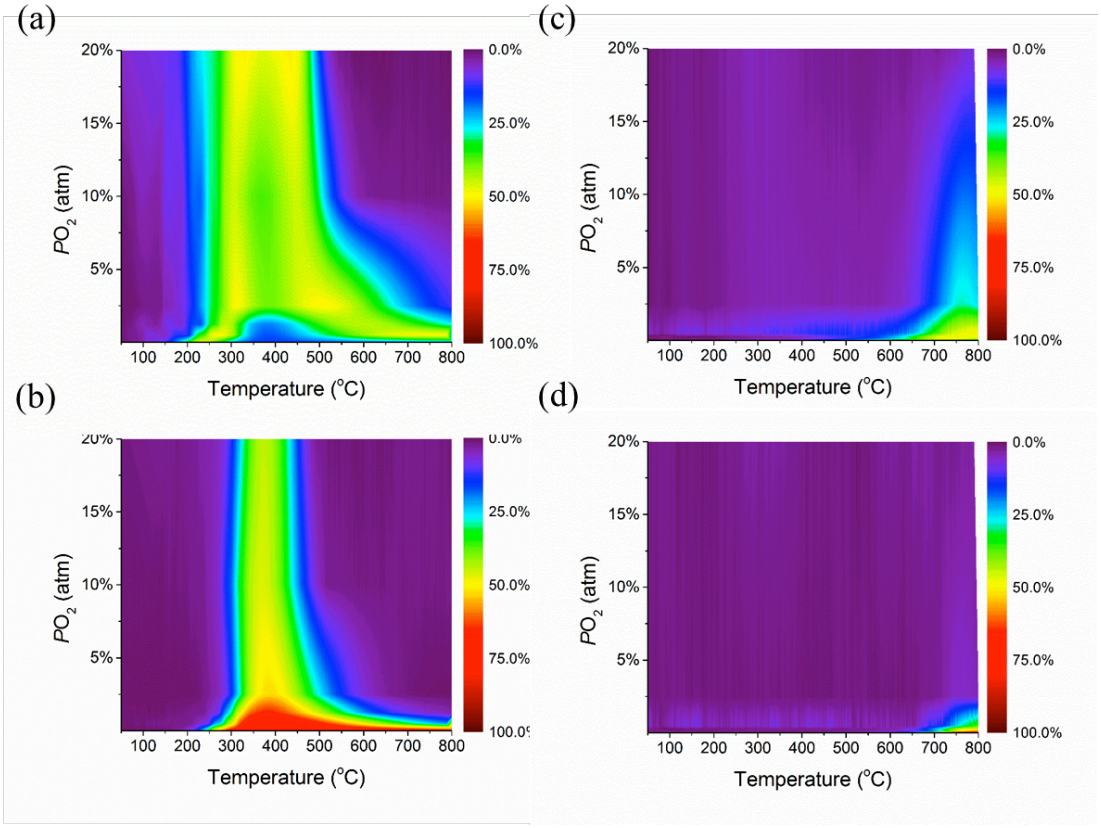

Figure 5-10. Contour plot of singly-exchanged and doubly-exchanged CO_2 with LSCF as a function of PO_2 and temperature, for data gathered from temperature programmed exchange experiments. (a) singly-exchanged, (b) doubly-exchanged on LSCF, and (c) singly-exchanged, (d) doubly-exchanged on LSM.

Figure 5-10 (c) and (d) show the contour plots of both singly and doubly exchanged CO_2 with LSM as a function of PO_2 and temperature. From these plots we can see that CO_2 doesn't show much exchange with LSM, especially at lower temperature, and the presence of O_2 severely limits CO_2 exchange with LSM. The PO_2 dependence of CO_2 exchange may be caused by surface oxygen stoichiometry or the preferential adsorption of O_2 on exchange sites. The difference in the contour plots of LSCF and LSM in Figure 5-10 suggest that LSM is generally unaffected by CO_2 under normal working conditions but LSCF shows a significant exchange with CO_2 in wide temperature and PO_2 ranges. We can determine that the highest isotope exchange reaction rates of CO_2 with LSCF is around 420-450°C.

5.4 Conclusions

Temperature programmed techniques are used to study the heterogeneous catalysis of LSM and LSCF on gaseous O_2 and CO_2 and to determine the dominant reactions at each temperature. To probe the interaction between contaminants and lattice oxygen at different temperatures, with and without the presence of gas phase oxygen, a technique called Isotope Saturated Temperature Programmed Exchange (ISTPX) has been developed. We have demonstrated the temperature ranges that CO_2 prefers to exchange with solid-phase oxygen for both LSM and LSCF. PO_2 and PCO_2 dependencies have been explored. This is the first time that the interaction of CO_2 and O_2 with LSM and LSCF have been illustrated. LSCF shows high catalytic activity toward breaking of the C-O bond in CO_2, along with heterogeneous exchange. Without the presence of O_2, single heteroexchange of CO_2 with LSCF is observed as low as 100°C. CO_2 dominates the surface reactions over O_2 on LSCF at low

temperature, with both single and double heteroexchange. At higher temperature (above 500°C), both CO_2 and O_2 exchange with the LSCF surface, as co-dominant reactions. The results suggest that the participation of CO_2 in the ORR on LSCF is significant. CO_2 exchange is both thermodynamically and kinetically favorable, especially in the low and intermediate temperature regions (<500°C). On the contrary, LSM shows limited heteroexchange with CO_2 due to a low concentration of surface vacancies. However, while flowing only CO_2 balanced in He (O_2<1ppb), we see some heteroexchange. This indicates that at higher PO_2 the concentration of vacancies is too low to allow exchange, or O_2 is preferentially adsorbed on the surface, occupying all of the available active sites. These results point the way to elucidate the heterogeneous catalysis of LSM and LSCF for O_2 and CO_2. This work enables us to further understand the degradation mechanisms. This result could potentially apply to the design of new materials for thermal splitting of CO_2 to generate fuels [127,136,137]. If we can utilize the catalytic activity of perovskites to create a composite material, combining them with a reducing agent, something to induce oxygen vacancies, it would be possible to generate fuels by dissociating CO_2 either electro- or thermo-chemically.

Chapter 6: 1:1 Isothermal Isotope Exchange (1:1 IIE)

6.1 Introduction

The dissociation of oxygen is a crucial reaction for a number of important technologies that rely on ionic transport of oxygen. The oxygen-oxygen bond is strong and requires a high energy to break it, about 500kJ/mol at room temperature[147]. Typically, high temperatures are required to thermally activate the dissociation of oxygen, but the temperature requirement can be decreased through the proper selection of catalyst materials. One important application of these oxygen catalyst materials is as cathodes of solid oxide fuel cells (SOFC). SOFCs have been demonstrated as great prospects for the electrochemical conversion of fuels, providing both high efficiency and high power density[3,7]. The operation of SOFCs is dependent on the reduction of oxygen at the cathode, followed by transport through a solid electrolyte to the anode, where the solid oxygen is used to oxidize a fuel. A closer look at this process highlights a key advantage of SOFCs over comparable technologies; oxygen gas, already abundant in air can be used to oxidize any fuel at the anode. In other fuel cell technologies, this is not the case. Recently, there has been significant effort to reduce the operating temperature of SOFCs to reduce the effects of degradation, and decrease the cost of interconnect materials[148-152]. Unfortunately, as operating temperature decreases polarization losses at the cathode increase dramatically, due to the thermally activated ORR. A fundamental understanding of the ORR is necessary to improve and enhance the performance of SOFC cathodes, allowing for lower temperature operation. In addition, contaminants in the air, such as

water and CO_2, have been reported to have deleterious effects on SOFC cathodes[23,37-46], causing material degradation and limiting the applications of SOFCs. Understanding of the interactions of multiple gaseous species on the cathode is essential to further improve cell performance.

$(La_{0.8}Sr_{0.2})_{0.95}MnO_{3-x}$ (LSM) and $La_{0.6}Sr_{0.4}Co_{0.2}Fe_{0.8}O_{3-x}$ (LSCF) are the most common cathode materials for SOFCs, and have been shown to have acceptable performance at high temperature. LSM is a pure electronic conductor with high catalytic activity towards the dissociation of oxygen. It is generally accepted that the transition metal Mn, in LSM, provides the catalytic properties necessary for oxygen dissociation[118,153]. LSM usually has a cation deficiency, leading to oxygen superstoichiometry, and a low concentration of surface vacancies. On the contrary, LSCF tends to compensate the charge balance resulted from the substitution of Sr in La site by creating oxygen vacancies. The high concentration of vacancies in LSCF makes it a mixed ionic electronic conductor (MIEC). Therefore, the oxygen transport mechanisms for LSCF and LSM are quite different[154].

The ORR consists of a series of steps and it involves not only catalyst promoted gas-surface reactions but also surface/solid diffusion processes[15,155-161]. We can use a two-step reaction model to describe the steps of the ORR [76,78]. The first step is dissociation, where the double bond in molecular oxygen is broken, and oxygen gas molecules become surface atoms. As the oxygen-oxygen bond is very strong, it is essential that the cathode surface can catalyze the reaction. In the second step, incorporation, the oxygen atoms need to overcome a second energy barrier to move from the surface into the lattice of the material. Once incorporated into the lattice the

transport of oxygen can be described by diffusion. Generally, the ORR is described by the surface exchange coefficient (k) to quantify the series of gas-surface reactions and diffusion coefficient (D) to define the solid phase oxygen transport. There are a number of methods aimed at gaining an understanding of the fundamental mechanisms of the ORR. The first is to apply an external potential, either an electrical or electrochemical potential, to disturb the equilibrium of the system and then observe changes in the material properties through the movement of oxygen[57,58,88,131]. Another approach is to use isotopically labeled oxygen as a tracer to study the self-surface exchange and self-diffusion processes without any externally applied field. There are two basic types of isotope exchange experiments, in which either solid phase or gas phase isotopic analysis is used. In the former, solid phase oxygen is quantified *ex-situ* in isotope exchange depth profiling (IEDP) using secondary ion mass spectrometry (SIMS)[69,70,141]. IEDP-SIMS provides the oxygen isotope distribution profile as a function of distance from the gas-solid interface after samples have been exposed to isotopically labeled oxygen for a given temperature and exposure time. The isotope distribution profile can then be fitted with a solution to the diffusion equations to determine the self-surface exchange coefficient (k^*) and self-diffusion coefficient (D^*). This technique requires less data processing and can provide localized studies to quantify different diffusion processes, such as grain boundary diffusion and bulk diffusion. However, the *ex-situ* nature of the experiment limits the scope of the technique to defining only an overall surface exchange (k) value comprised of all the steps in the ORR reaction rates and also has no ability to probe the interaction of the solid surface with different gases. Another issue that often arises in IEDP-SIMS is the

sample geometry, which can affect the fitting of *k* and *D* values. Often the geometry is such that surface exchange and diffusion are co-limiting, inhibiting simplification of the diffusion equations.

The second type of isotope exchange experiment is based on *in-situ* gas phase analysis[63,67,71,74,75,78,96]. With gas phase isotope exchange, we can probe not only the fundamental kinetics of the ORR but also the interaction of multiple gases at the gas-solid interface. This technique allows us to determine the rate of exchange and is not limited to a single reactant (oxygen). However, isotope exchange requires careful data processing to analyze the gaseous compositions. Steady state isotopic transient kinetics analysis (SSITKA) is a well-established technique to probe the kinetics of the catalytic reactions among reactants, intermediate species, and products[67,162]. The analysis of SSITKA focuses on the gas phase products and the surface reaction residence time constants (τ) of each species. For SOFC cathodes, oxygen isotope exchange yields no products, as the experiment is based on the self-exchange of oxygen with the solid material. In the SOFC cathode, the oxygen that is dissociated and incorporated into a solid phase is the one actually contributes to the overall redox reaction. Therefore, the "products" of isotope exchange are the oxygen in solid phase and gaseous oxygen isotopologues are the byproducts after surface exchange. Therefore, to study the kinetics of the ORR on SOFC cathode materials we use isothermal isotope exchange (IIE)[73-75,78]. The experimental set up of IIE is similar to SSITKA but IIE focuses more on exploring the relationship between gas-solid interfaces.

In normal IIE, the cathode powder is subjected to a complete switch in the gas environment, from $^{16}O_2$ to $^{18}O_2$, creating a non-equilibrium isotopic distribution at the start of the experiment. Reaction rates are determined by tracking the change in $^{16}O_2$, $^{16}O^{18}O$ and $^{18}O_2$ signals. However, there are a number of different sets of steps that can create each of these O_2 isotopologues, making it difficult to differentiate between the various paths and quantify the kinetics of each individual reaction. The nature of normal IIE allows us to probe the interaction between gas and solid, but is less adept for exploring gas-gas interactions on the surface.

Therefore, to further understand the ability of materials to catalyze the dissociation of oxygen molecules, we conducted IIE under the presence of both $^{16}O_2$ and $^{18}O_2$. The concentrations of $^{16}O_2$ and $^{18}O_2$ are equal, creating a 1:1 ratio, and therefore, we will refer to this technique as 1:1 IIE. By flowing both $^{16}O_2$ and $^{18}O_2$ into the system, we are able to determine the how well each cathode material can dissociate oxygen. The scrambled product $^{16}O^{18}O$ is formed when both $^{16}O_2$ and $^{18}O_2$ are dissociatively adsorbed on the surface followed by the recombination of ^{16}O and ^{18}O into the gas phase. The statistical distribution of $^{16}O_2$, $^{16,18}O_2$, and $^{18}O_2$ at each temperature provides insight into the levels of catalytic activity towards the dissociation of oxygen

In this research, we focus on the study of the catalytic activity of gas-surface reaction and the interactions of other oxygen-containing molecules on LSCF and LSM have been investigated. To determine effects of contaminants on SOFC cathodes, 1:1 IIE was also performed in the presence of water as well as CO_2. By introducing oxygen with and without the presence of these other oxygen-containing

species, we can directly observe their effects on the O_2 surface reactions. This is the first time the surface kinetics of SOFC cathodes has been investigated in the presence of the contaminants, CO_2 and water, using 1:1 IIE.

6.2 Experimental

Details of the experimental set up can be found in our previous works[76,78]. Figure 6-1 shows a schematic drawing of the experimental set up. Commercially available LSCF (Praxair) and LSM (Fuel Cell Materials) powders were tested. To allow for direct comparison, the amount of LSCF and LSM was normalized to a total surface area of 0.1 m^2. In our isotope exchange experiments we used a non-circulating plug-flow reactor, and for modeling purposes we assumed a differential-type reactor[81]. The flow rate through the reactor was fixed at 20 SCCM using mass flow controllers. Helium was used as a carrier gas in all experiments. The reactor exhaust flows across a capillary tube leading to a quadrupole mass spectrometer, where the composition was analyzed and recorded.

Before each 1:1 IIE experiment, the sample was pretreated at 800°C in a normal isotope $^{16}O_2$ environment with PO_2=0.05 for 30 minutes to ensure that the powder surface is clean and completely saturated with ^{16}O. After the pretreatment, the sample was brought to the temperature of interest and equilibrated in $^{16}O_2$ with PO_2=0.05. In a separate line isotopically labeled $^{18}O_2$ (Sigma-Aldrich; 95% pure), with a PO_2=0.025, and 1000ppm of Ar (Airgas), used as an inert tracer, was flowed. Then, using a pneumatically actuated valve, half of the $^{16}O_2$ flowing through the powder was switched to the $^{18}O_2$ flow with 1000ppm Ar tracer creating a 1:1 ratio of

^{16}O: ^{18}O. The evolution of oxygen species, $^{16}O_2$, $^{16}O^{18}O$, and $^{18}O_2$ were then recorded using the mass spectrometer.

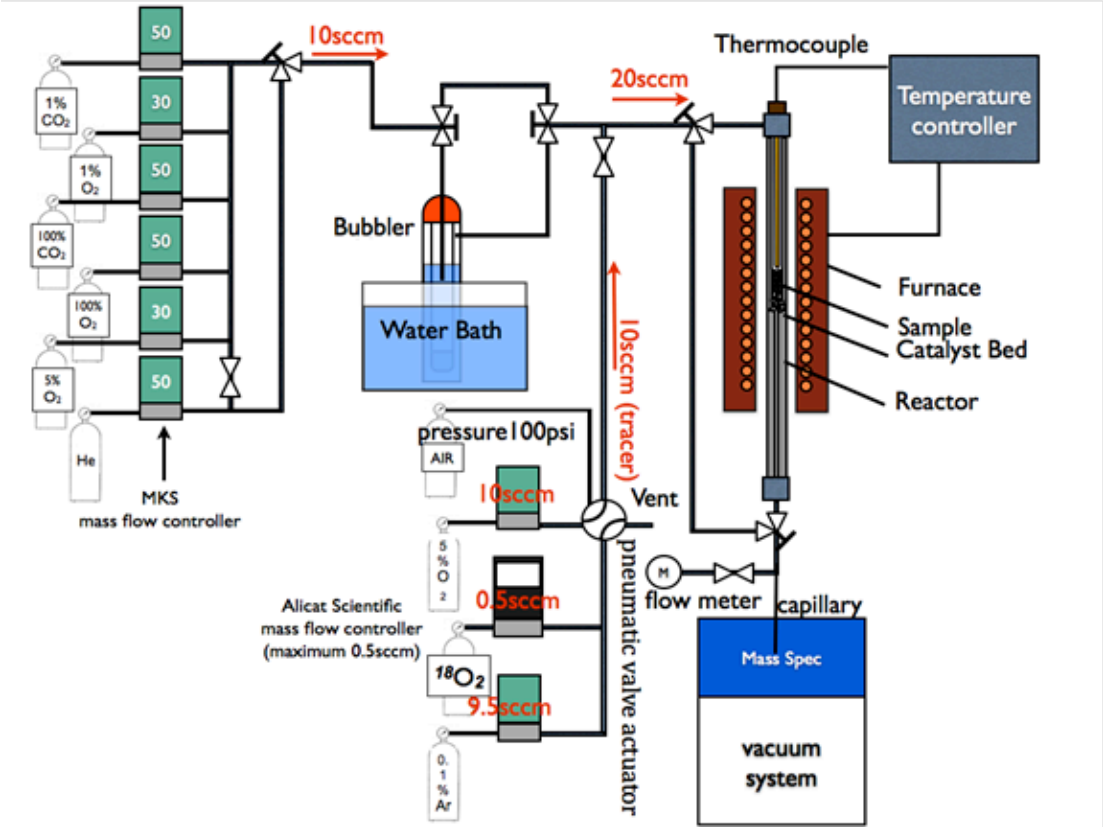

Figure 6-1. Experimental set up of oxygen isotope exchange

1:1 IIE experiments with the presence of contaminants was also performed, using the same experimental settings. To mimic the real operating condition, the concentrations of contaminants are fixed at low levels. The CO_2 concentration was fixed at 2500ppm. Due to the overlapping of the $^{18}O_2$ cracking fraction (m/z=18) and H_2O (m/z=18), deuterated water, or D_2O (m/z=20) was used instead. The D_2O concentration is fixed at 3000ppm by bubbling the carrier gas through an impinger submerged in a temperature controlled water bath.

6.3 Isotope Exchange Theory

There are two main types of surface oxygen exchange[66,82,163], homoexchange and heteroexchange. The rate of homoexchange, or homogeneous exchange, (R_0,) describes the catalytic acitivity of the metal oxide for dissociating oxygen without the participation of lattice oxygen. In heteroexchange, the exchange process involves the participation of lattice oxygen. Single heteroexchange (R_1) is the exchange of one oxygen atom in O_2 with one lattice, or solid phase, oxygen, while double heteroexchange (R_2) is the exchange of both atoms in O_2 with two atoms in the solid phase. The total rate of heteroexchange (R_{ex}) is the sum of both single and double heteroexchange:

$$R_{ex} = \frac{1}{2}R_1 + R_2 \qquad [6\text{-}1]$$

In typical IIE, where there is a complete switch of the gas phase oxygen isotope from $^{16}O_2$ to $^{18}O_2$ we cannot see the R_0 mechanism as homoexchange between two $^{18}O_2$ yields no recognizable difference. Instead, using normal IIE we aim to determine to the total rate of heteroexchange, R_{ex}. A detailed analysis of IIE for the quantification of kinetics and diffusion parameters can be found in our previous work[154]. Here we will focus on gaining a better understanding of the dissociation process for O_2 on LSM and LSCF cathode materials.

In contrast, for 1:1 IIE we can determine the catalytic activity of cathodes towards the dissociation of oxygen as there is the presence of both ^{18}O and ^{16}O in the gas phase. As stated previously, the gas composition flowing to the reactor in 1:1 IIE

is an equal mixture of $^{16}O_2$ and $^{18}O_2$, balanced in He. Using this experimental set up, we can determine the oxygen catalyst's "dissociation-ability" by analyzing the level of conversion from $^{16}O_2$ and $^{18}O_2$ to the mixed isotopologue $^{16}O^{18}O$. The first elementary step is dissociative adsorption, where O_2 molecules form isotopically labeled surface atoms[67,84]:

$$\frac{1}{2}\,{}^{16}O_2 + * \xrightarrow{k_1} {}^{16}O_* \qquad [6\text{-}2]$$

$$\frac{1}{2}\,{}^{18}O_2 + * \xrightarrow{k_1} {}^{18}O_* \qquad [6\text{-}3]$$

In Equation [6-2] and Equation [6-3], * denotes an available surface site, and k_1 is the forward rate constant and k_{-1} is the backward rate constant. After dissociative adsorption, atomic oxygen can recombine with another oxygen and desorb from the surface.

$${}^{16}O_* + {}^{18}O_* \xrightarrow{k_{-1}} {}^{16}O^{18}O \qquad [6\text{-}4]$$

$$2\,{}^{16}O_* \xrightarrow{k_{-1}} {}^{16}O_2 \qquad [6\text{-}5]$$

$$2\,{}^{18}O_* \xrightarrow{k_{-1}} {}^{18}O_2 \qquad [6\text{-}6]$$

The formation of $^{16}O^{18}O$ follows a series of surface reactions involving dissociative adsorption and desorption, and can be expressed as:

$$\frac{d[{}^{16}O^{18}O]}{dt}^{ex} = 2k_{-1}(S^2\Theta_*^2 k_1^2 \left([{}^{16}O_2]\right)^{1/2} \left([{}^{18}O_2]\right)^{1/2}) \qquad [6\text{-}7]$$

Where S is the number of active sites per unit surface area and Θ_* is the fraction of available surface sites. The forward and backward rate constants are temperature dependent and can be written as:

$$\frac{d[^{16}O^{18}O]^{ex}}{dt} = 2(S^2\Theta_*^2\left([^{16}O_2]\right)^{1/2}\left([^{18}O_2]\right)^{1/2})A_{-1}A_1^2\exp(\frac{E_{-1}+2E_1}{RT}) \qquad [6\text{-}8]$$

where A_1 and A_{-1} are the pre-exponential terms and E_1 and E_{-1} are the activation energies for the forward and backward reactions, respectively. The activation energy for the formation of $^{16}O^{18}O$ is the sum of the energy for forward and backward reactions, as O_2 needs to be dissociated and then be recombined back to gas phase. The slope of the Arrhenius plot can give us information about the activation of the exchange process on cathodes, as shown in Equation [6-8]. $^{16}O_2$ and $^{18}O_2$ concentrations after surface exchange can also be shown as:

$$\frac{d[^{16}O_2]^{ex}}{dt} = k_{-1}(S^2\Theta_*^2k_1^2[^{16}O_2]) \qquad [6\text{-}9]$$

$$\frac{d[^{18}O_2]^{ex}}{dt} = k_{-1}(S^2\Theta_*^2k_1^2[^{18}O_2]) \qquad [6\text{-}10]$$

Where $[^{16}O^{18}O]^{ex}$, $[^{16}O_2]^{ex}$, and $[^{18}O_2]^{ex}$ are the concentrations of the three isotopologues after surface exchange. The overall exchange reaction can be expressed as:

$$2^{16}O_2 + 2^{18}O_2 \leftrightarrow {}^{16}O_2 + 2^{16}O^{18}O + {}^{18}O_2 \qquad [6\text{-}11]$$

This equation describes the self-surface exchange process. The steady state exchange fraction (Ψ), describing the amount of dissociation, the concentration ratio of the three isotopologues[164]:

$$\Psi = \frac{\left([^{16}O^{18}O]^{ex}\right)^2}{\left([^{16}O_2]^{non-ex} + [^{16}O_2]^{ex}\right)\left([^{18}O_2]^{non-ex} + [^{18}O_2]^{ex}\right)} \qquad [6\text{-}12]$$

$[^{16}O_2]^{non\text{-}ex}$ and $[^{18}O_2]^{non\text{-}ex}$ are concentrations of $^{16}O_2$ and $^{18}O_2$ that are not participating in the exchange on the surface. The final concentrations of each oxygen isotopologue can be expressed as the sum of exchange and non-exchange O_2 concentration. Substituting equations [8], [10], and [11] into [13], Ψ can be expressed as:

$$\Psi = \frac{\left(2k_{-1}(S^2\Theta_*^2k_1^2\left([^{16}O_2]\right)^{1/2}\left([^{18}O_2]\right)^{1/2})\right)^2}{\left([^{16}O_2]^0 - S\Theta_*k_1[^{16}O_2]^{1/2} + k_{-1}(S^2\Theta_*^2k_1^2[^{16}O_2])\right)\left([^{18}O_2]^0 - S\Theta_*k_1[^{18}O_2]^{1/2} + k_{-1}(S^2\Theta_*^2k_1^2[^{18}O_2])\right)}$$

[6-13]

where $[^{16}O_2]^0$ and $[^{18}O_2]^0$ are the inlet O_2 concentrations for $^{16}O_2$ and $^{18}O_2$, respectively. Ψ allows us to determine the deviation from equilibrium during isotope exchange. If the solid surface has enough catalytic activity to dissociate all of the oxygen, $[^{16}O_2]^{non\text{-}ex}$ and $[^{18}O_2]^{non\text{-}ex}$ should be close to zero, and oxygen isotopologues should have a completely random distribution. In this case, the ratio of $^{16}O_2$: $^{16}O^{18}O$: $^{18}O_2$ should be 1:2:1 at equilibrium, leading to a value of 4 for Ψ:

$$\Psi = \frac{\left(2k_{-1}(S^2\Theta_*^2k_1^2[^{16}O_2]^{1/2}[^{18}O_2]^{1/2})\right)^2}{\left(k_{-1}(S^2\Theta_*^2k_1^2[^{16}O_2])\right)\left(k_{-1}(S^2\Theta_*^2k_1^2[^{18}O_2])\right)} = 4 \qquad [6\text{-}14]$$

The deviation of Ψ from 4 can provide information about the catalytic activity of a material towards the dissociation of oxygen at different temperatures. When other gaseous species are present in the system, the steady state concentrations of each oxygen-containing isotopologue will change. Consider the presence of CO_2 or D_2O, the exchange reactions between each gas species can be expressed as:

$$2\,{}^{18}O_2 + 3C^{16}O_2 \leftrightarrow {}^{16}O_2 + {}^{16}O^{18}O + C^{16}O_2 + C^{16}O^{18}O + C^{18}O_2 \qquad [6\text{-}15]$$

$${}^{18}O_2 + D_2\,{}^{16}O \leftrightarrow {}^{16}O^{18}O + D_2\,{}^{18}O \qquad [6\text{-}16]$$

The corresponding values of Ψ_{CO2} and Ψ_{D2O} can be calculated for all concentrations of gaseous species:

$$\Psi_{CO_2} = \frac{[{}^{16}O_2][{}^{16}O^{18}O][C^{16}O^{18}O][C^{18}O_2]}{[{}^{18}O_2]^2[C^{16}O_2]^2} \qquad [6\text{-}17]$$

$$\Psi_{D_2O} = \frac{[{}^{16}O^{18}O][D_2\,{}^{18}O]}{[{}^{18}O_2][D_2\,{}^{16}O]} \qquad [6\text{-}18]$$

Ψ_{CO2} and Ψ_{D2O} are determined from the concentrations of all gas species after surface exchange, and are functions of contaminant exchange, as well as O_2 exchange. Oxygen diffusion processes in 1:1 IIE and 1:1 IIE with CO_2 or water remain constant, as the time scale of our experiments limit the effects of these contaminants to surface reactions.

6.4 Results and Discussion

6.4.1 1. 1:1 IIE of LSM and LSCF

1:1 IIE of LSM and LSCF was conducted at different temperatures with a fixed PO_2=0.05. Figure 6-2 shows a summary of 1:1 IIE for (a) LSCF and (b) LSM for all temperatures studied. IIE is a really surface sensitive technique because the testing powder for IIE is about several hundred nanometers, which is in the range for surface exchange dominance[75]. The ability of the oxide catalyst to dissociate the oxygen gas molecules can be determined by observing the outlet gas ratio of $^{16}O_2$ (black): $^{16}O^{18}O$ (red): $^{18}O_2$ (blue). The final concentration of each oxygen isotopologue provides information about the catalytic activity of cathodes towards the dissociation of oxygen, and the time for each IIE experiment to reach steady state provides the information about reaction kinetics. As stated previously, if the inlet gas is totally dissociated on the oxide surface, the outlet gas will have a random distribution of oxygen isotopologues $^{16}O_2$: $^{16}O^{18}O$: $^{18}O_2$ =1:2:1, with Ψ equal to 4. We can see that for LSCF in Figure 6-2 (a), no gas-solid surface reactions occurs at 300°C because there is no formation of $^{16}O^{18}O$. However, at 350°C, there is an $^{34}O_2$ signal, indicating that a fraction of the $^{16}O_2$ and $^{18}O_2$ molecules have been dissociated and have recombined. The initial concentration of $^{18}O_2$ is about 22000ppm and Ψ at steady state has a value of 0.02, suggesting that only a portion of $^{18}O_2$ are dissociated and most of the $^{18}O_2$ are not participating in surface exchange on LSCF. At 500°C the final value of Ψ is 4, indicating that there is complete dissociation of all oxygen passing across the powder. Above 500°C, the reaction is no longer limited by dissociation, allowing us to clearly see incorporation of oxygen into the lattice. In

comparison, 1:1 IIE for LSM is shown in Figure 6-2 (b) and presents a different story for the dissociation of oxygen. First, it is clear that the maximum random distribution ratio of 1:2:1 does not occur until a much higher temperature than what we see for LSCF. The total level of the scrambled product $^{16}O^{18}O$, increases at a slower rate across the range of temperatures studied, indicating that LSM has a lower apparent activation energy for the exchange of oxygen. In LSM we can also see that below 750°C there is fast switching, indicated by the quick increase of the $^{18}O_2$ signal, suggesting that there is little or no incorporation of oxygen into the LSM lattice. This indicates that homoexchange between gaseous oxygen dominates on the LSM surface. The low ionic conductivity of LSM and the small total number of surface vacancies that are mobile, limit the number of ^{16}O on the surface that can exchange into the gas phase. However, as the temperature increases to 800°C, we see that the time to reach maximum Ψ increases, indicating a higher level of bulk exchange.

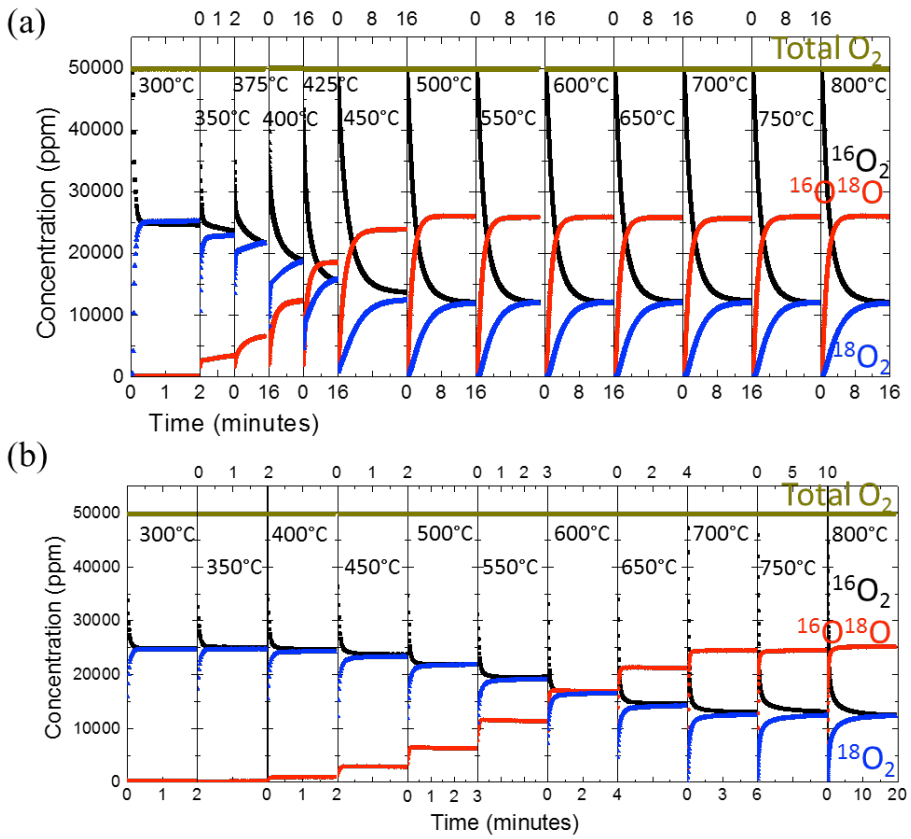

Figure 6-2 IIE of (a) LSCF and (b) LSM at different temperatures in PO_2=0.05. The ratio of $P^{32}O_2$: $P^{36}O_2$ flowing into the system is 1:1.

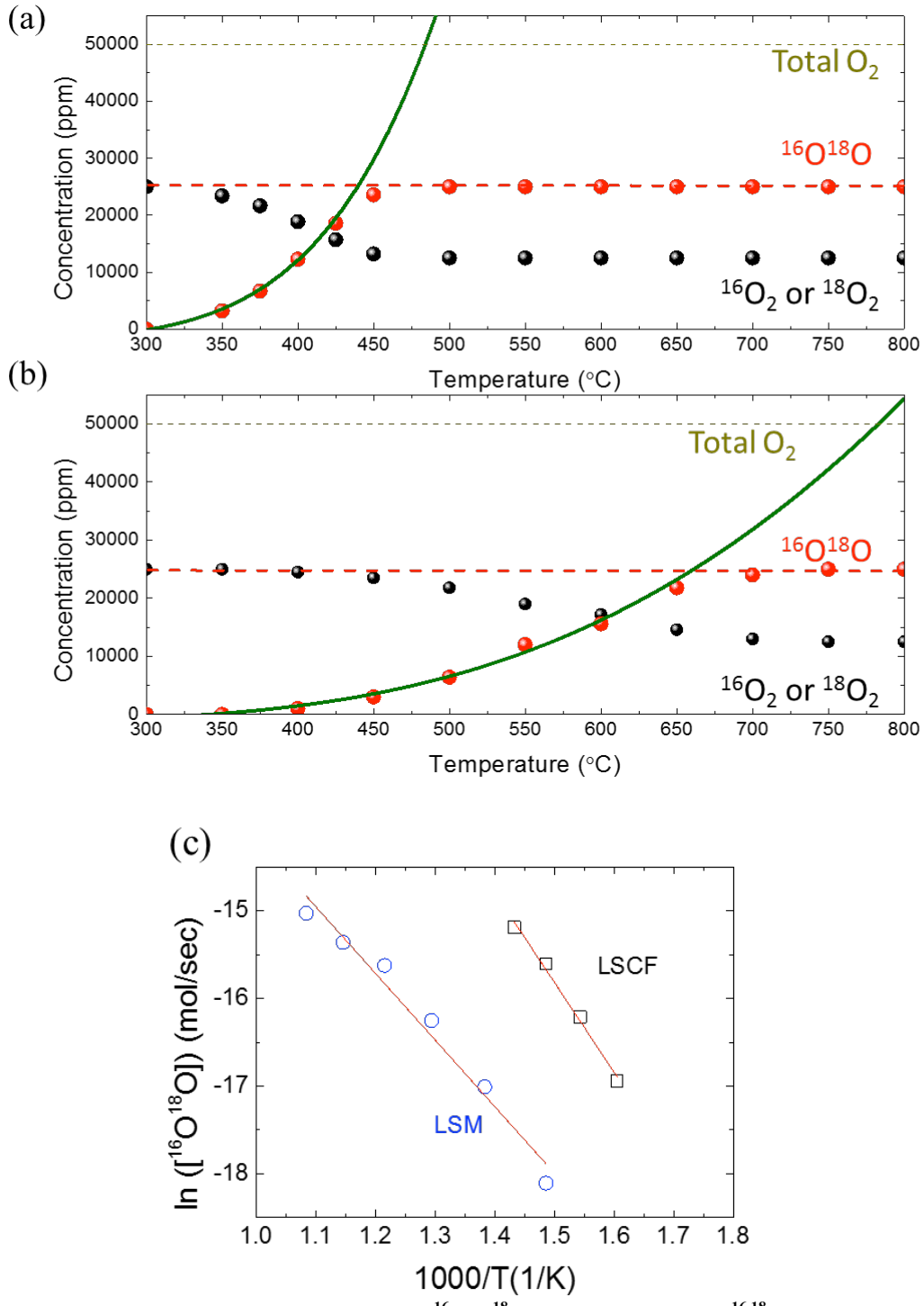

Figure 6-3. Equilibrium concentrations of $^{16}O_2$ ($^{18}O_2$) (black dots) and $^{16,18}O_2$ (red dots) for 1:1 IIE of (a) LSCF, and (b) LSM at different temperatures with PO_2=0.05. Equilibrium concentrations of $^{16,18}O_2$ increase with increasing temperature, reaching a fully random distribution of 1:2:1 ($^{16}O_2$:$^{16,18}O_2$:$^{18}O_2$) at 450°C for LSCF and 650°C for LSM. Arrhenius plot (c) of the steady-state concentration of $^{16}O^{18}O$ for LSCF and LSM.

The steady state concentrations of the mixed oxygen signal ($^{16}O^{18}O$, red) and the unmixed signals ($^{18}O_2$ ($^{16}O_2$), black) for (a) LSCF and (b) LSM are summarized in Figure 6-3. For LSCF, Figure 6-3 (a), the oxygen isotopologues quickly reach the equilibrium distribution of 1:2:1 by 450°C. Compared to LSCF, we can see that LSM does not reach the equilibrium distribution until 650°C, as shown in Figure 6-3 (b). The apparent activation energy for exchange is extracted from the Arrhenius plot of the steady state production rate of ln[$^{16}O^{18}O$] with respect to the reciprocal temperature in Figure 6-3 (c) and fitting them with Equation [9]. The relatively high catalytic activity towards the formation of $^{16}O^{18}O$ at low temperature for LSCF shown in Figure 6-3 (c) indicates that LSCF may be better at dissociation than LSM, at least under the tested conditions. The calculated apparent activation energy ($2E_1+E_{-1}$) for the exchange of oxygen on LSCF is around 85 kJ/mol, while the activation energy for LSM is around 63 kJ/mol. The intersection of these lines is known as the isokinetic temperature[80]. Above this temperature, catalysts with higher *E* values would have more rapid reactions. The calculated T_θ equals to 2.3K.

The ^{18}O exchange flux and fraction curves in solid and gas are displayed in Figure 6-4. The exchange flux curves describe the amount of ^{18}O that is entering the system, but not leaving in the form of $^{16}O^{18}O$ or $^{18}O_2$, and is therefore becoming part of the solid phase oxygen in the powder. Conversion fraction describes the amount of ^{18}O in the powder as a fraction of the total possible amount. For LSCF, we can see that there is no ^{18}O exchange flux at 300°C, as shown in Figure 6-4 (a). But as temperature increases, the amount of ^{18}O that is entering the solid phase increases dramatically. The amount of ^{18}O exchanged with lattice ^{16}O increases as a function of

temperature. Eventually, the ^{18}O fraction in lattice is in equilibrium with the ^{18}O fraction in the inlet gas, shown in the ^{18}O conversion fraction for LSCF in Figure 6-4 (b). Above 500°C, all inlet $^{18}O_2$ are dissociated and participated in the exchange process. The exchange flux follows a first order reaction at 600°C, suggesting that above this temperature diffusion is no longer limiting the overall reaction and that surface exchange is the rate limiting step[154]. The ^{18}O fraction in gas phase ($^{18}\alpha_g$) of LSCF is shown in Figure 6-4 (c). At lower temperature, $^{18}\alpha_g$ reaches steady state values very fast and the amount of ^{18}O exchanged with ^{16}O increases as the temperature increases, suggesting that the heteroexchange between ^{18}O and lattice ^{16}O is the one determines the total reaction time. For LSM, the exchange process is different. There is little to no ^{18}O exchange flux below 600°C, as shown in Figure 6-4 (d) and (e). Even though oxygen is dissociated on the surface below 600°C, as shown in Figure 6-3, there is almost no exchange between surface oxygen and lattice oxygen. It is likely that the low concentration of vacancies in LSM limits the incorporation step. De Souza[97] reports the diffusion coefficient (D*) for LSM is $4x10^{-16}$ (cm^2/s) and $3x10^{-15}$ (cm^2/s) at 700°C and 800°C, respectively, and the total reaction time for our experiments are near 20 minutes. Therefore, the diffusion length $(Dt)^{1/2}$ in LSM is close to 5 nm and 25nm, respectively. Therefore, the diffusion process is expected to cause a limited effect on surface concentrations ^{16}O and ^{18}O, even at 800°C. Figure 6-4 (f) shows the ^{18}O fraction in gas phase ($^{18}\alpha_g$) of LSM. When the temperature increases from 600°C to 800°C, the $^{18}\alpha_g$ curve takes more time to reach steady state, suggesting that the level of incorporation into the bulk of LSM is increasing.

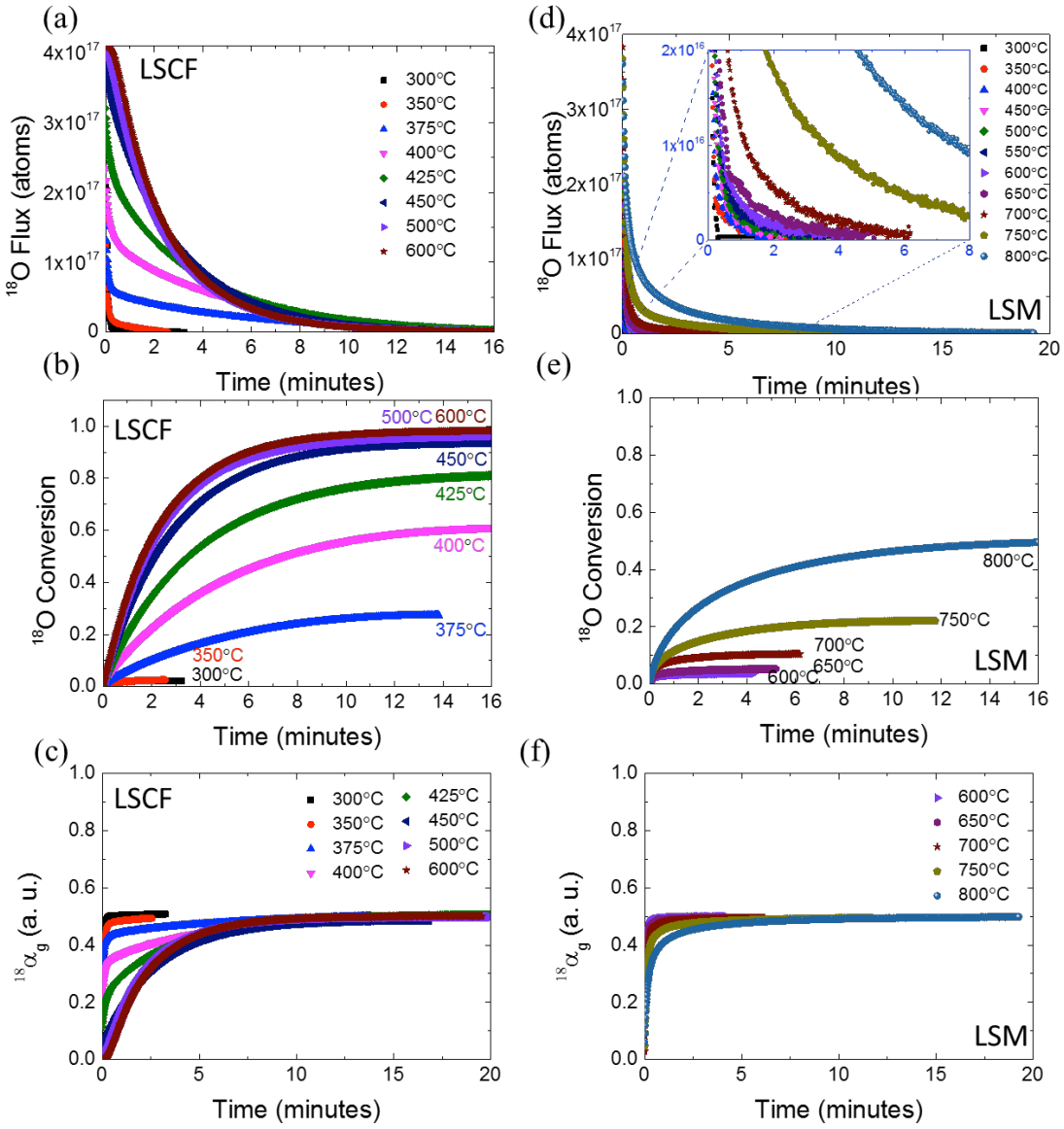

Figure 6-4. (a) ^{18}O exchange flux, (b) ^{18}O fraction in solid, and (c) ^{18}O fraction in gas phase ($^{18}\alpha_g$) for LSCF, and (d) ^{18}O exchange flux, (e) ^{18}O conversion fraction in solid, and (f) ^{18}O fraction in gas phase ($^{18}\alpha_g$) for LSM at different temperatures with a total PO2=0.05. The conversion fraction in solid is normalized to the inlet $^{16}O_2$:$^{18}O_2$ concentration.

The kinetic properties of LSCF and LSM are studied by considering the time (τ) for the $^{16}O^{18}O$ and $^{18}O_2$ signals to reach steady state and the time for Ψ to reach it's the steady state value. Figure 6-5 shows the τ's for 1:1 IIE of LSCF and LSM.

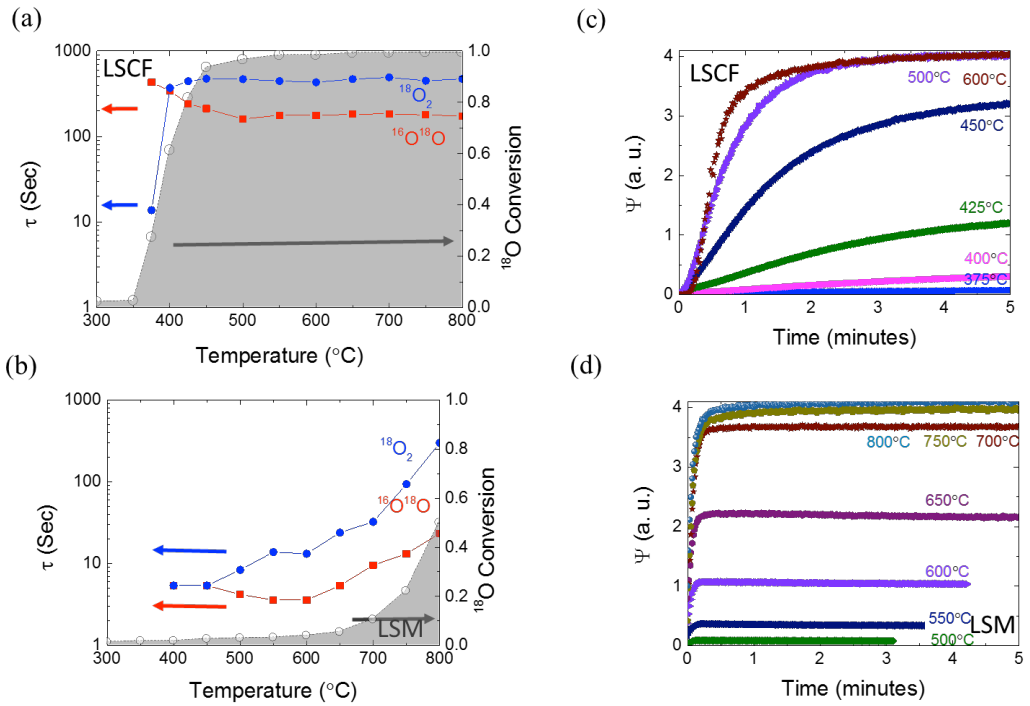

Figure 6-5. The summary of the exchange time for each isotopologue to reach steady state. τ of the $^{16}O^{18}O$ and $^{18}O_2$ signals and the accumulated ^{18}O conversion fraction of (a) LSCF and (b) LSM at different temperatures. Ψ of (c) LSCF and (d) LSM as a function of time at different temperatures

For LSCF, shown in Figure 6-5 (a), we can see that below 400°C the time required for $^{16}O^{18}O$ to reach its maximum is higher than for $^{18}O_2$. In contrast, above 400°C the opposite is true. We believe this is indicative of changes in the mechanisms for exchange as the temperature increases from 300 to 800°C. For LSM, shown in Figure 6-5 (b), we see that there is a decrease in τ for $^{16}O^{18}O$ between 400 and 600°C. This decrease is likely caused by faster kinetics for homogeneous exchange on the material. However, as temperature increases above 600°C we see that τ again increases, indicating that heterogeneous exchange is becoming more prevalent. τ for the $^{18}O_2$ signal appears to be more closely related to the heteroexchange process and the total fraction of ^{18}O accumulated in the solid phase for both LSCF and LSM. In Figure 6-5 (c) and (d) we see Ψ as a function of time at different temperatures for

LSCF and LSM, respectively. We can see for both LSCF and LSM, the final steady-state value of Ψ increases as temperature increases. The final value of Ψ indicates the amount total level of surface exchange, while any delay in Ψ reaching this value is caused by participation of solid phase ^{16}O.

6.4.2 2. The presence of CO_2 and water

1:1 IIE in the presence of contaminants was performed at different temperatures to determine the effects of contaminants on the ability of LSCF and LSM to dissociate oxygen. Figure 6-6 (a) and (c) shows the O_2 signals for 1:1 IIE of LSCF and LSM, respectively, with the presence of 2500ppm $C^{16}O_2$. In the presence of CO_2, $^{18}O_2$ begins to dissociate on LSCF above 400°C. Additionally, when CO_2 is present LSCF does not fully dissociate all of the oxygen entering the system until 600°C. Previously, without the presence of CO_2 this maximum level of dissociation was achieved at 500°C. Figure 6-6 (b) shows the CO_2 signal for 1:1 IIE of LSCF. $C^{16}O^{18}O$ starts to form at 350°C although there is no observable formation of $^{16}O^{18}O$. The CO_2 signals reach their full random distribution at 450°C and ^{18}O exchange with CO_2 dominates between 350°C and 500°C. It is important to note that $^{18}O_2$ gas is the only source of ^{18}O in the system, and any $C^{16}O^{18}O$ or $C^{18}O_2$ involves the participation of oxygen gas. There are two possible routes for the formation of isotopically labeled CO_2: the first is through homoexchange between $^{18}O_2$ and $C^{16}O_2$; second is a two-step exchange process where $^{18}O_2$ exchanges with lattice oxygen to form ^{18}O, and then $C^{16}O_2$ exchanges with this ^{18}O from the lattice forming isotopically labeled CO_2. Based on IIE of LSCF without the presence of CO_2 and our previous work using temperature programmed exchange[165]. We see that heteroexchange dominates for

LSCF across the tested temperature range. The increased temperature to reach the maximum statistical distribution, and the fact that both O_2 and CO_2 interact with LSCF through the heteroexchange process, indicates that both molecules occupy the same surface sites.

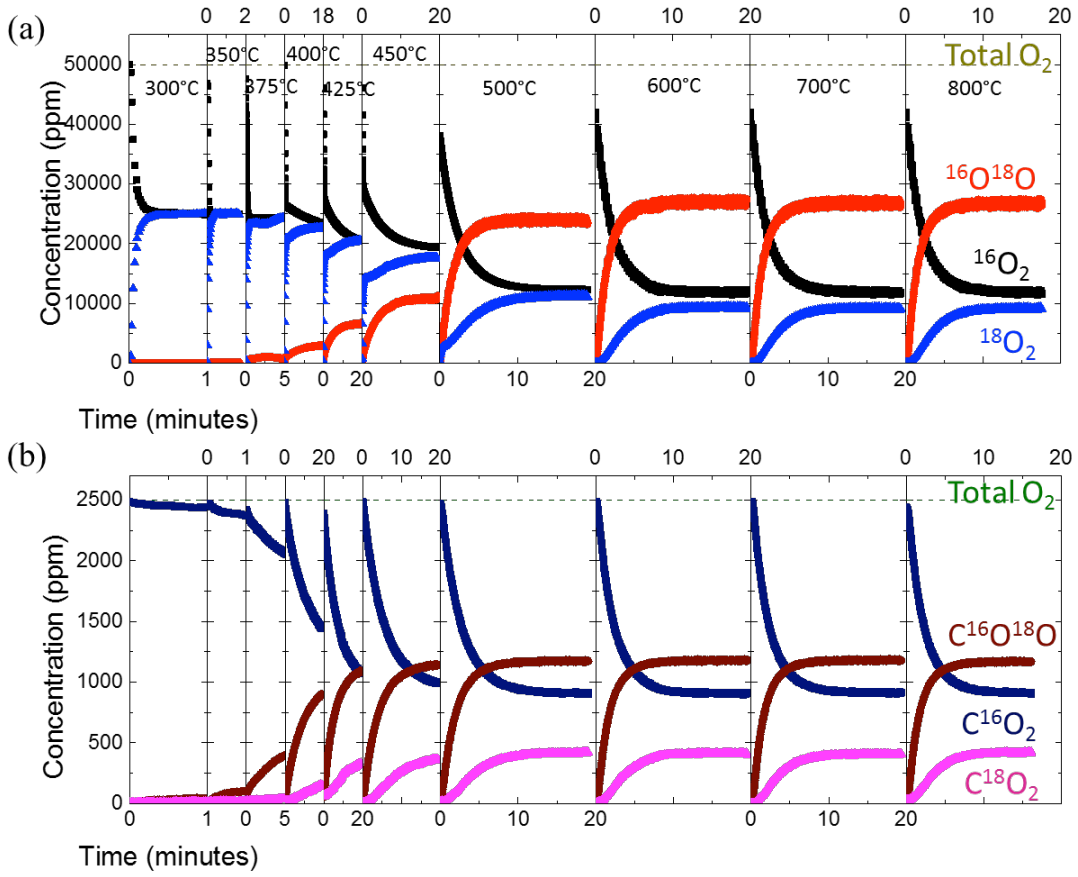

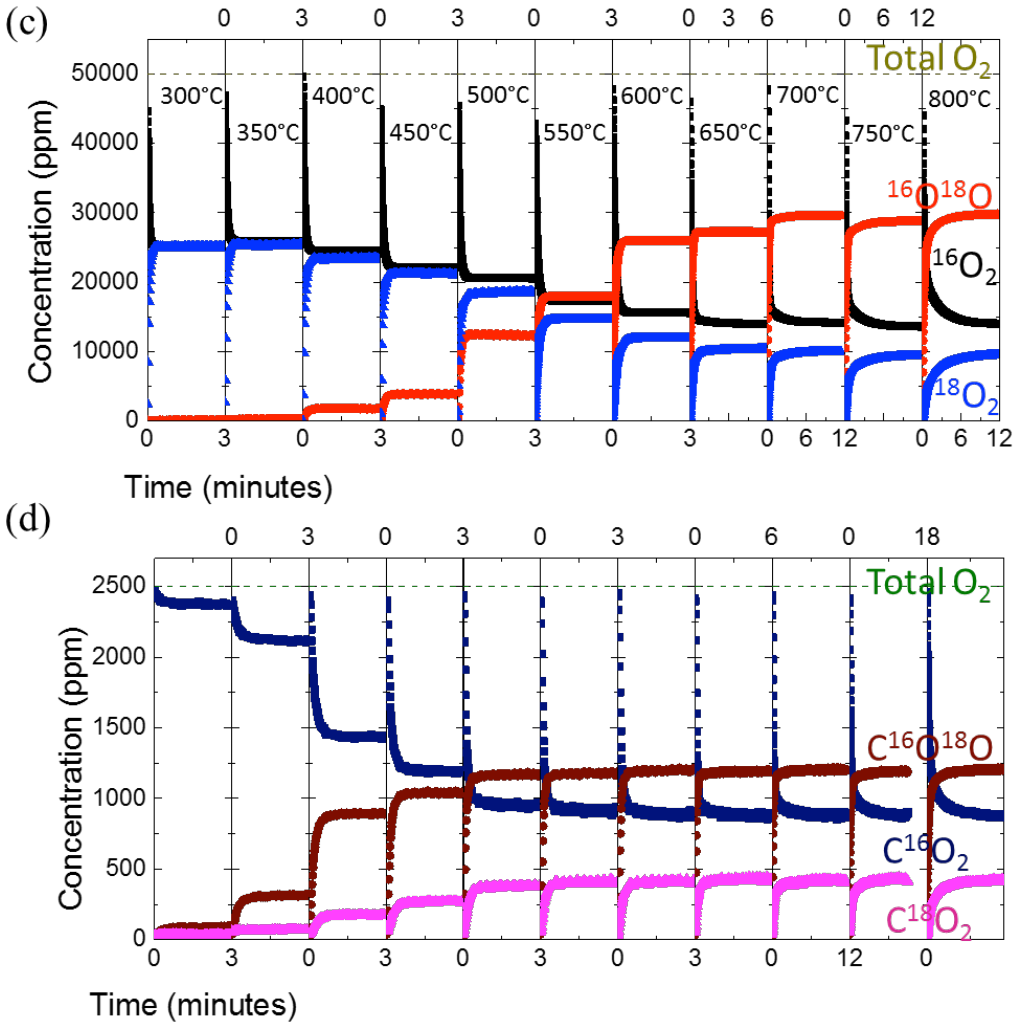

Figure 6-6. 1:1 IIE of LSCF and LSM at different temperatures in PO_2=0.05 with the presence of 2500ppm $C^{16}O_2$. (a) O_2 (b) CO_2 signals of LSCF and (c) O_2 (d) CO_2 signals of LSM.

LSM has a different response to the presence of CO_2. Figure 6-6 (c) and (d) show the O_2 and CO_2 signals for 1:1 IIE of LSM with 2500ppm CO_2. The O_2 signals show similar trends regardless of the presence of CO_2. With CO_2, O_2 begins to dissociate at 350°C through the homoexchange mechanism and has a maximum random distribution of oxygen isotopologues at a lower temperature. In Figure 6-6 (d), we can see the various CO_2 signals for 1:1 IIE of LSM. The formation of $C^{16}O^{18}O$ starts at 350°C and has the maximum random distribution above 500°C.

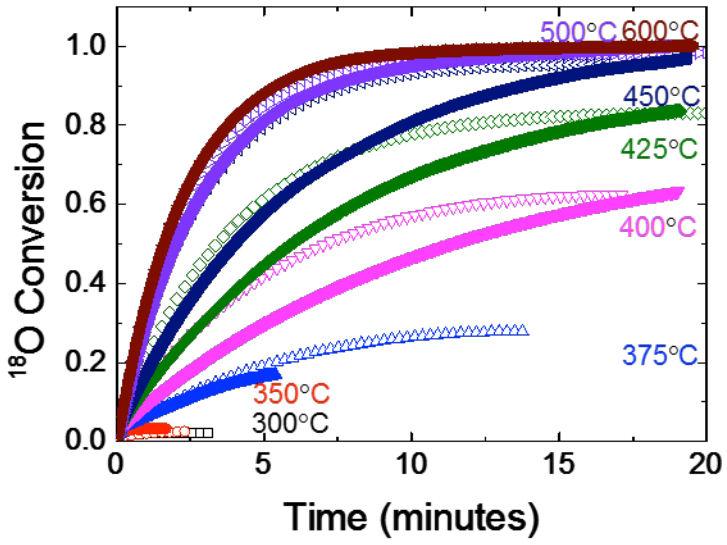

Figure 6-7. The ^{18}O conversion fraction as a function of time in 1:1 IIE of (a) LSCF and (b) LSM at different temperatures under PO_2=0.05 with the presence of 2500ppm $C^{16}O_2$. The open symbol is without the presence of CO_2 and the closed symbol represents the conversion curve with the presence of CO_2.

Figure 6-7 shows the fraction of ^{18}O in the solid as a function of time for IIE of LSCF with the presence of CO_2. The open symbols are for results without the presence of CO_2 while the closed symbols are for results with CO_2. We can see that the final fraction of ^{18}O in the solid phase remains the same for IIE with and without CO_2, but that the fraction increases at a slower, more constant rate. The decrease in the rate of change of the ^{18}O fraction may be explained by the competitive adsorption of CO_2 and O_2 leading to a slower overall exchange, but with transport in the solid remaining the same. On the contrary, we didn't observe any significant impact of CO_2 on the interaction of O_2 with LSM. CO_2 shows a minimal effect on the incorporation of ^{18}O into the solid phase, which can be attributed to a lack of surface vacancies of oxygen super-stoichiometric LSM. The majority of exchange occurring on the LSM

surface is homoexchange between the different gas molecules present, with little to no observable heteroexchange.

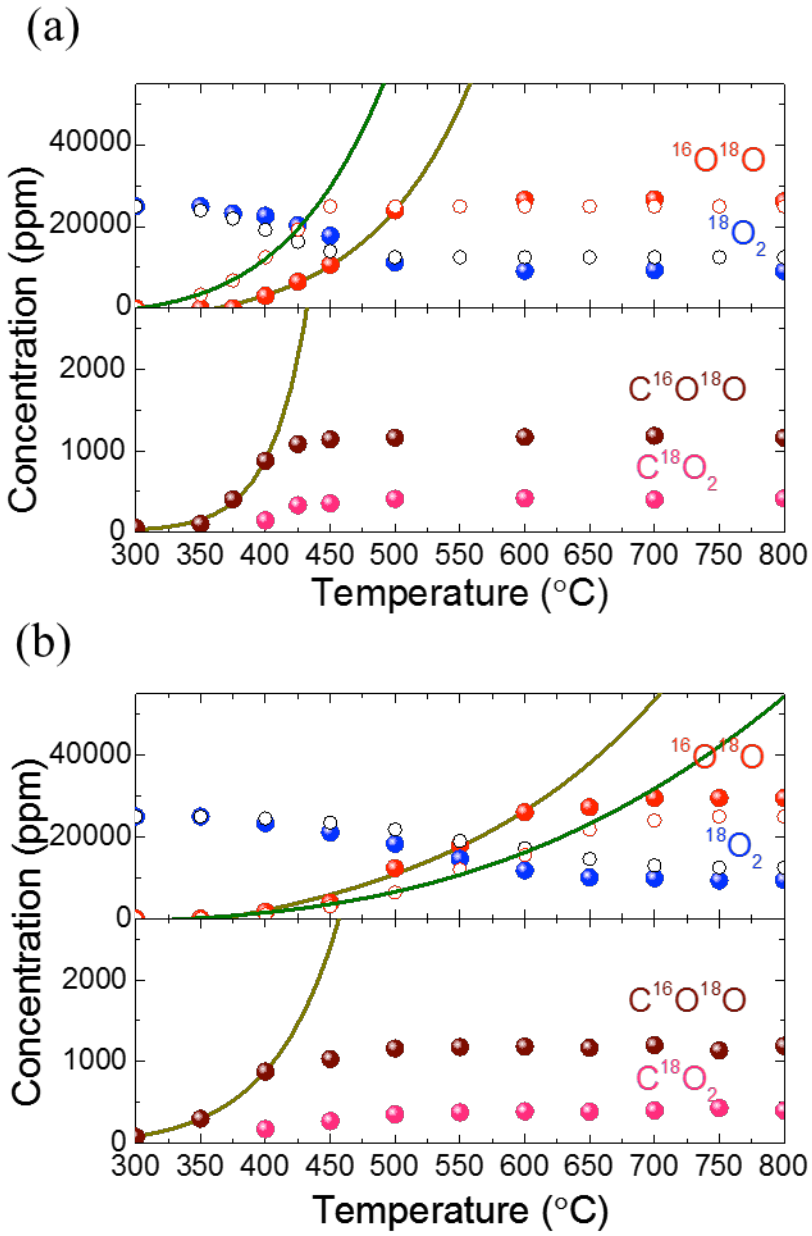

Figure 6-8. Steady state concentrations of $^{18}O_2$ (blue dots), and $^{16,18}O_2$ (red dots) for 1:1 IIE of (a) LSCF, and (b) LSM at different temperatures with the presence of CO_2. Steady state concentrations of $^{16,18}O_2$ increase with increasing temperature, reaching a fully random distribution of 1:2:1 ($^{16}O_2$:$^{16,18}O_2$:$^{18}O_2$) at (a) 500°C for LSCF and (b) 600°C for LSM.

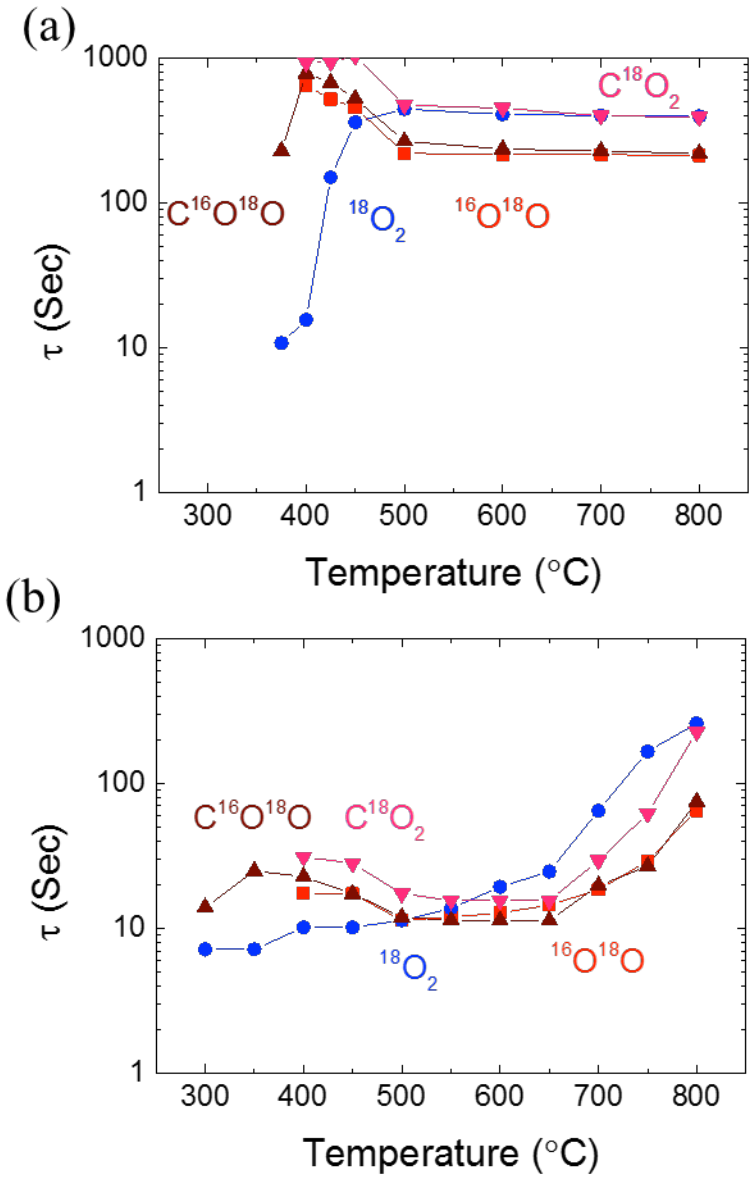

Figure 6-9. The time to reach steady state (τ) of the $^{16}O^{18}O$ and $^{18}O_2$ signals for (a) LSCF and (b) LSM at different temperatures with the presence of CO_2

We also consider the implications of the level of exchange we are seeing and its relationship to the overall catalytic activity and reaction kinetics of the materials. The steady state concentrations of 1:1 IIE of LSCF and LSM with the presence of CO_2 (solid symbols) at different temperatures are summarized in Figure 6-8 and the fitted line is shown in dark yellow. Steady state concentrations of 1:1 of LSCF and

LSM without the contaminants are represented by open symbols. The presence of CO_2 increases the temperature necessary for LSCF to be able to dissociate all inlet $^{18}O_2$. For LSM, the presence of CO_2 decreases the temperature required for the maximum statistical distribution of oxygen isotopologues. This shows a fundamental difference in the way these oxygen-containing molecules interact with the surface of LSM and LSCF. The causes may be related to the catalytic properties of Co, Fe and Mn, or the concentration of oxygen vacancies for the two materials, or, more likely, a combination of both of these factors. From the IIE results, homoexchange between O_2 and CO_2 dominates surface reactions on LSM and the presence of CO_2 seems to accelerate the overall homoexchange process.

Figure 6-9 shows the isotopic transient response of the oxygen isotope signals for LSCF and LSM at different temperatures with the presence of CO_2. The peak temperature for the transient response of the $^{16}O^{18}O$ signal for LSCF, shown in Figure 6-9 (a), remains the same, at around 400°C. The change in τ of $C^{16}O^{18}O$ and C18O2 have a similar shape that of $^{16}O^{18}O$, meaning that the formation of C16O18O and $C^{18}O_2$ are directly correlated to the oxygen dissociation process. For LSM in Figure 6-9 (b), the $C^{16}O^{18}O$ and $C^{18}O_2$ also share a similar shape as $^{16}O^{18}O$. The relaxation time of $^{16}O^{18}O$ decreases between 400°C and 650°C and then increases between 650°C to 800°C. This indicates changes in two different processes that depend on temperature. We believe that the decrease in τ between 400°C and 650°C is related to the increased kinetics for homogeneous exchange, but that between 650°C and 800°C, bulk lattice exchange increases rapidly, increasing the time for isotope signals to reach a steady state. Compared to IIE without the presence of CO_2, shown in

Figure 6-5 the presence of CO_2, for both LSCF and LSM, delays the time τ of $^{16}O^{18}O$ for all temperatures.

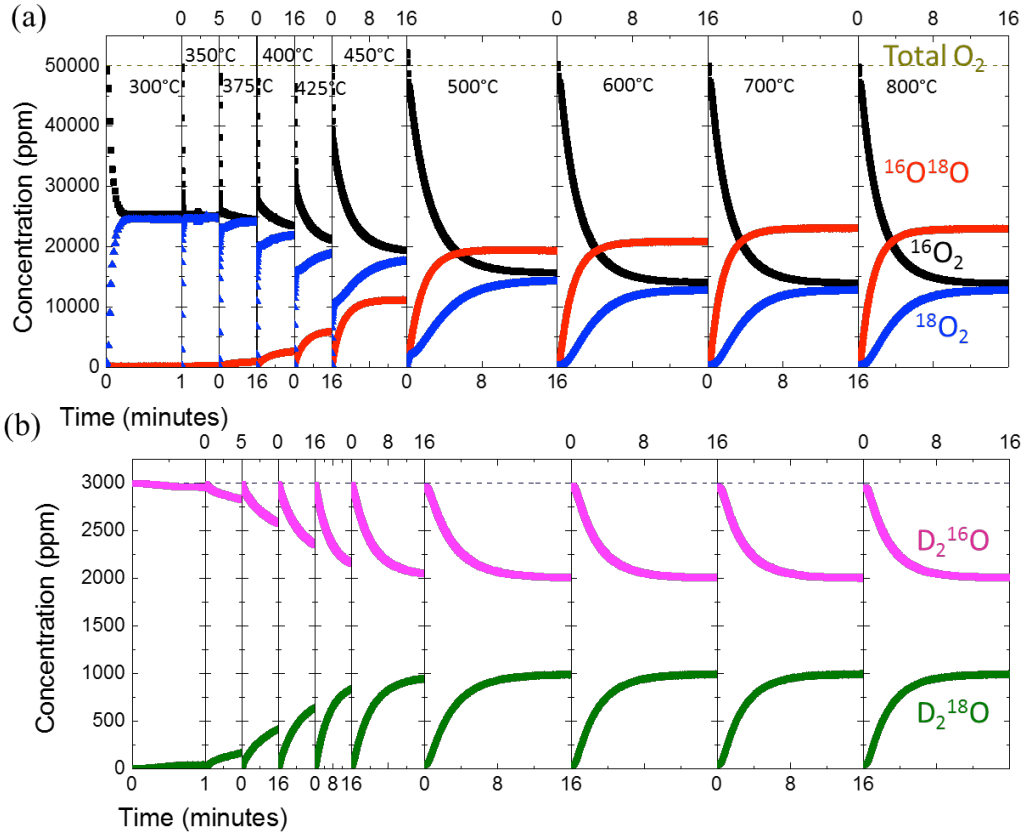

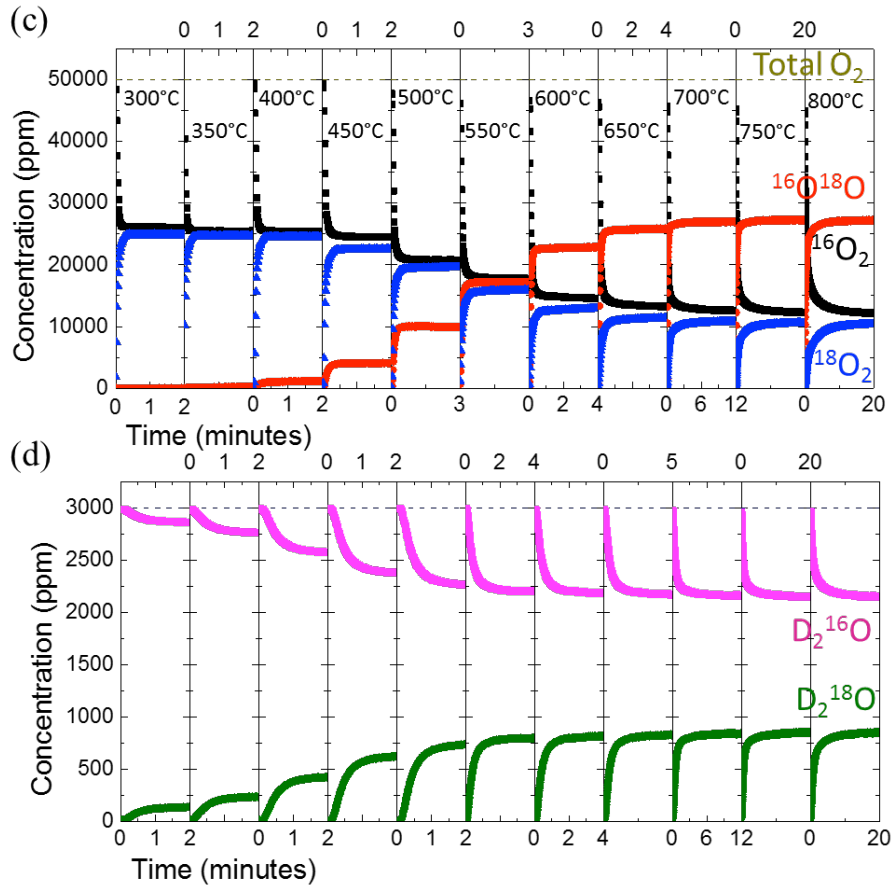

Figure 6-10. 1:1 IIE of LSCF and LSM at different temperatures in PO_2=0.05 with the presence of 3000ppm $D_2{}^{16}O$. (a) O_2,and (b) D_2O signals for LSCF; (c) O_2, and (d) D_2O signals for LSM

Water also shows a different impact on LSCF and LSM. 1:1 IIE of LSCF and LSM with the presence of water at different temperatures is shown in Figure 6-10. The $^{16}O^{18}O$ signal for LSCF, Figure 6-10 (a), shows an increase in temperature required to reach full dissociation of the inlet gas. O_2 starts to dissociate at 350°C (too low to see in the figure) and has a maximum random distribution between 500°C and 600°C. D_2O starts to exchange with ^{18}O at 300°C and has the maximum random distribution near 450°C. The heteroexchange between O_2, D_2O, and the LSCF surface, is still the dominant surface reaction. Figure 6-10 (c) shows the O_2 signal for IIE of LSM with the presence of D_2O at different temperatures. Similar to the

presence of CO_2 on LSM, the maximum random distribution of O_2 is achieved at a lower temperature, around 650°C, with the presence of D_2O. D_2O starts to exchange a small portion with ^{18}O at 350°C (hundreds of ppm) most likely through homoexchange. The maximum $D_2{}^{18}O$ concentrations achieved appear to be constant above 500°C.

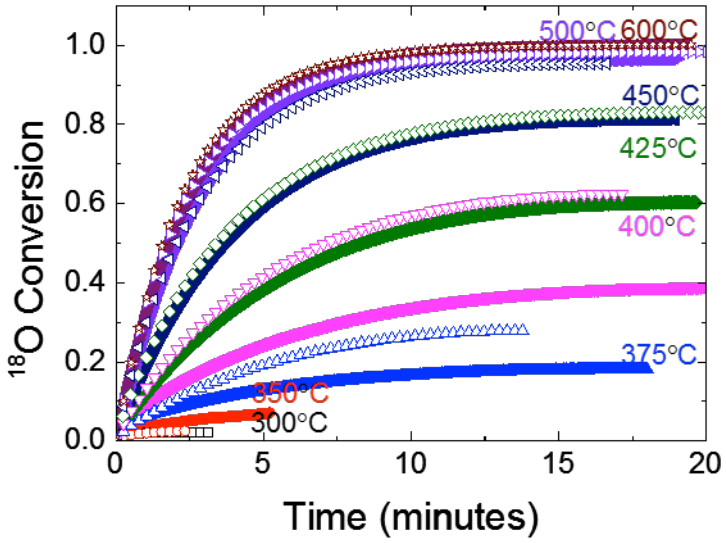

Figure 6-11. The ^{18}O conversion fraction as a function of time in 1:1 IIE of (a) LSCF and (b) LSM at different temperatures under PO_2=0.05 with the presence of 3000ppm $D_2{}^{16}O$. The open symbol is without the presence of D_2O and closed symbol is with the presence of D_2O.

Figure 6-11 shows the ^{18}O conversion fraction in the solid as a function of time for IIE of LSCF with the presence of D_2O. The open symbols are for IIE without the presence of D_2O and the closed symbols are for IIE with D_2O. The presence of D_2O for IIE on LSCF, shows the possibility of blocking of sites active toward heterogeneous exchange of O_2. This is indicated by the decrease in the final fraction of ^{18}O in the solid. This effect reduced as the temperature goes above 500°C. The presence of D_2O does not appear to change the ^{18}O fraction curves. This may be due

to the dominance of homoexchange on LSM, leaving the sites used for heteroexchange available.

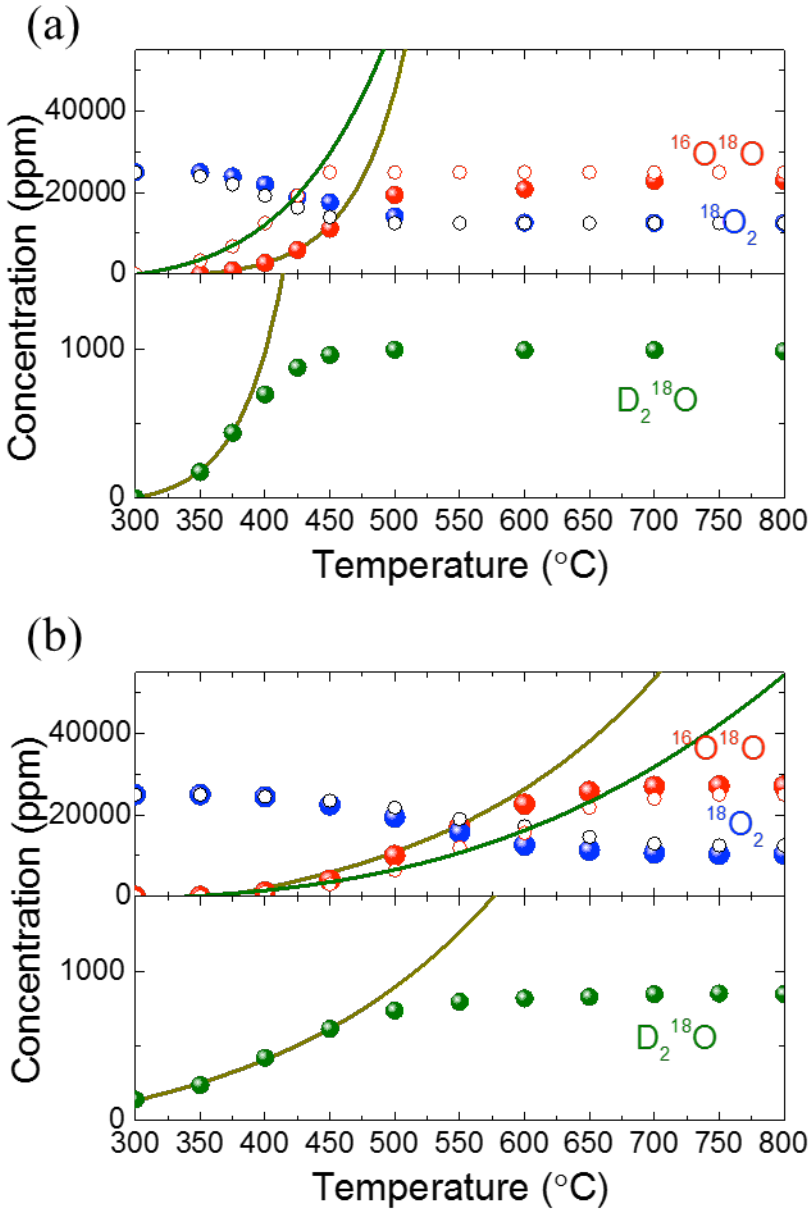

Figure 6-12. Steady state concentrations of $^{18}O_2$ (blue dots), and $^{16,18}O_2$ (red dots) in 1:1 IIE for (a) LSCF, and (b) LSM at different temperatures with the presence of CO_2. Steady state concentrations of $^{16}O^{18}O$ increase with increasing temperature, reaching a fully random distribution at (a) 500°C for LSCF and (b) 600°C for LSM.

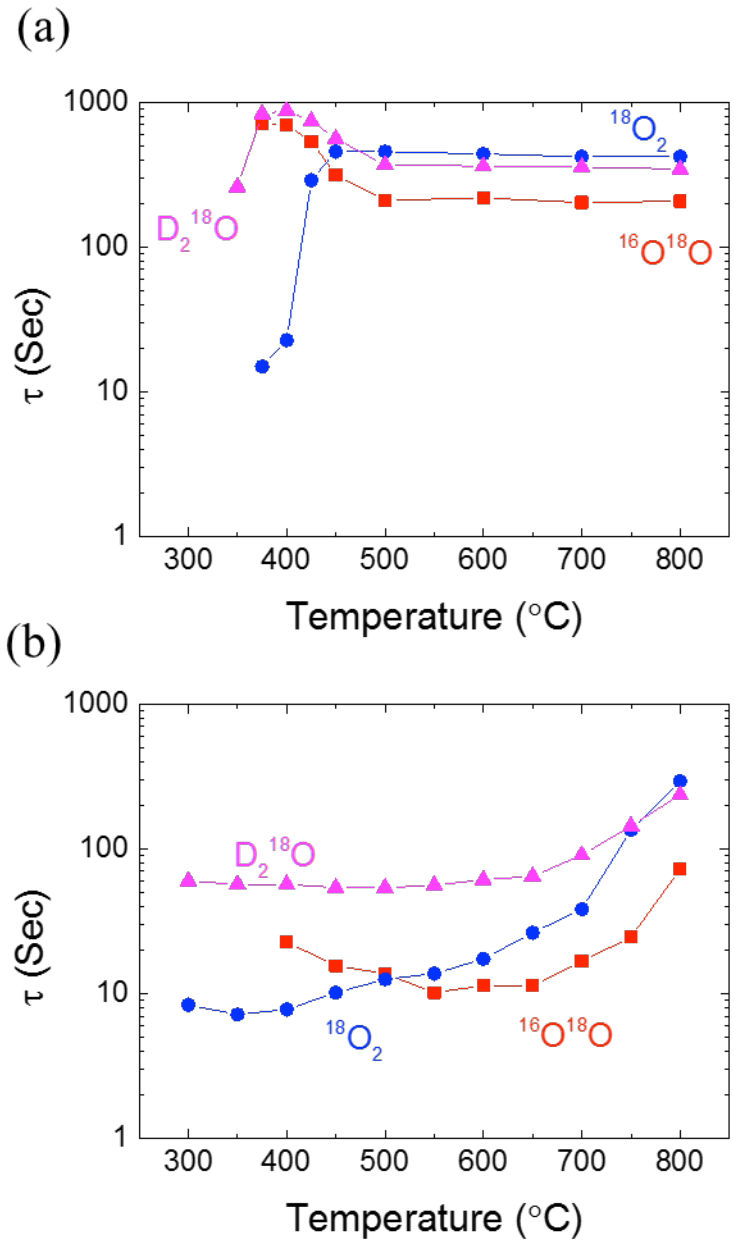

Figure 6-13. Time to steady state (τ) of the $^{16}O^{18}O$ and $^{18}O_2$ signals in 1:1 IIE for (a) LSCF and (b) LSM at different temperatures with the presence of $D_2{}^{16}O$.

The differences in the catalytic and kinetic factors in LSCF and LSM with the presence of water are shown in Figure 6-12 and Figure 6-13. Figure 6-12. (a) shows the effects of D_2O on the catalytic activity of LSCF. The presence of D_2O postpones the oxygen dissociation on LSCF to a higher temperature. Figure 12 (a) shows that

LSCF prefers to exchange with D_2O rather than O_2 at temperatures below 500°C. Figure 6-12 (b) shows the effects of D_2O on LSM, where homoexchange between D_2O and O_2 dominates below 600°C. The effects of D_2O on the kinetics of exchange on LSCF can be inferred from Figure 6-13 (a). The peak position of the time τ of $^{16}O^{18}O$ is still around 400°C. The time τ of $^{16}O^{18}O$ decreases from 400°C to 500°C and maintains the same order of magnitude up to 800°C. The relaxation times of D_2O as a function of temperature has a similar shape to those for $^{16}O^{18}O$, suggesting that the effects of D_2O are mainly on the dissociation process and the availability of surface sites. Figure 6-13(b) shows the effects of D_2O on the kinetics of LSM. The homoexchange rate on LSM increases as the temperature rises from 400°C to 600°C, leading to a decline in the time τ of $^{16}O^{18}O$. The time τ of $^{16}O^{18}O$ rises again at a higher temperature due to the change of exchange mechanism from homoexchange to heteroexchange. The time τ of D_2O is independent of the time τ of $^{16}O^{18}O$ and $^{18}O_2$ at low and intermediate temperature, but at high temperature appears to be related. D_2O may exhibit heteroexchange with LSM at higher temperature. Compared to the relaxation time of LSCF and LSM without contaminants, the presence of D_2O delays both of the τ's of $^{16}O^{18}O$ and $^{18}O_2$.

Impacts of CO_2 and water on the catalytic activity of different cathodes may have different mechanisms. The Arrhenius plot of $\ln[^{16}O^{18}O]$ with respect to reciprocal temperature for LSCF and LSM is shown in Figure 6-14. For LSCF, the formation of $^{16}O^{18}O$ decreases with the presence of CO_2 and water, indicating the contaminants may inhibit the surface catalytic reactions. This effect is a function of temperature and is reduced as the temperature increases. Possible mechanisms for this

effect are physical blocking or the formation of chemical complexes that change surface bonding energies[80]. On the contrary, for LSM, the presence of contaminants shows an increase in the formation of $^{16}O^{18}O$. One possible explanation for this is related to the dominance of the homoexchange process on LSM. Literature[163,166] shows that for some oxide materials, hydrated surfaces may have increased rates of homogeneous exchange due to the formation of surface complexes involving OH^-.

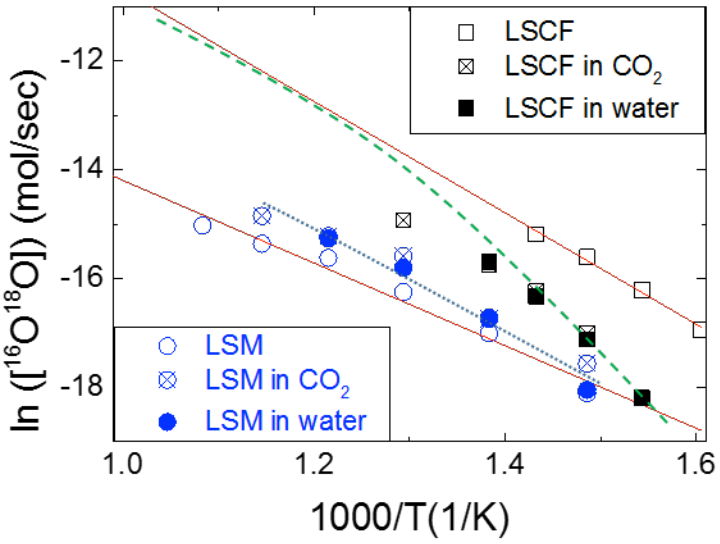

Figure 6-14. Arrhenius plot of the production rate of [$^{16}O^{18}O$] on LSCF (black) and LSM (blue) with the presence of CO_2 and water.

Isotope exchange results suggest that the presence of CO_2 and water affects the surface exchange mechanisms differently for the two materials studied. For LSCF, CO_2 shares the same exchange sites with O_2 and actively participates in the ORR, resulting in a decrease of LSCF's dissociation ability. Regarding the effects of water, results indicate blocking of available surface sites and a decrease in the total accumulated exchange in LSCF. In contrast CO_2 and D_2O show much smaller effects on the oxygen exchange properties of LSM than for LSCF. The homoexchange

process on LSM at lower temperatures limits the interaction of contaminants with the solid phase. Although the effects may be limited to changes in the rate of homoexchange for LSM, under real operating conditions these dissociated oxygen atoms may actively participate in the overall ORR.

6.5 Conclusions

The heterogeneous catalysis of the oxygen dissociation is an important step for the development of the SOFC. Oxygen isotope exchange is a prevailing technique to probe not only the fundamental catalytic properties of materials, but also the interactions of other gaseous species with the solid surface. LSCF and LSM show different mechanisms relating the exchange of oxygen, possibly related to the intrinsic difference in oxygen vacancy concentrations for the two materials. The dissociation of oxygen on the LSCF surface begins at 350°C. The bulk diffusion of oxygen in LSCF increases as a function of temperature, to the point where all lattice oxygen in LSCF participates in the exchange process, above 500°C. Heteroexchange dominates for LSCF over the entire temperature range tested. The dissociation of oxygen on the LSM surface begins at 400°C and increases much more slowly than for LSCF. A higher temperature is required for LSM to dissociate all of the O_2 entering the reactor. Homoexchange dominates for LSM in the low to intermediate temperature range, and LSM begins to show heteroexchange above 650°C.

The presence of contaminants shows limited impacts on LSCF and LSM at high temperature. The presence of CO_2 and water indicates blocking effects on the LSCF surface from 300°C to 600°C possibly resulting in two separate degradation

mechanisms. On the other hand, CO_2 and water can exchange with LSM through homoexchange mechanism. Therefore the presence of CO_2 and water has a minor immediate impact on the kinetics of the ORR on LSM. CO_2 and water effects on LSCF and LSM are more apparent below 600°C. As the temperature of SOFCs is further decreased, the impact of water and CO_2 on ORR kinetics may become more important. 1:1 IIE allows us to better distinguish between homoexchange and heteroexchange of oxygen molecules, as well as water and CO_2. The combination of 1:1 IIE with similar isotope exchange experiments can provide a well-defined picture of the oxygen reduction reaction. The aims of this study are to increase knowledge and information about the ORR for the development of new high performance SOFC cathodes materials.

Chapter 7: Statistical Analysis of Electrical Conductivity Relaxation Using Numerical Calculation

7.1 Introduction to the Analysis of Electrical Conductivity Relaxation

Electrical conductivity relaxation (ECR)[54-57,88,131,167-169] is a non-destructive technique to determine the kinetic parameters of a material and is widely applied for the characterization of the SOFC cathodes. It describes the oxygen transport behavior of the oxygen reduction reaction (ORR) under a given electrochemical potential.

In ECR, a solid sample with well-defined dimensions is subjected to a rapid change of PO_2, leading to a change in the electrochemical potential of the system. To equilibrate the system, the electrochemical potential drives oxygen into or out of the sample and the kinetic response for recovering from the disturbed system can be observed. This transient response can be measurement to obtain the relaxation curves. These relaxation plots can then be fitted with diffusion equations to extract kinetic parameters. Though the mathematical approach to describe the diffusion process has been well studied, the accuracy of kinetic parameters extracted from experimental data has been questioned because of the complexity of the diffusion equations[61,167,170-172]. Here we develop an analytic solution with increased fitting accuracy. Based on a numerical calculation with MATLAB codes developed in-house, the kinetic parameters can be statistically extracted from experimental data. In this study, different numbers of roots, up to 100 terms, are used to determine the effects of the numbers of roots on the fitting accuracy. This work delivers a robust strategy for

extracting the parameters out of non-linear equations with dependent variables. Improved fitting accuracy can help to obtain actual material properties, as well as be applied to distinguish the slight change of material properties due to surface modification or degradation.

7.2 Electrical Conductivity Relaxation Theory

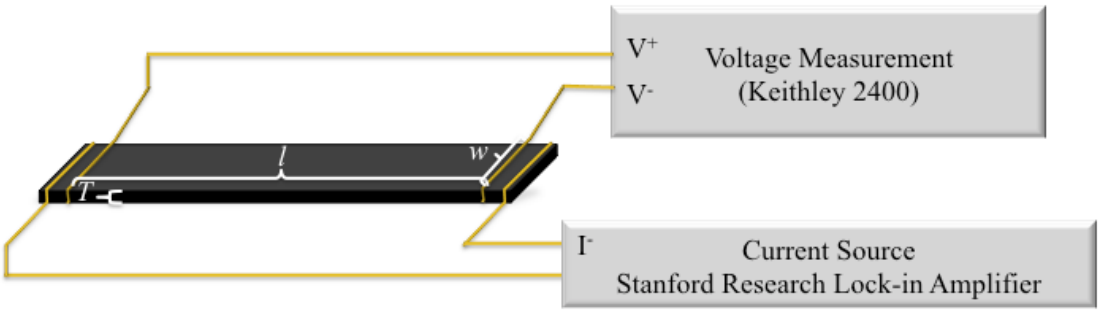

Figure 7-1. The experimental configuration for ECR and the geometry of the sample for mathematical calculation. A constant current is applied through the sample and the voltage drop across the sample is measured to determine the conductivity.

We can derive the general solution for ECR in a dense solid bar [55,61]. Figure 7-1 shows the configurations of the experimental set up for ECR and the corresponding geometry of the specimen for mathematical calculation. Consider a bar sample with dimensions of l, w, and T in the x, y, and z directions, respectively. If the lengths in l and w are much longer than the thickness (T), the surface area along the x-y plane (l x w) is much larger than x-z plane (l x T) and y-z plane (w x T). Then, the oxygen flux leaving from or coming into the surface along y and z directions is negligible. Therefore, we can simplify the problem to one-dimensional transport. The oxygen concentration in the solid can be calculated using Fick's second law:

$$\frac{\partial C}{\partial t} = D_{chem} \frac{\partial^2 C}{\partial x^2} \qquad [7\text{-}1]$$

where D_{chem} (cm^2/s) is the diffusion coefficient and C(x,t) ($\#/cm^3$) is the volumetric oxygen concentration as a function of time and distance. The oxygen flux flowing in or out of the sample equals the oxygen diffusion flux in the solid, the boundary condition at the gas-solid interface can be expressed as.

$$k_{chem}(C(\infty)-C(t)) = -D_{chem}\left.\frac{\partial C(t)}{\partial x}\right|_{x=\pm T/2} \qquad [7\text{-}2]$$

C(t) and C(∞) are oxygen concentrations at time *t* and at equilibrium, respectively. k_{chem} is the chemical surface exchange coefficient. The diffusion equation can be solved using the Laplace domain, as shown in Equation [7-3].

$$s\overline{C(z,s)} = D_{chem}\frac{\partial^2\overline{C(z,s)}}{\partial x^2} \qquad [7\text{-}3]$$

The general solution can be written as:

$$\overline{C(x,s)} = A\exp(\sqrt{\frac{s}{D_{chem}}}x) + B\exp(-\sqrt{\frac{s}{D_{chem}}}x) \qquad [7\text{-}4]$$

Substituting Equation [7-4] into the boundary condition in Equation [7-2], we can derive the general solution for diffusion in a planar sheet with a surface exchange reaction.

$$\frac{C(x,t)-C(0)}{C(\infty)-C(0)} = 1-\left[\sum_{n=1}^{\infty}\frac{2L\cos(\beta_n\,{}^{2x}\!/_{T})\exp\left(-\frac{\beta_n^2 D_{chem}t}{(T/2)^2}\right)}{\left(\beta_n^2+L^2+L\right)\cos\beta_n}\right] \qquad [7\text{-}5]$$

$$L = \frac{T}{2}\frac{k_{chem}}{D_{chem}} \qquad [7\text{-}6]$$

The β_n's are the roots of

$$\beta_n \tan \beta_n = L \qquad [7\text{-}7]$$

Here x denotes the distance from the solid surface in the z direction (thickness). C(t), C(∞), and C(0) are the concentration of oxygen in lattice at time t, at equilibrium, and initially. By integrating the oxygen concentration as a function of distance in the solid, the total oxygen concentration as a function of time can be shown as.

$$\frac{M(t)}{M_\infty} = \frac{\int_{-T/2}^{T/2} c(x,t)\,dx}{T(C(\infty) - C(0))} \qquad [7\text{-}8]$$

M(t) is the accumulated amount of oxygen leaving from or going into the solid sample at time t and M(∞) is the oxygen concentration of the solid at equilibrium. The change in conductivity of the sample is proportional to the change in the vacancy concentration in the solid. Therefore, the change in conductivity can be expressed as the change in the oxygen concentration.

$$\frac{\sigma(t) - \sigma(0)}{\sigma(\infty) - \sigma(0)} = \frac{M(t)}{M_\infty} = 1 - \left[\sum_{n=1}^{\infty} \frac{2L^2 \exp(-\frac{\beta_n{}^2 D_{chem} t}{(T/2)^2})}{\beta_n(\beta_n{}^2 + L^2 + L)} \right] \qquad [7\text{-}9]$$

This equation describes the relationship between the conductivity and the oxygen nonstoichiometry of the sample. By fitting the conductivity curve with Equation [7-9], kinetic parameters k_{chem} and D_{chem} can be extracted.

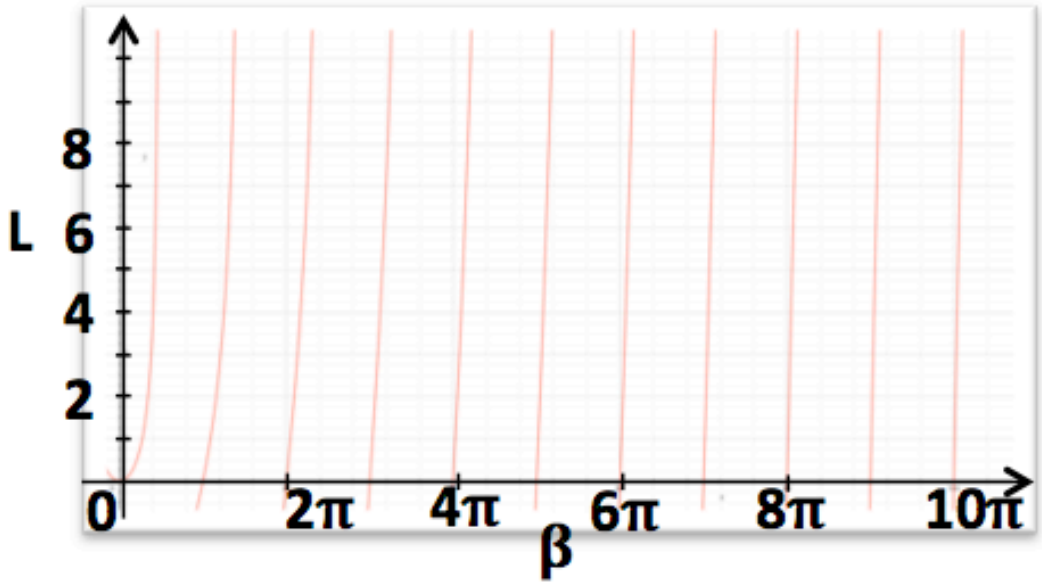

Roots of $\beta \tan \beta = L$

L	β_1	β_2	β_3	β_4	β_5	β_6
0	0	3·1416	6·2832	9·4248	12·5664	15·7080
0·01	0·0998	3·1448	6·2848	9·4258	12·5672	15·7086
0·1	0·3111	3·1731	6·2991	9·4354	12·5743	15·7143
0·2	0·4328	3·2039	6·3148	9·4459	12·5823	15·7207
0·5	0·6533	3·2923	6·3616	9·4775	12·6060	15·7397
1·0	0·8603	3·4256	6·4373	9·5293	12·6453	15·7713
2·0	1·0769	3·6436	6·5783	9·6296	12·7223	15·8336
5·0	1·3138	4·0336	6·9096	9·8928	12·9352	16·0107
10·0	1·4289	4·3058	7·2281	10·2003	13·2142	16·2594
100·0	1·5552	4·6658	7·7764	10·8871	13·9981	17·1093
∞	1·5708	4·7124	7·8540	10·9956	14·1372	17·2788

Figure 7-2. (a) β–L plot for the equation βtanβ=L and (b) Values of the first 6 roots of equation [7-6] for different regions of L values[61].

7.3 Simplification of Solutions to Different Rate Limiting Steps

Although Equation [7-9] conveys the relationship between kinetic parameters and the corresponding time-dependent conductivity curves, the fitting process of the diffusion equation with experimental data to extract kinetic parameters is a challenge due to the dependent variables β_n, L, and D_{chem}. Figure 7-2 shows values of the first 6 roots of solutions for Equation [7-7][61]. k_{chem} and D_{chem} determine the value of L. Once

L is fixed, β_n's can be determined. The change of each fitting parameter would lead to a non-linear change in other parameters. In addition, values for the extracted parameters might change by using different numbers of roots in Equation [7-7]. Moreover, the first initial guess for the normal fitting process is critical and the regression analysis may easily fall into a local minimum, rather than absolute minimum, of RMSE. These effects make the accurate determination of kinetic parameters difficult. Therefore, to increase the efficiency of fitting without sacrificing accuracy, we can simplify the equation to different forms based on the actual experimental conditions.

There are two different control regimes: surface exchange and diffusion control. We can assume that the total reaction is limited by either one of them. Then, the other transport is assumed to be very fast and always remains in quasi-equilibrium:

7.3.1 Surface Exchange Control Regime:

In the surface exchange controlled region, the diffusion process in a solid is considered to be fast and to not limit the reaction. At this particular condition, as a result of L<<1, β_1 dominates in Equation [7-9] and the contributions from the other roots can be ignored. Then, a series expansion can be used to approximate Equation [7-7] in the surface control regime.

$$\beta_1^2 = L \qquad [7\text{-}10]$$

Substituting Equation [7-10] into Equation [7-9], the normalized ^{18}O accumulation curve $M(t)/M(\infty)$ can be simplified as a first order reaction:

$$\frac{M(t)}{M_\infty} = 1 - \exp(-\frac{4k_{chem}t}{T}) \qquad [7\text{-}11]$$

In the surface exchange control regime, M(t)/M(∞) is only a function of the geometry factor (T) and surface exchange coefficient (k_{chem}).

7.3.2 Diffusion Control Regime

In the diffusion control regime, where L is much larger than 1, the diffusion in solid becomes a rate limiting step, and the process of oxygen surface exchange is fast enough that it can be seen as a constant oxygen flux source. In this case, the contribution of each β_n in Equation [7-9] cannot be ignored. As L approaches infinity, the roots of equation [7-6] are $\beta_n=(m+1/2)\pi$ and the equation [7-9] takes the form:

$$\frac{\sigma(t)-\sigma(0)}{\sigma(\infty)-\sigma(0)} = \frac{M(t)}{M_\infty} = 1 - \left[\sum_{m=0}^{\infty} \frac{8}{(2m+1)^2\pi^2} \exp\left(-\frac{(2m+1)^2\pi^2 D_{chem}t}{T^2}\right)\right] \qquad [7\text{-}12]$$

When diffusion is the rate-limiting step, the diffusion equation can be simplified to a sum of multiple exponential terms. The diffusion process can be seen as a series of pseudo first order reactions with different time constants (τ_m), which equal to $T^2/((2m+1)^2\pi^2 D_{chem})$ and are only a function of the geometric factor, T, and D_{chem}:

$$\frac{\sigma(t)-\sigma(0)}{\sigma(\infty)-\sigma(0)} = \frac{M(t)}{M_\infty} = 1 - \left[\sum_{m=0}^{\infty} \frac{8}{(2m+1)^2\pi^2} \exp\left(\frac{-t}{\tau_m}\right)\right] \qquad [7\text{-}13]$$

7.3.3 Numerical Calculation

In ECR, the parameter L can be altered by changing the sample thickness (T) or by changing temperature and/or PO_2 to manipulate D_{chem} and k_{chem}. If L falls into the region where D_{chem} and k_{chem} co-dominate the reaction, the assumptions for the

simplified equations in Equation [7-11] and [7-12] no longer hold and the general solution in Equation [7-9] needs to be taken into considered. To improve the accuracy in the determination of kinetic parameters in ECR, sensitivity analysis is needed[170]. Here we develop a mathematical solution to extract kinetic parameters based on a numerical calculation. The basic idea is simple. Ideal diffusion curves based on Equation [7-9] are generated and fitted with experimental data to get the best-fit curve with a minimum value of root mean square error (RMSE). This sensitivity analysis requires computing roots and a number of loops are needed to calculate each RMSE value. An in-house developed MATLAB code is used to do the computations and is listed in Appendix B. ECR Fitting Script.

The first step is to select the possible region of values for D and k. We can build a matrix with n rows of D and m columns of k values. Then, a D-k plane with n x m combination of D and k can be created, as shown in Figure 7-3 (a). Figure 7-3 (b) shows the relationship between $L[D_n,k_m]$ and the ratio of k_m/D_n. The corresponding $L[D_n,k_m]$ falls in the surface exchange controlled region if the value of k_m/D_n is close to zero. When the value of k_m/D_n changes, $L[D_n,k_m]$ values can vary, leading to the different dominant reaction regions. Based on the numerical calculation, roots for the solutions in Equation [7-7] can be approximated by finding the zeros of the tangent function near every period, π. A data matrix can be generated and each data point in the k-D plane, creating a mesh, as shown in Figure 7-3 (b). This mesh carries the information of the corresponding parameters, $L[D_n, k_m]$ and β_n's$[D_n, k_m]$. Consequently, we can generate ideal relaxation curves $M(t,D_n, k_m)$ according to the

corresponding parameters, followed by non-linear least square fitting of the experimental data to identify the best fit of parameters.

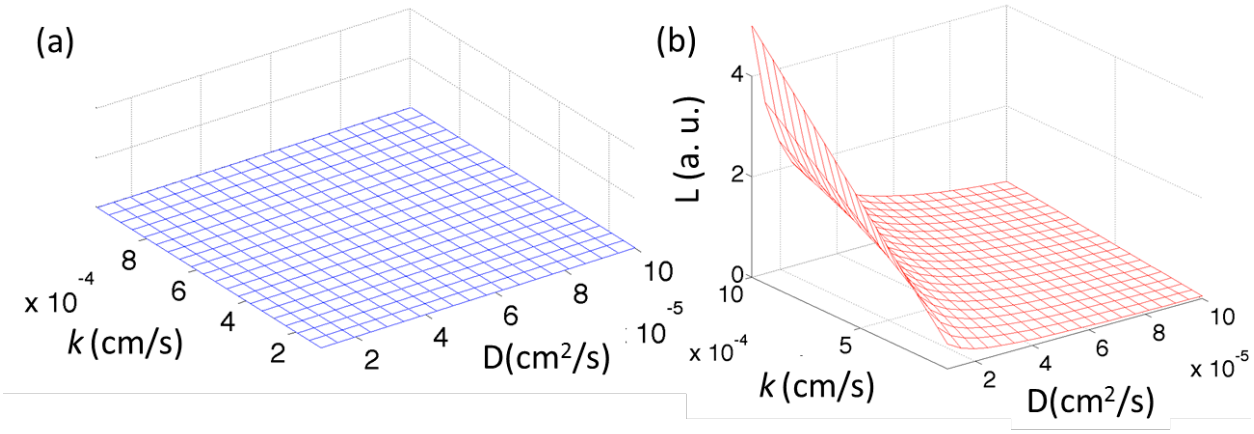

Figure 7-3. (a) D-*k* plane and (b) the generated L values based on the given *k* and D values in (a) with a fixed sample thickness (0.2cm).

To verify the accuracy of the fitting parameters, the RMSE is used to quantitatively evaluate the goodness of fit. RMSE is defined as the residual sum of squares divided by the number of degrees of freedom:

$$RMSE = \frac{1}{n}\sum_{i=1}^{\infty} w_i \left(\hat{Y}_i - Y_i\right)^2 \qquad [7\text{-}14]$$

where $\hat{Y}_i$ is the calculated value, Y_i is the experimental value, and n is the numbers of data points. To avoid misfitting due bad data points, a weighting factor (w_i) is applied in the regression analysis. Identification of the absolute minimum point of RMSE can lead us to the best-fit *k* and D values.

7.4 Experimental

A dense LSCF bar sample is placed in a quartz reactor, as shown in Figure 7-4. The oxygen partial pressure is controlled by balancing the O_2 and N_2 concentrations using mass flow controllers. The total flow rate of the O_2/N_2 mixture

gas is fixed at 300 SCCM. To minimize disturbance of the equilibrium state of the system and to increase the accuracy of extracted k values at a given temperature and oxygen partial pressure, the change in PO_2 for each ECR measurement is less than ΔPO_2=0.02.

The change in PO_2 will change the electrochemical potential across the sample and change the steady state of the system. To determine the impacts of the step size of ΔPO_2, ECR is performed under ΔPO_2 ~ 0.02 or 0.1. Also, to determine the effects of the flush time, two different sizes of reactors are used to provide different magnitudes of dead volume. The reactors are designed to have a dead volume close to 5 mL and 350mL, measured by Archimedes method. The residence time (τ_f) can be calculated according to the equation [59]:

$$\tau_f = \frac{V_r}{R_V}\frac{T_{RT}}{T_r} \qquad [7\text{-}15]$$

Where R_V is the flow rate of gas, V_r and T_r are the volume and temperature of the reactor, and T_{RT} is room temperature. For two different reactors, the flush times are estimated to be ~ 0.3 seconds and 19 seconds at 800°C. An oxygen sensor is connected to the outlet of the reactor to monitor the change in oxygen partial pressure as a function of time. DC four-probe measurements are used to measure the re-equilibration process of the sample after a step-wise PO_2 change. The configuration of the conductivity measurement is shown in Figure 7-1. A lock-in amplifier SR830 is used to provide a constant current across the sample. To avoid disturbing the electrochemical equilibrium of the system, the applied current is limited to micro-amps. The voltage drop in the sample is measured using a Keithley 2000, and the conductivity is determined through Ohm's law. The mass flow controllers, the lock-in

amplifier, the oxygen sensor, and the temperature of the furnace are automated through LabVIEW (National Instruments), and the block diagram is shown in Appendix C. LabVIEW block diagram for ECR. To obtain two different sets of experimental data with different L values, ECR is performed on LSCF with two different thicknesses, 0.1 cm and 0.2 cm, at PO_2's near 0.025 and 1.000 at 800°C.

Figure 7-4. Experimental set up for the DC four-probe measurement. A bar sample is placed in a quartz reactor with 4 gold wires connected to the sample: the two wires nearest the ends apply current while the two inner wires measure the voltage response. Notice that the dead volume of this reactor is less than 5mL

Figure 7-5 shows the fitting results of ECR for the 0.1 cm thick LSCF sample at 800°C under a change of PO_2 from 0.19 to 0.21. A 3D plot and contour plot of the error mapping of RMSE on the D-k plane are presented in Figure 7-5 (a) and (b), resepectively. From the error mapping in the k_{chem} and D_{chem} plane, we can see an increase in the fitting accuracy when changing the estimated k_{chem} and D_{chem} values. The global minimum of RMSE illustrates the best fits for k_{chem} and D_{chem} values. The

best fitting results can be identified to have values of k_{chem}=4.4x10^{-4} (cm/s) and D_{chem}=3x10^{-5} (cm^2/s). The fitting results show insensitivity to changes in D_{chem} because this reaction falls into the surface exchange dominant region. The best-fit curve (red line) is compared to the ECR data in Figure 7-5 (c).

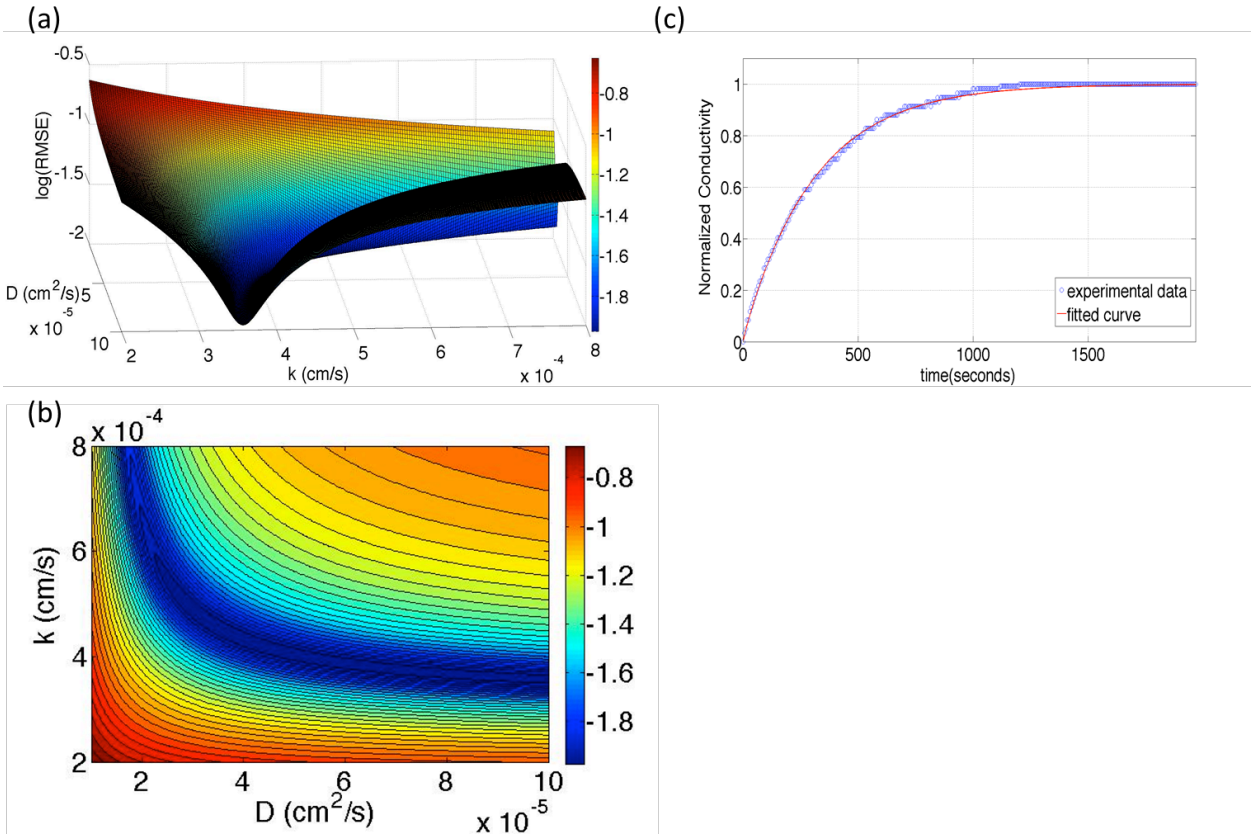

Figure 7-5. A 3D plot with color mapping of the RMSE for ECR of LSCF, and (b) the corresponding contour plot. The color scale is the log(RMSE) of the fitting parameters k_{chem} and D_{chem}, showing a global minimum where the best fitting results occur (blue). (c) Experimental data (○) and the best fitted curve (red line) for ECR of LSCF with 0.1 cm in thickness. The sample was measured at 800°C with a change of PO_2 from 0.21 to 0.19 atm.

The fitting results of ECR for thick LSCF sample (0.2cm) are shown in Figure 7-6. As the sample thickness increases, L becomes large. The error mapping plot in Figure 7-6 (a) shows more sensitivity toward changes in D_{chem}. This is due to the thickness of the sample, which increases L value. The best-fit curve is shown in

Figure 7-6 (b) with the same k_{chem}=4.4x10^{-4} (cm/s) but an increased D_{chem}=3.6x10^{-5} (cm^2/s) by just varying the thickness of the testing sample.

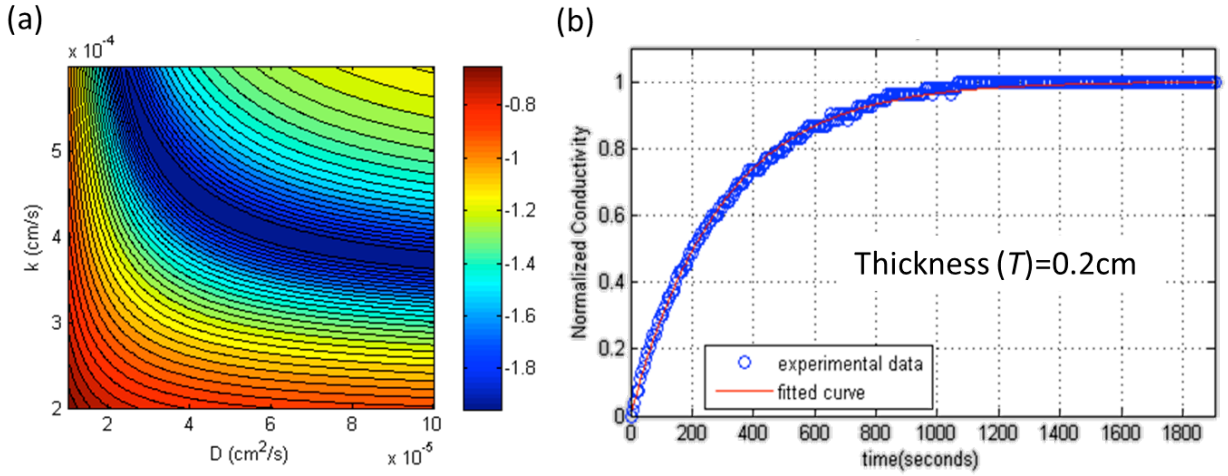

Figure 7-6. Contour plot of the RMSE for ECR of LSCF. The color scale is log(RMSE) of the fitting parameters k_{chem} and D_{chem}, showing a global minimum where the best-fit result occurs (blue). (b) The corresponding ECR curve of LSCF at 800°C with a sample thickness of 0.2 cm. The sample was measured at 800°C with a change of PO_2 from 0.21 to 0.19 atm.

The impact of the number of roots that are used for the fitting is shown in Figure 7-7 for changes in PO_2 of (a) 0.17 to 0.19, and (b) 0.19 to 0.21. Both of the changes in PO_2 show similar trends. From Figure 7 we can see that the k value is underestimated and D value is overestimated if the diffusion equation only uses β_1. Using only β_1 causes a 6% deviation for k and a 7 deviation for D, as compared to first 100 β terms (fitting parameters are listed in Appendix D. ECR fitting parameters for LSCF at 800ºC under PO_2=0.19-0.21). The deviation decreases to less than 1% if we consider only the first 10 β terms. Therefore, it is important to consider the contribution of the numbers of β terms used to fit the data.

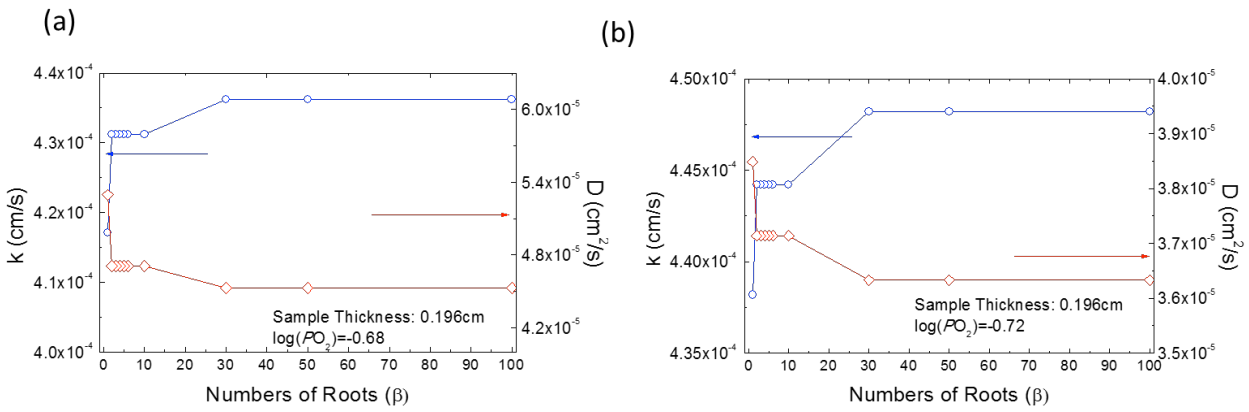

Figure 7-7. The change in kchem values by using different numbers of roots in the diffusion Equation [7-9] for LSCF at 800°C with a PO_2 change from (a) 0.17 to 0.19 and (b) 0.19 to 0.21.

The log-log plots of log(PO_2) versus log(k_{chem}) and log(D_{chem}) are shown in Figure 7-8 (a) (b), respectively. This work is consistent with literature values. D_{chem} shows insensitivity to changes in PO_2, and k_{chem} shows a PO_2 dependence of 0.7. The slope of the PO_2 dependence can be used to determine which oxygen species contribute to the rate-limiting step. The results suggest that it's a mixture of two types of oxygen intermediate species and is consistent with the results of Cheuh et al.

The effects of a larger change in PO_2 and the flush time on ECR measurements are studied using different reactor dead volumes. Figure 7-9 shows the log-log plot of log(PO_2) versus log(k_{chem}) with a flush time of 19 seconds and with a larger change in PO_2 ($\Delta PO_2 \sim 0.1$). In comparison to the ECR results with a flush time of 0.3 seconds and a $\Delta PO_2 = 0.1$ in Figure 7-9, the PO_2 dependence changes from 0.7 to 0.43. There are a few possible reasons for the deviation of the PO_2 dependence. First, it could be attributed to the impact of the higher electrochemical potential due to the larger ΔPO_2 driving the movement of oxygen. Or it could be an effect of flush time, causing a slower change in PO_2, becoming more pronounced in the low PO_2

region. Regardless, the results suggest that the experimental set-up can easily alter measurement results. Proper design and calibration of the system is therefore necessary to obtain the accurate results.

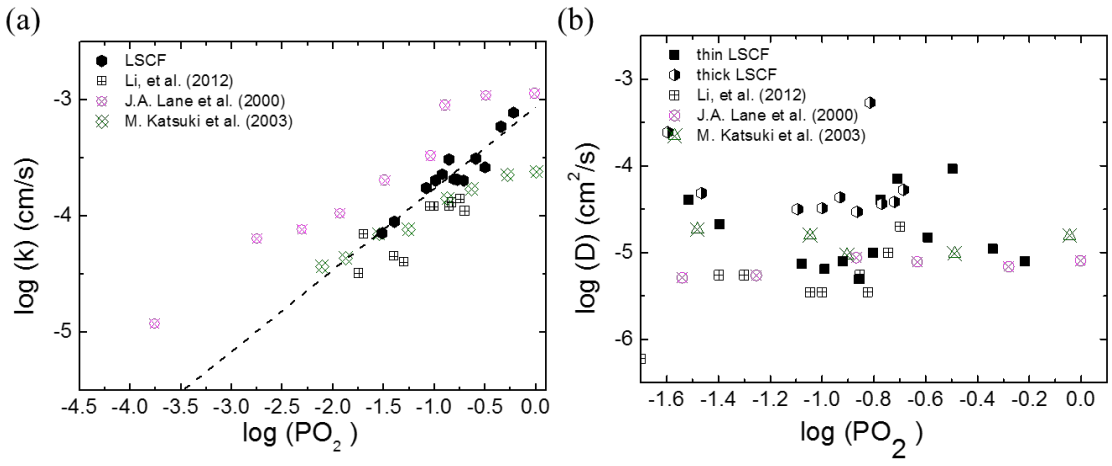

Figure 7-8. Plots of log (PO_2) versus (a) log (k_{chem}) and (b) log (D_{chem}) for LSCF sample, with a comparison to literature values [57,94,173].

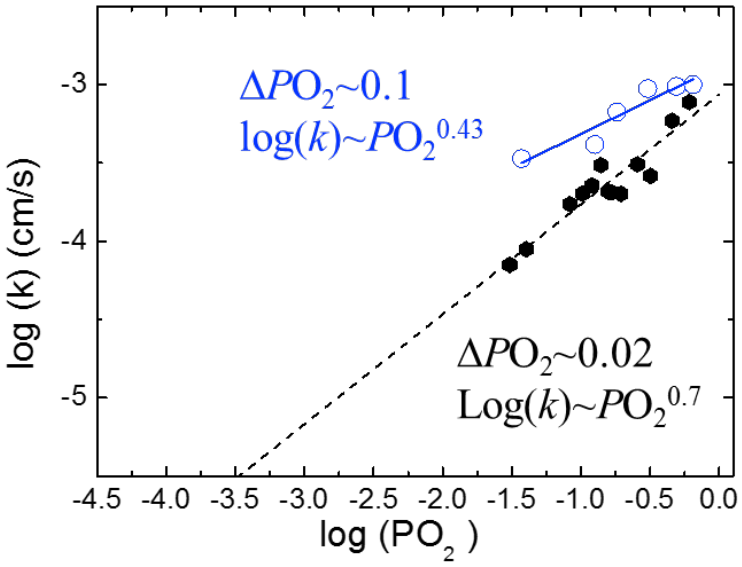

Figure 7-9. Plots of log (PO_2) versus log (k_{chem}) for LSCF samples measured in reactors with different dead volumes (5mL and 350mL) and different ΔPO_2 (0.02 and 0.1).

7.5 Conclusions

ECR is a useful technique to obtain kinetic parameters of conductive oxide materials. By controlling the sample thickness, the relaxation curves can become more dependent on either surface exchange or bulk diffusion. In the extreme cases, where either surface exchange or diffusion is the rate-limiting step, the diffusion equation can be simplified to a first order chemical reaction or a sum of a series of pseudo-first order reactions, respectively. When the two processes are co-limiting, it is essential to use the non-simplified diffusion equation to correctly obtain the fitting parameters.

A numerical method is used to evaluate the roots of the solution, and non-linear regression analysis is used to stochastically compute the best-fit parameters k_{chem} and D_{chem}. The error-map of RMSE shows a change in sensitivity from k_{chem} to D_{chem} by changing the sample thickness. Up to 100 β terms are used to extract accurate k_{chem} and D_{chem} values. The number of roots used to fit the data is important and may change accuracy of the results.

In addition the impact of flush time and the larger change in PO_2 on ECR has also been investigated, and may have an effect on the PO_2 dependence of k_{chem}. Because ECR is a highly sensitive measurement technique, improper experimental set up may lead to extraction of inaccurate kinetic parameters. To improve accuracy of the results, proper design of the experimental set-up is important. This study provides a robust strategy to extract kinetic parameters from ECR, and has been implemented to acquire accurate k_{chem} values for surface modified LSCF samples at different temperatures and oxygen partial pressures, presented in Chapter 8:.

Chapter 8: Enhancement of $La_{0.6}Sr_{0.4}Co_{0.2}Fe_{0.8}O_{3-\delta}$ Surface Exchange through Ion Implantation

8.1 Introduction

Solid oxide fuel cells (SOFCs) are one of the most promising technologies for the future of clean energy, due mostly to their high efficiency in the conversion of chemical energy directly to electricity, as well as their fuel flexibility[1,3,7,174]. Reducing operating temperatures for SOFCs, from high temperature (800-1000°C) to intermediate temperature (<700°C), is essential to decrease the system cost for commercialization. Some of the major obstacles for decreasing operating temperature are the ionic transport and catalytic properties of SOFC cathodes. This is a direct impact of the high activation energy for the oxygen reduction reaction (ORR) [9]. Mixed ionic-electronic conductors (MIEC) cathode materials, such as $La_{0.6}Sr_{0.4}Co_{0.2}Fe0.8O_{3-\delta}$ (LSCF), are attractive because an MIEC allows the ORR to occur at active sites on the entire surface of cathode material, instead of being limited only to the triple phase boundary region[14,15,18,175]. However, for LSCF, the oxygen transport is limited by its surface activity and its long-term stability at high temperature [22,46,73,99,128]. Therefore, to improve the performance of LSCF we may look for a way to modify the surface region to improve the surface activity and enhance the stability. There have been a variety of approaches and efforts made to modify the surface of LSCF to improve performance and durability[176-181]. $La_{0.8}Sr_{0.2}MnO_3$ (LSM), $Ce_{0.8}Sm_{0.2}O_{1.9}$ (SDC), and $La_{0.6}Sr_{0.4}CoO_{3-\delta}$(LSC) nanoparticles infiltrated on LSCF have been demonstrated to improve the LSCF

cathode performance. The enhancement of cathode performance may be due to the increase of available surface sites or surface vacancies, the improvement of catalytic ability toward dissociation, or the prevention of surface phase-segregation. It has been shown previously that LSCF has fast bulk kinetics, but is limited by dissociation of oxygen on the surface, and that LSM shows good oxygen dissociation, but is limited by incorporation [73,75]. In addition, it has been reported that the Mn occupied B sites on the ABO_3 perovskite surface have high activity for the catalytic dissociation of oxygen [75,180,182,183].

In this study we investigated a surface modified cathode based on an LSCF bulk material, for fast oxygen ion diffusion into the lattice, with LSM on the surface to enhance oxygen dissociation. Dense LSCF samples were prepared and the surfaces modified using ion implantation[184,185]. Ion implantation uses an ion beam to modify a material's chemical and electronic properties. The ion beam can also create local damage to the solid sample at the near surface region by atom displacement, potentially creating various surface vacancies. To study the influence of the surface modification of Mn ion implantation on LSCF, the kinetic properties of the material, such as chemical diffusion coefficient, D_{chem}, and effective chemical surface reaction coefficient, k_{chem} were characterized by electrical conductivity relaxation (ECR). ECR is a common technique used to investigate the kinetics of oxygen transport properties[173]. In order to investigate these properties with ECR samples were placed in a closed environment and the oxygen partial pressure of the environment was rapidly changed to pump oxygen in and out of the sample, resulting in a change of the concentrations of defects, which was measured by changes in the samples electrical

conductivity. We then extracted the kinetic parameters D_{chem} and k_{chem} to better understand the change in ORR kinetics for LSCF samples with and without surface modification.

To understand the influence of the modified LSCF surface after ion implantation, the surface compositions and binding energies were probed using x-ray photoelectron spectroscopy (XPS). The correlation between the ion implantation and the change of k_{chem} was investigated. Results show that at certain Mn doping levels and ion energies, the surface modification shows an enhancement of the surface exchange rate of LSCF, while others seem to show that Mn implantation can reduce the oxygen surface exchange rate. The ion implantation technique provides a unique method to modify the near surface layer and potentially enhance the performance of LSCF. ECR provides insight to further understand the fundamental mechanisms that govern the ORR. The results not only help us to further improve cathode performance and durability, but also present an alternate approach to achieve this goal.

8.2 Experimental

Commercial $La_{0.6}Sr_{0.4}Co_{0.2}Fe_{0.8}O_{3-\delta}$ (LSCF) powders (Praxair Specialty Ceramics, USA) were pressed and sintered in air at 1400°C for 4 hours. Bars of approximately 20 mm X 2 mm X 1 mm were cut from the sintered pellets and polished using 1μm diamond compound. The samples were implanted using a Varian VIISta High Current implanter. The implanter uses a ribbon beam that impinges on a scanned surface that held the LSCF samples. The samples were ion implanted with different manganese doping concentrations (from $1x10^{16}$ to $1x10^{17}/cm^2$) and different ion energies (10keV and 40keV) to study both the effects of concentration and ion

energy. By controlling the different ion energies and implantation doses, we can get LSCF samples with different Mn ion distribution profiles in the near surface region.

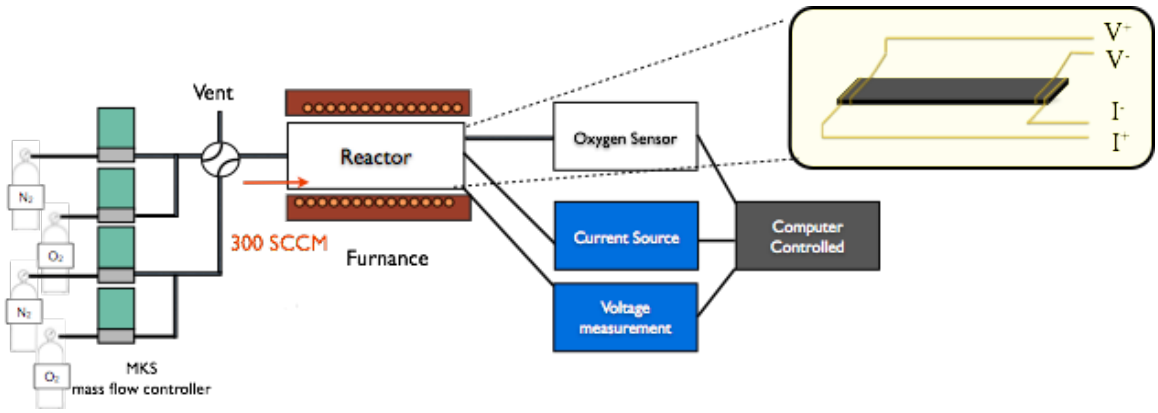

Figure 8-1. Schematic of ECR experimental set up

Figure 8-1 shows the ECR experimental set up. A nitrogen and oxygen gas mixture was fed into the reactor using individual mass flow controllers, and the total flow rate was fixed at a high level to induce sharp step changes in the oxygen partial pressure, which was monitored through an yttria stabilized zirconia (YSZ) oxygen sensor. A lock-in amplifier (Stanford Research SR830) is used to measure the conductivity change of individual samples. Small measurement currents/voltages were used to prevent electronic disturbance in the system. The mass flow controllers, the lock-in amplifier, the oxygen sensor, and the temperature of the furnace are automated through LabVIEW (National Instruments). To ensure accurate measurement at different PO_2, the change in PO_2 is kept relatively small (~0.02 atm). The conductivity relaxation profile is acquired by four-probe DC measurements and fit with Crank's solution[61] to the diffusion equations. XPS measurements were performed using a monochromatic aluminum X-ray source in a Kratos Axis 165 X-

ray photoelectron spectrometer operated at 1400keV. CASAXPS software is used to analyze and qualify the XPS spectra.

8.3 Conductivity Relaxation Theoretical Background

The kinetic properties of the material that can be obtained are based on the measurement of the transient response to a step change in the chemical potential. In ECR, a rapidly changing PO_2 leads to a change in the chemical potential of the sample. Therefore, the concentrations of defects will change, affecting the electrical properties[55,57,61]. If we assume the chemical potential driving force for the oxygen surface exchange rate on MIEC is linear with relation to the oxygen concentration gradient between the gas phase and the solid phase. The boundary conditions of the oxygen flux on the surface of the sample can be represented by:

$$-D_{chem}\left.\frac{\partial C}{\partial x}\right|_{x=\pm T/2} = k_{chem}(C(\infty)-C(t)) \qquad [8\text{-}1]$$

Where C(t) is the actual concentration of oxygen just within the sample and C(∞) is the concentration required to maintain equilibrium with the surrounding atmosphere. k_{chem} is the effective chemical surface exchange coefficient of the sample after surface modification. k_{chem} describes the linear driving force for the oxygen molecule dissociation and incorporation into the lattice. D_{chem} is the chemical diffusion coefficient, describing the ability of oxygen ions to diffuse through the lattice under the chemical potential gradient, and T is the sample thickness. The change in conductivity as a function of time has a linear relationship to the change in concentration of oxygen vacancies in the sample. Consider Crank's solution[61] for diffusion in a plane:

$$\frac{\sigma(t)-\sigma(0)}{\sigma(\infty)-\sigma(0)}=\frac{\delta(t)-\delta(0)}{\delta(\infty)-\delta(0)}=\frac{M(t)}{M(\infty)}=1-\left[\sum_{n=1}^{\infty}\frac{2L^2\exp\left(-\frac{\beta_n^2 D_{chem}t}{(T/2)^2}\right)}{\beta_n^2\left(\beta_n^2+L^2+L\right)}\right] \quad [8\text{-}2]$$

$$L=\frac{T}{2}\frac{k_{chem}}{D_{chem}} \quad [8\text{-}3]$$

$$\beta_n\tan\beta_n=L \quad [8\text{-}4]$$

where σ(t), σ(0), and σ(∞) are the conductivity of the sample at time t, zero, and equilibrium, respectively. δ(t), δ(0), and δ(∞) are the oxygen nonstoichiometries at time t, 0, and at equilibrium, respectively. M(t) is the accumulated total amount of oxygen leaving or entering the sample at time (t), and M(∞) is the accumulated total amount of oxygen at equilibrium. β_n are the infinite roots of L. L is a function of the sample thickness, $k_{chem,}$ and D_{chem}, where $k_{chem,}$ and D_{chem} are material properties and the sample thickness is the experimental parameter. The characteristic thickness [12] has been defined to provide a reference for whether the bulk diffusion or surface exchange dominates the reaction:

$$L_c=\frac{D_{chem}}{k_{chem}} \quad [8\text{-}5]$$

Because L_c is the internal property of the material, the proper choice of sample thickness allows the experiments to be sensitive to either surface exchange or bulk diffusion[73,74]. Our focus is on the surface phenomena of the samples after surface modification. Therefore, relatively thin samples were prepared. In this study, the thickness of the ion implanted LSCF samples is about 0.05 to 0.1cm, which is on the

order of L_C for LSCF, at ~0.07cm[75]. The similarity between sample size and L_C allows us to accurately fit both k_{chem} and D_{chem}. The data was fitted with the numerical calculation provided in Equation [8-2] using an in-house Matlab program which generates the ideal diffusion curves based on the kinetics parameters k_{chem} and D_{chem} along with other experimental factors. Following fitting, a least squares regression of the experimental data is used to find a global minimum for fitting error. In this study, 100 β terms are considered. To accurately measure k_{chem} values, LSCF samples with two different thicknesses (0.1 and 0.2 cm) are measured to normalize k_{chem} values [172] at different oxygen partial pressures and temperatures.

8.4 Results and Discussion

The depth profiles of Mn ions in the LSCF bar are calculated using SRIM [186], assuming LSCF has a theoretical density 6.36 g/cm^3 and a perovskite stoichiometry of ABO_3, where La and Sr occupy the A site, and Co and Fe occupy the B site. Figure 8-2 shows the Monte Carlo calculations of 100 ion trajectories for (a) 10keV and (b) 40keV ion energies for Mn implantation into LSCF. The simulation demonstrates that Mn ions are located in the near surface region and cause the displacement of atoms. The Mn ion distribution profiles of different ion energy with $1x10^{16}$/cm^2 dose is computed in Figure 8-2 (c). The projected range is expected to reach a maximum at 70Å and 200Å for 10keV and 40keV ion energies, respectively. At lower ion energy, Mn ions are located close to the surface region, and have a relatively high concentration of manganese focused near 70Å from the surface. At higher Mn ion energy, the Mn shows a broadened distribution of penetration depth, with a peak at

200 Å in from the surface. Figure 8-2 (d) shows the effects of different doping levels, for which the total Mn concentration depends on the dose of Mn ions.

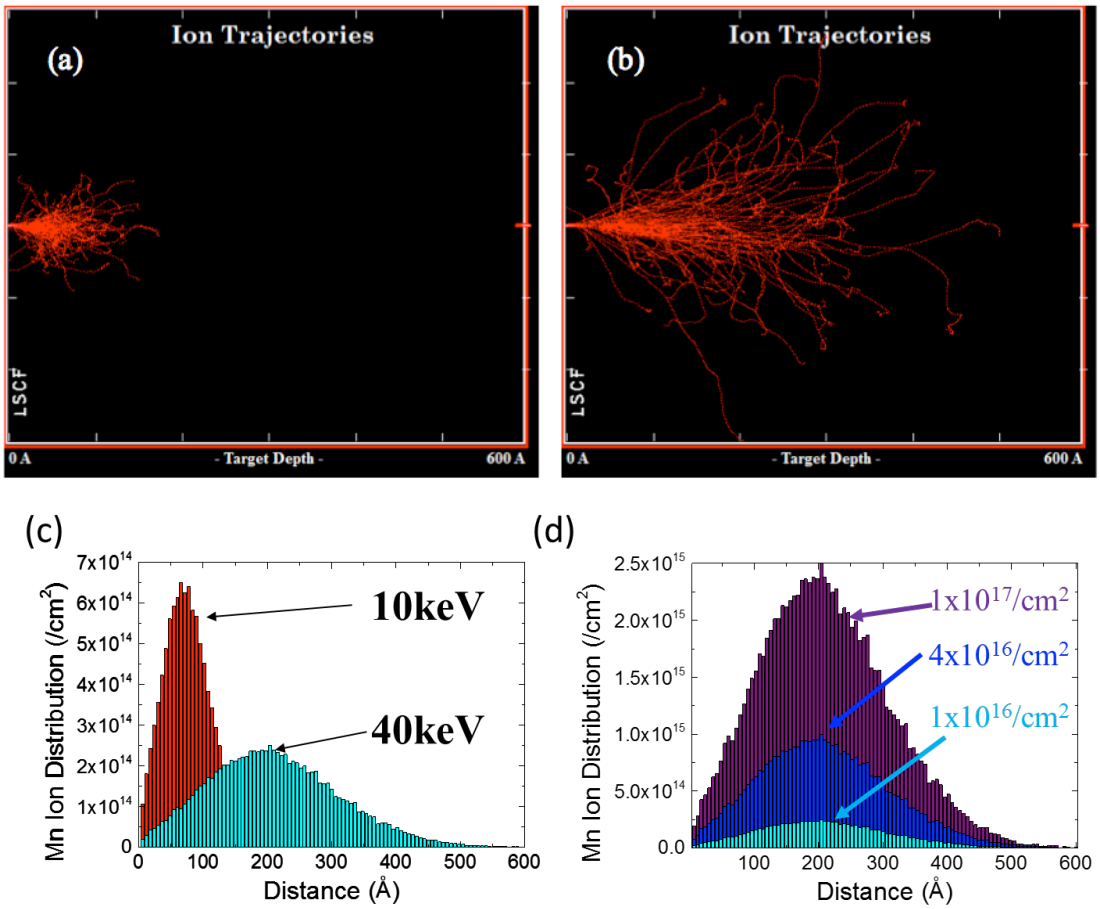

Figure 8-2. Monte Carlo calculations of 100 ion trajectories for Mn ion implantations into LSCF with (a) 10keV and (b) 40keV ion energies. Mn ion statistical distribution curves of samples with (c) different ion energies at the same $1x10^{16}/cm^2$ dose and (d) different doping levels at 40keV implantation energy.

Ion implantation can also cause atom displacement and vacancies by transferring energy and momentum from the ions to atoms in the target material. Figure 8-3 shows a simulation of a displacement/vacancy distribution generated by the ion implantation process. Samples with 10keV ion energy have a higher density of vacancies in the near surface region, and samples with 40keV have a greater total number of vacancies, more evenly distributed in the near surface region of LSCF. The

right axis shows the total number of vacancies generated by ion implantation with different ion energy. Mn ions with higher accelerating voltages have enough energy to generate more vacancies. The calculation shows that for the same doping level, 40keV can form more than double the number of vacancies than 10keV. The formation of vacancies in the near surface region is believed to increase the surface exchange rate due to the vacancy transport mechanism on the surface[47].

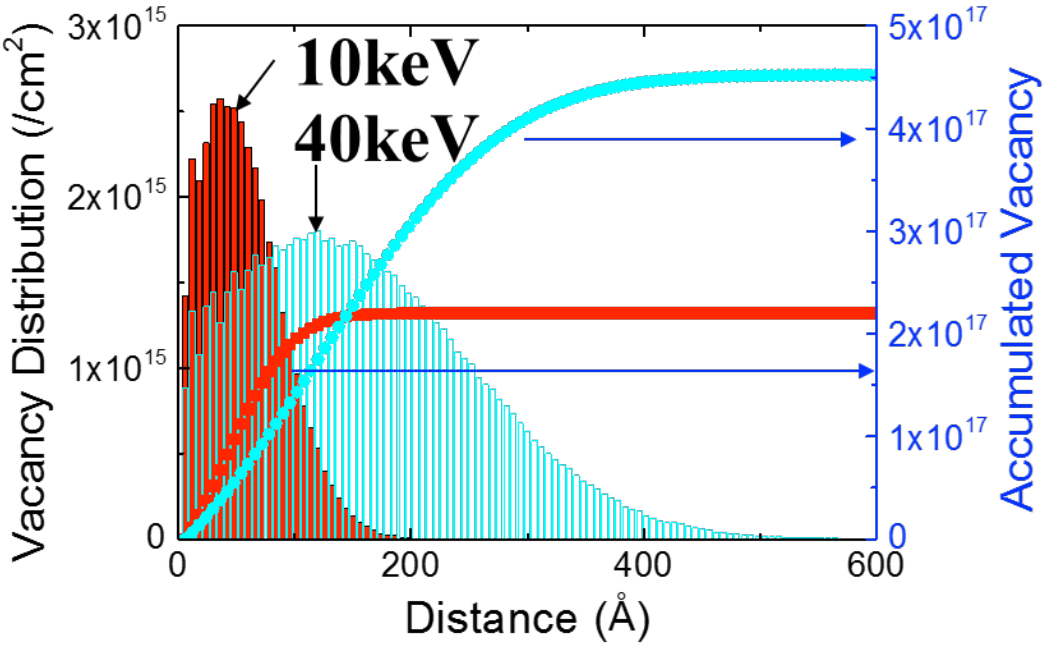

Figure 8-3. Calculation of displacement/vacancy statistical distribution and accumulated vacancies of different ion energies.

Figure 8-4 displays the electrical conductivity relaxation curve of LSCF at 800°C with (blue dots) and without (black dots) surface modification (40keV $1x10^{16}/cm^2$) during a change of PO_2 from 0.21 atm. to 0.19 atm. The red lines are the fitted curves, described by the diffusion equations for the bar shaped samples. The rapid change of the conductivity relaxation curve of Mn ion implanted LSCF samples

during the re-equilibrium process indicates the improvement of oxygen surface exchange rate after surface modification.

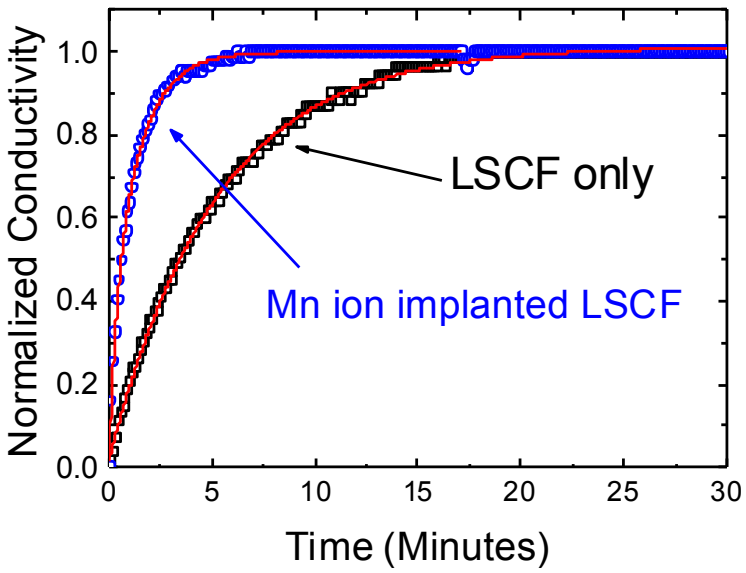

Figure 8-4. ECR curves of (a) LSCF (black square □), and (b) LSCF with Mn ion implantation (40keV, 1x10^{16} /cm^2) (blue circle ○). The samples were measured at 800 °C with the rapid change of PO_2 from 0.21 to 0.19 atm. The best fit curve is shown in red.

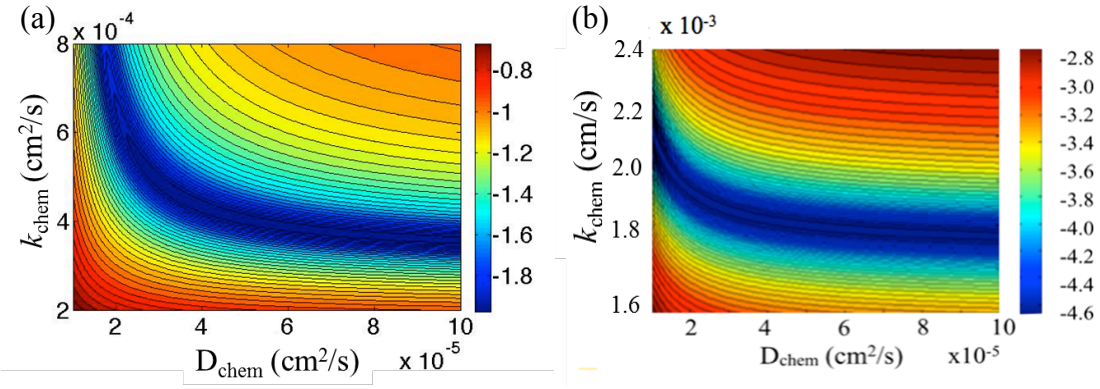

Figure 8-5. The color mapping of root-mean-square error (RMSE) for ECR on (a) LSCF and (b) LSCF with Mn ion implantation (40keV, 1x10^{16}/cm^2). The color scale is the logarithm of the root-mean-square error (RMSE) of the fitting parameters k_{chem} and D_{chem}, showing a global minimum where

The error mapping of the root-mean-square error (RMSE), for the fitting of kinetic parameters k_{chem} and D_{chem} to the relaxation curves in Figure 8-4, are presented in Figure 8-5. From the error mapping in the k_{chem} and D_{chem} plane, we can see an increase in the fitting accuracy when changing the estimated k_{chem} and D_{chem} values[94,187]. The global minimum (blue region) in Figure 8-5 illustrates the best fitting for k_{chem} and D_{chem} values for two different samples. D_{chem} appears to be insensitive to Mn ion implantation, but k_{chem} increases almost an order of magnitude to 1.9×10^{-3} cm/s after Mn ion implantation.

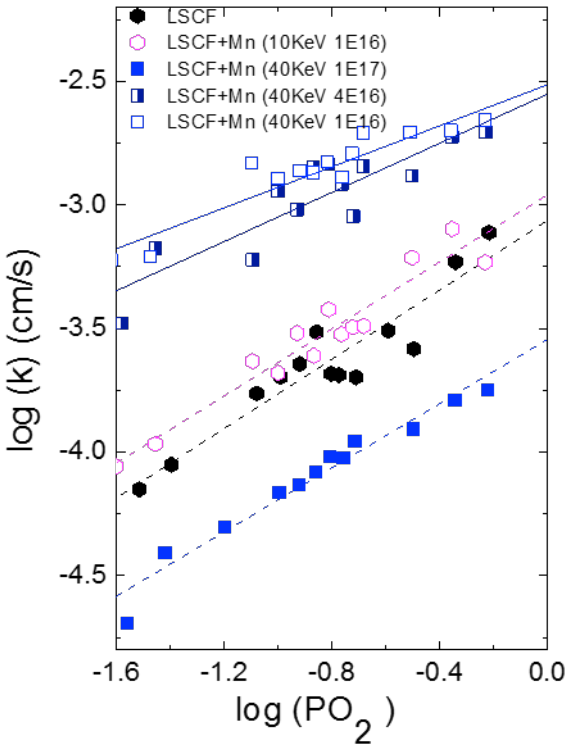

Figure 8-6. log (PO_2) versus log (k_{chem}) of LSCF samples with different concentrations and ion implantation energies.

Figure 8-6 shows a double log plot of k_{chem} values of ion implanted LSCF samples at different oxygen partial pressures. k_{chem} changes with different doping levels and doping energies of Mn ions. In the case where the ion implantation energy is 40keV, doping at low levels ($1x10^{16}/cm^2$ and $4x10^{16}/cm^2$) increases the surface exchange rate and changes the oxygen partial pressure dependence of LSCF. The samples implanted with lower concentrations of Mn ions show a slight decrease in their slopes, log (k_{chem})/log (PO_2), as compared to the baseline LSCF sample. This change in PO_2 dependence may be caused by an alternate rate-limiting step for the ORR, or a change in the materials kinetic properties cause by the ion implantation [148]. At higher Mn doping levels ($1x10^{17}/cm^2$) the effective surface exchange coefficient decreases even lower than the non-modified LSCF, suggesting that the higher Mn doping may cause damage to the near surface region of the sample, decreasing the catalytic ability of the cathode surface. When the ion implantation energy is 10keV, the Mn ion implanted LSCF shows a slight enhancement of the effective surface exchange rate. Although we see an increase in surface exchange for the 10keV sample, the 40keV $1x10^{16}/cm^2$ sample shows a much greater increase in surface exchange. This may be caused by the larger distribution of Mn atoms throughout the near surface region, where the implanted Mn ions may enhance the dissociation ability of the LSCF at the surface and create more available vacancies for oxygen to incorporate at the near surface without destroying the perovskite structure. The 10keV sample shows a higher concentration of Mn ions at the surface, which may cause impurity phases such as manganese oxide.

Figure 8-7 shows the Arrhenius plots of log (k_{chem}) versus 1000/T for the Mn ion implanted LSCF samples from PO_2= (a) 0.19 to 0.21 and (b) 0.17 to 0.19atm. The surface exchange rates at different PO_2 show similar temperature dependence. The apparent activation energy for the effective surface exchange rate of each sample is calculated based on the slope of the Arrhenius plots. The surface exchange rate of LSCF has an activation energy of about 2eV. For both partial pressures in Figure 8-7, the Mn ion implanted LSCF samples show a slight decrease in the activation energy of k_{chem}, except for the highest doping sample (40keV $1x10^{17}/cm^2$), indicating the high Mn doping level may change the reaction mechanism on the surface.

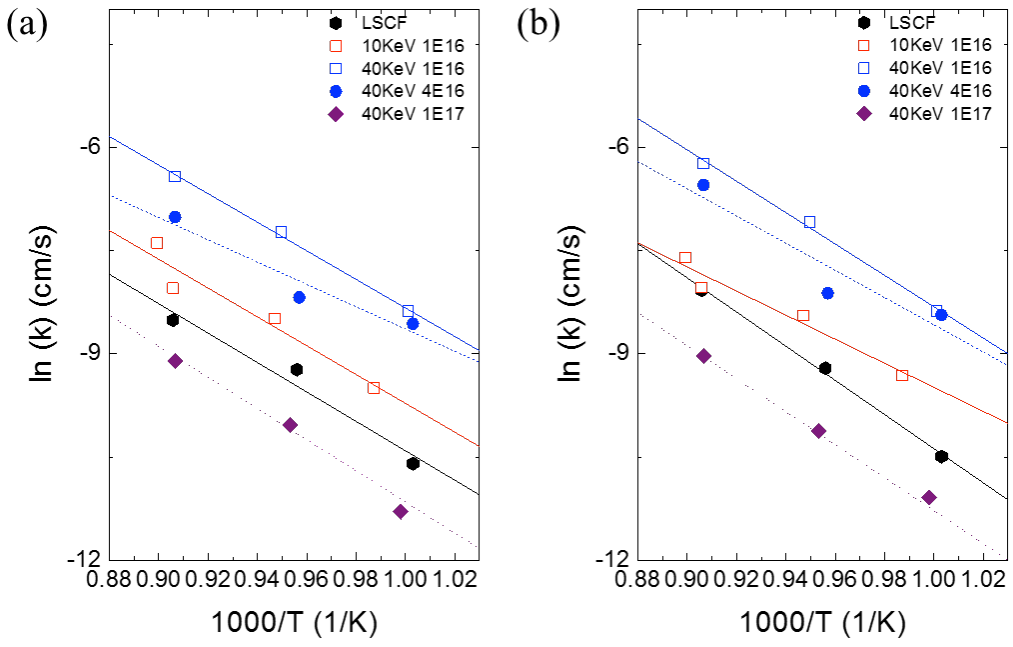

Figure 8-7. log (k_{chem}) of LSCF with different Mn ion implantation energies as a function of temperature at (a) PO_2=0.21 and (b) PO_2=0.19 atm.

The surface properties of Mn ion implanted LSCF samples were analyzed by XPS. Figure 8-8shows the XPS spectra of Mn 2p for the LSCF samples with different

Mn ion doping energies and doping levels. XPS data shows clear Mn 2p spectra, meaning that Mn ions are actually implanted into the LSCF samples. The Mn 2p peak is located near 643 eV and the satellite peak is near 654 eV. It is difficult to determine the valence state of Mn by the Mn 2p spectra because Mn^{2+}, Mn^{3+}, and Mn^{4+} all have overlapping peaks[122,188]. Figure 8-8 (a) shows the Mn 2p spectra of the Mn ion implanted LSCF with 40keV ion energy at different doping levels. The Mn 2p peak shows an increase with the increase of the Mn ion doping concentration. The influence of the different ion energies in the Mn 2p spectra is shown in Figure 8-8 (b). The Mn 2p spectra has a similar shape and intensity for both of the ion energies, and the sample with 10keV ion energy shows a slightly higher intensity than the 40keV implanted sample, suggesting that more Mn ions are located near the surface (within 100 Å) in the 10keV sample (less penetration).

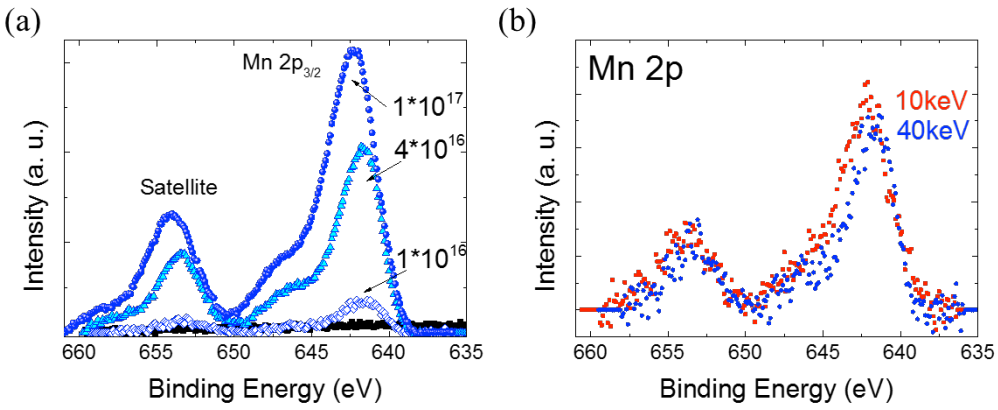

Figure 8-8. Mn ($2p_{3/2}$) spectrum of the Mn ion implanted LSCF samples with (a) different doping level at 10keV, and (b) with different Mn ion energy (10keV and 40keV) at $1x10^{16}/cm^2$ doping level, obtained through XPS.

To compare the concentration of Mn on each sample, the Mn signal on the surface is normalized to the total number of A site atoms, i.e. the sum of the La and Sr signals, because the perovskite ABO_3 structure has a 1:1 ratio of A:B atom sites.

Table I summarizes the concentrations of Mn on the surface of the ion implanted LSCF samples based on the ratio of intensity of Mn 2p signal to the sum of La and Sr signals. The effective k_{chem} values obtained from ECR (800ºC, ΔPO_2 from 0.21 to 0.19) are also listed in table I. Comparing samples with the same doping levels but different ion energies, we can see that the lower ion energy sample, 10keV, has a higher concentration of Mn closer to the surface, indicating that the sample with 10keV has a narrow Mn distribution as well as a high density of surface damage. The sample with 40keV implantation has a broader Mn distribution and a deeper penetration depth.

Table 8-I. Summary of the normalized concentrations of manganese (Mn/(La+Sr)) on the surface of the Mn ion implanted LSCF samples by XPS at the incident angle 0°.

Mn ion implanted LSCF (ion energy, doping level)	Mn/(La+Sr) (%)	k_{chem} (cm/s) (800ºC)
No ion implantation	0	4.4×10^{-4}
10keV, 1×10^{16} /cm^2	14	5.2×10^{-4}
40keV, 1×10^{16} /cm^2	5	1.9×10^{-3}
40keV, 4×10^{16} /cm^2	44	1.4×10^{-3}
40keV, 1×10^{17} /cm^2	157	1.1×10^{-4}

Although the lower ion energy sample, 10keV, has a higher concentration of Mn at the surface, the damage of ion implantation is also concentrated in this region. This damage may limit the enhancement of the surface exchange rate. For the samples with 40keV, the concentration of Mn increases with increasing doping levels, as shown in Table I. XPS results show that the higher doping level samples, with 40 keV accelerating voltage, have higher Mn concentrations in the near surface region, and a less significant enhancement of $k_{chem.}$ This decrease in the performance could be due to damage caused by these higher doping levels.

It is apparent, from XPS measurements, that there is an indirect relationship between the surface concentration of Mn ions, and the enhancement of the effective surface exchange coefficient, k_{chem}. However, a closer look at the difference between the 10keV sample and the two with lower doping concentrations at 40keV, we can see that there are more factors playing a role. The sample at 10keV with $1x10^{16}/cm^2$ doping, has a Mn concentration at the surface of ~14% of the B sites, while the sample at 40keV with $4x10^{16}/cm^2$ doping has a Mn concentration of 44% of the B sites. Although the increase in Mn B site concentration at the surface has a negative correlation with k_{chem}, the 10keV sample does not increase k_{chem} as significantly as the 40keV $4x10^{16}/cm^2$ sample. There are three possible factors determining the effect of ion implantation on the oxygen surface exchange rate. First, the manganese ions in the near surface region could contribute to the catalytic process of oxygen dissociation. Second, an increase in surface vacancies induced by the ion implantation could provide more sites for the ORR to take place. Finally, ion implantation can potentially cause damage to the perovskite structure, leading to a decrease in the materials ORR catalytic properties.

For the highest doping level sample, $1x10^{17}cm^2$, manganese is highly enriched on the surface of the sample, and is much more abundant than the observed A site atoms (~157%). Therefore, in the near surface layer, instead of maintaining the LSCF perovskite structure the surface is damaged and transformed into manganese oxide. As manganese oxide is not as catalytically active toward the oxygen reduction process, this high doping level is detrimental to the materials surface exchange rate.

8.5 Conclusions

The surface modification of LSCF through Mn ion implantation enhances the oxygen surface exchange rate by an order of magnitude. This is the first reported enhancement of SOFC cathode performance by using the ion implantation technique. The oxygen transport properties of the modified LSCF samples are investigated by ECR. Samples with a variety of ion implantation energies and doping levels have been reviewed, and it has been shown that increased doping levels can eventually lead to a decrease in performance due to sample damage. The ion implantation technique is a powerful tool to change the surface chemistry and electronic structure of a material, resulting in a change in the materials catalytic properties, especially at the near-surface. XPS data shows that Mn is present in the near surface region for the Mn ion implanted LSCF samples. Performance enhancement of LSCF by surface modification using Mn ions, may be due to the increase of available surface sites, generated by high energetic Mn ion bombardment, and/or the addition of Mn in the near surface layer that is catalytically active toward the dissociation of oxygen. The damage due to a high concentration of Mn ion implantation may also limit the enhancement effects. Excessive doping of Mn likely forms a thin layer of manganese oxide on the surface, eventually destroying the perovskite structure, and decreasing the materials ability to dissociate oxygen. The results allow us to further investigate the ORR mechanism as well as to design and engineer new cathode materials/structures that can improve cathode performance and durability.

Chapter 9: Future Work

1. Gas phase isotopic oxygen exchange is a powerful tool to determine the kinetics of the ORR in real-time and can be widely applied to other potential cathode materials or composites, such as $Ba_xSr_{(1-x)}Co_yFe_{(1-y)}O_{3-\delta}$ (BSCF), double perovskite materials, LSCF-GDC, LSM-YSZ, and LSM- erbia-stabilized bismuth oxide (ESB).
2. BSCF has been demonstrated as a high performance cathode material, exhibiting high activity toward to ORR. Despite the performance of BSCF as an SOFC cathode, there are long-term stability issues, especially in the presence of CO_2. Temperature programmed isotope exchange would be a useful tool to determine the impacts of CO_2 on the degradation process.
3. Common impurities in air, such as CO_2 and water, may cause different impacts on the cathode and electrolyte composites, such as LSM/YSZ and LSCF/GDC. ISTPX can be performed on these composites to determine the effects of CO_2 and water.
4. From 1:1 IIE, LSM shows good catalytic activity toward the dissociation of oxygen, via homoexchange. The results suggest that LSM has enough ability to dissociate oxygen but it needs to connect to another ionic conductor to incorporate the dissociated oxygen into the solid phase. It would be interesting to compare LSM with LSM/YSZ composite using 1:1 IIE to examine the effects of ionic conductor on the ORR. The difference between homoexchange and heteroexchange can also be investigated.

5. For Mn ion implanted LSCF samples, the effects of the Mn concentration on LSCF can be qualitatively verified by other characterization techniques, such as X-ray fluorescence.
6. The ORR is a complex, multi-step process consisting of a series of elementary reactions. A key to understanding the ORR is identification of the individual mechanisms involved, and more specifically, the rate-determining step (RDS). *In-operando* oxygen isotope exchange can potentially probe the mechanistic kinetic rates of the ORR under polarization. Combining *in-situ* oxygen isotope exchange with an external applied potential we can study the catalytic properties of materials under conditions better representative of real operation. The presence of electrical or electrochemical potentials can have a significant effect on a number of steps in the ORR, especially those involving charge transfer. Unlike previous gas phase isotope exchange, where the interaction of isotopically labeled oxygen is governed only by self-exchange, our *in-operando* experiments will include electrochemical driving forces. As such, we expect significant changes in the behavior and kinetics of the materials under these conditions.
7. Results have indicated that high performance materials, those more catalytically active toward the oxygen reduction reaction, appear to also have higher rates of degradation. Surface modification is a promising method to further improve the durability and enhance the performance of SOFC cathodes. Other techniques, such as infiltration or thin film depositions, can

potentially maintain or even increase the catalytic activity towards oxygen dissociation, and may also serve to prevent degradation.

Appendices

Appendix A. Calibrations for the Isotope Exchange Experimental Set Up

Flow Rate Calibration

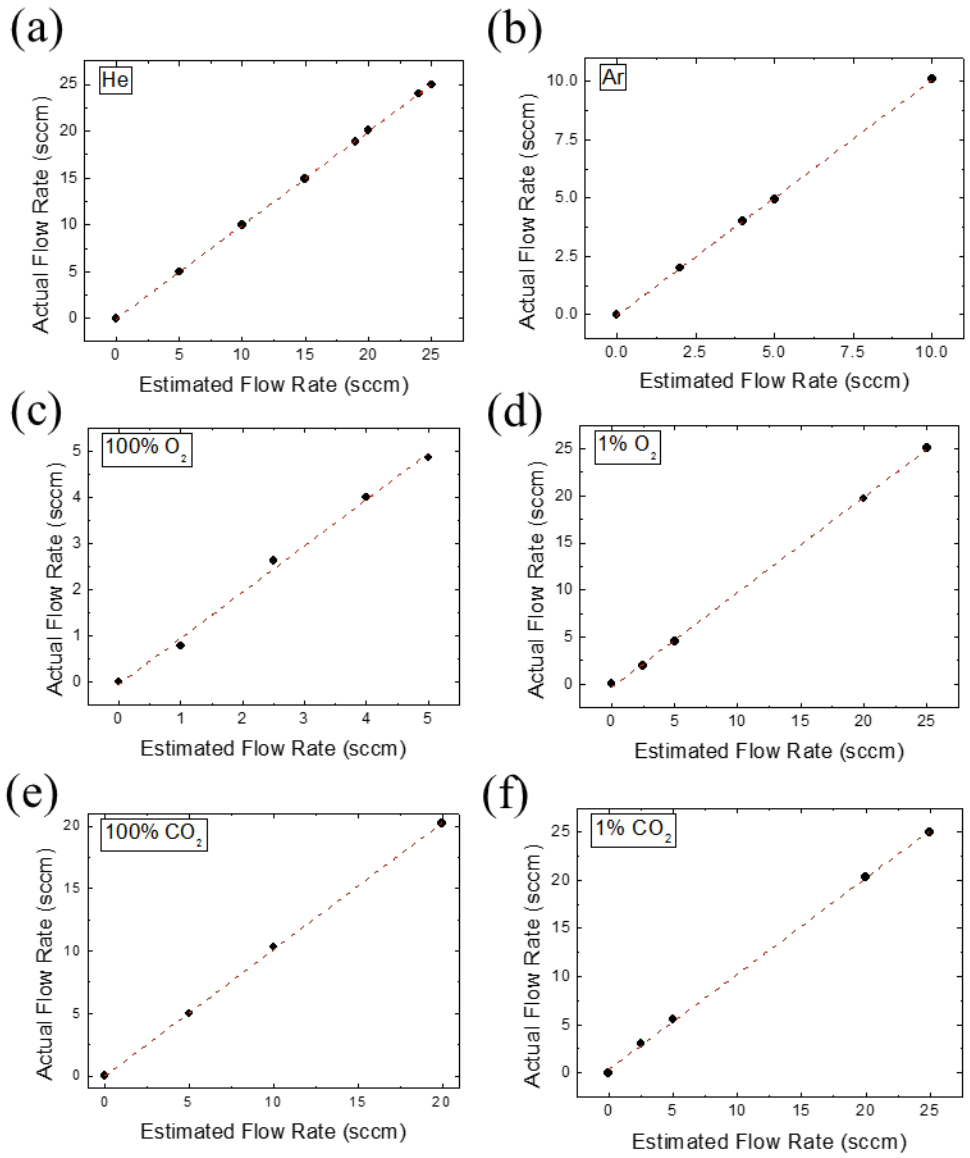

Figure A-1. Calibrations of flow rates of multiple gases: helium (a); argon (b); oxygen concentrations of 100% (c) and 1% (d); and carbon dioxide concentrations of 100% (e) and 1% (f).

To quantify our experimental data it is necessary to calibrate the actual flow rate of each mass flow controller. Flow rates were verified using a bubble-meter. Then the estimated flow rate is compared to the measured flow rate and the gas property parameters of the mass flow controller are adjusted to match the two flow rates. The calibrations are performed repeatedly until the actual flow rate matches with the estimated flow rate within 1% accuracy. Figure A-1 shows the calibrations of flow rates for different gases. Calibrations were performed to achieve highest accuracy near the experimental flow conditions.

Mass Spectrometer Calibration

To obtain accurate concentration measurements from the mass spectrometer calibration of the signal intensity is necessary. Signals were calibrated by flowing different known concentrations of each gas at a constant flow rate of 20*sccm* and recording the intensity signal obtained on the mass spectrometer. A linear relationship between gas concentration and signal intensities was established for each gas, as shown in Figure A-2. The linear equation was then used to convert the recorded experimental intensities into concentrations of parts per million (*ppm*). To ensure the accuracy in the concentration measurements, the calibration of the signal intensity is performed BOTH BEFORE and AFTER each isotope exchange experiment.

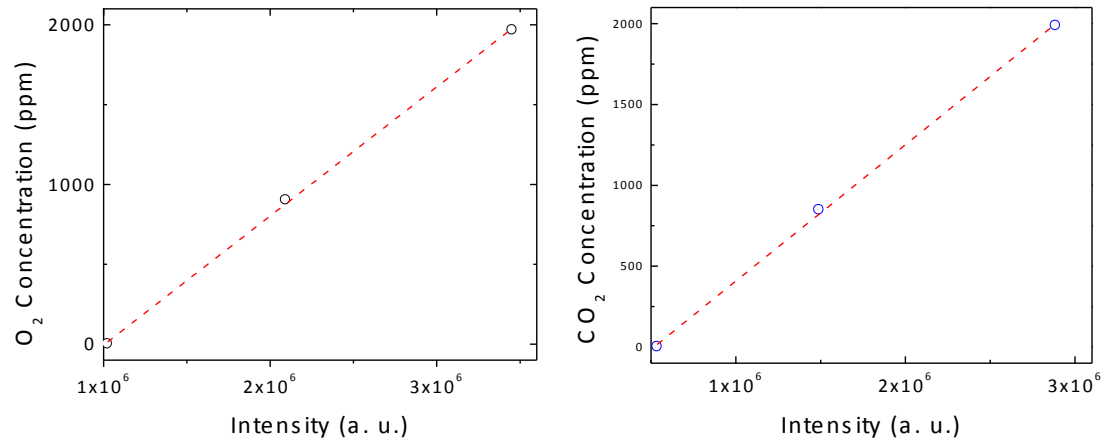

Figure A-2. Examples of Mass Spectrometer Calibrations. We can convert mass spectrometer intensities to concentrations of oxygen (a) and carbon dioxide (b).

Switch Time Calibration

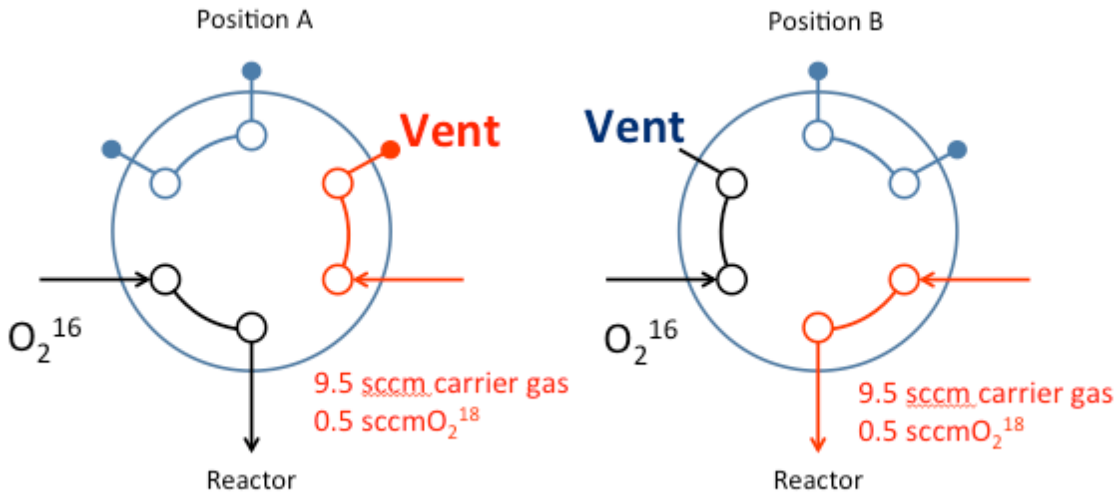

Figure A-3. Design and implementation of the pneumatic valve actuator. Position A allows $^{16}O_2$ to flow to the reactor while $^{18}O_2$ is vented. Position B vents $^{16}O_2$ and allows $^{18}O_2$ to flow to the reactor.

We have installed an air actuated valve to control switching between $^{16}O_2$ and $^{18}O_2$ gasses. This device allows us to remove any human error that would be involved in manually turning a switch, and also provides much faster switching times. The design/implementation of the valve can be seen in Figure 9-3. In 'position A' $^{16}O_2$

flows through the valve to the reactor, while $^{18}O_2$ is vented as to prevent pressure build up in system which may cause higher and/or variable flow rates during switching. This same concept applies to 'position B' as well, only $^{18}O_2$ is flowing to the reactor and $^{16}O_2$ is vented.

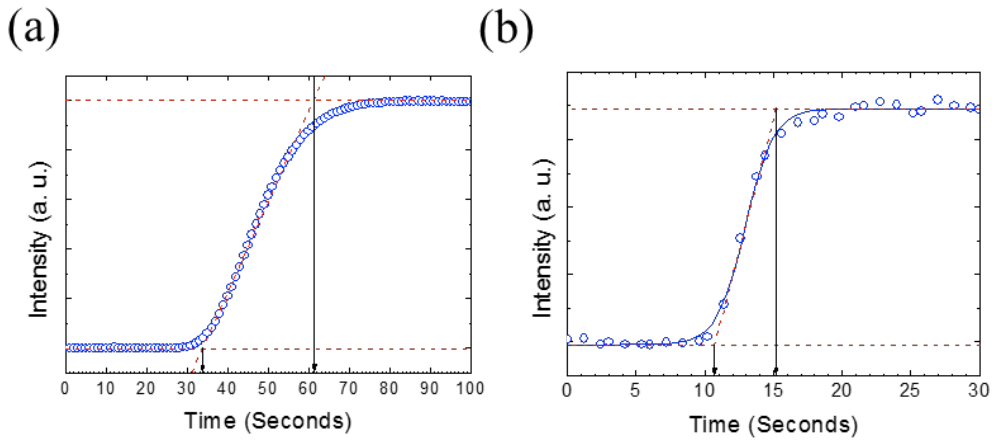

Figure A-4. Comparison of switch times for ball valve (a) and pneumatic valve actuator (b).

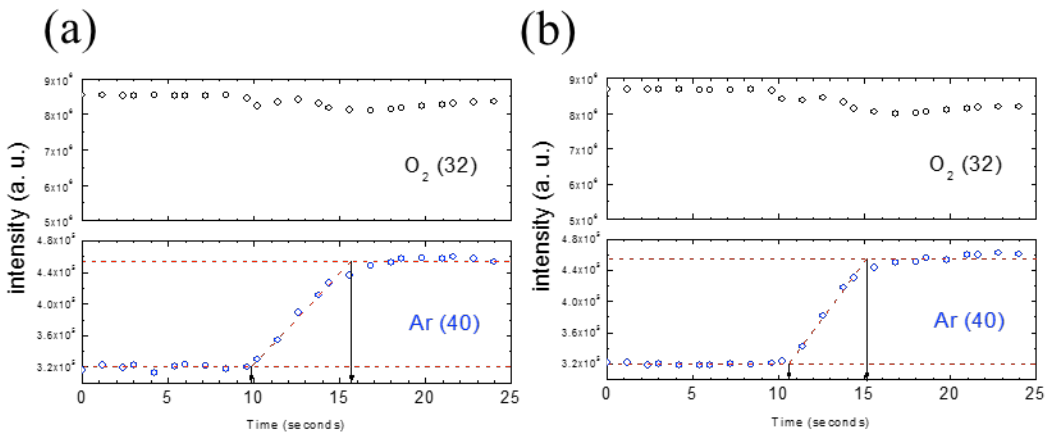

Figure A-5. Graphs show the isobaric switch and switch times of pneumatic valve actuator, represented Ar (40 m/z signal), and ability to maintain steady flow, represented by O_2 (32 m/z signal). The pressure provided to the DVI, 50psi (a) and 80psi (b), changes the time it takes to perform a switch. Lower pressures producing longer switch times.

Figure A-4 provides data on the switching times recorded before and after the installation of the pneumatic valve actuator and the digital valve interface (DVI). As can be seen in the Figure A-4 (a) the switch time using the three-way ball valve is

approximately thirty seconds. This can be decreased to approximately 5 seconds when using the pneumatic valve, as shown in Figure A-4 (b). The switch time is important for IIE experiments as it affects the ability to fit data generated at the beginning of the experiment, shortly after the $^{18}O_2$ is first detected. The valve was tested using $^{16}O_2$ flowing through both the A and B positions. Figure A-5 (a) and Figure A-5 (b) show that a 5 second switch time is repeatable, and that there is little to no change in the level of oxygen that results from flowing in 'position A' versus 'position B'. This is a result of the fast switching time as well as the accurate calibration of the different mass flow controllers being used.

Reactor Furnace

During initial temperature programmed desorption experiments (TPD) we became aware of issues affecting the control of our furnace. One of the main issues was non-linear heating. As a result of 'bursts' of high power output unwanted oscillations in the mass/charge (m/z) signals in the mass spectrometer were detected. This is apparent in data collected during a TPD experiment in which the CO_2 signal is oscillating in unison with furnace temperature, as shown in Figure A-6 (a). After reconstruction of the furnace and tuning of the furnace controller, we were able to remove the oscillations present in the heating curve and therefore the detrimental effects they may have had on data analysis. The new heating curve is shown in Figure A-6 (b).

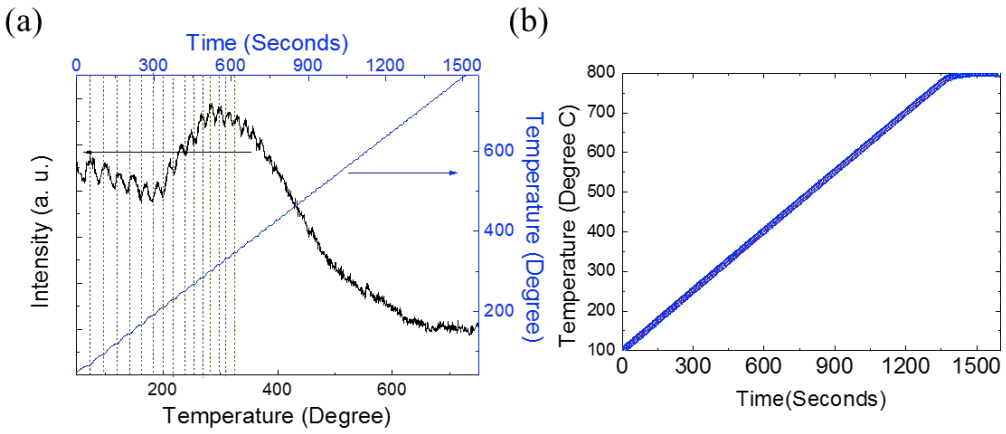

Figure A-6. (a) CO_2 TPD on LSM (black curve) and the heating curve (blue). Oscillations in the CO_2 (44 m/z) can be correlated with the oscillations in the furnace temperature profile. (b) The post-reconstruction furnace temperature profile. Blue dots are data points and red line is the fitted curve.

Water contaminants

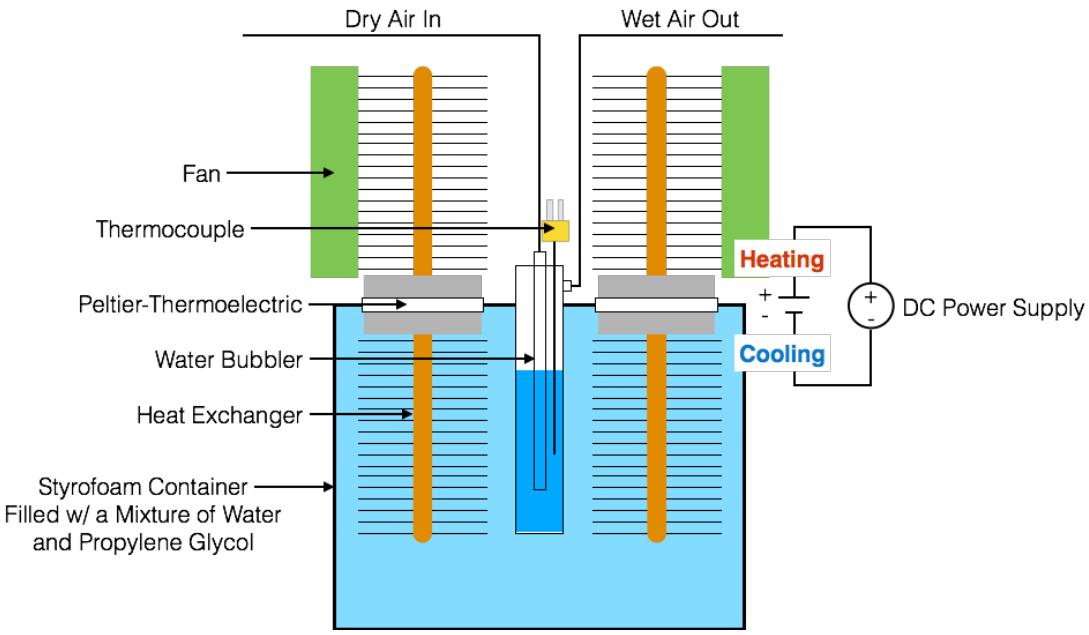

Figure A-7: Schematic drawing of new water-cooling system. Cooling is achieved using two Peltier-thermoelectrics (TE) connected to two heat sinks on the 'cold-side' that are submerged in a bath mixture of water and propylene glycol (to reduce freezing point), contained inside a Styrofoam box. The TEs are powered using a 12V-20A-DC power supply, through which the TEs act as a heat pump, drawing heat from the bath, which is then removed using two heat sinks w/ attached fans on the 'hot-side'. The water bubbler is submerged and cooled inside bath. The system is controlled with a PID temperature controller connected to a thermocouple located inside the water bubbler.

In order to properly control the water partial pressure used for degradation tests on cathode powders we designed and built a temperature controlled water-cooling bath. The water-cooling system, shown schematically in Figure A-7, uses two 150W Peltier-thermoelectrics (TE), which are both connected to two heat sinks. One of the heat sinks on each TE is submerged inside a Styrofoam box that contains a mixture of water and propylene glycol, to decrease the freezing temperature and avoid any ice buildup on the heat exchanger fins. The other heat exchangers are located outside of the Styrofoam container and have attached fans that blow air across the fins to remove heat. When a voltage is applied across the TE, heat is pumped from the bath to the ambient air above. The system is controlled using a PID loop temperature controller, which has a temperature input provided thermocouple located inside the water bubbler and an output that controls a solid-state relay (SSR). The SSR is used to regulate the amount of power that is supplied to the TEs, in turn controlling the amount of cooling applied to the bath.

Using this system we can now provide stable concentrations of water to use in the powder testing system, and operate the water bubbler at a variety of conditions. By stably varying the concentration of water we can more accurately elucidate how the presence of water affects the ORR.

A water bubbler was installed in the *in-situ* isotope exchange system to serve as an water contamination source. The gas flows into a 25mL glass impinger through a fritted nozzle. The impinger is placed into a large ice bath to help maintain the water temperature at 0°C. Table A-I shows the water vapor pressure at different temperatures. By controlling the water temperature the desired degree of

humidification can be achieved. All degrees of humidification in these experiments will be presented in mole percentage (*mol%*). The gas pipe from the humidifier to the reactor is appropriately heated to avoid water condensation. Figure 9-8 shows the calibration of water concentration. Signals were calibrated by flowing different known concentrations at a constant flow rate of 20 SCCM and recording the intensity signal obtained on the mass spectrometer. A linear equation was then used to convert the recorded experimental intensities into concentrations of parts per million (*ppm*). D_2O was limited to low concentrations to prevent damage to the mass spectrometer.

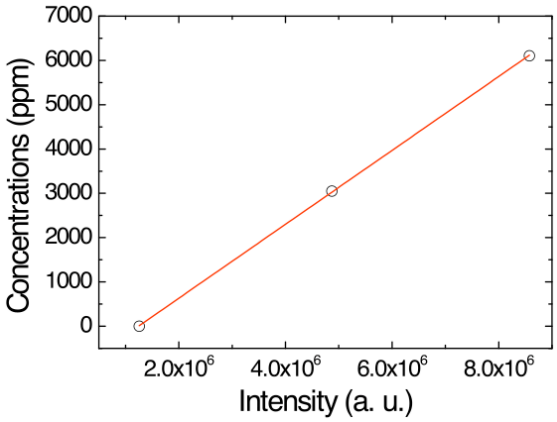

Figure A-8 Mass spectrometer calibration to convert mass spectrometer intensities to concentration of water.

Table A-I. Mass spectrometer calibration to convert mass spectrometer intensities to concentration of water(NIST Standard Reference Database 69: NIST Chemistry WebBook).

Temperature (°c)	Water vapor pressure (mol%)
4	0.0066101
5	0.0071078
6	0.0076384
7	0.0082038
8	0.0088059
9	0.0094467
10	0.010128
11	0.010853
12	0.011623
13	0.012441
14	0.013309
15	0.01423

```
clc
clear all
global T;
tic;
%load 'experimental data'; % read the value of t,Mex from the file
%input parameters:
fprintf('please enter the following parameters');
pause(2);
%fprintf(', Sr Yilin Huang:');
fprintf(' \n');
%input experimental file
FILENAME=input('experimental data filename:','s');
Ds=input('enter the lower bound D(start) (cm^2/s):?');
Df=input('enter the upper bound D(finish)(cm^2/s):?');
ks=input('enter the lower bound k(start) (cm/s):?');
kf=input('enter the upper bound k(finish) (cm/s):?');
T=input('enter the sample thickness(cm):?');
PO2=input('final oxygen partial pressure(logPO2)=?');
%%
%open experimental file
fopenfile=fopen(FILENAME);
A=fscanf(fopenfile,'%g %g' ,[2 inf]);
fclose(fopenfile);
t=A(1,:);
Mex=A(2,:);
endt=max(t);
n=length(t);
%%
%Creat D-K mesh   %change Dc=repmat(Dp,1,nk);
D=Dc';
%x-m-dimension  y-n-dimension meshgrid will create a mesh with nxm
not
%mxn,so change to ndgrid
Lmesh=(T.*km./Dn)/2;
%contour(D,k,L); axis square
%Lline=L(:);
%mat1=ones(size(L));
%z1=zeros(size(L));
%y=@(x,L) x.*tan(x).*mat1-L;
%b1g=mat1.*0.9;
%x=fminsearch(@(x) y,b1g);
%one1=ones(size(Lline));
%fminus=@(x,L) x.*tan(x).*one1-Lline;
%b1=fzero(@(x) fminus(x,L), 0.9);
%x=fminsearch(@(x) fminus(x,L),0.9);
%x = fsolve(@(x) fminus(x,L), 0.2 );
%x=fminsearch(@(x) fminus(x,L), 0.2);
%x=fminbnd(@(x) fminus(x,L), 0, 0.2);
%%
%reduce dimension to 1D
L=Lmesh(:);
Lz=L';
nLz=length(Lz);
nLx=length(L);
%%
```

```
%Calculate beta values to five terms
fminus=@(x,vL) x.*tan(x)-vL;
b1c=ones(1,nLz);b2c=ones(1,nLz);b3c=ones(1,nLz);b4c=ones(1,nLz);b5c=
ones(1,nLz);
b6c=ones(1,nLz);b7c=ones(1,nLz);b8c=ones(1,nLz);b9c=ones(1,nLz);b10c
=ones(1,nLz);
b11c=ones(1,nLz);b12c=ones(1,nLz);b13c=ones(1,nLz);b14c=ones(1,nLz);
b15c=ones(1,nLz);
b16c=ones(1,nLz);b17c=ones(1,nLz);b18c=ones(1,nLz);b19c=ones(1,nLz);
b20c=ones(1,nLz);
b21c=ones(1,nLz);b22c=ones(1,nLz);b23c=ones(1,nLz);b24c=ones(1,nLz);
b25c=ones(1,nLz);
b26c=ones(1,nLz);b27c=ones(1,nLz);b28c=ones(1,nLz);b29c=ones(1,nLz);
b30c=ones(1,nLz);
b31c=ones(1,nLz);b32c=ones(1,nLz);b33c=ones(1,nLz);b34c=ones(1,nLz);
b35c=ones(1,nLz);
b36c=ones(1,nLz);b37c=ones(1,nLz);b38c=ones(1,nLz);b39c=ones(1,nLz);
b40c=ones(1,nLz);
b41c=ones(1,nLz);b42c=ones(1,nLz);b43c=ones(1,nLz);b44c=ones(1,nLz);
b45c=ones(1,nLz);
b46c=ones(1,nLz);b47c=ones(1,nLz);b48c=ones(1,nLz);b49c=ones(1,nLz);
b50c=ones(1,nLz);
b51c=ones(1,nLz);b52c=ones(1,nLz);b53c=ones(1,nLz);b54c=ones(1,nLz);
b55c=ones(1,nLz);
b56c=ones(1,nLz);b57c=ones(1,nLz);b58c=ones(1,nLz);b59c=ones(1,nLz);
b60c=ones(1,nLz);
b61c=ones(1,nLz);b62c=ones(1,nLz);b63c=ones(1,nLz);b64c=ones(1,nLz);
b65c=ones(1,nLz);
b66c=ones(1,nLz);b67c=ones(1,nLz);b68c=ones(1,nLz);b69c=ones(1,nLz);
b70c=ones(1,nLz);
b71c=ones(1,nLz);b72c=ones(1,nLz);b73c=ones(1,nLz);b74c=ones(1,nLz);
b75c=ones(1,nLz);
b76c=ones(1,nLz);b77c=ones(1,nLz);b78c=ones(1,nLz);b79c=ones(1,nLz);
b80c=ones(1,nLz);
b81c=ones(1,nLz);b82c=ones(1,nLz);b83c=ones(1,nLz);b84c=ones(1,nLz);
b85c=ones(1,nLz);
b86c=ones(1,nLz);b87c=ones(1,nLz);b88c=ones(1,nLz);b89c=ones(1,nLz);
b90c=ones(1,nLz);
b91c=ones(1,nLz);b92c=ones(1,nLz);b93c=ones(1,nLz);b94c=ones(1,nLz);
b95c=ones(1,nLz);
b96c=ones(1,nLz);b97c=ones(1,nLz);b98c=ones(1,nLz);b99c=ones(1,nLz);
b100c=ones(1,nLz);
for    vn=1:nLz
    vL=Lz(:,vn);

   b1c(vn)=fzero(@(x) fminus(x,vL), [0,1.56]);
   b2c(vn)=fzero(@(x) fminus(x,vL), [3.14,4.67]);
   b3c(vn)=fzero(@(x) fminus(x,vL), [6.28,7.78]);
   b4c(vn)=fzero(@(x) fminus(x,vL), [9.42,10.89]);
   b5c(vn)=fzero(@(x) fminus(x,vL), 12.5);%(12.56,15)
   b6c(vn)=fzero(@(x) fminus(x,vL), [15.7,17.11]);
   b7c(vn)=fzero(@(x) fminus(x,vL), [17.3,20.3]);%(17.45,20.2)
   b8c(vn)=fzero(@(x) fminus(x,vL), [20.56,23.32]);
   b9c(vn)=fzero(@(x) fminus(x,vL), [23.78,26.45]);
   b10c(vn)=fzero(@(x) fminus(x,vL), [27,29.56]);
   b11c(vn)=fzero(@(x) fminus(x,vL),[30.05,32.67]);
   b12c(vn)=fzero(@(x) fminus(x,vL),[33.3,35.79]);
   b13c(vn)=fzero(@(x) fminus(x,vL), [36.44,38.9]);
```

```
    b14c(vn)=fzero(@(x) fminus(x,vL), [39.57,42.02]);
    b15c(vn)=fzero(@(x) fminus(x,vL), [42.71,45.13]);
    b16c(vn)=fzero(@(x) fminus(x,vL), [46.06,48.33]);
    b17c(vn)=fzero(@(x) fminus(x,vL), [49.28,51.37]);
    b18c(vn)=fzero(@(x) fminus(x,vL), [52.15,54.48]);
    b19c(vn)=fzero(@(x) fminus(x,vL), [55.74,57.6]);
    b20c(vn)=fzero(@(x) fminus(x,vL), [59.17,60.72]);
    b21c(vn)=fzero(@(x) fminus(x,vL), [62.04,63.84]);
    b22c(vn)=fzero(@(x) fminus(x,vL), [65, 66.96]);
%??????????????????????
    b23c(vn)=fzero(@(x) fminus(x,vL), [68.1,70.08]);
    b24c(vn)=fzero(@(x) fminus(x,vL), [71.3,73.20]);
    b25c(vn)=fzero(@(x) fminus(x,vL), [74.5,76.32]);
    b26c(vn)=fzero(@(x) fminus(x,vL), [77.6,79.44]);
    b27c(vn)=fzero(@(x) fminus(x,vL), [80.8,82.57]);
    b28c(vn)=fzero(@(x) fminus(x,vL), [83.9,85.69]);
    b29c(vn)=fzero(@(x) fminus(x,vL), [87.1,88.81]);
    b30c(vn)=fzero(@(x) fminus(x,vL), [90.2,91.94]);
     b31c(vn)=fzero(@(x) fminus(x,vL), [93.42,95.06]);
    b32c(vn)=fzero(@(x) fminus(x,vL), [96.58,98.19]);
    b33c(vn)=fzero(@(x) fminus(x,vL), [99.74,101.31]);
    b34c(vn)=fzero(@(x) fminus(x,vL), [102.9,104.44]);
    b35c(vn)=fzero(@(x) fminus(x,vL), [106.05,107.57]);
    b36c(vn)=fzero(@(x) fminus(x,vL), [109.21,110.70]);
    b37c(vn)=fzero(@(x) fminus(x,vL), [112.37,113.82]);
    b38c(vn)=fzero(@(x) fminus(x,vL), [115.52,116.95]);
    b39c(vn)=fzero(@(x) fminus(x,vL), [118.68,120.08]);
    b40c(vn)=fzero(@(x) fminus(x,vL), [121.83,123.21]);
     b41c(vn)=fzero(@(x) fminus(x,vL), [124.98,126.34]);
    b42c(vn)=fzero(@(x) fminus(x,vL), [128.14,129.45]);
    b43c(vn)=fzero(@(x) fminus(x,vL), [131.29,132.6]);
    b44c(vn)=fzero(@(x) fminus(x,vL), [134.44,135.73]);
    b45c(vn)=fzero(@(x) fminus(x,vL), [137.6,138.86]);
    b46c(vn)=fzero(@(x) fminus(x,vL), [140.75,141.99]);
    b47c(vn)=fzero(@(x) fminus(x,vL), [143.90,145.12]);
    b48c(vn)=fzero(@(x) fminus(x,vL), [147.05,148.25]);
    b49c(vn)=fzero(@(x) fminus(x,vL), [150.20,151.39]);
    b50c(vn)=fzero(@(x) fminus(x,vL),[153.36,154.52]);
    b51c(vn)=fzero(@(x) fminus(x,vL), [156.51,157.65]);
    b52c(vn)=fzero(@(x) fminus(x,vL),[159.66,160.78]);
    b53c(vn)=fzero(@(x) fminus(x,vL),[162.81,163.92]);
    b54c(vn)=fzero(@(x) fminus(x,vL), [165.96,167.05]);
    b55c(vn)=fzero(@(x) fminus(x,vL), [169.1,170.18]);
    b56c(vn)=fzero(@(x) fminus(x,vL), [172.26,173.31]);
    b57c(vn)=fzero(@(x) fminus(x,vL), [175.4,176.45]);
    b58c(vn)=fzero(@(x) fminus(x,vL), [178.56,179.58]);
    b59c(vn)=fzero(@(x) fminus(x,vL), [181.7,182.72]);
    b60c(vn)=fzero(@(x) fminus(x,vL), [184.85,185.85]);
    b61c(vn)=fzero(@(x) fminus(x,vL), [188,188.99]);

    b62c(vn)=fzero(@(x) fminus(x,vL), [191.1,192.12]);
    b63c(vn)=fzero(@(x) fminus(x,vL), [194.3,195.26]);
    b64c(vn)=fzero(@(x) fminus(x,vL), [197.45,198.39]);
    b65c(vn)=fzero(@(x) fminus(x,vL), [200.6,201.53]);
    b66c(vn)=fzero(@(x) fminus(x,vL), [203.75,204.66]);
    b67c(vn)=fzero(@(x) fminus(x,vL), [206.89,207.8]);
    b68c(vn)=fzero(@(x) fminus(x,vL), [210.04,210.93]);
    b69c(vn)=fzero(@(x) fminus(x,vL), [213.19,214.07]);
```

```
    b70c(vn)=fzero(@(x) fminus(x,vL), [216.3,217.21]);
    b71c(vn)=fzero(@(x) fminus(x,vL), [219.48,220.34]);
    b72c(vn)=fzero(@(x) fminus(x,vL), [222.63,223.48]);
    b73c(vn)=fzero(@(x) fminus(x,vL), [225.77,226.62]);
    b74c(vn)=fzero(@(x) fminus(x,vL), [228.92,229.75]);
    b75c(vn)=fzero(@(x) fminus(x,vL), [232.07,232.89]);
    b76c(vn)=fzero(@(x) fminus(x,vL), [235.22,236.03]);
    b77c(vn)=fzero(@(x) fminus(x,vL), [238.36,239.16]);
    b78c(vn)=fzero(@(x) fminus(x,vL), [241.51,242.3]);
    b79c(vn)=fzero(@(x) fminus(x,vL), [244.65,245.44]);
    b80c(vn)=fzero(@(x) fminus(x,vL), [247.8,248.57]);
    b81c(vn)=fzero(@(x) fminus(x,vL), [250.95,251.71]);
    b82c(vn)=fzero(@(x) fminus(x,vL), [254.09,254.85]);
    b83c(vn)=fzero(@(x) fminus(x,vL), [257.23,257.99]);
    b84c(vn)=fzero(@(x) fminus(x,vL), [260.38,261.12]);
    b85c(vn)=fzero(@(x) fminus(x,vL), [263.53,264.26]);
    b86c(vn)=fzero(@(x) fminus(x,vL), [266.67,267.40]);
    b87c(vn)=fzero(@(x) fminus(x,vL), [269.82,270.54]);
    b88c(vn)=fzero(@(x) fminus(x,vL), [272.96,273.67]);
    b89c(vn)=fzero(@(x) fminus(x,vL), [276.11,276.81]);
    b90c(vn)=fzero(@(x) fminus(x,vL), [279.25,279.95])
    b91c(vn)=fzero(@(x) fminus(x,vL), [282.4,283.09]);
    b92c(vn)=fzero(@(x) fminus(x,vL), [285.54,286.23]);
    b93c(vn)=fzero(@(x) fminus(x,vL), [288.69,289.36]);
    b94c(vn)=fzero(@(x) fminus(x,vL), [291.83,292.50]);
    b95c(vn)=fzero(@(x) fminus(x,vL), [294.98,295.64]);
    b96c(vn)=fzero(@(x) fminus(x,vL), [298.12,298.78]);
    b97c(vn)=fzero(@(x) fminus(x,vL), [301.27,301.92]);
    b98c(vn)=fzero(@(x) fminus(x,vL), [304.41,305.06]);
    b99c(vn)=fzero(@(x) fminus(x,vL), [307.56,308.19]);
    b100c(vn)=fzero(@(x) fminus(x,vL),[310.70,311.33]);
end
%%
%Conductivity Relaxation Diffusion Equation (function:Meshfunc.m)
%M=1-2.*(L.^2./(b1.^2.*(b1.^2+L.^2+L))).*exp(-
b1.^2.*D.*t/(T./2).^2)-2.*(L.^2./(b2.^2.*(b2.^2+L.^2+L))).*exp(-
b2.^2.*D.*t./(T./2).^2)-2.*(L.^2./(b3.^2.*(b3.^2+L.^2+L))).*exp(-
b3.^2.*D.*t/(T./2).^2)-2.*(L.^2./(b4.^2.*(b4.^2+L.^2+L))).*exp(-
b4.^2.*D.*t/(T./2).^2)-2.*(L.^2./(b5.^2.*(b5.^2+L.^2+L))).*exp(-
b5.^2.*D.*t/(T./2).^2);
M=ones(n,nLz);
for    te=1:nLz
    tL=Lz(:,te);
tb1=b1c(:,te);tb2=b2c(:,te);tb3=b3c(:,te);tb4=b4c(:,te);tb5=b5c(:,te
);tb6=b6c(:,te);tb7=b7c(:,te);tb8=b8c(:,te);tb9=b9c(:,te);tb10=b10c(
:,te);tb11=b11c(:,te);tb12=b12c(:,te);tb13=b13c(:,te);tb14=b14c(:,te
);tb15=b15c(:,te);tb16=b16c(:,te);tb17=b17c(:,te);tb18=b18c(:,te);tb
19=b19c(:,te);tb20=b20c(:,te);tb21=b21c(:,te);tb22=b22c(:,te);tb23=b
23c(:,te);tb24=b24c(:,te);tb25=b25c(:,te);tb26=b26c(:,te);tb27=b27c(
:,te);tb28=b28c(:,te);tb29=b29c(:,te);tb30=b30c(:,te);tb31=b31c(:,te
);tb32=b32c(:,te);tb33=b33c(:,te);tb34=b34c(:,te);tb35=b35c(:,te);tb
36=b36c(:,te);tb37=b37c(:,te);tb38=b38c(:,te);tb39=b39c(:,te);tb40=b
40c(:,te);tb41=b41c(:,te);tb42=b42c(:,te);tb43=b43c(:,te);tb44=b44c(
:,te);tb45=b45c(:,te);tb46=b46c(:,te);tb47=b47c(:,te);tb48=b48c(:,te
);tb49=b49c(:,te);tb50=b50c(:,te);tb51=b51c(:,te);tb52=b52c(:,te);tb
53=b53c(:,te);tb54=b54c(:,te);tb55=b55c(:,te);tb56=b56c(:,te);tb57=b
57c(:,te);tb58=b58c(:,te);tb59=b59c(:,te);tb60=b60c(:,te);tb61=b61c(
:,te);tb62=b62c(:,te);tb63=b63c(:,te);tb64=b64c(:,te);tb65=b65c(:,te
```

```
);tb66=b66c(:,te);tb67=b67c(:,te);tb68=b68c(:,te);tb69=b69c(:,te);tb
70=b70c(:,te);tb71=b71c(:,te);tb72=b72c(:,te);tb73=b73c(:,te);tb74=b
74c(:,te);tb75=b75c(:,te);tb76=b76c(:,te);tb77=b77c(:,te);tb78=b78c(
:,te);tb79=b79c(:,te);tb80=b80c(:,te);tb81=b81c(:,te);tb82=b82c(:,te
);tb83=b83c(:,te);tb84=b84c(:,te);tb85=b85c(:,te);tb86=b86c(:,te);tb
87=b87c(:,te);tb88=b88c(:,te);tb89=b89c(:,te);tb90=b90c(:,te);tb91=b
91c(:,te);tb92=b92c(:,te);tb93=b93c(:,te);tb94=b94c(:,te);tb95=b95c(
:,te);tb96=b96c(:,te);tb97=b97c(:,te);tb98=b98c(:,te);tb99=b99c(:,te
);tb100=b100c(:,te);
tD=Dc(:,te);
   M(:,te)=Meshfunc100(...
       tb1,tb2,tb3,tb4,tb5,tb6,tb7,tb8,tb9,tb10,...
       tb11,tb12,tb13,tb14,tb15,tb16,tb17,tb18,tb19,tb20,...
       tb21,tb22,tb23,tb24,tb25,tb26,tb27,tb28,tb29,tb30,...
       tb31,tb32,tb33,tb34,tb35,tb36,tb37,tb38,tb39,tb40,...
       tb41,tb42,tb43,tb44,tb45,tb46,tb47,tb48,tb49,tb50,...
       ...
       tb51,tb52,tb53,tb54,tb55,tb56,tb57,tb58,tb59,tb60,...
       tb61,tb62,tb63,tb64,tb65,tb66,tb67,tb68,tb69,tb70,...
       tb71,tb72,tb73,tb74,tb75,tb76,tb77,tb78,tb79,tb80,...
       tb81,tb82,tb83,tb84,tb85,tb86,tb87,tb88,tb89,tb90,...
       tb91,tb92,tb93,tb94,tb95,tb96,tb97,tb98,tb99,tb100,...
       tL,tD,T,t);
end
Mr=M';
MexR=Mex';
%%
%error
ERR=ones(n,nLz);
for nm=1:nLz
ERR(:,nm)=(M(:,nm)-MexR);
end
%Sum of Squares Due to Error
%Mean Squared Error
MSE=SERR_S/n;
%calculate Root Mean Squared Error (fit standard error and standard
error
%of the regression)
RMSE=MSE.^(1/2);
%COME BACK to 3D array
%A_SERR_SR=A_SERR_S';
%ERR_Map= reshape(A_SERR_SR, nD,nk);1
ERR_Map= reshape(RMSE,nD,nk);
%%
%Find minium DK  MfuncA

b1_Ans=b1c(1,minIndex);b2_Ans=b2c(1,minIndex);b3_Ans=b3c(1,minIndex);
b4_Ans=b4c(1,minIndex);b5_Ans=b5c(1,minIndex);b6_Ans=b6c(1,minIndex);
b7_Ans=b7c(1,minIndex);b8_Ans=b8c(1,minIndex);b9_Ans=b9c(1,minIndex);
b10_Ans=b10c(1,minIndex);
b11_Ans=b11c(1,minIndex);b12_Ans=b12c(1,minIndex);b13_Ans=b13c(1,min
Index);
b14_Ans=b14c(1,minIndex);b15_Ans=b15c(1,minIndex);b16_Ans=b16c(1,min
Index);
b17_Ans=b17c(1,minIndex);b18_Ans=b18c(1,minIndex);b19_Ans=b19c(1,min
Index);
b20_Ans=b20c(1,minIndex);
```

```
b21_Ans=b21c(1,minIndex);b22_Ans=b22c(1,minIndex);b23_Ans=b23c(1,min
Index);
b24_Ans=b24c(1,minIndex);b25_Ans=b25c(1,minIndex);b26_Ans=b26c(1,min
Index);
b27_Ans=b27c(1,minIndex);b28_Ans=b28c(1,minIndex);b29_Ans=b29c(1,min
Index);
b30_Ans=b30c(1,minIndex);
b31_Ans=b31c(1,minIndex);b32_Ans=b32c(1,minIndex);b33_Ans=b33c(1,min
Index);
b34_Ans=b34c(1,minIndex);b35_Ans=b35c(1,minIndex);b36_Ans=b36c(1,min
Index);
b37_Ans=b37c(1,minIndex);b38_Ans=b38c(1,minIndex);b39_Ans=b39c(1,min
Index);
b40_Ans=b40c(1,minIndex);
b41_Ans=b41c(1,minIndex);b42_Ans=b42c(1,minIndex);b43_Ans=b43c(1,min
Index);
b44_Ans=b44c(1,minIndex);b45_Ans=b45c(1,minIndex);b46_Ans=b46c(1,min
Index);
b47_Ans=b47c(1,minIndex);b48_Ans=b48c(1,minIndex);b49_Ans=b49c(1,min
Index);
b50_Ans=b50c(1,minIndex);

b51_Ans=b51c(1,minIndex);b52_Ans=b52c(1,minIndex);b53_Ans=b53c(1,min
Index);
b54_Ans=b54c(1,minIndex);b55_Ans=b55c(1,minIndex);b56_Ans=b56c(1,min
Index);
b57_Ans=b57c(1,minIndex);b58_Ans=b58c(1,minIndex);b59_Ans=b59c(1,min
Index);
b60_Ans=b60c(1,minIndex);
b61_Ans=b61c(1,minIndex);b62_Ans=b62c(1,minIndex);b63_Ans=b63c(1,min
Index);
b64_Ans=b64c(1,minIndex);b65_Ans=b65c(1,minIndex);b66_Ans=b66c(1,min
Index);
b67_Ans=b67c(1,minIndex);b68_Ans=b68c(1,minIndex);b69_Ans=b69c(1,min
Index);
b70_Ans=b70c(1,minIndex);
b71_Ans=b71c(1,minIndex);b72_Ans=b72c(1,minIndex);b73_Ans=b73c(1,min
Index);
b74_Ans=b74c(1,minIndex);b75_Ans=b75c(1,minIndex);b76_Ans=b76c(1,min
Index);
b77_Ans=b77c(1,minIndex);b78_Ans=b78c(1,minIndex);b79_Ans=b79c(1,min
Index);
b80_Ans=b80c(1,minIndex);
b81_Ans=b81c(1,minIndex);b82_Ans=b82c(1,minIndex);b83_Ans=b83c(1,min
Index);
b84_Ans=b84c(1,minIndex);b85_Ans=b85c(1,minIndex);b86_Ans=b86c(1,min
Index);
b87_Ans=b87c(1,minIndex);b88_Ans=b88c(1,minIndex);b89_Ans=b89c(1,min
Index);
b90_Ans=b90c(1,minIndex);
b91_Ans=b91c(1,minIndex);b92_Ans=b92c(1,minIndex);b93_Ans=b93c(1,min
Index);
b94_Ans=b94c(1,minIndex);b95_Ans=b95c(1,minIndex);b96_Ans=b96c(1,min
Index);
b97_Ans=b97c(1,minIndex);b98_Ans=b98c(1,minIndex);b99_Ans=b99c(1,min
Index);
b100_Ans=b100c(1,minIndex);
M_Ans=Meshfunc100(...
```

```
    b1_Ans,b2_Ans,b3_Ans,b4_Ans,b5_Ans,...
    b6_Ans,b7_Ans,b8_Ans,b9_Ans,b10_Ans,...
    b11_Ans,b12_Ans,b13_Ans,b14_Ans,b15_Ans,...
    b16_Ans,b17_Ans,b18_Ans,b19_Ans,b20_Ans,...
    b21_Ans,b22_Ans,b23_Ans,b24_Ans,b25_Ans,...
    b26_Ans,b27_Ans,b28_Ans,b29_Ans,b30_Ans,...
    b31_Ans,b32_Ans,b33_Ans,b34_Ans,b35_Ans,...
    b36_Ans,b37_Ans,b38_Ans,b39_Ans,b40_Ans,...
    b41_Ans,b42_Ans,b43_Ans,b44_Ans,b45_Ans,...
    b46_Ans,b47_Ans,b48_Ans,b49_Ans,b50_Ans,...
    ...
    b51_Ans,b52_Ans,b53_Ans,b54_Ans,b55_Ans,...
    b56_Ans,b57_Ans,b58_Ans,b59_Ans,b60_Ans,...
    b61_Ans,b62_Ans,b63_Ans,b64_Ans,b65_Ans,...
    b66_Ans,b67_Ans,b68_Ans,b69_Ans,b70_Ans,...
    b71_Ans,b72_Ans,b73_Ans,b74_Ans,b75_Ans,...
    b76_Ans,b77_Ans,b78_Ans,b79_Ans,b80_Ans,...
    b81_Ans,b82_Ans,b83_Ans,b84_Ans,b85_Ans,...
    b86_Ans,b87_Ans,b88_Ans,b89_Ans,b90_Ans,...
    b91_Ans,b92_Ans,b93_Ans,b94_Ans,b95_Ans,...
    b96_Ans,b97_Ans,b98_Ans,b99_Ans,b100_Ans,...
    L_Ans,D_Ans,T,t);

ERR_Ans=ERR_Map(Erow,Ecol);

%%
%Graph

% (cm^2/s)');ylabel ('k (cm/s)');zlabel ('Error map');

subplot (2,2,1);mesh(Dn,km,ERR_Map);grid on;...
    xlabel ('D (cm^2/s)');ylabel ('k (cm/s)');zlabel ('Root Mean
Squared Error (RMSE)');colorbar;
    axis([min(Dp),max(Dp),min(k),max(k)]);

subplot (2,2,2);surf(Dn,km,logE);
axis([min(Dp),max(Dp),min(k),max(k)]);...
    xlabel ('D (cm^2/s)');ylabel ('k (cm/s)');zlabel
('log(RMSE))');colorbar;

subplot (2,2,3);contourf(Dn,km,logE,32);...
    xlabel ('D (cm^2/s)');ylabel ('k (cm/s)');zlabel
('log(RMSE)');colorbar;

subplot (2,2,4);plot(t,Mex,'O');hold on;plot(t,M_Ans,'r');grid on;...
    axis([0,endt, 0, 1.1]);xlabel ('time(seconds)'); ylabel
('Normalized Conductivity');...
    title ('Conductivity Relaxation');legend('experimental
data','fitted curve','Location','Best');
text(max(t)/2,0.5, ['D=',num2str(D_Ans)]);text(max(t)/2,0.4,
['k=',num2str(k_Ans)]);
hold off;

rotate3d;
%determine characteristic length
lc=D_Ans/k_Ans;
```

```
%calculate time
toc;
%print data
fprintf(' \n')
fprintf('lc= %6.4f cm \n',lc);
fprintf('L= %6.4f \n',L_Ans);
fprintf('best fitted k= %8.3e cm/s \n',k_Ans);
fprintf('best fitted D= %8.3E cm^2/s \n',D_Ans);
fprintf('thickness= %6.4f cm \n',T);
fprintf('logPO2= %6.4f  \n',PO2);
fprintf('total elapsed time= %6f seconds \n',toc);
fprintf('RMSE= %8.3E \n',ERR_Ans);
```

Appendix C. LabVIEW block diagram for ECR

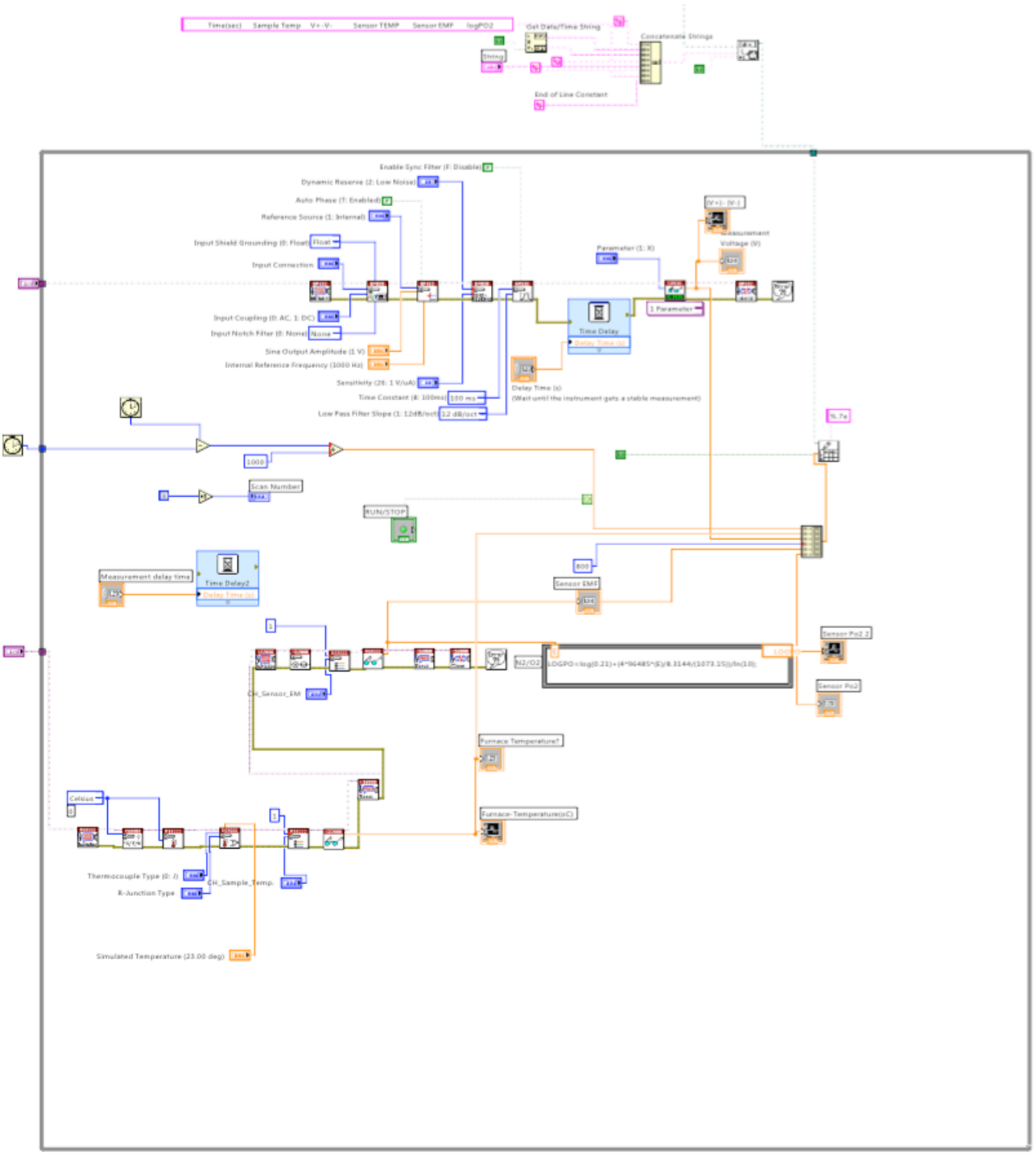

Appendix D. ECR fitting parameters for LSCF at 800ºC under PO_2=0.19-0.21

k= 4.362e-04 cm/s	lc= 0.1038 cm	thickness= 0.1960 cm
D= 4.528E-05 cm^2/s	L= 0.9441	logPO2= -0.6860
beta1= 0.84231646	beta34= 103.68121248	beta67= 207.34966832
beta2= 3.41157253	beta35= 106.82255063	beta68= 210.49119301
beta3= 6.42899448	beta36= 109.96390332	beta69= 213.63271971
beta4= 9.52358861	beta37= 113.10526934	beta70= 216.77424832
beta5= 12.64091875	beta38= 116.24664760	beta71= 219.91577876
beta6= 15.76776759	beta39= 119.38803715	beta72= 223.05731095
beta7= 18.89946856	beta40= 122.52943711	beta73= 226.19884482
beta8= 22.03397015	beta41= 125.67084670	beta74= 229.34038031
beta9= 25.17023251	beta42= 128.81226522	beta75= 232.48191733
beta10= 28.30767314	beta43= 131.95369202	beta76= 235.62345584
beta11= 31.44594068	beta44= 135.09512655	beta77= 238.76499578
beta12= 34.58481071	beta45= 138.23656825	beta78= 241.90653708
beta13= 37.72413321	beta46= 141.37801667	beta79= 245.04807970
beta14= 40.86380412	beta47= 144.51947135	beta80= 248.18962359
beta15= 44.00374900	beta48= 147.66093191	beta81= 251.33116869
beta16 47.14391318	beta49= 150.80239797	beta82= 254.47271497
beta17= 50.28425564	beta50= 153.94386919	beta83= 257.61426238
beta18= 53.42474498	beta51= 157.08564275	beta84= 260.75581089
beta19= 56.56535676	beta52= 160.22711757	beta85= 263.89736044
beta20= 59.70607167	beta53= 163.36859692	beta86= 267.03891100
beta21= 62.84687427	beta54= 166.51008055	beta87= 270.18046255
beta22= 65.98775205	beta55= 169.65156821	beta88= 273.32201504
beta23= 69.12869476	beta56= 172.79305969	beta89= 276.46356844
beta24= 72.26969395	beta57= 175.93455479	beta90= 279.60512273
beta25= 75.41074256	beta58= 179.07605330	beta91= 282.74667787
beta26= 78.55123991	beta59= 182.21755507	beta92= 285.88823383
beta27= 81.69239335	beta60= 185.35905991	beta93= 289.02979059
beta28= 84.83357931	beta61= 188.50056768	beta94= 292.17134812
beta29= 87.97479431	beta62= 191.64207823	beta95= 295.31290640
beta30= 91.11603534	beta63= 194.78359144	beta96= 298.45446540
beta31= 94.25729980	beta64= 197.92510716	beta97= 301.59602510
beta32= 97.39858543	beta65= 201.06662529	beta98= 304.73758549
beta33= 100.53989024	beta66= 204.20814571	beta99= 307.87914653
		beta100= 311.0207082

References

1 Baur, E. & Preis, H. Über Brennstoff‐Ketten mit Festleitern. *Zeitschrift für Elektrochemie und angewandte physikalische Chemie* **43**, 727-732 (1937).

2 Minh, N. Q. Ceramic fuel cells. *Journal of the American Ceramic Society* **76**, 563-588 (1993).

3 Wachsman, E. D. & Lee, K. T. Lowering the temperature of solid oxide fuel cells. *Science* **334**, 935-939, doi:10.1126/science.1204090 (2011).

4 Steele, B. C. H. Oxygen ion conductors and their technological applications.pdf>. *Materials Science and Engineering B* (1992).

5 Larminie, J. & Dicks, A. *Fuel cell systems explained*. 2nd edn, (J. Wiley, 2003).

6 Singhal, S. C. & Kendall, K. *High-temperature solid oxide fuel cells : fundamentals, design, and applicatons*. (Elsevier Advanced Technology, 2003).

7 Wachsman, E. D., Marlowe, C. A. & Lee, K. T. Role of solid oxide fuel cells in a balanced energy strategy. *Energy & Environmental Science* **5**, 5498, doi:10.1039/c1ee02445k (2012).

8 Jabbar, M. H. A. . (2012).

9 Ivers-Tiffée, E., Weber, A. & Herbstritt, D. Materials and technologies for SOFC-components. *Journal of the European Ceramic Society* **21**, 1805-1811 (2001).

10 Williams, M. C., Strakey, J. P., Surdoval, W. A. & Wilson, L. C. Solid oxide fuel cell technology development in the US. *Solid State Ionics* **177**, 2039-2044 (2006).

11 Voorhoeve, R. J. H., Remeika, J. P. & Trimble, L. E. DEFECT CHEMISTRY AND CATALYSIS IN OXIDATION AND REDUCTION OVER PEROVSKITE‐TYPE OXIDES. *Annals of the New York Academy of Sciences* **272**, 3-21 (1976).

12 Carter, S. *et al.* Oxygen transport in selected nonstoichiometric perovskite-structure oxides. *Solid State Ionics* **53**, 597-605 (1992).

13 Nitadori, T., Kurihara, S. & Misono, M. Catalytic properties of La 1− x A′ x MnO 3 (A′ = Sr, Ce, Hf). *Journal of Catalysis* **98**, 221-228 (1986).

14 Mastrikov, Y. A., Merkle, R., Heifets, E., Kotomin, E. A. & Maier, J. Pathways for oxygen incorporation in mixed conducting perovskites: A DFT-based mechanistic analysis for (La, Sr) MnO3− δ. *The Journal of Physical Chemistry C* **114**, 3017-3027 (2010).

15 Adler, S. B. Factors governing oxygen reduction in solid oxide fuel cell cathodes. *Chemical reviews* **104**, 4791-4844 (2004).

16 Mizusaki, J. *et al.* Electronic conductivity, Seebeck coefficient, defect and electronic structure of nonstoichiometric La 1− x Sr x MnO 3. *Solid state ionics* **132**, 167-180 (2000).

17 Jiang, S. P. A comparison of O 2 reduction reactions on porous (La, Sr) MnO 3 and (La, Sr)(Co, Fe) O 3 electrodes. *Solid State Ionics* **146**, 1-22 (2002).

18 Nitadori, T., Muramatsu, M. & Misono, M. Valence control, reactivity of oxygen, and catalytic activity of lanthanum strontium cobalt oxide (La2-xSrxCoO4). *Chemistry of Materials* **1**, 215-220 (1989).
19 Stevenson, J. W., Armstrong, T. R., Carneim, R. D., Pederson, L. R. & Weber, W. J. Electrochemical Properties of Mixed Conducting Perovskites La1− x M x Co1− y Fe y O 3− δ (M= Sr, Ba, Ca). *Journal of the Electrochemical Society* **143**, 2722-2729 (1996).
20 Hsiao, Y. C. & Selman, J. R. The degradation of SOFC electrodes. *Solid State Ionics* **98**, 33-38 (1997).
21 Simner, S. P., Anderson, M. D., Engelhard, M. H. & Stevenson, J. W. Degradation Mechanisms of La–Sr–Co–Fe–O3 SOFC Cathodes. *Electrochemical and Solid-State Letters* **9**, A478-A481 (2006).
22 Yokokawa, H., Tu, H., Iwanschitz, B. & Mai, A. Fundamental mechanisms limiting solid oxide fuel cell durability. *Journal of Power Sources* **182**, 400-412 (2008).
23 Benson, S. J., Waller, D. & Kilner, J. A. Degradation of La0. 6Sr0. 4Fe0. 8Co0. 2 O 3− δ in Carbon Dioxide and Water Atmospheres. *Journal of The Electrochemical Society* **146**, 1305-1309 (1999).
24 Raz, S., Sasaki, K., Maier, J. & Riess, I. Characterization of adsorbed water layers on Y 2 O 3-doped ZrO 2. *Solid State Ionics* **143**, 181-204 (2001).
25 Sakai, N. *et al.* Effect of Water on Oxygen Transport Properties on Electrolyte Surface in SOFCs I. Surface Reaction Mechanism of Oxygen Isotope Exchange on Solid Oxide Electrolytes. *Journal of the Electrochemical Society* **150**, A689-A694 (2003).
26 Zhao, Z. *et al.* A comparison on effects of CO 2 on La 0.8 Sr 0.2 MnO 3+ δ and La 0.6 Sr 0.4 CoO 3− δ cathodes. *Journal of Power Sources* **222**, 542-553 (2013).
27 Nielsen, J., Hagen, A. & Liu, Y.-L. Effect of cathode gas humidification on performance and durability of Solid Oxide Fuel Cells. *Solid State Ionics* **181**, 517-524 (2010).
28 Nielsen, J. & Mogensen, M. SOFC LSM: YSZ cathode degradation induced by moisture: An impedance spectroscopy study. *Solid State Ionics* **189**, 74-81 (2011).
29 Yokokawa, H. Thermodynamic and SIMS analyses on the role of proton/water in oxygen reduction process and related degradations in solid oxide fuel cells. *Solid State Ionics* **225**, 6-17 (2012).
30 Matsuzaki, Y. & Yasuda, I. Dependence of SOFC cathode degradation by chromium-containing alloy on compositions of electrodes and electrolytes. *Journal of The Electrochemical Society* **148**, A126-A131 (2001).
31 Van Der Heide, P. A. W. Systematic x‐ray photoelectron spectroscopic study of La1− xSrx ‐ based perovskite ‐ type oxides. *Surface and interface analysis* **33**, 414-425 (2002).
32 Ten Elshof, J. E., Bouwmeester, H. J. M. & Verweij, H. Oxidative coupling of methane in a mixed-conducting perovskite membrane reactor. *Applied Catalysis A: General* **130**, 195-212 (1995).

33 Oh, D., Gostovic, D. & Wachsman, E. D. Mechanism of La0. 6Sr0. 4Co0. 2Fe0. 8O3 cathode degradation. *Journal of Materials Research* **27**, 1992-1999 (2012).
34 Chen, A. *et al.* Effect of La2Zr2O7 on interfacial resistance in solid oxide fuel cells. *Journal of The Electrochemical Society* **157**, B1624-B1628 (2010).
35 Backhaus-Ricoult, M. SOFC–a playground for solid state chemistry. *Solid State Sciences* **10**, 670-688 (2008).
36 Haider, M. A. & McIntosh, S. Evidence for two activation mechanisms in LSM SOFC cathodes. *Journal of The Electrochemical Society* **156**, B1369-B1375 (2009).
37 Hagen, A., Neufeld, K. & Liu, Y. L. Effect of Humidity in Air on Performance and Long-Term Durability of SOFCs. *Journal of The Electrochemical Society* **157**, B1343, doi:10.1149/1.3459904 (2010).
38 Selman, Y. C. H. a. J. R. The Degradation of SOFC Electrodes. *Solid State Ionics* **98**, 33-38 (1997).
39 Zhao, Z. *et al.* High- and low- temperature behaviors of La0.6Sr0.4Co0.2Fe0.8O3−δ cathode operating under CO2/H2O-containing atmosphere. *International Journal of Hydrogen Energy* **38**, 15361-15370, doi:10.1016/j.ijhydene.2013.09.089 (2013).
40 Zhao, Z. *et al.* A comparison on effects of CO2 on La0.8Sr0.2MnO3+δ and La0.6Sr0.4CoO3−δ cathodes. *Journal of Power Sources* **222**, 542-553, doi:10.1016/j.jpowsour.2012.09.023 (2013).
41 Bucher, E., Sitte, W., Klauser, F. & Bertel, E. Impact of humid atmospheres on oxygen exchange properties, surface-near elemental composition, and surface morphology of La0.6Sr0.4CoO3−δ. *Solid State Ionics* **208**, 43-51, doi:10.1016/j.ssi.2011.12.005 (2012).
42 Guo, X. Low temperature degradation mechanism of tetragonal zirconia ceramics in water: role of oxygen vacancies. *Solid State Ionics* **112**, 113-116 (1998).
43 Jiang, S. P. Issues on development of (La,Sr)MnO3 cathode for solid oxide fuel cells. *Journal of Power Sources* **124**, 390-402, doi:10.1016/s0378-7753(03)00814-0 (2003).
44 Nielsen, J., Hagen, A. & Liu, Y. L. Effect of cathode gas humidification on performance and durability of Solid Oxide Fuel Cells. *Solid State Ionics* **181**, 517-524, doi:10.1016/j.ssi.2010.02.018 (2010).
45 Nielsen, J. & Mogensen, M. SOFC LSM:YSZ cathode degradation induced by moisture: An impedance spectroscopy study. *Solid State Ionics* **189**, 74-81, doi:10.1016/j.ssi.2011.02.019 (2011).
46 Oh, D., Gostovic, D. & Wachsman, E. D. Mechanism of La0.6Sr0.4Co0.2Fe0.8O3 cathode degradation. *Journal of Materials Research* **27**, 1992-1999, doi:10.1557/jmr.2012.222 (2012).
47 Maier, J. On the correlation of macroscopic and microscopic rate constants in solid state chemistry. *Solid State Ionics* **112**, 197-228 (1998).
48 Maier, J. *Physical chemistry of ionic materials : ions and electrons in solids*. (Wiley, 2004).

49 Adler, S. B., Lane, J. A. & Steele, B. C. H. Electrode Kinetics of Porous Mixed‐Conducting Oxygen Electrodes. *Journal of The Electrochemical Society* **143**, 3554-3564 (1996).

50 Adler, S. B. Mechanism and kinetics of oxygen reduction on porous La 1− x Sr x CoO 3− δ electrodes. *Solid State Ionics* **111**, 125-134 (1998).

51 Itoh, T. & Nakayama, M. Using in situ X-ray absorption spectroscopy to study the local structure and oxygen ion conduction mechanism in (La0.6Sr0.4)(Co0.2Fe0.8)O3− δ . *Journal of Solid State Chemistry* **192**, 38-46, doi:10.1016/j.jssc.2012.03.021 (2012).

52 Itoh, T. *et al.* Oxygen partial pressure dependence of in situ X-ray absorption spectroscopy at the Co and Fe K edges for (La0.6Sr0.4)(Co0.2Fe0.8)O3−δ. *Solid State Communications* **152**, 278-283, doi:10.1016/j.ssc.2011.11.031 (2012).

53 Zeng, Y. & Lin, Y. S. A transient TGA study on oxygen permeation properties of perovskite-type ceramic membrane. *Solid State Ionics* **110**, 209-221 (1998).

54 Preis, W. Oxygen exchange kinetics of La0.4Sr0.6FeO3?? by simultaneous application of conductivity relaxation and carrier gas coulometry. *Solid State Ionics* **175**, 393-397, doi:10.1016/j.ssi.2003.12.045 (2004).

55 Ten Elshof, J. E., Lankhorst, M. H. R. & Bouwmeester, H. J. M. Oxygen Exchange and Diffusion Coefficients of Strontium‐Doped Lanthanum Ferrites by Electrical Conductivity Relaxation. *Journal of the Electrochemical Society* **144**, 1060-1067 (1997).

56 S. Wang, P. A. W. v. d. H., C. Chavez, A.J. Jacobson, S.B. Adler. An electrical conductivity relaxation study of La0.6Sr0.4Fe0.8Co0.2O3−δ. *Solid State Ionics* **156**, 201-208 (2003).

57 J.A. Lane, S. J. B., D. Waller, J.A. Kilner. Oxygen transport in La0.6Sr0.4Co0.2Fe0.8O3−δ. *Solid State Ionics* **121**, 201-208 (1999).

58 Wang, S. High temperature properties of La0.6Sr0.4Co0.8Fe0.2O3−δ phase structure and electrical conductivity. *Solid State Ionics* **159**, 71-78, doi:10.1016/s0167-2738(03)00027-4 (2003).

59 Den Otter, M. W., Bouwmeester, H. J. M., Boukamp, B. A. & Verweij, H. Reactor flush time correction in relaxation experiments. *Journal of the Electrochemical Society* **148**, J1-J6 (2001).

60 Boukamp, B. A., den Otter, M. W. & Bouwmeester, H. J. M. Transport processes in mixed conducting oxides: combining time domain experiments and frequency domain analysis. *Journal of Solid State Electrochemistry* **8**, 592-598 (2004).

61 Crank, J. *The mathematics of diffusion*. (Clarendon Press, 1956).

62 Bouwmeester, H. J. *et al.* A novel pulse isotopic exchange technique for rapid determination of the oxygen surface exchange rate of oxide ion conductors. *Physical chemistry chemical physics : PCCP* **11**, 9640-9643, doi:10.1039/b912712g (2009).

63 M.W. den Otter, B. A. B., H.J.M. Bouwmeester. Theory of oxygen isotope exchange. *Solid State ionics* **139**, 89-94 (2001).

64 S. Lacombe, H. Z., C. Mirodatos. Oxidative Coupling of Methane over Lanthana Catalysts- II. A Mechanistic Study Using Isotope Transient Kinetics. *Journal of Catalysis* **11**, 9640-9643 (1995).
65 S.L. Shannon, J. G. G., Jr. . Characterization of Catalytic Surfaces by Isotopic-Transient Kinetics during Steady State Reaction. *Chemical Reviews* **95**, 677-695 (1995).
66 Boreskov, G. K. *Heterogeneous catalysis*. (Nova Science Publishers, 2003).
67 Hargreaves, J. S. J., Jackson, S. D. & Webb, G. *Isotopes in heterogeneous catalysis*. (Imperial College Press ;
Distributed by World Scientific Pub., 2006).
68 De Souza, R. A. & Kilner, J. A. Oxygen transport in La1−xSrxMn1−yCoyO3±δ perovskites: Part I. Oxygen tracer diffusion. *Solid State Ionics* **106**, 175-187, doi:http://dx.doi.org/10.1016/S0167-2738(97)00499-2 (1998).
69 Kilner, J. A., Skinner, S. J. & Brongersma, H. H. The isotope exchange depth profiling (IEDP) technique using SIMS and LEIS. *Journal of Solid State Electrochemistry* **15**, 861-876, doi:10.1007/s10008-010-1289-0 (2011).
70 Desouza, R., Zehnpfenning, J., Martin, M. & Maier, J. Determining oxygen isotope profiles in oxides with Time-of-Flight SIMS. *Solid State Ionics* **176**, 1465-1471, doi:10.1016/j.ssi.2005.03.012 (2005).
71 Bal'zhinimaev, B. S., Sadovskaya, E. M. & Suknev, A. P. Transient isotopic kinetics study to investigate reaction mechanisms. *Chemical Engineering Journal* **154**, 2-8, doi:10.1016/j.cej.2009.04.035 (2009).
72 Justin S. J. Hargreaves, S. D. J., Geoff Webb. Isotopes In Heterogeneous Catalysis (2006).
73 Armstrong, E. N., Duncan, K. L., Oh, D. J., Weaver, J. F. & Wachsman, E. D. Determination of Surface Exchange Coefficients of LSM, LSCF, YSZ, GDC Constituent Materials in Composite SOFC Cathodes. *Journal of The Electrochemical Society* **158**, B492, doi:10.1149/1.3555122 (2011).
74 Armstrong, E. N., Duncan, K. L. & Wachsman, E. D. Surface Exchange Coefficients of Composite Cathode Materials Using In Situ Isothermal Isotope Exchange. *Journal of The Electrochemical Society* **158**, B283, doi:10.1149/1.3528270 (2011).
75 Armstrong, E. N., Duncan, K. L. & Wachsman, E. D. Effect of A and B-site cations on surface exchange coefficient for ABO3 perovskite materials. *Physical chemistry chemical physics : PCCP* **15**, 2298-2308, doi:10.1039/c2cp42919e (2013).
76 Kan, C. C., Kan, H. H., Van Assche, F. M., Armstrong, E. N. & Wachsman, E. D. Investigating Oxygen Surface Exchange Kinetics of La[sub 0.8]Sr[sub .20]MnO[sub 3-δ] and La[sub 0.6]Sr[sub 0.4]Co[sub 0.2]Fe[sub 0.8]O[sub 3-δ] Using an Isotopic Tracer. *Journal of The Electrochemical Society* **155**, B985, doi:10.1149/1.2952542 (2008).
77 Kan, C. C. & Wachsman, E. D. Identifying Drivers of Catalytic Activity Through Systematic Surface Modification of Cathode Materials. *Journal of The Electrochemical Society* **156**, B695, doi:10.1149/1.3110983 (2009).

78 Kan, C. C. & Wachsman, E. D. Isotopic-switching analysis of oxygen reduction in solid oxide fuel cell cathode materials. *Solid State Ionics* **181**, 338-347, doi:10.1016/j.ssi.2009.12.011 (2010).
79 Henny, J. M. & Annaland, M. S. A novel pulse isotopic exchange technique for rapid determination of the oxygen surface exchange rate of oxide ion conductors. *Physical chemistry chemical physics* **11**, 9640-9643 (2009).
80 Boudart, M. & Djéga-Mariadassou, G. *Kinetics of heterogeneous catalytic reactions*. (Princeton University Press, 1984).
81 Ertl, G., Knözinger, H. & Weitkamp, J. *Handbook of heterogeneous catalysis*. (VCH, 1997).
82 Klier, K., Novakova, J. & Jiru, P. Exchange reactions of oxygen between oxygen molecules and solid oxides. *Journal of Catalysis* **2**, 479-484 (1963).
83 Boreskov, G. K., Eley, D. D., Pines, H. & Weisz, P. B. (15Academic Press, New York, 1964).
84 Chorkendorff, I. & Niemantsverdriet, J. W. *Concepts of modern catalysis and kinetics*. (Wiley-VCH, 2003).
85 Christmann, K. *Introduction to surface physical chemistry*. (Steinkopff Verlag ;
Springr-Verlag, 1991).
86 Maier, J. On the correlation of macroscopic and microscopic rate constants in solid state chemistry. *Solid State Ionics* **112**, 197-228 (1998).
87 den Otter, M. W., Bouwmeester, H. J. M., Boukamp, B. A. & Verweij, H. Reactor Flush Time Correction in Relaxation Experiments. *Journal of The Electrochemical Society* **148**, J1, doi:10.1149/1.1337604 (2001).
88 Bouwmeester, H. J. M., Den Otter, M. W. & Boukamp, B. A. Oxygen transport in La0.6Sr0.4Co1−y Fe y O3−δ. *Journal of Solid State Electrochemistry* **8**, 599-605, doi:10.1007/s10008-003-0488-3 (2004).
89 Kilner, J. A., De Souza, R. A. & Fullarton, I. C. Surface exchange of oxygen in mixed conducting perovskite oxides. *Solid State Ionics* **86–88, Part 2**, 703-709, doi:http://dx.doi.org/10.1016/0167-2738(96)00153-1 (1996).
90 Dhallu, M. & Kilner, J. A. Oxygen Transport in YSZ / LSM Composite Materials. *Journal of Fuel Cell Science and Technology* **2**, 29, doi:10.1115/1.1840840 (2005).
91 Mirodatos, C. Use of isotopic transient kinetics in heterogeneous catalysis. *Catalysis Today* **9**, 83-95, doi:http://dx.doi.org/10.1016/0920-5861(91)85011-V (1991).
92 Boreskov, G. K. Forms of oxygen bonds on the surface of oxidation catalysts. *Discussions of the Faraday Society* **41**, 263-276, doi:10.1039/DF9664100263 (1966).
93 Sadovskaya, E. M. *et al.* Kinetics of Oxygen Exchange over CeO2−ZrO2 Fluorite-Based Catalysts. *The Journal of Physical Chemistry A* **111**, 4498-4505, doi:10.1021/jp0687706 (2007).
94 Li, Y., Gerdes, K., Horita, T. & Liu, X. Surface Exchange and Bulk Diffusivity of LSCF as SOFC Cathode: Electrical Conductivity Relaxation and Isotope Exchange Characterizations. *Journal of the Electrochemical Society* **160**, F343-F350, doi:10.1149/2.044304jes (2013).

95 Yoo, J., Verma, A., Wang, S. & Jacobson, A. J. Oxygen Transport Kinetics in SrFeO[sub 3−δ], La[sub 0.5]Sr[sub 0.5]FeO[sub 3−δ], and La[sub 0.2]Sr[sub 0.8]Cr[sub 0.2]Fe[sub 0.8]O[sub 3−δ] Measured by Electrical Conductivity Relaxation. *Journal of The Electrochemical Society* **152**, A497, doi:10.1149/1.1854617 (2005).

96 Ivanov, D. V., Sadovskaya, E. M., Pinaeva, L. G. & Isupova, L. A. Influence of oxygen mobility on catalytic activity of La–Sr–Mn–O composites in the reaction of high temperature N2O decomposition. *Journal of Catalysis* **267**, 5-13, doi:10.1016/j.jcat.2009.07.005 (2009).

97 De Souza, R. A., Kilner, J. A. & Walker, J. F. A SIMS study of oxygen tracer diffusion and surface exchange in La0.8Sr0.2MnO3+δ. *Materials Letters* **43**, 43-52, doi:http://dx.doi.org/10.1016/S0167-577X(99)00228-1 (2000).

98 Mai, A. *et al.* Time-dependent performance of mixed-conducting SOFC cathodes. *Solid State Ionics* **177**, 1965-1968, doi:10.1016/j.ssi.2006.06.021 (2006).

99 Simner, S. P., Anderson, M. D., Engelhard, M. H. & Stevenson, J. W. Degradation Mechanisms of La–Sr–Co–Fe–O[sub 3] SOFC Cathodes. *Electrochemical and Solid-State Letters* **9**, A478, doi:10.1149/1.2266160 (2006).

100 Williams, M. C. Solid oxide fuel cells: fundamentals to systems. *Fuel Cells* **7**, 78-85 (2007).

101 Matsuzaki, Y. & Yasuda, I. Dependence of SOFC Cathode Degradation by Chromium-Containing Alloy on Compositions of Electrodes and Electrolytes. *Journal of The Electrochemical Society* **148**, A126, doi:10.1149/1.1339869 (2001).

102 Lee, S. N., Atkinson, A. & Kilner, J. A. Effect of Chromium on La0.6Sr0.4Co0.2Fe0.8O3- Solid Oxide Fuel Cell Cathodes. *Journal of the Electrochemical Society* **160**, F629-F635, doi:10.1149/2.099306jes (2013).

103 Jiang, S. P. & Chen, X. Chromium deposition and poisoning of cathodes of solid oxide fuel cells – A review. *International Journal of Hydrogen Energy* **39**, 505-531, doi:10.1016/j.ijhydene.2013.10.042 (2014).

104 Park, E., Taniguchi, S., Daio, T., Chou, J.-T. & Sasaki, K. Comparison of chromium poisoning among solid oxide fuel cell cathode materials. *Solid State Ionics* **262**, 421-427, doi:10.1016/j.ssi.2014.01.047 (2014).

105 Lai, S. Y., Ding, D., Liu, M., Liu, M. & Alamgir, F. M. Operando and In situ X-ray Spectroscopies of Degradation in La0.6 Sr0.4 Co0.2 Fe0.8 O3-delta Thin Film Cathodes in Fuel Cells. *ChemSusChem* **7**, 3078-3087, doi:10.1002/cssc.201402670 (2014).

106 Ebbesen, S. D., Graves, C., Hauch, A., Jensen, S. r. H. & Mogensen, M. Poisoning of Solid Oxide Electrolysis Cells by Impurities. *Journal of The Electrochemical Society* **157**, B1419, doi:10.1149/1.3464804 (2010).

107 Hayd, J., Yokokawa, H. & Ivers-Tiffee, E. Hetero-Interfaces at Nanoscaled (La,Sr)CoO3- Thin-Film Cathodes Enhancing Oxygen Surface-Exchange Properties. *Journal of the Electrochemical Society* **160**, F351-F359, doi:10.1149/2.017304jes (2013).

108 Martin, D. & Duprez, D. Mobility of surface species on oxides. 1. isotopic exchange of 18O2 with 16O of SiO2, Al2O3, ZrO2, MgO, CeO2, and CeO2-Al2O3. Activation by noble metals. Correlation with oxide basicity. *The Journal of Physical Chemistry* **100**, 9429-9438 (1996).
109 Sadovskaya, E. M., Goncharov, V. B., Gulyaeva, Y. K., Popova, G. Y. & Andrushkevich, T. V. Kinetics of the H218O/H216O isotope exchange over vanadia–titania catalyst. *Journal of Molecular Catalysis A: Chemical* **316**, 118-125, doi:10.1016/j.molcata.2009.10.009 (2010).
110 Frolov, D. D. *et al.* Oxygen exchange on nanocrystalline tin dioxide modified by palladium. *Journal of Solid State Chemistry* **186**, 1-8, doi:10.1016/j.jssc.2011.11.028 (2012).
111 Marikutsa, A. V. *et al.* Role of PdOxand RuOyClusters in Oxygen Exchange between Nanocrystalline Tin Dioxide and the Gas Phase. *The Journal of Physical Chemistry C* **117**, 23858-23867, doi:10.1021/jp408646k (2013).
112 Sadykov, V. *et al.* Oxygen mobility and surface reactivity of PrNi1−xCoxO3+δ–Ce0.9Y0.1O2−δ cathode nanocomposites. *Solid State Ionics* **262**, 707-712, doi:10.1016/j.ssi.2014.01.020 (2014).
113 Harada, K., Oishi, T., Hamamoto, S. & Ishihara, T. Lattice Oxygen Activity in Pr- and La-Doped CeO2for Low-Temperature Soot Oxidation. *The Journal of Physical Chemistry C* **118**, 559-568, doi:10.1021/jp410996k (2014).
114 Kalenik, Z. & Wolf, E. E. Transient and isotopic studies of the oxygen transport and exchange during oxidative coupling of methane on Sr promoted La2O3. *Catalysis letters* **9**, 441-449 (1991).
115 Vanasscheiv, F. & Wachsman, E. Isotopically labeled oxygen studies of the NOx exchange behavior of La2CuO4 to determine potentiometric sensor response mechanism. *Solid State Ionics* **179**, 2225-2233, doi:10.1016/j.ssi.2008.08.014 (2008).
116 Winter, E. R. S. Exchange reactions of oxides. Part IX. *Journal of the Chemical Society A: Inorganic, Physical, Theoretical*, 2889-2902, doi:10.1039/J19680002889 (1968).
117 Arai, H., Yamada, T., Eguchi, K. & Seiyama, T. Catalytic combustion of methane over various perovskite-type oxides. *Applied catalysis* **26**, 265-276 (1986).
118 Nitadori, T., Kurihara, S. & Misono, M. Catalytic properties of $La_{1-x}A_x MnO_3$(A= Sr, Ce, Hf). *Journal of Catalysis* **98**, 221-228 (1986).
119 Yang, C.-K., Yamazaki, Y., Aydin, A. & Haile, S. M. Thermodynamic and kinetic assessments of strontium-doped lanthanum manganite perovskites for two-step thermochemical water splitting. *Journal of Materials Chemistry A* **2**, 13612-13623 (2014).
120 Mizusaki, J., Tagawa, H., Naraya, K. & Sasamoto, T. Nonstoichiometry and thermochemical stability of the perovskite-type $La_{1-x}Sr_xMnO_{3-\delta}$. *Solid State Ionics* **49**, 111-118 (1991).
121 Mizusaki, J. *et al.* Electronic conductivity, Seebeck coefficient, defect and electronic structure of nonstoichiometric $La_{1-x}Sr_xMnO_3$. *Solid State Ionics* **132**, 167-180 (2000).

122 Huber, A.-K. *et al.* In situ study of activation and de-activation of LSM fuel cell cathodes – Electrochemistry and surface analysis of thin-film electrodes. *Journal of Catalysis* **294**, 79-88, doi:10.1016/j.jcat.2012.07.010 (2012).
123 Shih, S.-J. *et al.* Mn Valence Determination for Lanthanum Strontium Manganite Solid Oxide Fuel Cell Cathodes. *Journal of The Electrochemical Society* **158**, B1276, doi:10.1149/1.3625279 (2011).
124 Backhaus-Ricoult, M. SOFC – A playground for solid state chemistry. *Solid State Sciences* **10**, 670-688, doi:10.1016/j.solidstatesciences.2007.11.021 (2008).
125 Backhausricoult, M. Interface chemistry in LSM–YSZ composite SOFC cathodes. *Solid State Ionics* **177**, 2195-2200, doi:10.1016/j.ssi.2006.08.011 (2006).
126 Teraoka, Y., Honbe, Y., Ishii, J., Furukawa, H. & Moriguchi, I. Catalytic effects in oxygen permeation through mixed-conductive LSCF perovskite membranes. *Solid State Ionics* **152**, 681-687 (2002).
127 Yang, C.-K., Yamazaki, Y., Aydin, A. & Haile, S. M. Thermodynamic and kinetic assessments of strontium-doped lanthanum manganite perovskites for two-step thermochemical water splitting. *Journal of Materials Chemistry A* **2**, 13612, doi:10.1039/c4ta02694b (2014).
128 S.J. Benson, D. W., and J.A. Kilner. Degradation of LSCF in Carbon Dioxide and Water Atmospheres. *Journal of the Electrochemical Society* **146**, 1305-1309 (1999).
129 Ivers-Tiffee, J. H. a. Detailed Electrochemical Study on Nanoscaled La0.6Sr0.4CoO3-δ SOFC Thin-Film Cathodes in Dry, Humid and CO2-Containing Atmospheres. *Journal of the Electrochemical Society* **160**, F1197-F1206, doi:0013-4651/2013/160(11)/F1197/10/ (2013).
130 Kim, J. *et al.* Degradation mechanism of electrolyte and air electrode in solid oxide electrolysis cells operating at high polarization. *International Journal of Hydrogen Energy* **38**, 1225-1235, doi:10.1016/j.ijhydene.2012.10.113 (2013).
131 Isamu Yasuda, M. H. Electrical Conductivity and Chemical Diffusion Coefficient of Strontium-Doped Lanthanum Manganites. *Journal of Solid State Chemistry* **123**, 382-390 (1996).
132 Junichiro Mizusaki, H. T., Kazunori Naraya, Tadashi Sasamoto. Nonstoichiometry and thermochemical stability of the perovskite-type Lal _xSrxMnO3. *Solid State ionics* **49**, 111-118 (1991).
133 Junichiro Mizusaki, Y. Y., Hiroyuki Kamata, Kouji Ohyama, Naoya Mori, Hiroshi Takai, Hiroaki Tagawa, Masayuki Dokiya, Kazunori Narayac Tadashi Sasamoto, Hideaki Inaba, Takuya Hashimoto. Electronic conductivity, Seebeck coefficient, defect and electronic structure of nonstoichiometric La12xSrxMnO3. *Solid State Ionics* **132**, 167-180 (2000).
134 N. Yamazoe, Y. T. OXIDATION CATALYSIS OF PEROVSKITES --- RELATIONSHIPS TO BULK STRUCTURE AND COMPOSITION. *Catalysis Today* **8**, 175-199 (1990).
135 Taihei Nitadori, S. K., Makoto Misono. Catalytic Properties of La1-xA'xMnO3(A'=Sr,Ce,Hf). *Journal of Catalysis* **98**, 221-228 (1986).

136 Scheffe, J. R. & Steinfeld, A. Oxygen exchange materials for solar thermochemical splitting of H2O and CO2: a review. *Materials Today* **17**, 341-348, doi:10.1016/j.mattod.2014.04.025 (2014).
137 Scheffe, J. R., Weibel, D. & Steinfeld, A. Lanthanum–Strontium–Manganese Perovskites as Redox Materials for Solar Thermochemical Splitting of H2O and CO2. *Energy & Fuels* **27**, 4250-4257, doi:10.1021/ef301923h (2013).
138 Tan, X. *et al.* Oxygen permeation behavior of La0.6Sr0.4Co0.8Fe0.2O3 hollow fibre membranes with highly concentrated CO2 exposure. *Journal of Membrane Science* **389**, 216-222, doi:10.1016/j.memsci.2011.10.032 (2012).
139 Bucher, E., Gspan, C., Hofer, F. & Sitte, W. Sulphur poisoning of the SOFC cathode material La0.6Sr0.4CoO3-δ. *Solid State Ionics* **238**, 15-23, doi:10.1016/j.ssi.2013.03.007 (2013).
140 Yang, Q. & Lin, J. Y. S. Fixed-bed performance for production of oxygen-enriched carbon dioxide stream by perovskite-type ceramic sorbent. *Separation and Purification Technology* **49**, 27-35, doi:10.1016/j.seppur.2005.08.004 (2006).
141 Horita, T. *et al.* Imaging of Oxide Ionic Diffusion at Cathode/Interlayer/Electrolyte Interfaces in Solid Oxide Fuel Cells: Effects of Long-Term Operation. *Journal of the Electrochemical Society* **159**, F476-F481, doi:10.1149/2.069208jes (2012).
142 Sakai, N. *et al.* Application of SIMS analyses on oxygen transport in SOFC materials. *Applied Surface Science* **252**, 7045-7047, doi:10.1016/j.apsusc.2006.02.187 (2006).
143 Z. Kalenik, E. E. W. Transient and Isotopic Studies of the Oxygen Transport and Exchange During Oxidative Coupling of Methane on Sr Promoted La2O3. *Catalysis Letters* **9**, 441-450 (1991).
144 K. Klier, J. N., P. Jiru. Exchange Reactions of Oxygen between Oxygen Molecules and Solid Oxides. *Journal of Catalysis* **2**, 479-484 (1963).
145 Boreskov. *Advanced Catalysis* **15** (1964).
146 Backhaus-Ricoult, M. *et al.* In-situ study of operating SOFC LSM/YSZ cathodes under polarization by photoelectron microscopy. *Solid State Ionics* **179**, 891-895, doi:10.1016/j.ssi.2008.02.033 (2008).
147 Speight, J. G. *Lange's handbook of chemistry*. Vol. 1 (McGraw-Hill New York, 2005).
148 Chueh, W. C. & Haile, S. M. Electrochemistry of mixed oxygen ion and electron conducting electrodes in solid electrolyte cells. *Annual review of chemical and biomolecular engineering* **3**, 313-341, doi:10.1146/annurev-chembioeng-073009-101000 (2012).
149 Gorte, R. J. & Vohs, J. M. Catalysis in solid oxide fuel cells. *Annual review of chemical and biomolecular engineering* **2**, 9-30, doi:10.1146/annurev-chembioeng-061010-114148 (2011).
150 Li, Y., Gemmen, R. & Liu, X. Oxygen reduction and transportation mechanisms in solid oxide fuel cell cathodes. *Journal of Power Sources* **195**, 3345-3358, doi:10.1016/j.jpowsour.2009.12.062 (2010).

151 Liu, M., Lynch, M. E., Blinn, K., Alamgir, F. M. & Choi, Y. Rational SOFC material design: new advances and tools. *Materials Today* **14**, 534-546, doi:10.1016/s1369-7021(11)70279-6 (2011).
152 Yokokawa, H. Overview of Intermediate-Temperature Solid Oxide Fuel Cells. 17-43, doi:10.1007/978-0-387-77708-5_2 (2009).
153 Harrison, W. A. Oxygen atoms and molecules at La 1− x Sr x MnO 3 surfaces. *Physical Review B* **81**, 045433 (2010).
154 Y.L. Huang, C. P., E. D. Wachsman. Oxygen Isotope Exchange Experiments on SOFC Cathode Materials. (2015).
155 Barbucci, A., Carpanese, P., Cerisola, G. & Viviani, M. Electrochemical investigation of mixed ionic/electronic cathodes for SOFCs. *Solid State Ionics* **176**, 1753-1758, doi:10.1016/j.ssi.2005.04.027 (2005).
156 Chroneos, A., Vovk, R. V., Goulatis, I. L. & Goulatis, L. I. Oxygen transport in perovskite and related oxides: A brief review. *Journal of Alloys and Compounds* **494**, 190-195, doi:10.1016/j.jallcom.2010.01.071 (2010).
157 Fleig, J. SOLIDOXIDEFUELCELLCATHODES: Polarization Mechanisms and Modeling of the Electrochemical Performance. *Annual Review of Materials Research* **33**, 361-382, doi:10.1146/annurev.matsci.33.022802.093258 (2003).
158 Kawada, T. Perovskite Oxide for Cathode of SOFCs. 147-166, doi:10.1007/978-0-387-77708-5_7 (2009).
159 Lee, Y.-L., Kleis, J., Rossmeisl, J., Shao-Horn, Y. & Morgan, D. Prediction of solid oxide fuel cell cathode activity with first-principles descriptors. *Energy & Environmental Science* **4**, 3966, doi:10.1039/c1ee02032c (2011).
160 Pavone, M., Ritzmann, A. M. & Carter, E. A. Quantum-mechanics-based design principles for solid oxide fuel cell cathode materials. *Energy & Environmental Science* **4**, 4933, doi:10.1039/c1ee02377b (2011).
161 Sun, C., Hui, R. & Roller, J. Cathode materials for solid oxide fuel cells: a review. *Journal of Solid State Electrochemistry* **14**, 1125-1144, doi:10.1007/s10008-009-0932-0 (2009).
162 Shannon, S. L. & Goodwin Jr, J. G. Characterization of catalytic surfaces by isotopic-transient kinetics during steady-state reaction. *Chemical reviews* **95**, 677-695 (1995).
163 Boreskov, G. K. Forms of oxygen bonds on the surface of oxidation catalysts. *Discussions of the Faraday Society* **41**, 263-276 (1966).
164 Doornkamp, C., Clement, M. & Ponec, V. The isotopic exchange reaction of oxygen on metal oxides. *Journal of Catalysis* **182**, 390-399 (1999).
165 Y. L. Huang, C. P., E. D. Wachsman. Fundamental impact of humidity on SOFC cathodes Degradation Mechanism. (2015).
166 Pietrowski, M. J., De Souza, R. A., Fartmann, M., ter Veen, R. & Martin, M. Oxygen Isotope Transport Properties of Yttria-Stabilized Zirconia (YSZ) in O2- and H2O-Containing Atmospheres. *Fuel Cells*, n/a-n/a, doi:10.1002/fuce.201300087 (2013).
167 Kudo, H., Yashiro, K., Hashimoto, S.-i., Amezawa, K. & Kawada, T. Simulation of oxygen diffusion process on electrical conductivity relaxation. *Solid State Ionics* **262**, 696-700, doi:10.1016/j.ssi.2014.01.009 (2014).

168 Mauvy, F. *et al.* Chemical oxygen diffusion coefficient measurement by conductivity relaxation—correlation between tracer diffusion coefficient and chemical diffusion coefficient. *Journal of the European Ceramic Society* **24**, 1265-1269, doi:10.1016/s0955-2219(03)00500-4 (2004).
169 van der Haar, L. M., den Otter, M. W., Morskate, M., Bouwmeester, H. J. M. & Verweij, H. Chemical Diffusion and Oxygen Surface Transfer of La[sub 1−x]Sr[sub x]CoO[sub 3−δ] Studied with Electrical Conductivity Relaxation. *Journal of The Electrochemical Society* **149**, J41, doi:10.1149/1.1446874 (2002).
170 Ciucci, F. Electrical conductivity relaxation measurements: Statistical investigations using sensitivity analysis, optimal experimental design and ECRTOOLS. *Solid State Ionics* **239**, 28-40, doi:10.1016/j.ssi.2013.03.020 (2013).
171 Cox-Galhotra, R. A. & McIntosh, S. Unreliability of simultaneously determining kchem and Dchem via conductivity relaxation for surface-modified La0.6Sr0.4Co0.2Fe0.8O3−δ. *Solid State Ionics* **181**, 1429-1436, doi:10.1016/j.ssi.2010.08.006 (2010).
172 Li, Y., Gerdes, K., Diamond, H. & Liu, X. An improved method to increase the predictive accuracy of the ECR technique. *Solid State Ionics* **204-205**, 104-110, doi:10.1016/j.ssi.2011.09.017 (2011).
173 Katsuki, M., Wang, S., Dokiya, M. & Hashimoto, T. High temperature properties of $La_{0.6}Sr_{0.4}Co_{0.8}Fe_{0.2}O_{3-\delta}$ oxygen nonstoichiometry and chemical diffusion constant. *Solid State Ionics* **156**, 453-461 (2003).
174 Minh, N. Q. & Takahashi, T. *Science and technology of ceramic fuel cells*. (Elsevier, 1995).
175 Jiang, S. P. A comparison of O_2 reduction reactions on porous (La, Sr) MnO_3 and (La, Sr)(Co, Fe) O_3 electrodes. *Solid State Ionics* **146**, 1-22 (2002).
176 Lynch, M. E. *et al.* Enhancement of La0.6Sr0.4Co0.2Fe0.8O3-δ durability and surface electrocatalytic activity by La0.85Sr0.15MnO3±δ investigated using a new test electrode platform. *Energy & Environmental Science* **4**, 2249, doi:10.1039/c1ee01188j (2011).
177 Lee, S., Miller, N. & Gerdes, K. Long-Term Stability of SOFC Composite Cathode Activated by Electrocatalyst Infiltration. *Journal of the Electrochemical Society* **159**, F301-F308, doi:10.1149/2.067207jes (2012).
178 Li, Y., Gerdes, K. & Liu, X. Oxygen Transport Kinetics in Infiltrated SOFCs Cathode by Electrical Conductivity Relaxation Technique. *Journal of the Electrochemical Society* **160**, F554-F559, doi:10.1149/2.056306jes (2013).
179 Poulidi, D. *et al.* Electrochemical promotion of a Pt catalyst supported on La0.6Sr0.4Co0.2Fe0.8O3−δ hollow fibre membranes. *Solid State Ionics* **225**, 382-385, doi:10.1016/j.ssi.2012.03.010 (2012).
180 Ding, D., Li, X., Lai, S. Y., Gerdes, K. & Liu, M. Enhancing SOFC cathode performance by surface modification through infiltration. *Energy & Environmental Science* **7**, 552, doi:10.1039/c3ee42926a (2014).
181 Zhu, X. *et al.* Development of La0.6Sr0.4Co0.2Fe0.8O3−δ cathode with an improved stability via La0.8Sr0.2MnO3-film impregnation. *International*

Journal of Hydrogen Energy **38**, 5375-5382, doi:10.1016/j.ijhydene.2013.02.091 (2013).

182 Mutoro, E., Crumlin, E. J., Biegalski, M. D., Christen, H. M. & Shao-Horn, Y. Enhanced oxygen reduction activity on surface-decorated perovskite thin films for solid oxide fuel cells. *Energy & Environmental Science* **4**, 3689, doi:10.1039/c1ee01245b (2011).

183 Huang, Y., Vohs, J. M. & Gorte, R. J. SOFC Cathodes Prepared by Infiltration with Various LSM Precursors. *Electrochemical and Solid-State Letters* **9**, A237, doi:10.1149/1.2183867 (2006).

184 White, C. W., McHargue, C. J., Sklad, P. S., Boatner, L. A. & Farlow, G. C. Ion implantation and annealing of crystalline oxides. *Materials science reports* **4**, 41-146 (1989).

185 Chen, C. H. *et al.* Ion implantation induced enhancement of magnetoresistance in La0. 67Ca0. 33MnO3. *Applied physics letters* **69**, 3089-3091 (1996).

186 Biersack, J. P. & Haggmark, L. G. A Monte Carlo computer program for the transport of energetic ions in amorphous targets. *Nuclear Instruments and Methods* **174**, 257-269 (1980).

187 Ciucci, F. A statistical perspective on oxygen diffusion and surface exchange experiments: Sensitivity analysis, parameter estimation and robust optimal experimental design. *Solid State Ionics* **232**, 97-105, doi:10.1016/j.ssi.2012.11.013 (2013).

188 Nesbitt, H. W. & Banerjee, D. Interpretation of XPS Mn (2p) spectra of Mn oxyhydroxides and constraints on the mechanism of MnO2 precipitation. *American Mineralogist* **83**, 305-315 (1998).

Bibliography

Yi-Lin Huang was born in Taipei, Taiwan. He went to National Tsing-Hua University, Taiwan for his bachelor's and master degree in Materials Science & Engineering. During these years, he enjoyed research and built up a solid background in the surface/interface science and the use of synchrotron radiation source. After the mandatory military service in Taiwan, he joined Institute of Physics, Academia Sinica, Taiwan to continue his research work on the synthesis of high purity materials and solid state physics.

To pursue the formal education, he moved to the states in 2009 and attended the University of Maryland in Materials Science & Engineering for the degree of doctor of philosophy. He is interested in clean energy and his PhD research focuses on characterizing the catalytic and kinetic behavior of metal oxides for different applications.

He is dedicated to bringing happiness to people surrounding him and he wishes his work could contribute to the human future.